

Aging Mechanisms of Electrodes in LiFePO₄/Graphite Batteries

Alex Juul Søggaard
Jonas Ilum Sørensen

A thesis submitted in partial fulfillment of the
requirements for the degree of

**Master of Science (MSc) in Engineering
(Materials and Nanotechnology) with
specialization in nanomaterials and
nanophysics**

at Aalborg University

Faculty of Engineering and Science
Department of Materials and Production



AALBORG UNIVERSITY
STUDENT REPORT

3rd June, 2021



AALBORG UNIVERSITY

STUDENT REPORT

Ninth and Tenth Semester

Engineering and Science

Nanotechnology

Skjernvej 4A

9220 Aalborg East

Title:

Aging Mechanisms of Electrodes in
LiFePO₄/Graphite Batteries

Project:

Master's Thesis

Project period:

September 2020 - June 2021

Project group:

MNNF9/10 5.321A

Members:

Alex Juul Søgaaard

Jonas Ilum Sørensen

Supervisor:

Kjeld Pedersen

Number of pages: 121

Appendix: 3

Ended: 03-06-2021

Abstract:

In this master's thesis a pristine, a calendar-aged, and multiple cycle-aged commercial cylindrical LiFePO₄/Graphite batteries are investigated post-mortem to analyse the effect of the cycle depth and the average state-of-charge at constant temperature, to the aging of the electrodes. A methodology for post-mortem analysis of LiFePO₄/Graphite batteries was established which includes the disassembly process and procedure for preparing the electrodes for further examination. The electrodes were examined with scanning electron microscopy, energy dispersive x-ray spectroscopy, Raman spectroscopy, cyclic voltammetry, chronopotentiometry, and electrochemical impedance spectroscopy. For the graphite anodes, it is reported that a larger cycle depth enhances the formation of cracks and a high SOC_{avg} accelerates the loss of lithium ions. Changes in the elemental composition of the cathodes are proposed to be correlated to structural changes and an increase in the resistance of the carbon coating on the cathodes is reported for the cycle-aged cases. It is suggested that the majority of the capacity fade stems from the aging of the anode. This work may be used as a basis for further investigation of the effect of larger cycle depth, of structural changes to the cathode, and of the composition of the solid electrolyte interface layer.

Resumé

Verdenssamfundet står på tærsklen til en ny energialder, hvor bæredygtige kilder og løsninger er i højsædet. En række af disse kilder, herunder sol- og vindenergi, er ofre for intermitterende produktion, hvilket medfører pålidelighedsproblemer på elnettet. Der forskes i løsninger på pålidelighedsproblemet og på den voksende belastning af elnettet forårsaget af overgangen til en elektrificeret transportsektor.

Genopladelige batterier eller akkumulatorer, især lithium-ion akkumulatorer, er blevet foreslået som en attraktiv løsning til begge problemstillinger. Især indenfor transportsektoren er behovet for akkumulatorer accelereret de seneste år og det lader ikke til at stagnere foreløbigt. Selvom elektrificeringen ved brug af akkumulatorer tilsyneladende er succesfuld giver den anledning til en række problemstillinger. Især kapaciteten, levetiden, bæredygtigheden og ydeevnen af de nuværende akkumulatorer er væsentlige områder, man ønsker at forbedre.

I dette kandidatspeciale er lithium-ion akkumulatorer, baseret på lithium-jern-fosfat / grafit kemien, blevet undersøgt. Denne kemi er særdeles velegnet til applikationer, hvor en høj effekt er ønsket, eftersom denne kemi tillader en høj afladningsrate. Formålet med afhandlingen var at forstå hvordan akkumulatorernes elektroder aldres, når de kontinuerligt bliver op- og afladet. Batterier degraderet med en accelereret aldringsmetodologi ved konstant temperatur, men med forskellig op- og afladningsdybde, samt forskellig gennemsnitlig ladningstilstand, blev adskilt post-mortem. Et tilsvarende batteri, der ikke gennemgik den accelererede test metodologi, blev brugt som reference. Herefter blev elektroderne undersøgt med mikroskopi, spektroskopi og elektrokemiske teknikker. Elektrodernes morfologi og elementare sammensætning blev undersøgt henholdsvis med et skannende elektron mikroskop og energidispersiv røntgenspektroskopi, imens deres krystallinitet og densitet af krystaldefekter blev undersøgt med Raman spektroskopi. I tillæg til dette blev elektrodernes elektrokemiske interkalationsreaktioner undersøgt med cyklisk voltammetri og lithium-jern-fosfat elektrodernes kapacitet blev bestemt med kronopotentiometri. For at evaluere elektrodernes ydeevne blev elektrokemisk impedansspektroskopi brugt til at kvantificere deres elektriske modstandsbidrag.

Baseret på resultaterne fra de eksperimentelle metoder foreslåes det, at en større op- og afladningsdybde forstærker formationen af revner i grafit elektroderne og at en høj gennemsnitlig ladningstilstand accelererer kapacitetstabet af batteriet gennem vækst af et faststof-elektrolyt kontaktfladelag. Desuden antyder resultaterne for lithium-jern-fosfat elektroderne en sammenhæng mellem deres materialestruktur og elementare sammensætning, samt at den elektriske modstand i deres kulstofbelægning er større i de degraderede tilfælde i forhold til referencen. På baggrund af resultaterne

fremsættes hypotesen, at størstedelen af kapacitetstabet i lithium-jern-fosfat / grafit akkumulatorer tildeles aldring af grafit elektroden og især til væksten af faststof-elektrolyt kontaktfladelaget.

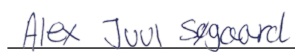
Resultaterne i dette kandidatspeciale kan bruges som belæg for yderligere undersøgelser: af effekten af op- og afladningsdybden, af formationen af revner i grafit elektroden, af de materialestrukturelle ændringer i lithium-jern-fosfat og af den molekulære og elementare sammensætning af faststof-elektrolyt kontaktfladelaget.

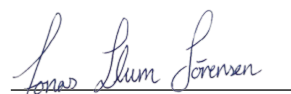
Preface

This Master's thesis was written as a 60 ECTS project during the 9th and 10th semester as part of the authors fulfillment of the requirements for the degree of Master of Science (MSc) in Engineering (Materials and Nanotechnology) with specialization in nanomaterials and nanophysics at the Department of Materials and Production at Aalborg University. The IEEE citation style is used to refer to literature. References to equations and figures are numbered according to their chapter and section, and are abbreviated as Eq. (#) and Fig. #, respectively.

Acknowledgements

We would like to thank our supervisor **Kjeld Pedersen** for his guidance throughout the thesis process. We would like to acknowledge our co-supervisors Associate Professor **Daniel-Ioan Stroe** and Associate Professor **Leonid Gurevich** for being invaluable with respect to guidance on the full battery level and on the microscopic material level, respectively. Additionally, we would like to thank our close colleagues PhD students **Yaqi Li** and **Jia Guo** for professional sparing and a good working relationship.


Alex Juul Søgaard


Jonas Ilum Sørensen

List of Abbreviations

1D	One-dimensional
CV	Cyclic voltammetry
CE	Counter electrode
CNLS	Complex non-linear least-squares
CP	Chronopotentiometry
CPE	Constant phase element
EEC	Equivalent electrical circuit
EIS	Electrochemical impedance spectroscopy
EOL	End-of-life
EV	Electric vehicle
FEC	Full equivalent cycles
ICE	Initial coulombic efficiency
IEC	International Electrotechnical Commission
LAM	Loss of active material
LIB	Lithium-ion battery
LLI	Loss of Lithium ion inventory
LM	Levenberg-Marquardt
NLS	Non-linear least-squares
RE	Reference electrode
RS	Raman spectroscopy
SEI	Solid electrolyte interface
SEM	Scanning electron microscope
SOC	State-of-charge
SOH	State-of-health
TC	Test case
TLM	Transmission line model
WE	Working electrode

Chemical Abbreviations

DEC	Diethyl carbonate
DMC	Dimethyl carbonate
EC	Ethylene carbonate
LFP	Lithium iron phosphate, LiFePO_4
LiTFSI	Lithium bis(trifluoromethanesulfonyl)imide, $\text{Li}[\text{N}(\text{SO}_2\text{CF}_3)_2]$
LPF	Lithium phosphorodifluoridate, LiPO_2F_2
NCA	Lithium nickel cobalt aluminium oxide, LiNiCoAlO_2
NMC	Lithium nickel manganese cobalt oxide, LiNiMnCoO_2
PE	Polyethylene
PP	Polypropylene
VC	Vinylene carbonate

Contents

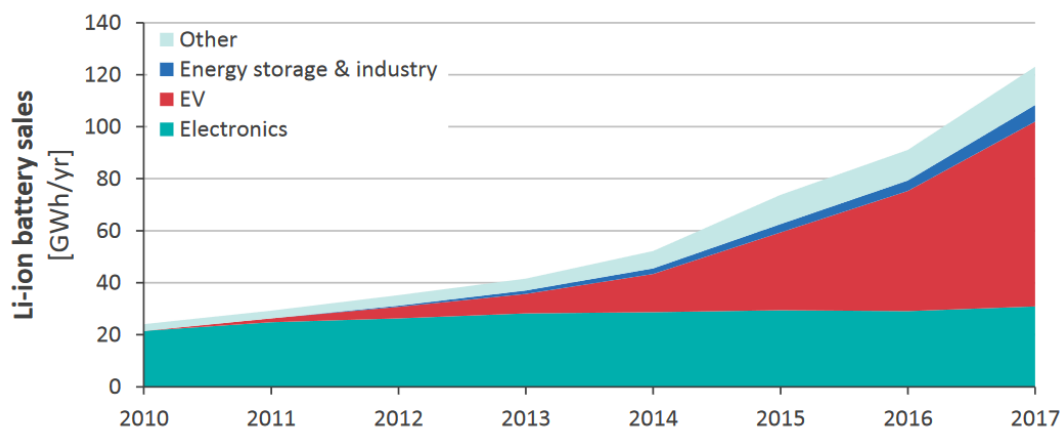
1	Introduction	1
1.1	The History of the Lithium-Ion Battery	2
1.2	The Motivation and Scope of the Project	5
2	The Electrochemical Cell	7
2.1	Terminology	9
2.2	Primary vs. Secondary Batteries	10
3	Working Principle of Li-ion Battery	13
3.1	Lithium-ion batteries	13
3.2	Graphite Intercalation Compound Anode	17
3.2.1	Intercalation Mechanisms and Structural Changes of Graphite .	18
3.2.2	Solvent Co-Intercalation	20
3.2.3	Irreversible Charge Loss	22
3.2.4	Improvement of the Anode and Future Aspects	22
3.3	Lithium Iron Phosphate Cathode	24
3.3.1	Lithium Insertion and Extraction Mechanism	24
3.3.2	Electrochemical Properties of LiFePO_4	26
3.4	Nonaqueous Electrolyte and Solid-Electrolyte Interface	29
3.4.1	Electrochemical Stability of the Electrolyte and the Solid Elec- trolyte Interface	30
3.5	Polyolefin Separator	35
4	Aging Mechanisms of LFP/G Lithium Ion Battery	37
4.1	Cracking of Graphite Particles	38
4.2	Growth of SEI Film on Anode	39
4.2.1	Iron Dissolution and Precipitation	39
4.3	Formation of a Covering Layer on the Anode	40
4.4	Structural Degradation of LiFePO_4 Cathode	41
4.4.1	Agglomeration of Carbon Black Coating	42
5	Experimental Methods	43
5.1	Disassembly methodology	46
5.2	Surface Morphology Analysis	47
5.3	Energy Dispersive X-ray Spectroscopy	48
5.4	Raman Spectroscopy	49
5.4.1	Statistical Analysis of the RS Maps	51

5.5	Electrochemical Cell Setup and -Techniques	51
5.5.1	Cyclic Voltammetry	53
5.5.2	Chronopotentiometry	56
5.5.3	Electrochemical Impedance Spectroscopy	56
6	Experimental Results	61
6.1	Scanning Electron Microscopy Analysis	61
6.2	Energy Dispersive X-Ray Spectroscopy	66
6.3	Raman Spectroscopy	70
6.4	Cyclic Voltammetry	81
6.5	Chronopotentiometry	85
6.6	Electrochemical Impedance Spectroscopy	86
7	Discussion	91
7.1	Morphology and Structural Change to Graphite Anodes	91
7.2	Mechanism for Capacity Fade of the Anode	93
7.3	Composition of SEI Layer and Possible Implications	94
7.4	Electrochemical Performance of LiFePO_4	95
7.5	Degradation of the Cathode's Carbon Coating	97
7.6	Iron Dissolution and Structural Changes to LiFePO_4	97
7.7	Capacity Fade for $\text{LiFePO}_4/\text{Graphite}$ Batteries	98
8	Conclusion	101
	Bibliography	105
A	Theoretical Concepts, Methods, and Derivations	115
A.1	The Electrical Potential Difference	115
A.2	Cyclic Voltammetry (CV)	116
A.3	Electrochemical Impedance Spectroscopy	127
A.4	Non-Linear Least-Squares Fitting	145
A.5	Calculating the FWHM for Raman spectroscopy	152
B	Equipment and Procedures	155
B.1	Glovebox Assembly	155
B.2	Procedure: Purging of Glovebox	159
B.3	Procedure: Disassembly of Batteries	160
B.4	Procedure: Electrochemical Measurements	161
C	Additional Results	163
C.1	SEM Micrographs	163
C.2	Mean Anode Particle Size	164
C.3	Raman Spectroscopy Maps	167
C.4	Energy Dispersive X-ray Spectroscopy	173

1 Introduction

We have stepped into a new century which will be defining for our future existence and livelihood. Our ingenuity and determination is in a race against time to limit the effects of and possibly halt the climate changes. With only 100 seconds to midnight on the doomsday clock [1] the transition to renewable and sustainable energy sources such as wind, and solar power is vital to win the race. The transition has proven to be difficult due to the intermittency of these energy sources but the solution may be found in grid energy storage such as batteries or through Power-to-X. Both cases store the excess energy from the renewable sources available at certain times of the day or year by converting it to chemical energy, to a fuel such as methane or methanol, to thermal energy with heat pumps, to potential energy as in hydro power reservoirs, etc. Some conversions may not be feasible in certain parts of the world and therefore the transition to renewable energy sources relies on a multitude of these conversion techniques. Another possibility is to use electrical vehicles as distributed energy resources as they for the majority of the day is in parked condition [2, 3].

The development of rechargeable batteries is fueled by both the intermittency issue with renewable energy sources, by the electrification of the transportation sector, and by our demand for increased battery life for portable devices. The increasing demand for lithium-ion batteries is apparent from the evolution in sales from 2010 to 2017 as seen in Fig. 1.1a and from the projections seen in Fig. 1.1b.



(a)

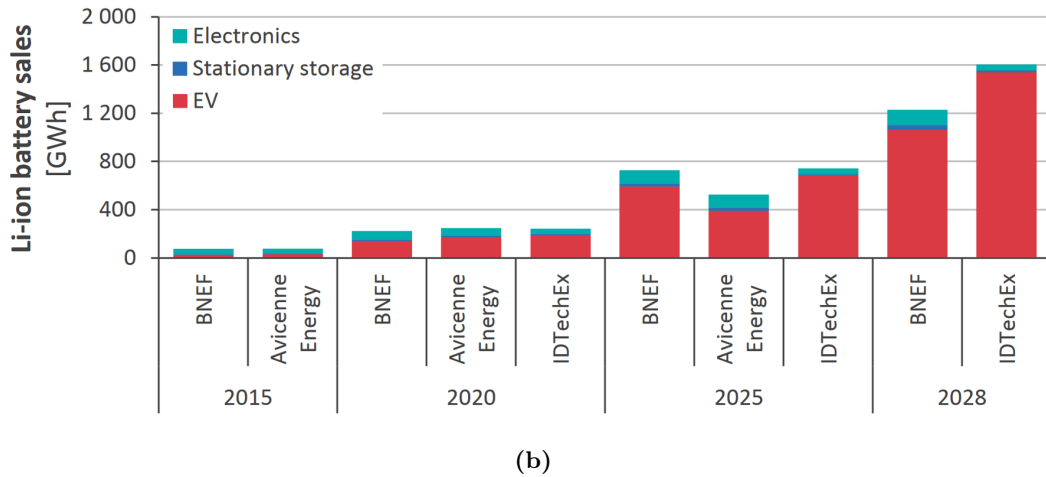


Figure 1.1: Global lithium-ion battery sales. (a) Evolution from 2010 to 2017 where *electronics* includes portable electronics, and *EV* includes battery- and plug-in electric vehicles. *Energy storage & industry* includes stationary storage, uninterruptible power supplies, telecom batteries, and industry. *Other* includes medical devices, power tools, electric bikes, and gardening tools. (b) Projections from research organisations for lithium-ion battery sales in electronics, stationary storage, and electric vehicles. Figures are reused from "*JRC science for policy report: Li-ion batteries for mobility and stationary storage applications*" [4].

1.1 The History of the Lithium-Ion Battery

The origin of the rechargeable battery is said to be found in the oil crisis in the western world in the 1970s which revealed the fragility of their dependence on imported oil. This propelled the investigation of both solar and wind power forward and due to their intermittency it encouraged the improvement of rechargeable batteries [5]. The foundations for the rechargeable lithium battery was laid down in the late 1960s with the commercialisation of non-rechargeable lithium batteries [6]. The transition to rechargeable lithium batteries was known to require an intercalation compound which could accommodate lithium ions. In 1976 M. Stanley Whittingham from Exxon Mobil Corporation reported promising performance results for a secondary lithium battery with a lithium titanium disulfide, LiTiS_2 , cathode, a lithium metal anode, and an organic liquid electrolyte. The battery however faced a severe shortcoming upon repeated cycling as dendrites of lithium grew from the anode to the cathode and thereby resulted in an internal short circuit. This meant that the anode could not be made from lithium metal as long as a liquid electrolyte was used. The solution to the dendrite formation was found in a proposal made by Michel Armand in 1970; a rocking-chair battery i.e. a rechargeable lithium battery wherein lithium ions are transported between intercalation compound electrodes. This rocking-chair mechanism gave the lithium-ion batteries their name as lithium ions are transported back and forth between the anode and cathode. [6]

In the same year as M. Stanley Whittingham developed the LiTiS_2/Li battery, J. O. Besenhard and G. Eichinger achieved intercalation of lithium ions into graphite

with stoichiometry up to LiC_6 but due to the lack of a suitable electrolyte which prevented co-intercalation and thereby exfoliation, graphite was not considered to be a viable option for the anode. However, in 1983 Rachid Yazami and co-workers successfully achieved reversible intercalation of lithium ions in graphite using a solid polymer electrolyte [7]. The dream of making a lithium-ion battery with a liquid electrolyte utilising the rocking-chair concept was not abandoned and with continuous research through the 1980s a solution emerged [6].

A research team led by Yoshio Nishi at Sony Corporation found that both soft and hard carbon could be used as anode materials since they were compatible with the commonly used propylene carbonate electrolyte solvent [6, 8]. Simultaneously, key research in lithium cobalt oxide, LiCoO_2 , as a cathode material was conducted by John B. Goodenough and his group at the University of Oxford in 1980 and thus the way for commercialisation was paved [9]. In the midst of success another problem emerged, the high potential of the LiCoO_2 cathode made it difficult to find a suitable material for the current collector other than the precious metals like gold and platinum. The issue was solved by Akira Yoshino's group when they found that aluminium forms a passivation layer upon contact with the electrolyte [10].

Only 14 years after the initial work by M. Stanley Whittingham, Sony Corporation commercialised a lithium-ion battery with a LiCoO_2 cathode, a soft carbon anode, and an electrolyte composed of lithium hexafluorophosphate, LiPF_6 , dissolved in propylene- and diethyl carbonate. The battery featured an energy density of 80 Wh kg^{-1} and a voltage of 4.1 V [8]. It however had multiple drawbacks, especially the cyclic performance due to the soft carbon anode. It suffered from the same exfoliation problem, however not as severe, as graphite. In 1990 hard carbon was not available commercially due to a lack of suitable precursors so Yoshio Nishi's team at Sony Corporation set out to develop a synthesis method for a precursor. In 1992 Sony released a second generation of their lithium-ion batteries where they had adopted the hard carbon as anode. The battery featured a voltage of 4.2 V and an energy density of 120 Wh kg^{-1} . [8]

Simultaneously with Sony's launch of the first commercial lithium-ion battery, J. R. Dahn and co-workers found that reversible intercalation of lithium ions into graphite was possible when using ethylene carbonate (EC) as co-solvent due to the formation of a solid electrolyte interface (SEI) film. This launched the quest for finding electrolyte compositions of EC which were suitable for 4 V cathodes, had great ionic conductivity, and electrode wettability. In 1993, D. Guyomard and J. M. Tarascond found that a mixture of EC and dimethyl carbonate (DMC) had all of the aforementioned properties and was compatible with graphite. Therefore, almost all lithium-ion batteries after 1994 have had graphite anodes. In the following years, much effort was put into improving the first cycle Coulombic efficiency, the reversible capacity, and the cycle life of lithium-ion batteries. This was done by inter alia stabilising the SEI formation with electrolyte additives and improving the performance of the electrodes. [7]

The early history of the lithium-ion battery, is outlined in Fig. 1.2.

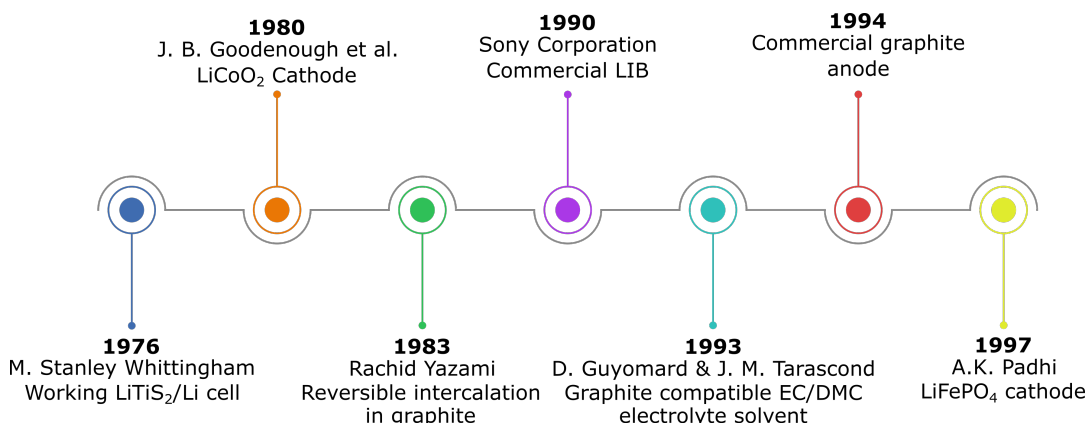


Figure 1.2: Timeline of the early development of lithium-ion batteries.

The LiCoO_2 cathode material comes with a set of challenges due to its price, toxicity, and safety. These issues encouraged the development of other cathode materials and in 1997, A. K. Padhi and co-workers developed a lithium iron phosphate cathode, LiFePO_4 [9]. The LiFePO_4 material has a theoretical specific capacity of 170 mAh g^{-1} and an average potential of 3.4 V vs. Li/Li^+ . This is lower than that of LiCoO_2 which has a specific capacity of 274 mAh g^{-1} and a average potential of 3.8 V [11]. The development of LiFePO_4 was primarily driven by its abundance, non-toxicity, safety, and environmental benignity [12]. The issues with LiFePO_4 are low ionic- and electronic conductivity, and low volume energy density due to low tap density. The low electronic conductivity was attempted to be improved by S. Y. Chung and his colleagues in 2002 by doping LiFePO_4 with cations like Nb^{5+} , Ti^{4+} , and W^{6+} . The origin of the increased conductivity was later revealed to most likely be due to the carbonaceous precursors stemming from the fabrication method [13]. Therefore, the most common procedure for increasing both the ionic- and electronic conductivity is to reduce the size of the LiFePO_4 particles and to coat them with carbonaceous material. In 2006, Xie et al. [12] achieved a tap density of LiFePO_4 of 1.8 g cm^{-3} , which is slightly lower than that of LiCoO_2 , $>2.2 \text{ g cm}^{-3}$.

Much of the aforementioned progress in lithium-ion batteries was either done by or based on the work of M. Stanley Whittingham, John B. Goodenough, Rachid Yazami, Akira Yoshino, and Yoshio Nishi. For their invaluable contribution to the development of the lithium-ion battery John B. Goodenough, Rachid Yazami, Akira Yoshino, and Yoshio Nishi were awarded the Charles Stark Draper Prize in 2014. Furthermore, M. Stanley Whittingham, John B. Goodenough, and Akira Yoshino received the Nobel Prize in Chemistry in 2019.

1.2 The Motivation and Scope of the Project

The development of lithium-ion batteries has come a long way in only a few decades and it is currently more relevant than ever. The $\text{LiFePO}_4/\text{Graphite}$ chemistry is promising for lithium-ion batteries in high power output applications and in the electrification of the transportation sector due to the capability of high discharge rates. The potential of the $\text{LiFePO}_4/\text{Graphite}$ system makes it of great interest and therefore it is important to understand the mechanisms responsible for aging and degradation of the battery. The aging may result in increased impedance, and capacity- and power fade. The mechanisms responsible for aging are believed to be a complex interplay of chemical and mechanical processes some of which are electrolyte decomposition and reduction, loss of active material and lithium ion inventory, structural deterioration of electrodes, and changes in the morphology of the separator [14].

The aging process of a battery can be monitored by performing charging and discharging cycles while frequently measuring e.g. its impedance and capacity. The monitoring gives a measure of the state of health (SOH) which decreases as the battery ages. The decrease in SOH cannot commonly be attributed to a particular physical or chemical mechanism occurring inside the battery. The scope of this master's thesis is to examine some of the mechanisms responsible for the aging by disassembling cycle-aged cylindrical 26650 $\text{LiFePO}_4/\text{Graphite}$ batteries from A123. The batteries have been aged at constant temperature of 42.5 °C, at different cycle depths, and at different average state-of-charge (SOC). Due to the complex interplay of the aging mechanisms the scope is delimited to:

- ▶ Establish a post-mortem analysis methodology for disassembling the batteries and preparing the electrodes for investigation.
- ▶ Deduce a correlation between the electrochemical behavior of the anode and the cathode, and the aging conditions through cyclic voltammetry, chronopotentiometry, and electrochemical impedance spectroscopy.
- ▶ Establish a possible relation between the morphology of the anode and the cathode, the electrochemical behavior, and the aging conditions through scanning electron microscopy analysis, cyclic voltammetry, chronopotentiometry, and electrochemical impedance spectroscopy.
- ▶ Investigate the composition and structure of the anode and the cathode with energy dispersive x-ray spectroscopy and Raman spectroscopy, and relate the findings to the morphology- and electrochemical analysis.

2 The Electrochemical Cell

This chapter seeks to present a description of the principles of operation of an electrical battery and its main components namely the cathode, anode, separator, and electrolyte. Afterwards, the main terms and parameters used when discussing battery performance are defined and lastly the concept of primary and secondary batteries is introduced.

An electrical battery or just battery is a device that converts chemical energy, stored in its active materials, into electrical energy through an electrochemical oxidation-reduction, redox, reaction. A redox reaction is characterised by transfer of electrons between the participating species. This results in the loss of electrons of one species i.e., oxidation, and gain of electrons of the other species i.e., reduction. Additionally, any redox reaction can be represented as the difference of two reduction half-reactions. These conceptual reactions show how electrons are transferred during the reaction. A half-reaction where z electrons are transferred is described by a redox couple as



An electrochemical cell utilises an electrochemical redox reaction to transfer electrons from the participating active materials, known as the electrodes, through an external electrical circuit. If the redox reaction is spontaneous, a flow of charge through the external circuit gives rise to an electric current. This cell type is termed a galvanic cell and is capable of performing electrical work until the overall cell reaction reaches equilibrium. A galvanic cell is shown schematically in Fig. 2.1. In contrast, the electrolytic cell requires a flow of electrons to drive a non-spontaneous chemical reaction. In this project the galvanic cell will be referred to as a cell.

To maintain charge neutrality electrons are transferred through the cell's external circuit while ions flow between the electrodes through an ionic conductor termed the electrolyte. The electrodes of the cell were originally named depending on the polarity of the ions that flow to them during the redox reaction; anions flow to the anode and cations flow to the cathode. The naming of the electrodes can also be as follows; the electrode where oxidation occurs is the anode, the electrode where reduction occurs is the cathode. In a galvanic cell, electrons are released from the anode and enters the cathode, hence the conventional current flows from the cathode to the anode. Thus, the anode and cathode are also referred to as the negative and positive electrode, respectively. Furthermore, an electrode in contact with its electrolyte forms an electrode compartment. The compartment may be shared between the two electrodes or

there may be two different compartments depending on the cell design. [15]

To avoid electron transfer directly through the electrolyte and thus internal short-circuiting the cell a separator is used to electrically separate the two electrodes. The separator is however permeable to the electrolyte and hence it facilitates ionic conductivity as desired. A separator material could for instance be a salt bridge or a semipermeable membrane. [15–17]

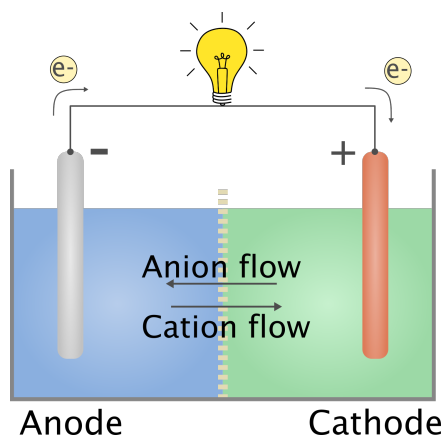


Figure 2.1: A galvanic cell with two electrode compartments. A spontaneous redox reaction drives electrons through the external circuit where a light bulb is lit by the current produced. Anions and cations flow from one compartment to the other through the separator to maintain charge neutrality.

A battery consists of one or more galvanic cells electrically connected in series or parallel depending on the desired operating voltage and capacity. Additionally, batteries include other components necessary for operation such as current collectors, leads, and casing. Multiple batteries may be connected into more advanced devices such as battery packs which often include a battery management system. A schematic of the configuration of a battery pack, and a battery is shown in Fig. 2.2. [18]

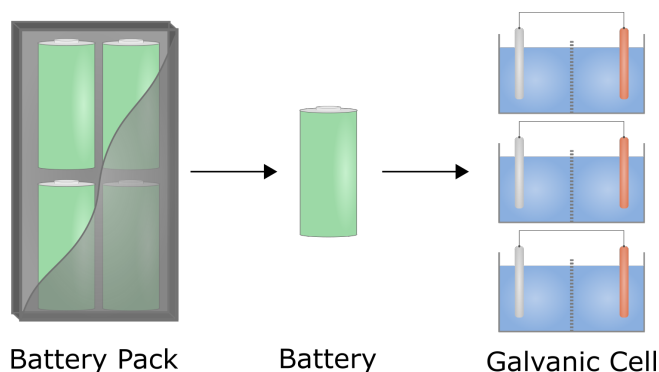


Figure 2.2: Schematic showing the concept of a galvanic cell, a battery, and a battery pack. The battery pack is a functional device which is composed of multiple batteries connected in series or parallel or both, to yield the desired voltage and capacity. A battery is also a functional device and is composed of one or more galvanic cells depending on the desired voltage and capacity.

2.1 Terminology

The forthcoming sections include a description of the terminology and parameters used when discussing battery characteristics.

Voltage

The voltage of a battery is the electrical potential difference of the galvanic cell(s) of which it consists. The electrical potential difference is proportional to the Gibbs free energy, $\Delta_r G$, of the redox reaction occurring in the galvanic cell. The cell potential can be calculated from the Nernst equation which is derived and elaborated in Appendix A.1. At standard conditions the cell potential becomes the standard cell potential denoted by E^\ominus , and it can be determined as the difference between the standard reduction potential of the two half-reactions

$$E_{\text{cell}}^\ominus = E_{\text{Red}}^\ominus(\text{Cathode}) - E_{\text{Red}}^\ominus(\text{Anode}). \quad (2.2)$$

Capacity

The capacity of a battery is a measure of the amount of charge, expressed in coulombs, that can be extracted from it. Often the more practical unit ampere-hour (Ah) is used instead. The capacity is a function of the available electrode active material and is therefore often expressed as specific capacity i.e. capacity per unit mass (Ah kg^{-1}) instead. The specific capacity is strongly affected by various external factors such as temperature and discharge current, and hence there should be a clear distinction between a measured specific capacity of a real battery and a theoretical specific capacity calculation of an electrochemical cell. [16]

The theoretical specific capacity for a half-reaction can be calculated by considering the formula

$$C_{\text{specific}} = xF/nM, \quad (2.3)$$

where x is the stoichiometric number of electrons transferred in the half-reaction, F is the Faraday constant, n is the stoichiometric number of the participating active material, and M is the molar mass of the participating active material [19].

Specific energy

The specific energy indicates the amount of energy that can be extracted from the battery and is expressed per unit mass as Wh kg^{-1} . The specific energy is calculated as

$$\text{Specific energy} = \text{Specific capacity} \times \text{Voltage}. \quad (2.4)$$

A similar characteristic of a battery is the energy density given in Wh L^{-1} . [16]

Specific power

Specific power describes the highest amount of power a battery can deliver normalised to the battery mass. Specific power is thus given in W kg^{-1} . Additionally, the power density is the maximum deliverable power normalised to the battery volume. [16]

$$\text{Specific power} = \text{Maximum discharge current} \times \text{Voltage} / \text{Battery mass.} \quad (2.5)$$

Rate characteristics

Charging and discharging rates of a battery is characterised by the C-rate to normalise against the capacity. C-rate has the unit of h^{-1} and is defined as

$$\text{C-rate} = \text{Current} / \text{Capacity.} \quad (2.6)$$

The C-rate is commonly expressed as either a multiple or a fraction of C . For instance, a battery with 1 Ah capacity discharged with a 5 A discharge current yields a $5C$ discharge rate and the battery will be fully discharged in 0.2 hour. It should be noted that the real battery capacity may strongly depend on the discharge rate. A nominal capacity at a specific discharge rate is provided by the manufacturer. The C-rates are given in relation to this nominal capacity as in Eq. (2.6). [20]

2.2 Primary vs. Secondary Batteries

The reversibility of the oxidation-reduction reaction shown in Eq. (2.1) shows that by applying a sufficient voltage the spontaneous reaction can be driven in reverse. Some batteries efficiently utilise this reversibility which enables many cycles of charging and discharging. These rechargeable batteries are termed secondary batteries or accumulators. A secondary battery can thus act as a storage device for electrical energy. In contrast, primary batteries are designed for single use only, hence these batteries act only as a one time converter from chemical to electrical energy. Below are listed some of the most common primary and secondary batteries. [21]

Primary	Secondary
– Alkaline zinc-manganese dioxide	– Nickel-metal hydride
– Zinc-silver oxide	– Lead-acid
– Lithium metal anode	– Lithium-ion

Primary batteries have for more than 100 years been and still is a simple, portable, and convenient source of power with little to no maintenance required. An advantage

of the primary battery is the ability to quickly be replaced in situations where charging is not possible such as military- or emergency situations [22]. Generally modern primary batteries feature a longer shelf life compared to secondary batteries which can be subject to a large degree of self-discharge if stored near full capacity. Additionally, accelerated self-discharging is typically observed at elevated temperatures [23]. Applications of primary batteries are typically low power devices such as electronic clocks, cardiac pacemakers, and TV remotes [22].

Secondary batteries can require maintenance to counteract consequences of parasitic reactions that can occur during charging and discharging. An example is the lead-acid cell where the cell voltage of ~ 2 V is sufficient to split the aqueous electrolyte thus developing H_2 and O_2 gas. Refilling with water is thus required to maintain optimal performance and lifetime of the battery [24]. Applications of secondary batteries can be divided into two major categories. These are applications where secondary batteries are used as energy storage devices and those where secondary batteries are discharged during use and charged afterwards. The first category includes for instance standby power supplies, and grid energy storage. The latter category includes for instance rechargeable consumer electronics, and plug-in electric vehicles. This category is similar to the application range of primary batteries however secondary batteries are used instead for convenience, cost savings, and due to the typically higher power density [22, 25].

In Fig. 2.3 a bar chart of specific energy for various battery chemistries are shown.

Both primary and secondary batteries come in a wide range of shapes and sizes, and are based on various electrochemical systems. The electrochemical system and shape of batteries are standardised according to the International Electrotechnical Commission with the purpose to simplify interchangeability and provide guidance on safety [26]. In Fig. 2.4 a variety of commercial secondary batteries are shown.

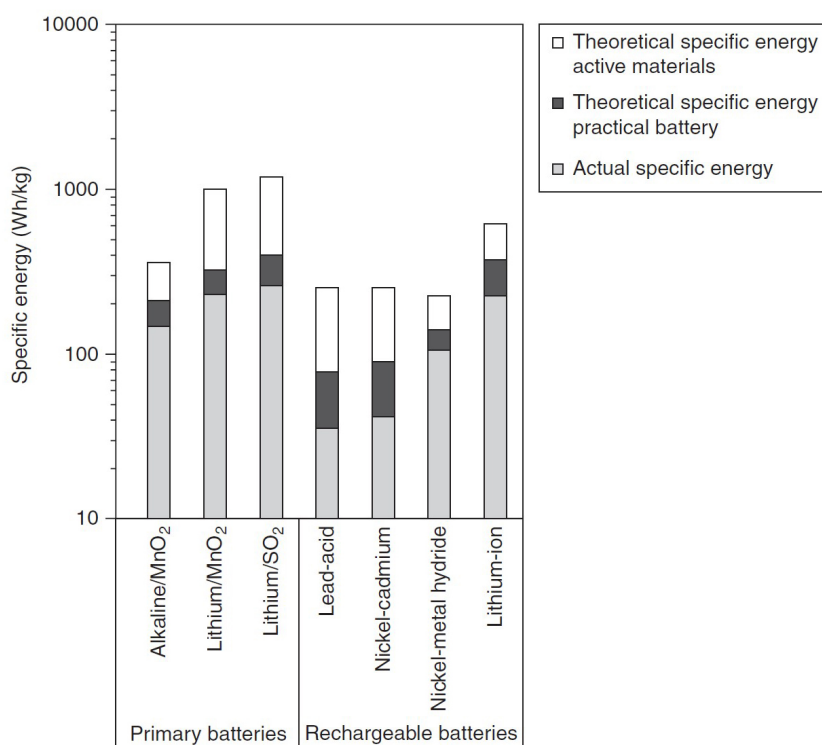


Figure 2.3: Bar chart comparison of specific energy for various primary (left) and secondary batteries (right). As the battery industry is rapidly growing this chart from 2011 only serves as a guideline for the general trend. White refers to the theoretical specific energy based on the active materials, (see Eq. (2.3)). Black refers to the theoretical specific energy accounting for electrolyte and non-reactive components. Grey refers to the actual specific energy measured at optimal discharge conditions. Adapted by permission from McGraw-Hill, D. Linden and T. B. Reddy, "Basic Concepts" in "Linden's Handbook of Batteries", 4th ed., McGraw-Hill (2011) [16].



Figure 2.4: Different types of secondary batteries. First row from left to right: Lead-acid automotive battery 12 V, HR6 Ni-MH rechargeable 1.2 V, prismatic Li-ion 3.7 V, and Li-ion button cell type LIR2032 3.6 V. Second row from left to right: Li-ion polymer pouch 3.7 V, and CGR18650 cylindrical Li-ion batteries with LiNiCoMnO₂ cathode, 3.6 V, assembled into a laptop battery pack operating at 10.8 V. For image references see [27].

3 Working Principle of Li-ion Battery

This chapter begins by introducing the working principle of the lithium-ion battery and particularly the type examined in this project. The remaining part of the chapter is divided into sections concerning each major internal component: The anode, cathode, electrolyte, and separator. Each section seeks to explain the relevant mechanisms that take place during operation of the battery along with brief descriptions of relevant performance enhancement possibilities.

3.1 Lithium-ion batteries

Lithium-ion batteries (LIBs) are a type of secondary batteries, where the rechargeable attribute is due to the reversible transfer of Li^+ ions between the electrodes during charging and discharging. Most commercially available LIBs utilise intercalation chemistry, where upon charging and discharging Li^+ is extracted from one electrode, dissolved in the electrolyte, and inserted into the other electrode without incurring significant changes to the structure of the electrodes. [28]

Lithium-ion batteries include a liquid, polymer, gel, or ceramic electrolyte where the liquid type consists of a lithium salt dissolved in an organic solvent. LIBs are commonly based on a shared electrode compartment with a porous polymer separator of typically polyethylene or polypropylene. [28, 29]

Several cathode and anode candidates exist that facilitates intercalation of Li^+ ions. For the anode a graphite based material is widely used which will be elaborated in Section 3.2. The commercially successful cathode materials are lithium iron phosphate, LiFePO_4 , and lithium metal oxide compounds, LiMO_2 , where M refers to one or more transitional metals i.e. Mn, Co, or Ni. Some examples are; LiMn_2O_4 , LiCoO_2 , LiNiMnCoO_2 , and LiNiCoAlO_2 . Intercalation of Li^+ into these compounds is possible due to their crystal structure. [28]

When comparing the cathode materials LiCoO_2 , LiNiMnCoO_2 , LiNiCoAlO_2 , LiMn_2O_4 , and LiFePO_4 it is seen that LiNiCoAlO_2 has superior specific- and volumetric capacity of 200 mAh kg^{-1} and 700 mAh cm^{-3} , respectively. On the other hand, the LiMn_2O_4 shows superior average voltage of 4.1 V. The comparison is illustrated in the spiderweb diagram in Fig. 3.1. [11]

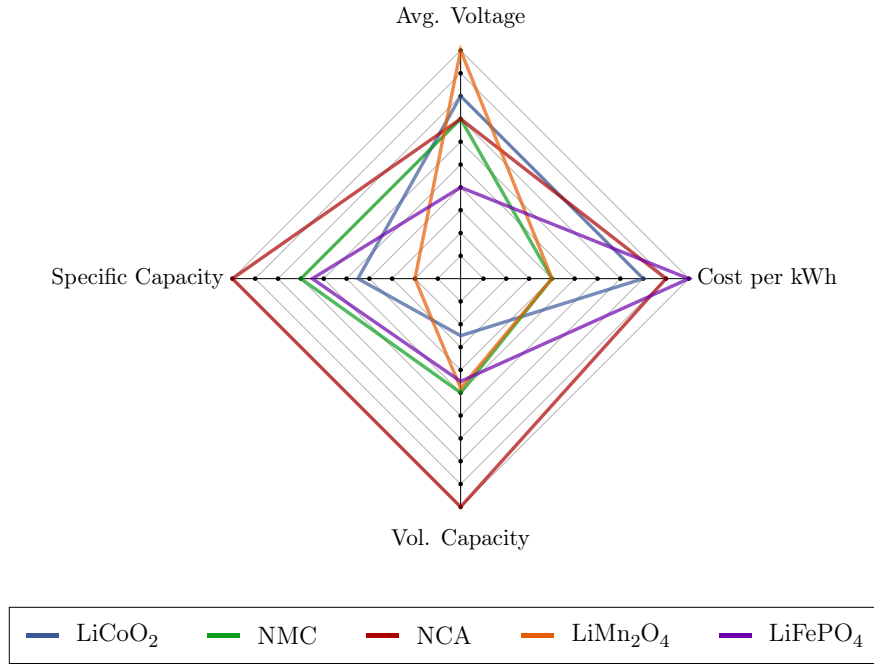


Figure 3.1: Comparison of voltage, cost per kWh, volumetric capacity, and specific capacity for the cathode materials: LiCoO₂, LiNi_{0.33}Mn_{0.33}Co_{0.33}O₂ (NMC), LiNi_{0.8}Co_{0.15}Al_{0.05}O₂ (NCA), LiMn₂O₄, and LiFePO₄. The diagram is based on [11, 30].

Furthermore, the electronic conductivity of LiFePO₄ is the lowest of the five mentioned materials and therefore, the LiFePO₄ particles are often made smaller relative to the others. Smaller particle size yields a lower volumetric energy density and this is why LiFePO₄ is not used in portable devices or EVs. Despite these disadvantages, LiFePO₄ is still used due to its great thermal stability and better battery safety. Better safety characteristics can be attributed to the strong covalent P-O bond compared to e.g. the Co-O bond. The abundance of iron and the smaller particles of LiFePO₄ which facilitates a high charge/discharge current makes it a popular choice for grid storage for wind- and solar power. The disadvantage of using LiCoO₂, LiNiMnCoO₂, and LiNiCoAlO₂ is the need for cobalt which due to its low abundance and to its extraction process present both economical and environmental issues. The LiNiCoAlO₂ shows overall great performance but has been observed to suffer from severe capacity fade at elevated temperatures of 40-70 °C. The high average voltage of LiMn₂O₄ and its lack of cobalt makes it an appealing cathode material. If the lithium content in the compound is too low, the manganese has however been observed to dissolve and migrate to the anode and thereby limiting the cycle life of the battery. [9, 11]

The working principle of a discharging LIB based on a graphite anode and a LiFePO₄ cathode is shown schematically in Fig. 3.2. The current collectors at the anode and cathode are made from copper and aluminium foils, respectively. Aluminium is chosen since it forms a passivation layer due to the lithium salt in the electrolyte [31]. Therefore, aluminium does not corrode even though the potential at the cathode is

higher than its reduction potential. Copper is chosen as the anode current collector due to its electrochemical stability and high reduction potential.

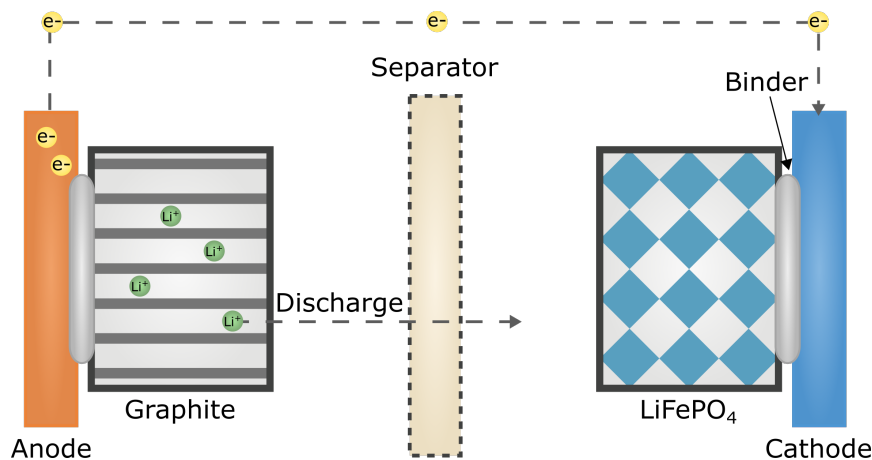


Figure 3.2: Working principle of a lithium-ion battery. While discharging the graphite electrode is oxidised and electrons are ejected into the copper current collector and into the external circuit. During the oxidation Li^+ ions are extracted from the anode and dissolved in the electrolyte. Lithium ions then pass through the separator and is inserted into the LiFePO_4 cathode which receives electrons from the external circuit through an aluminium current collector. This sequence is reversed during charging of the battery. The two electrodes are attached to the current collectors with a binder material.

Lithium-ion batteries comes in a variety of shapes. Four common battery designs are cylindrical, coin, prismatic, and pouch and they are shown below in Fig. 3.3.

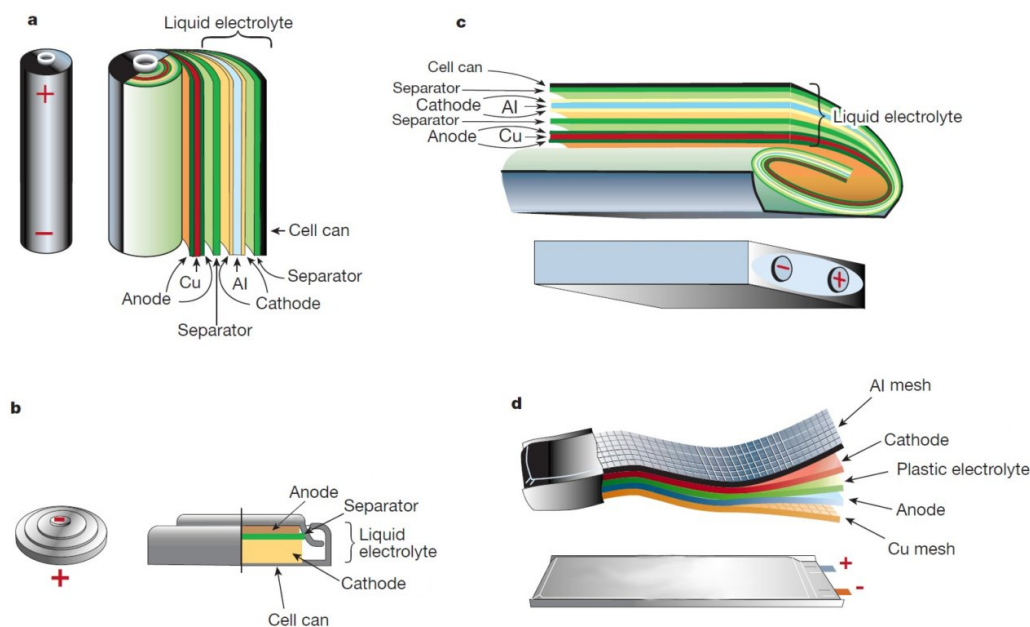
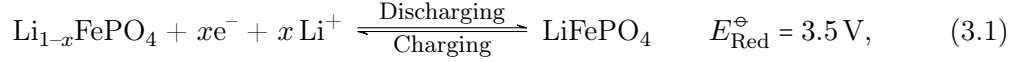


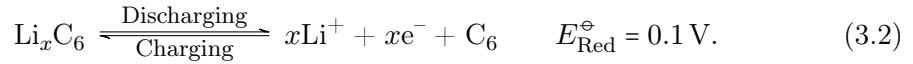
Figure 3.3: Four common designs for lithium-ion batteries, where (a) cylindrical, (b) coin, (c) prismatic, and (d) pouch. The plastic electrolyte in the pouch type is gel-like and flexible. Adapted by permission from Nature, Tarascon, JM., Armand, M., "Issues and challenges facing rechargeable lithium batteries", Nature 414, 359–367 (2001) [32].

The lithium-ion batteries investigated in this thesis are 26650 cylindrical batteries where the numbers refer to a diameter of 26 mm and length of 65.0 mm. These batteries utilize a LiFePO_4 cathode and a graphite anode. The electrolyte consists of the lithium salt, LiPF_6 , dissolved in a mixture of ethylene carbonate (EC) and diethyl carbonate (DEC) or dimethyl carbonate (DMC) at 1 M concentration.

The electrochemical system can be represented by two half-reactions. The reduction at the cathode during discharging is shown as the forward reaction below



and oxidation at the anode during discharging is shown as the forward reaction below



Each standard potential of the half-reactions are versus a Li/Li^+ reference electrode [33, 34]. It is clear from the half-reactions that de-/intercalation of Li^+ into either electrodes is required for discharging and charging of the battery. The total cell reaction can be written as the sum of the two half reactions



and the standard cell potential from Eq. (2.2) becomes $E_{\text{cell}}^\ominus = 3.4\text{ V}$. From the half reactions it is seen that if the battery is being charged or discharged the graphite is either the cathode or the anode, respectively. In the following the graphite electrode and the LiFePO_4 electrode is referred to as the anode and the cathode, respectively.

A theoretical specific capacity can be calculated for each half-reaction using Eq. (2.3). From Eq. (3.1), reduction at the cathode yields

$$C_{\text{specific}} = \frac{1 \cdot 96485\text{ C mol}^{-1}}{1 \cdot 158\text{ g mol}^{-1}} = 170\text{ mAh g}^{-1}, \quad \text{Cathode} \quad (3.4)$$

and from Eq. (3.2) oxidation at the anode, yields

$$C_{\text{specific}} = \frac{1 \cdot 96485\text{ C mol}^{-1}}{6 \cdot 12\text{ g mol}^{-1}} = 372\text{ mAh g}^{-1}, \quad \text{Anode}. \quad (3.5)$$

Equations (3.4) and (3.5) assumes complete de-/intercalation of Li^+ from the active materials i.e. $x = 1$. This is however not typically the case in real LiFePO_4 /graphite batteries where insertion and extraction of Li^+ , especially at the cathode, limits $x < 1$ and the actual specific capacity is hence lower than the theoretical prediction. [28, 33]

3.2 Graphite Intercalation Compound Anode

The anode is covered with particles of graphite which is an allotrope of carbon that is composed of sp^2 hybridised graphene layers. Graphene is in turn a single layer of carbon atoms arranged in a 2D honeycomb lattice. It is planar due to the sp^2 hybridisation which occurs when the 2s and two out of the three 2p orbitals of carbon combine to three sp^2 orbitals. The three sp^2 orbitals are shared among three neighbouring carbon atoms to form σ -bonds. Neighbouring graphene layers are held together by van der Waals forces and π - π interactions stemming from the last remaining 2p orbital. The van der Waals and π - π interactions are weak compared to the in-plane C-C covalent bonds. The graphene layers in graphite are commonly found in a Bernal stacking order (ABA) where half of the carbon atoms in layer A are situated below or above carbon atoms in layer B while the other half is not. Graphite can also occur in the lesser common rhombohedral stacking order (ABC). [35] Both stacking orders are shown in Fig. 3.4.

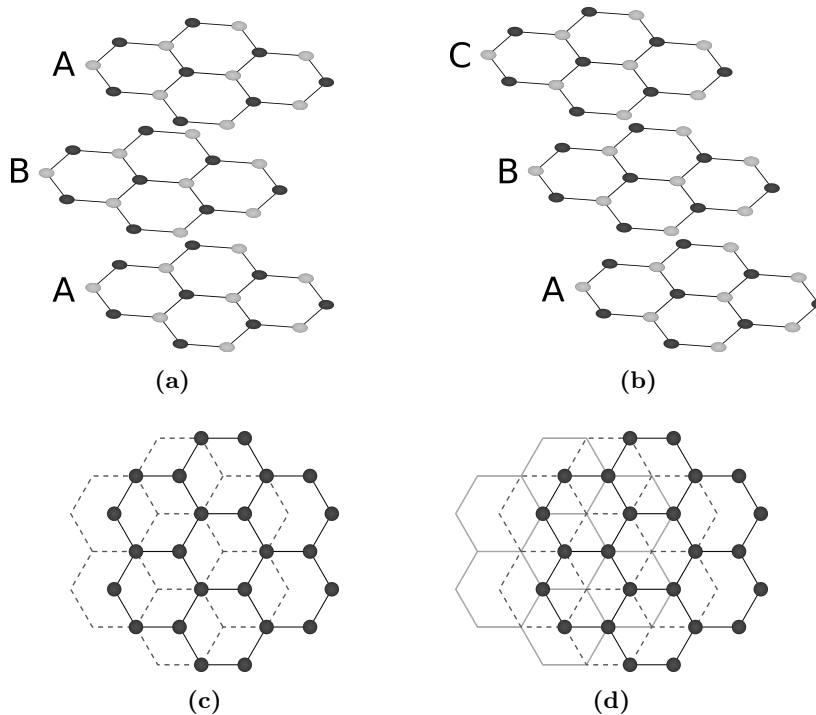


Figure 3.4: Schematic of the crystal structure of graphite. (a) Bernal (ABA) stacking sequence where dark carbon atoms in A layers are situated below and above light ones in B layers. Dark and light carbon atoms in layer A and B, respectively, are situated above and below hexagon centers. (b) Rhombohedral (ABC) stacking sequence where the positioning of the atoms in layer A and B are identical to that of the Bernal sequence. The position of atoms in layer C relative to those in layer B is equivalent to the position of atoms in layer B relative to those in layer A. Top view of the (c) Bernal stacking sequence, and (d) Rhombohedral stacking sequence.

The morphology of graphite can be characterised by a basal plane and an edge plane. The former being the plane parallel to the graphene layers and the latter the plane

perpendicular to the layers, as seen in Fig. 3.5a. The edge plane may be subdivided into zigzag or armchair surfaces as seen in Fig. 3.5b. [35]

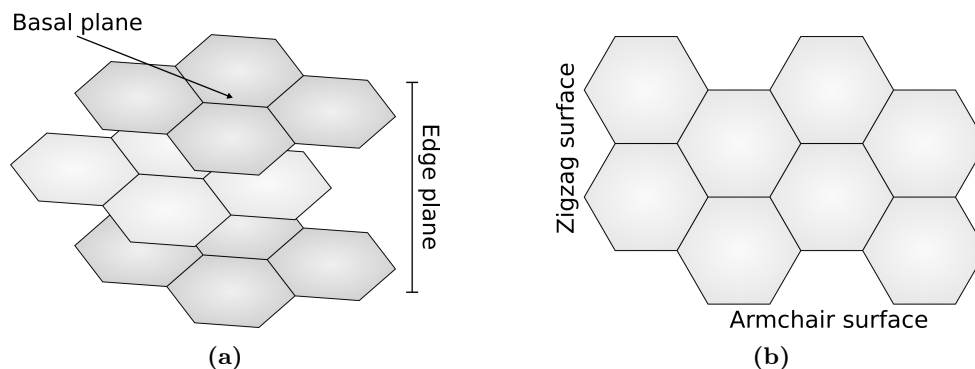


Figure 3.5: Schematic of Bernal (ABA) crystal structure. (a) View of the stacking sequence with the basal and edge plane denoted. (b) Top view of basal plane. The distinct zigzag and armchair surfaces that make up the edge planes are denoted.

3.2.1 Intercalation Mechanisms and Structural Changes of Graphite

When charging the LIB, electrons and lithium ions move externally and internally, respectively, from the LiFePO_4 to the graphite. The graphite undergoes reduction which facilitates the lithiation i.e. intercalation of the lithium cations. Intercalation is the process of insertion into layered structures and it is possible due to the flexible graphene layers. The flexibility stems from the rather weak van der Waals forces and $\pi - \pi$ interactions between adjacent graphene layers. Furthermore, it is worth noting that the interlayer distance i.e. the d -spacing of the graphene layers is 3.35 \AA while the σ -bond length between carbon atoms is 1.42 \AA . This rather long interlayer distance compared with the Van der Waals radius of lithium, 1.82 \AA , facilitates the intercalation process [36].

The intercalation of lithium ions in graphite occurs at a potential of $0.25 \text{ V} - 0.01 \text{ V}$ vs. Li/Li^+ and starts from the edge plane since the basal plane obstructs the ions, however, crystallographic defects will enable intercalation through the basal plane. In general the kinetics of the intercalation process follow a staging formation. The staging phenomenon is related to the energy required to perturb the van der Waals gap between the graphene layers to allow lithium cations to enter. The repulsive Coulomb interaction between two lithium ions is however weak compared to the required lattice perturbation energy and thus localised collection of lithium ions i.e. islands, is favored compared to a random distribution. The staging mechanism can be explained with the Daumas-Hérold model, as seen in Fig. 3.6. [35]

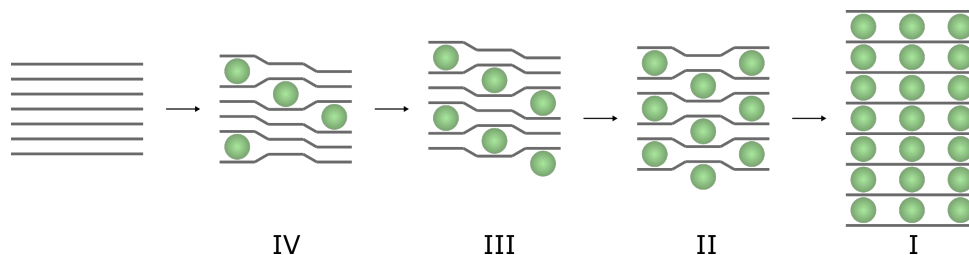


Figure 3.6: Schematic of the Daumas-Hérol model for intercalation of lithium islands (green spheres) into graphite. The intercalation occurs as a staging mechanism where the stage number, IV through I, refers to number of graphene layers separating two intercalate layers.

The stages are named according to the number of graphene layers separating two intercalate layers, i.e. stage four refers to two lithium interlayers being separated by four graphene layers. As the lithium ions intercalate into the graphite, the graphene layers deform around the ions which locally increases the d -spacing. The spread out distribution of lithium islands is favored since it minimises the distortion of the lattice which is seen in stage-IV and -III. The graphite intercalation compound transitions from stage-III to -I as both more lithium ions intercalate and already intercalated lithium ions diffuse. Due to the weak van der Waals interactions and the π -bonds, the flexibility of the graphene layers is great enough for intercalation to proceed to stage-I. As the concentration of lithium approaches the theoretical stoichiometry, LiC_6 , the d -spacing increases by $\sim 10\%$ to 3.70 \AA and the stacking sequence changes from ABA to AIA, where I is the intercalated lithium layer. [35, 37]

In stage-I the stoichiometry of the intercalated compound is LiC_6 where lithium is situated in the center of the hexagonal carbon rings. This structure is shown schematically in Fig. 3.7. Graphite intercalation compounds with higher lithium density, LiC_2 - LiC_4 , can form at elevated temperature and high pressure [37].

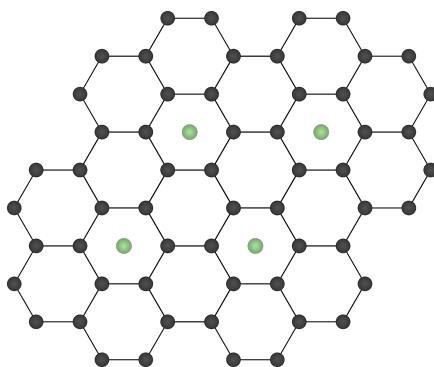


Figure 3.7: Schematic of in-plane distribution of Li^+ (green) in graphene (black) as LiC_6 .

The staging phenomena can be observed in galvanostatic reduction of graphite to LiC_6 as seen in the charge profile in Fig. 3.8a and in the cyclic voltammogram in Fig. 3.8b. The charge curve shows a change in the slope at certain specific capacities which

implies a phase change from one stage to another. The peaks in the voltammogram correspond to changes from one stage to another since the reduction potential of stages are different. [35, 37]

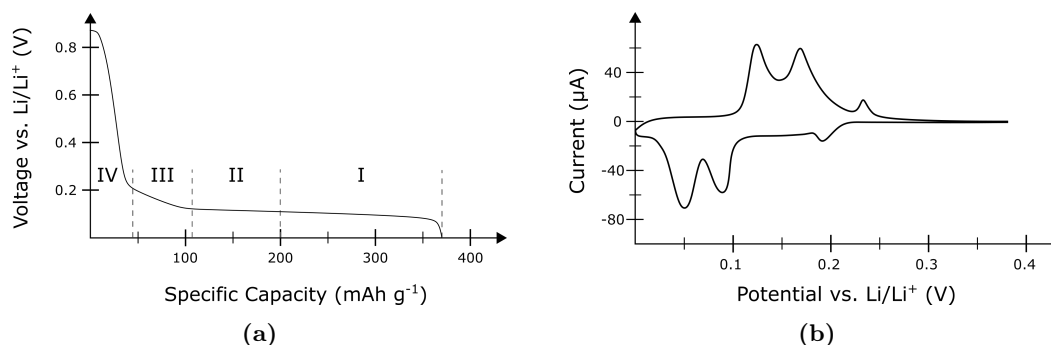


Figure 3.8: (a) Charge profile of graphite vs. Li/Li⁺ where the transition from one intercalation stage to another is apparent from the change in slope. (b) Cyclic voltammogram of graphite where the peaks in current correspond to stage transitions. The schematic figures are adapted from experimental data from Li et al. [37].

3.2.2 Solvent Co-Intercalation

The intercalation of Li⁺ can be accompanied by intercalation of solvated lithium ions, Li⁺(solv)_y, where solv refers to electrolyte components. When the lithium salt, LiPF₆, is added to the polar organic solvent, it disassociates into Li⁺ and PF₆⁻. The lithium cations solvate by interacting with the solvent molecules through electrostatic forces. These forces cause the solvent molecules to orientate in order to minimise the interaction energy. This layer of solvent molecules is polarised and will cause another layer of solvent molecules to attract due to van der Waals forces as seen in Fig. 3.9. As the solvent molecules are attracted to the cation, the separation distance between attracted solvent molecules becomes smaller resulting in steric hindrance, a repulsive interaction arising due to the Pauli exclusion principle. The layers of solvent molecules are known as the solvation shell of the lithium ion. It is useful to introduce the Stokes radius when considering solvated lithium ions which is the total radius of both the lithium ion and its solvation shell. The shell will also likely contain anions and cations in addition to the solvent molecules some of which may stem from reactions involving impurities and solvent molecules which will be covered in Section 3.4.1. The co-intercalation is influenced by the Stokes radius of the solvated lithium ions since it occurs via the edge plane. A large Stokes radius compared to the *d*-spacing of the graphene layers impedes the intercalation process. [35, 37]

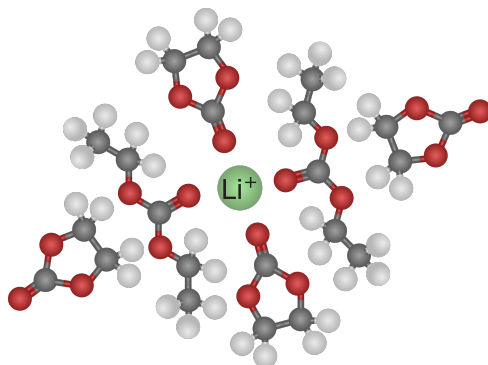


Figure 3.9: Schematic of a solvated lithium ion. The solvation shell is here depicted as being composed of DEC (linear molecules) and EC (cyclic molecules). For the solvent molecules, carbon, oxygen, and hydrogen atoms are dark grey, red, and light grey, respectively.

The intercalation of both solvated and unsolvated lithium ions requires the interlayer distance of the graphene layers to increase. This expansion energy depends inter alia on the Stokes radius of the solvated lithium ions and the flexibility of the graphene layers. Due to the latter, intercalation often starts close to the outer graphene layers as the flexibility is greater and hence the expansion energy is lower. This is schematically shown in Fig. 3.10. As the intercalation proceeds the bending of the outer graphene layers is increased and eventually they cannot be bend any more and further intercalation is inhibited. The bending is more pronounced with increasing Stokes radius. [35, 37]

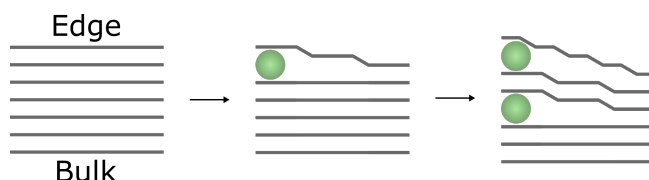


Figure 3.10: Schematic of the bending of the outer graphene layers in graphite as intercalation proceeds.

During the early stages of intercalation when the content of lithium in graphite is low i.e. Li_xC_6 where $x \leq 0.33$, the intercalation of solvated lithium ions is thermodynamically favored compared to intercalation of unsolvated lithium ions. In this stage of intercalation the perturbation of the graphite lattice is small due to the low content of intercalated lithium. The available space in the lattice facilitates the accommodation of large solvent molecules. These intercalated solvated compounds are thermodynamically unstable and undergo reduction processes. The kinetics of the reduction depend on the composition of the compound but in general the decomposition is associated with an irreversible capacity fade of the battery. The solvent co-intercalation problem is often solved by using solvents and electrolyte additives that promotes the formation of a solid-electrolyte interface (SEI) film on the surface of the graphite. One of the most common solvents, which is also used in the type of LIBs investigated in this

project, is a mixture of ethylene carbonate (EC) and diethyl carbonate (DEC) or dimethyl carbonate (DMC). [35, 37]

3.2.3 Irreversible Charge Loss

The intercalation of lithium into graphite is theoretically fully reversible, however, it is observed that the first de-/intercalation cycle only recovers around 80 % of the charge. This loss is mainly a consequence of the formation of a solid electrolyte interface film. The formation of the SEI will be elaborated in Section 3.4.1. The subsequent cycles show close to 100 % recovery. Besides the loss due to the SEI film formation, impurities such as water and oxygen have been reported to participate in irreversible reduction processes with the graphite. Additionally, lithium may also incorporate irreversibly into the graphite matrix e.g. at domain boundaries in poly-crystalline graphite. The irreversible charge loss in the first cycle is related to the initial Coulomb efficiency (ICE) that is the ratio of extractable charge to the charge put into the battery.

The ICE can be increased by surface modification of the graphite to minimise the loss to SEI film formation. Multiple surface modifications have been investigated such as metal-graphite composites, thin metal and metal oxide coatings, and polymer coatings. Another method is to coat the graphite particles with a layer of amorphous carbon with vapor deposition which has been shown to enhance the ICE from ~80 % to ~90 %. When coating the graphite particles the weight of the battery increases and results in significantly reduced specific energy. The reduction can be limited by employing spherical graphite particles to lower the amount of carbon coating required. [7, 35, 37]

3.2.4 Improvement of the Anode and Future Aspects

One of the major limitations for LIBs in high power output applications is the diffusion of lithium in the graphite during de-intercalation. The power density can be increased by minimising the diffusion length since the diffusion time is proportional to the diffusion length squared as

$$t \propto \frac{L^2}{D_{\text{Li}}}, \quad (3.6)$$

where t , L , and D_{Li} is the diffusion time, -length, and -coefficient, respectively. The diffusion length can be lowered by reducing the particle size of the graphite. However, decreasing the size of the particles increases the total surface area and thus increasing the area at which the SEI film forms. [38]

In state-of-the-art LIBs two types of graphite are being used; natural flake- and synthetic graphite both of which are poly-crystalline. The main difference is that in natural flake graphite the numerous single crystalline domains are oriented in the same direction while in synthetic graphite particle the domain orientation is more random. The natural flake graphite particles are hence anisotropic while the synthetic graphite particles are more isotropic. The common manufacturing procedure for both natural

flake- and synthetic graphite is not sustainable since natural graphite is extracted from ore deposits and synthetic graphite is produced by heat treatment of petroleum coke. Progress has been made towards replacing the carbon source in the production of synthetic graphite with a sustainable one like biomass or bio-waste e.g. plastic bags [39]. The advantage of using synthetic graphite is that it has a higher purity grade, a lower thermal expansion, higher stability, longer cycle life, and a larger fraction of edge planes compared to natural flake graphite. The larger fraction of edge planes results in increased de-/lithiation rates. A disadvantage that comes with synthetic graphite is that the particles are often composed of smaller domains compared to the natural flake type and hence it has a larger fraction of domain interfaces which leads to lower capacity. Due to the manufacturing process of synthetic graphite it is more expensive than natural graphite. Both types of graphite is used for LIBs but for different applications e.g. synthetic graphite is often used for LIBs in EVs due to the higher purity, quality, and stability while natural flake graphite is typically used in LIBs for portable consumer electronics where a long cycle life is traded for lower cost. [7]

Optimising the properties of the graphite particles can only converge the specific capacity towards to the theoretical value of 372 mAh g^{-1} . In order to go further it is necessary to modify the anode material. One solution is to introduce silicon into the graphite in the form of understoichiometric SiO_x where ($x < 2$). The silicon oxide should be understoichiometric as higher oxygen content lowers the reversible capacity since silicon oxide compounds partake in irreversible alloying with lithium to form Li_4SiO_4 and hence leads to a low ICE. Elemental silicon alloys reversibly with lithium to form $\text{Li}_{3.75}\text{Si}$. On the other hand Li_4SiO_4 acts as a buffer for the volume changes that occur during cycling. Some of the limitations and challenges of adding understoichiometric SiO_x to graphite is the mentioned volume variations, cycle life, and overall electrochemical performance. The volume changes can be buffered by reducing the composite particle size to nanoscale, however this gives rise to another set of challenges such as increased surface area, increased cost, and difficult manufacturing procedures. Silicon oxide has already been introduced into graphite anodes with a ball-milling process [40, 41]. [7]

The next step towards even higher specific capacities could be a pure silicon anode where the overall reaction is



The theoretical capacity of silicon is 3578 mAh g^{-1} which is almost a tenfold increase compared to the 372 mAh g^{-1} for graphite. However, the challenges faced when introducing silicon into graphite are further amplified when the anode is pure silicon, especially the volume changes is a major challenge. [7]

3.3 Lithium Iron Phosphate Cathode

The cathode is composed of a current collector made of aluminium foil which is coated with a layer of LiFePO_4 . This compound has a polyanionic olivine structure where the unit cell is primitive orthorhombic, i.e. the lattice parameters are $a \neq b \neq c$ with angles $\alpha = \beta = \gamma = 90^\circ$. The crystal structure can be visualised as phosphorus tetrahedra PO_4 , and lithium- LiO_6 and iron octahedra FeO_6 . The LiFePO_4 structure is shown in Fig. 3.11. Each phosphorus tetrahedron share one- and two-edges with iron and lithium octahedra, respectively, when viewed along the c -axis as seen in Fig. 3.11b. When viewing the structure along the a -axis the lithium octahedra form a chain along the b -axis as seen in Fig. 3.11c. [13]

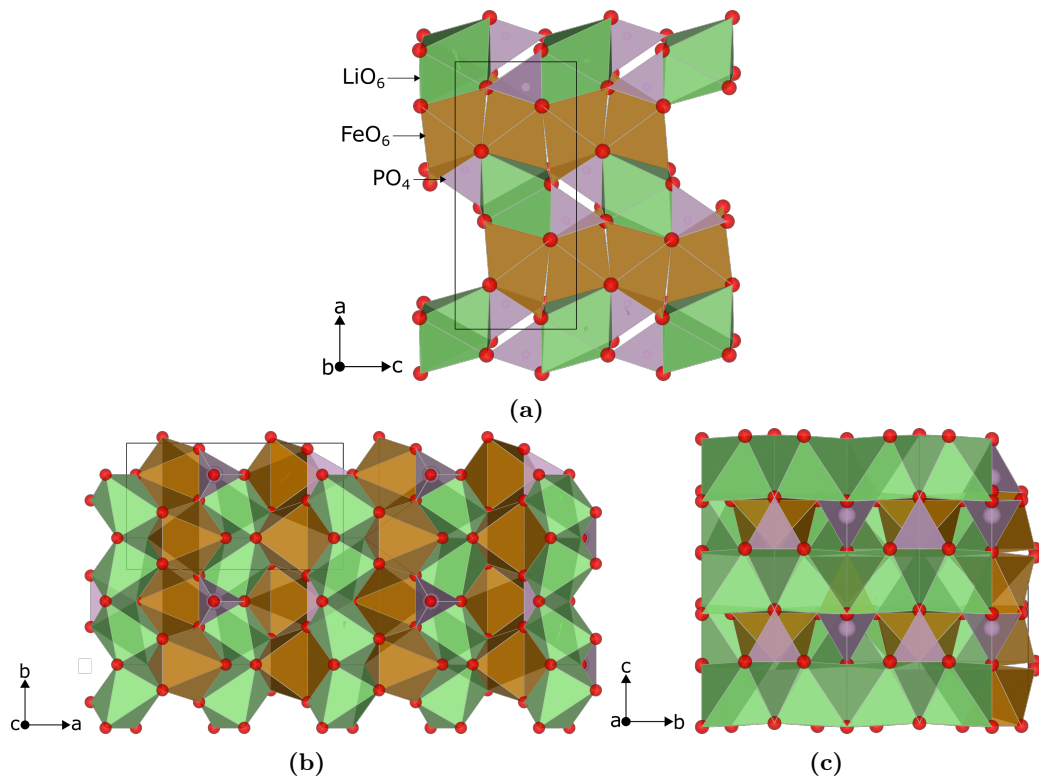


Figure 3.11: Crystal structure of LiFePO_4 with LiO_6 (green), FeO_6 (brown), and PO_4 (purple) polyhedra units. The oxygen atoms are depicted as red spheres and the unit cell is outlined. (a) View along b -axis. (b) View along c -axis. (c) View along a -axis. The images are rendered with Vesta [42].

3.3.1 Lithium Insertion and Extraction Mechanism

The LiFePO_4 allows for reversible de-/lithiation with a theoretical specific capacity of 170 mAh g^{-1} as calculated in Eq. (3.4) and a reduction potential of 3.4 V vs. Li/Li^+ . The lithium in LiFePO_4 is situated in 1D channels along the b - and c -axes as seen in Fig. 3.12a. Diffusion of lithium ions occur through these channels but mainly the ones along the b -axis since they have the lowest activation energy [43].

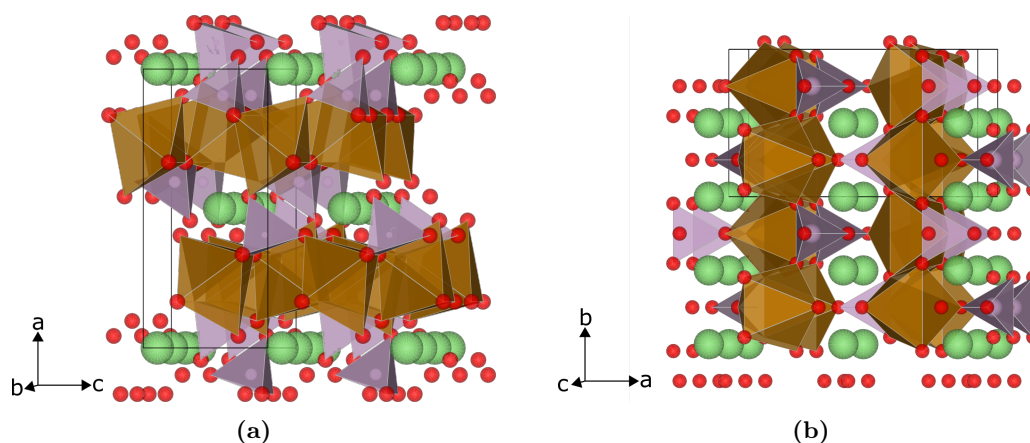


Figure 3.12: Crystal structure of LiFePO_4 with FeO_6 (brown), and PO_4 (purple) polyhedra units. Lithium and oxygen are depicted as green and red spheres, respectively. **(a)** View of the 1D channels where lithium is situated along the b-axis. **(b)** View of the 1D lithium channels along the c-axis. The images are rendered with Vesta [42].

The extraction/insertion process in LiFePO_4 is commonly regarded as a two-phase mechanism. Multiple theoretical models explaining the process have been suggested through the years, but the experimental results are often contradictory. A model proposed by Laffont et al. [43], based on studies with high-resolution electron energy loss spectroscopy, suggested an asynchronous extraction and insertion. The model can be explained by considering a single phase LiFePO_4 particle where the delithiation process starts at the surface of the particle since the energy barrier for removing lithium here is lowest. When an outer lithium ion has been removed from the 1D channel its neighbour will diffuse and fill the void. This will create a domino effect and result in a shift in the position of all the lithium ions in that channel towards the edge. The diffusion of lithium out of the particle will incur a phase transformation in the particle core as it undergoes oxidation to FePO_4 . This leads to a structure where two single phase areas are separated by an abrupt interface as shown schematically in Fig. 3.13a.

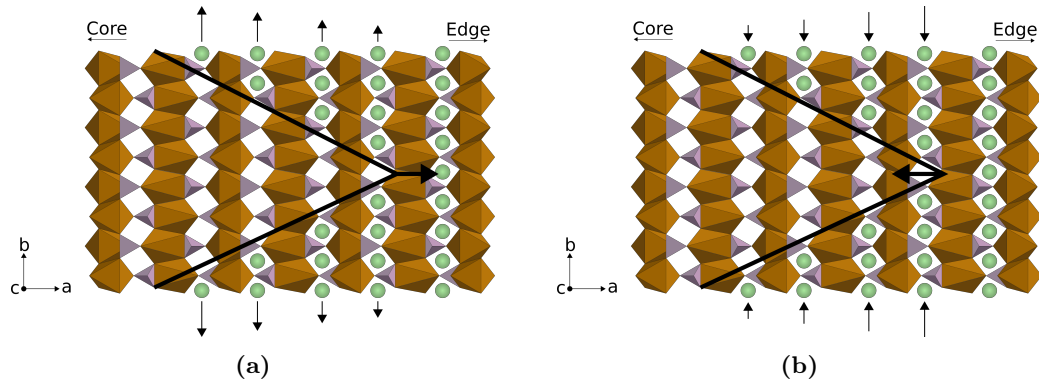


Figure 3.13: De-/lithiation model of $\text{LiFePO}_4/\text{FePO}_4$. The crystal structure is viewed along the c -axis where FeO_6 and PO_4 are depicted as brown- and purple polyhedra, respectively. The arrows along the b -axis represent the likelihood of extraction/insertion with the longest arrow indicating the channel where lithium is most likely to be extracted/inserted. **(a)** The delithiation occurs from the core of the LiFePO_4 particle. The abrupt interface (black) moves to the edge as lithium ions (green) are extracted. **(b)** The lithiation occurs from the edge of the FePO_4 and the interface moves towards the core as lithium is inserted.

The 1D channels with fewest lithium ions will empty first as it is energetically more favorable since fewer ions will be involved in the shift. The formation of the FePO_4 phase is coherent with the parent phase LiFePO_4 as the crystal structure is unchanged and the change in the lattice parameters is not too great. The a and b parameters decrease with 5.0% and 3.7%, respectively, while the c parameter increases with 1.9% when LiFePO_4 delithiates to FePO_4 . [43]

The lithiation of FePO_4 occurs from the edge of the particles and is governed by the following two competing phenomena: The amount of lithium ions which have to be shifted and the perturbation of the lattice. The perturbation when FePO_4 lithiates is smaller close to the LiFePO_4 phase and hence the energy required is lower. The first phenomenon tends to fill the emptiest channels first while the second tends to promote insertion of Li^+ into channels closer to the LiFePO_4 phase since it is more energetically favorable. The second phenomenon is experimentally observed to be dominant and thus lithium intercalation is preferred in the unfilled channel closest to the LiFePO_4 phase as seen in Fig. 3.13b. [43]

3.3.2 Electrochemical Properties of LiFePO_4

The de-/lithiation process depends on lithium diffusion and electron transfer in the $\text{LiFePO}_4/\text{FePO}_4$ particles. The reversible capacity is observed to decrease with increasing current density. The specific capacity has been observed to increase with increasing temperature. These observations imply that the de-/lithiation process is controlled by the transport kinetics of either the electrons or the lithium ions. The electrical and ionic conductivities of LiFePO_4 at room temperature are low and about $10^{-9} \text{ S cm}^{-1}$ and $10^{-5} \text{ S cm}^{-1}$, respectively.

The electrochemical behaviour of the de-/lithiation process is shown in the discharge profile presented in Fig. 3.14. The curve can be divided into three regions, similar to that of graphite. In the first region, (I), a rapid voltage drop is seen, which is because lithium can easily lithiate the surface layers of the FePO_4 particles. In the second region, (II), the voltage remains essentially constant, ~ 3.4 V. The intercalation of lithium in this stage requires the $\text{FePO}_4/\text{LiFePO}_4$ interphase to move towards the core of the particle. The energetic cost of moving this interphase remains essentially constant until it approaches the core. [44]

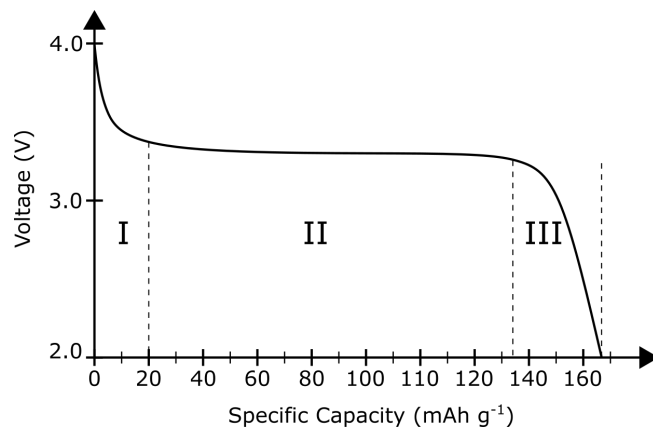


Figure 3.14: Schematic of a continuous discharge curve ($C/10$) for LiFePO_4 vs. Li/Li^+ . The curve is divided into three regions based on the intercalation model. The schematic is inspired by experimental data from P. P. Prosini [44].

At the end of discharge, (III), the voltage is observed to drop rapidly. This behaviour can be explained with the following model which is schematically illustrated in Fig. 3.15. The shift of the innermost lithium atom will result in an electron hole. This hole is compensated by an electron stemming from the anode. The low electrical conductivity impedes the electron and the hole will begin to move towards the surface of the particle to reach the electron. At the end of discharge the LiFePO_4 phase is extended far into the particle and thus the distance from the hole to the electron is large. Since the electron is impeded the iron atom at the surface is in a Fe^{+1} state. This excess negative charge will attract a lithium ion which results in an injection of a second electron. This second electron reduces the Fe^{1+} to Fe^0 and another lithium ion is then inserted. The hole then reaches the surface and a third electron is injected to neutralise it.

The reduction of iron to Fe^0 and resulting presence of two additional lithium ions block the channel and hence prevents further lithium intercalation.

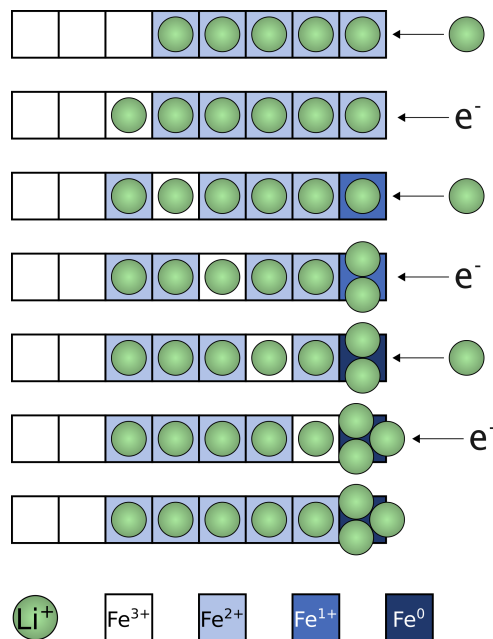


Figure 3.15: Schematic of the intercalation mechanism at the end of discharge. The insertion of a lithium ion results in a hole which migrates to the edge of the particle. An electron is ejected from the electrode to compensate for the hole but due to the low electrical conductivity the hole migrates slowly and the electron is impeded. The negative charge stemming from the electron reduces the iron from Fe^{2+} to Fe^{1+} and attracts a lithium ion which results in a second electron being supplied from the electrode. This can occur once more and results in Fe^0 and lithium phosphate. A third electron is supplied once the hole reaches the edge of the particle. The figure is inspired by [44].

Performance Increase of LiFePO_4

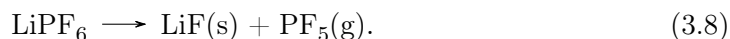
The kinetics of the lithium insertion mechanism are limited by the electrical- and the ionic conductivity of the cathode. If the discharge rate is too high, iron will reduce to Fe^0 at the surface of the particle due to the low ionic- and electrical conductivity of $\text{LiFePO}_4/\text{FePO}_4$. The effect of the low conductivities can be mitigated by decreasing the size of the $\text{LiFePO}_4/\text{FePO}_4$ particles since it will shorten the diffusion length. In addition to a decreased diffusion length the interface area between the electrolyte and the electrode is increased with decreasing particle size which improves the lithium insertion and extraction reaction rate. The size of the particles are in general on the scale of 100 nm while some are even less than 40 nm. [13, 45]

The performance and specific capacity of the cathode is further enhanced by coating the particles with a conductive material. A common choice is carbon due to its good electrical conductivity and chemical stability [46]. It is however important that the coating does not inhibit lithium diffusion to the particles. A carbon coating thickness of ~ 6 nm was found to be the best compromise [47]. The electrical conductivity was seen to increase from $10^{-9} \text{ S cm}^{-1}$ to $10^{-4} \text{ S cm}^{-1}$ [45]. Furthermore, a carbon coating has shown to increase the specific capacity to $> 180 \text{ mAh g}^{-1}$ which is beyond the theoretical limit of 170 mAh g^{-1} . This is due to a trapping mechanism of lithium ions between the carbon layer and the LiFePO_4 particle [46].

3.4 Nonaqueous Electrolyte and Solid-Electrolyte Interface

The batteries considered in this project have a liquid electrolyte which serves the purpose of enabling the conduction of ions from the anode to the cathode and vice versa. Commonly the electrolyte used in LIBs is based on a lithium salt dissolved in a nonaqueous solvent. The nonaqueous solvent allows for a larger, compared to an aqueous solvent, electrochemical window i.e. the voltage range at which it is stable, which in turn yields a higher specific energy. Additionally, the nonaqueous solvent often have a larger liquid range and better solubility for the lithium salts but the drawbacks are lower conductivity, flammability and environmental issues. [48]

The choice of electrolyte solvent is complicated as the ionic mobility has to be high in order to achieve low internal resistance, its electrochemical window has to match the potential range of the anode and cathode, and it has to be inert to the constituents of the battery. A common choice is ethylene carbonate (EC), a cyclic carbonate ester, which is a polar aprotic solvent that allows for high concentration of lithium salts, typically 1 M. However, the high dynamic viscosity, μ , of EC limits the ionic mobility as described by the drag force. The dynamic viscosity of EC is 1.9 mPas at 40 °C which is almost thrice as high as that for water, 0.65 mPas. The viscosity can be lowered by adding an appropriate solvent such as diethyl carbonate (DEC) or dimethyl carbonate (DMC) to EC. Both of which are less polar and less viscous than EC. The electrolyte solvent is therefore often a mixture of EC and either DEC or DMC in a 1:1 v/v solution. The salt of choice is commonly LiPF_6 since it yields a high ionic conductivity and have a large electrochemical window of 1.3 V to 4.5 V vs. Li/Li^+ . The addition of LiPF_6 prevents corrosion of the aluminium current collector by creating a protective AlF_3 film. A downside to LiPF_6 is its poor thermal stability at elevated temperatures, > 55 °C, where it decomposes as



The toxic gas pentafluorophosphorane, PF_5 , initiates polymerisation of the solvent and hence degrades the performance of the battery. Additionally, LiPF_6 hydrolyses easily in the presence of trace amounts of water to form HF. Despite the disadvantages of using LiPF_6 it is still chosen more often compared to alternative such as LiClO_4 , LiAsF_6 , and LiBF_4 . These lithium salts, including LiPF_6 , all have their advantages and disadvantages e.g. LiBF_4 has the highest ionic mobility but participates in formation of a SEI of poor quality. Furthermore, LiClO_4 and LiAsF_6 are explosive and toxic, respectively, invalidating them for practical usage. In addition to the aforementioned lithium salts, another alternative to LiPF_6 is lithium bis(trifluoromethanesulfonyl)imide (LiTFSI), $\text{Li}[\text{N}(\text{SO}_2\text{CF}_3)_2]$ which has a higher solubility, better thermal stability, and is more chemical inert. It, however, does not form a protective film on the aluminium current collector and therefore the aluminium corrodes. This can be

mitigated by using a blend of LiTFSI and LiPF₆. [31, 48, 49]

3.4.1 Electrochemical Stability of the Electrolyte and the Solid Electrolyte Interface

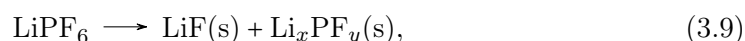
When a newly assembled LIB undergo the first charge/discharge cycle an interface film forms at the anode. This film is the consequence of reduction of the electrolyte that occurs due to the low potential at the anode. The electrochemical window depends on the species present in the electrolyte e.g. anions from the lithium salt. For isolated EC molecules the oxidation potential is around 7 V vs. Li/Li⁺ while in the vicinity of PF₆⁻ or another EC molecule it is around 5-6 V vs. Li/Li⁺. The interplay between the electrolyte and the salt is, in regard to the electrochemical stability, further complicated when additives are introduced into the solution. [50–52]

Formation of Anode Electrolyte Interface Film

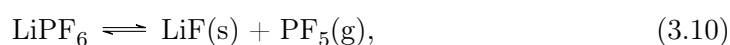
When the lithium-ion battery is charged the potential at the anode decreases and at 0.25 V vs. Li/Li⁺ the lithiation of graphite initiates. The intercalation continues until 0.01 V vs. Li/Li⁺. The low potential at the anode facilitates the reduction of the electrolyte since it is outside its electrochemical window. The majority of the reduction processes take place between 0.8 V and 0.2 V vs. Li/Li⁺ and results in organic and inorganic species. Some of these reduction products are insoluble and precipitate onto the surface of the graphite particles where they form a passivation film known as the solid electrolyte interface film. This film inhibits further reduction of the electrolyte by being electrically insulating however still permeable for lithium ions. [7, 49, 53]

The formation mechanism of the SEI film is considered to be a complex interplay of multiple reduction processes which depend on inter alia temperature, current, and electrolyte concentration. In general the SEI formation process can be divided into two steps. The first being the reductive decomposition of the electrolyte into new chemical species and the second being precipitation of the chemical species onto the graphite surface.

The decomposition of the electrolyte involves reduction of the lithium salt as



where both products precipitates since they are insoluble. Trace water facilitates an undesired reaction with the lithium salt to form hydrofluoric acid as



The carbonaceous solvent molecules reduce in general via either a one- or two-electron reduction process. The exact reduction processes are still debated and the following

is based on work by An et al. [49] and Asenbauer et al. [7]. The ethylene carbonate mainly undergoes one-electron reduction processes. An overview of possible reduction pathways is shown in Fig. 3.16. The two intermediate products, after one reduction step, reduce further by another one-electron reduction. A third reaction may take place by either a dimerisation to form the product, $(\text{CH}_2\text{OCO}_2\text{Li})_2$, or by Li^+ stabilisation. Some of the reduction pathways form either ethylene or carbon monoxide gas. The radicals of the reduced intermediate electrolyte species react with lithium ions to form insoluble products and hence all of the lithium containing products will partake in the formation of the SEI film.

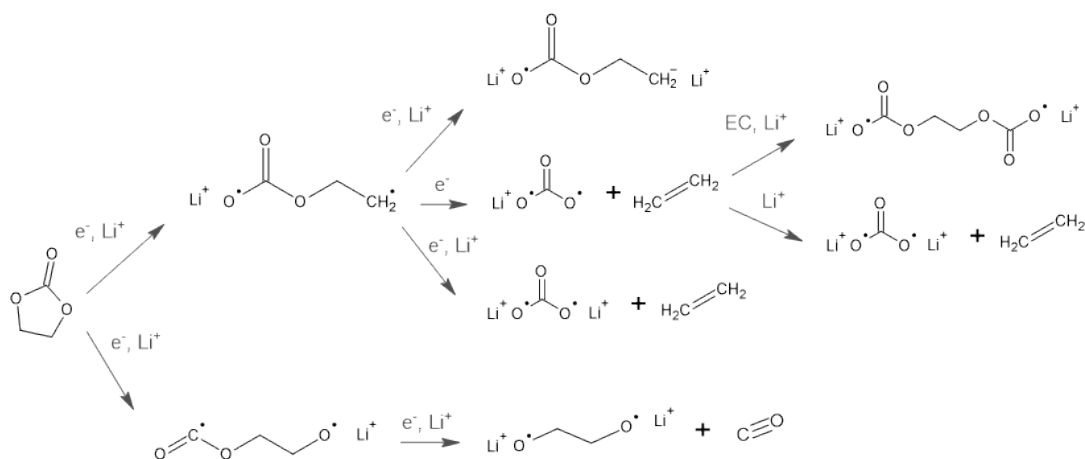


Figure 3.16: One-electron reduction of ethylene carbonate. The first reduction produces radical intermediates which participate in a second reduction to form more stable compounds. The by-products ethylene and carbon monoxide are volatile and do not react further.

The ethylene carbonate can also undergo two-electron reduction processes which yield similar products. These reaction pathways are shown in Fig. 3.17.

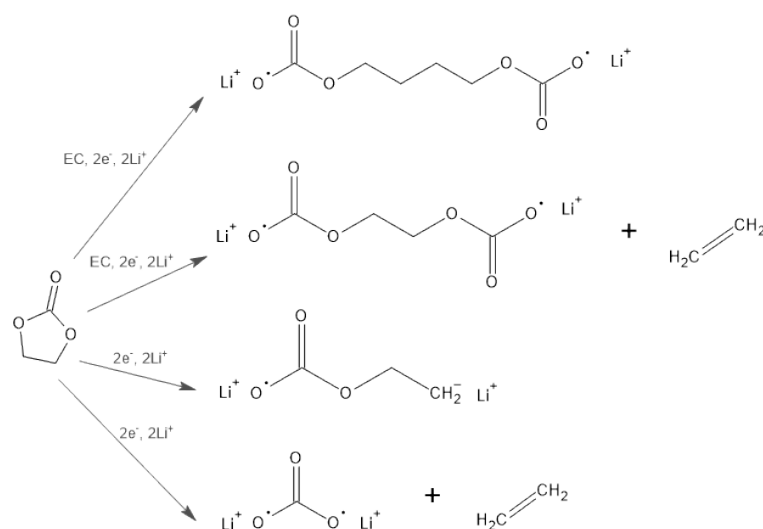


Figure 3.17: Two-electron reduction of ethylene carbonate. In the presence of other EC compounds a dimerisation can take place.

In addition to the one- and two-electron reduction processes EC can also be involved in secondary reactions which involve hydrofluoric acid or water or both. The hydrofluoric acid stems from the reaction in Eq. (3.11) while water is an impurity stemming from the battery manufacturing process. Furthermore, EC can polymerise in the presence of PF_5 as it attacks the carbonyl functional group which opens the ring in the EC molecule. The opened ring has radical ends which facilitate polymerisation by attacking other EC molecules and thereby causing a polymerisation as seen in Fig. 3.18. [49, 54, 55]

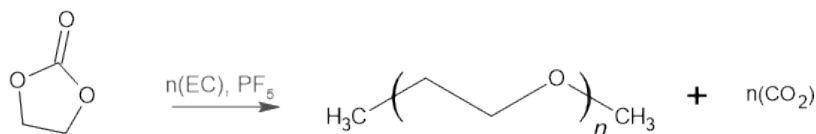


Figure 3.18: Polymerisation of EC molecule in the presence of PF_5 .

Diethyl carbonate can also undergo one- and two-electron reductions. The one-electron reduction path is shown in Fig. 3.19 where the reduction occurs at one of the binding sites between the oxygen and the ethyl group. This creates a radical ethyl and a radical carbonate group. The carbonate group is stabilised by the lithium ion while the ethyl radical may undergo a second reduction to form an ethyl anion.

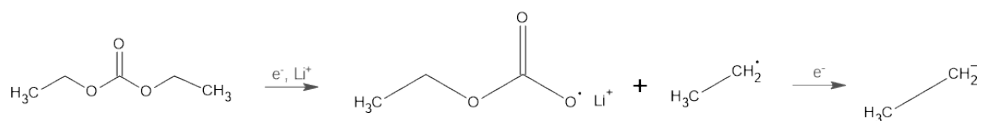


Figure 3.19: One-electron reduction of DEC. The first reduction of DEC is followed by a second one of the ethyl radical to form an ethyl anion.

The two-electron reduction process of DEC can follow two pathways as shown in Fig. 3.20. The first one is a double reduction of the carbonate group to form radical ends, stabilised by lithium ions, and butane. The second pathway is similar to the one-electron reduction process.

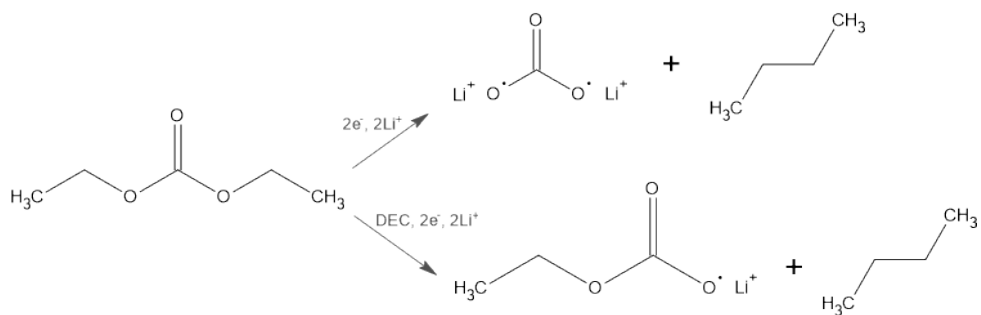


Figure 3.20: Two-electron reduction of DEC. If another DEC is not present the product is lithium carbonate and butane while if it is present the products are similar with an ethyl group on the carbonate.

Similar to EC, DEC can participate in secondary reactions as shown in Fig. 3.21 where the presence of hydrofluoric acid causes a protonation of the radical carbonate group. The result is alcohol groups, LiF precipitation, and CO₂ gas.

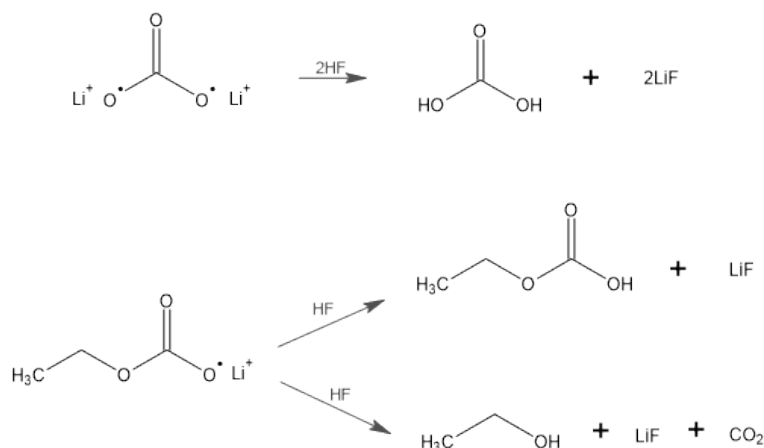


Figure 3.21: Secondary reactions of DEC facilitated by hydrofluoric acid stemming from degradation of LiFP₆ in the presence of water.

The reduction mechanisms presented occur mainly in the vicinity of the graphite anode and are responsible for the components from which the SEI is formed. This makes the composition of the SEI a complex interplay of the different solvent molecules, lithium ions, and impurities present. [49, 54]

The solid-electrolyte interface film is reported to have a mosaic like structure, as seen in Fig. 3.22, composed of the organic and inorganic compounds presented previously. The layer closest to the graphite particles is comprised of compounds which are thermodynamically stable toward the graphite such as LiF and Li₂CO₃. This inorganic layer is covered by some of the decomposed organic products such as (CH₂OCO₂Li)₂ and inorganic compounds like LiF. [49, 54]

The SEI covering the basal and edge planes of the graphite have different thickness and composition. The basal plane SEI is composed mostly of the organic reduction products of the solvent while the SEI on the edge plane consists mostly of inorganic reduction products stemming from the salt. The mechanism responsible for this difference is not yet fully verified. A proposed theory is that since the intercalation occurs from the edge plane, the solvated lithium ions may decompose in-between the graphene layers and thus result in increased inorganic reduction products. [54]

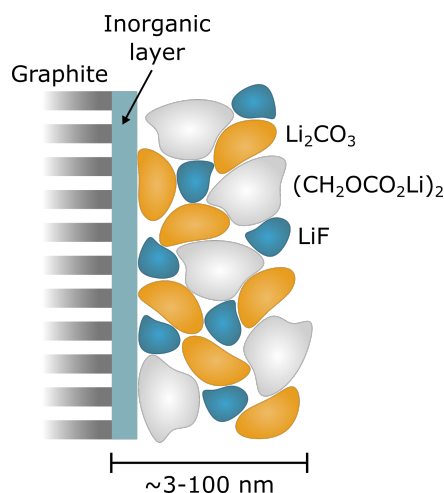


Figure 3.22: Schematic of the double layer structure of the SEI. The layer closest to the graphite is comprised mostly of insoluble inorganic compounds while the outer layer is made up of both organic and inorganic compounds. The thickness of the SEI layer is reported to be between 3 and 100 nm depending on the cycling conditions and level of degradation of the battery [49].

Electrolyte solvent decomposition products are not observed at the LiFePO_4 cathode and hence it is not covered with a SEI film. However, a surface film composed of LiF , LiPF_6 , Li_xF_y , and Li_xPOF_y compounds is present at the cathode electrolyte interface. This film is considered to be very stable and to not limit the performance of the LIB since the thickness of this film is sub-nanometer. It is not reported to increase as the battery ages. [56]

Furthermore, a study of the chemical composition of the surface of the cathode particles done by Sun et al. [57] showed no obvious changes between batteries aged at different C-rates.

The Effect of Electrolyte Additives

The thickness and the composition of the SEI can be altered with additives. The most common ones are vinylene carbonate (VC) and lithium difluorophosphate LiPO_2F_2 (LPF). They are added to the electrolyte in trace concentrations. [58]

In addition to the reduction reactions presented in Section 3.4.1 a trans-esterification can occur between EC and DEC. The result is the linear diethyl 2,5 dioxahexane dicarboxylate (DEDOHC) molecule which is known to increase the impedance of the LIB. A study done by Qian et al. [58] showed that the addition of only VC inhibits the trans-esterification but results in a thicker SEI due to a complete consumption of VC. The addition of both VC and LPF showed to inhibit the trans-esterification and prevent complete consumption of VC yielding a thinner SEI film.

3.5 Polyolefin Separator

The purpose of the separator is to avoid internal short circuits by electronically separating the electrodes while still allowing ionic current to close the circuit. In cylindrical batteries where the electrodes are tightly wound the separator also mechanically separates the electrodes. The separator is therefore a flexible and porous material. Several types of separators are found in commercial batteries, where for LIBs a porous polymer film is the most common choice. Different kind of polymers can be used but typically polyolefins such as polypropylene (PP) and polyethylene (PE) or a combination are chosen due to mechanical and chemical stability at a reasonable cost. The separator can be composed of either a single polymer film or a stack of films. A trilayer configuration such as PP/PE/PP features thermal fuse-like behaviour as the melting point of PE is lower than PP. The melting point of PE is ~ 135 °C and if the battery is subjected to unusual high temperatures the PE layer melts and hence the pores close and ionic current is inhibited to flow. The higher melting point of PP, ~ 165 °C, ensures structural stability of the separator until the PE layer is fully melted and the circuit is opened. This shutdown mechanism prevents internal short circuiting and the risk of thermal runaway is reduced. [59]

Some of the main parameters for characterising porous polymer separators are thickness, porosity, pore size and -shape, and tortuosity. The film thickness varies typically from 10-40 μm , where trilayer separators are thicker than monolayer films. Each parameter should be tuned such that the separator complies with requirements for mechanical strength, dimensional stability, wettability, ionic resistance, chemical-, and thermal stability for a given LIB design.

Next comes a short description of some of the separator parameters and how the ionic resistance depends upon them.

Porosity

Porosity denoted by ε defines the volume ratio between voids and the geometric volume of the separator. Depending on processing conditions LIB separators have a porosity of approximately 0.3-0.6. The pore size and shape vary by process conditions but are typically 60-300 nm they can however be larger up to about 1 μm . A high porosity facilitates retention of more electrolyte which allows ionic transport whereas a too high porosity can lead to mechanical instability. [60]

Fabrication of porous polymer separators can be broadly divided into wet processes and dry processes. The processes are distinguished in whether a solvent, typically a hydrocarbon liquid, is added prior to extrusion of the polymer films. Afterwards both processes employ a stretching step where the micro pores are formed. In general the dry process films exhibit distinct slit-like pores whereas the wet process films show a more tortuous and interconnected microstructure with spherical or elliptical pores. [61, 62]

Tortuosity

Tortuosity, τ , is a parameter used to quantify a tortuous curve. The tortuosity can be simply defined as the ratio of the arc length from a point A to a point B along the curve to the displacement, \overline{AB} . In a porous polymer separator the tortuosity factor relates the actual mean path of the lithium ions through the pores to the displacement from one side of the separator to the other. A higher tortuosity increases the mean path length and the ionic resistance whereas a less tortuous separator has a larger risk of dendritic growth of lithium which can short circuit the battery. [60].

Ionic resistance

The ionic resistance of the separator filled with electrolyte is part of the total internal resistance of the battery. The ionic resistance can be written as

$$R_{\text{ion}} = \rho_e \frac{\tau L}{\varepsilon A} = \rho_s \frac{L}{A}, \quad (3.12)$$

where ρ_e is the bulk electrolyte resistivity, and L and A are the separator thickness and geometrical area, respectively. The factor $\tau/\varepsilon = \rho_s/\rho_e$, where ρ_s is the ionic resistivity of the electrolyte filled separator, can be determined by electrical conductivity measurements, whereas localised information of the tortuosity can be determined with e.g. x-ray microscopy [63]. From Eq. (3.12) the ionic conductivity of the electrolyte filled separator is $\sigma_s = \sigma_e \varepsilon/\tau$ with typical values ranging from 10^{-3} S cm $^{-1}$ to 10^{-1} S cm $^{-1}$, where $\sigma_e = \rho_e^{-1}$ is the bulk electrolyte conductivity [60, 61].

4 Aging Mechanisms of LFP/G Lithium Ion Battery

This chapter begins with an introduction to the concept of LIB aging. It is followed by an examination of different aging mechanisms relevant to the observations presented in Chapter 6.

During its lifespan, a LIB will likely experience various operating temperatures, charge and discharge rates, and depth-of-discharge ranges. These parameters influence the lifespan of the LIB which is often divided into two categories, calendar life and cycle life. The former is related to degradation of the battery when it is not in use and the latter to when it is. For some applications like electric vehicles, the aging of the battery is a combination of the two since the battery will degrade both when it is parked and when the vehicle is driven. The battery life and thereby the level of degradation is commonly characterised by the state-of-health (SOH) as

$$\text{SOH}(t) = \frac{\text{discharge capacity}(t)}{\text{discharge capacity}(t = 0)}, \quad (4.1)$$

where t is the aging time. The SOH depends on the capacity of the battery which is related to the amount of anode and cathode active material, and available lithium ions. The aging mechanisms may be divided into two major categories: Increased impedance and loss of lithium ion inventory (LLI) or loss of active material (LAM), or both. The former results in a power fade due to the increased resistance and since the charge and discharge cut-off voltages remain the same it will also result in a capacity fade. The latter may be understood with an analogy to a water tank model as seen in Fig. 4.1 where LLI is analogous to loss of water in the tank while LAM is analogous to a reduction of the tank's volume. The active material comprises both the graphite and LiFePO_4 .

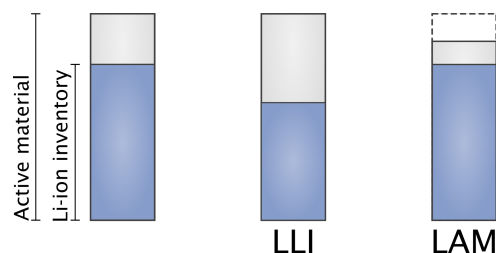


Figure 4.1: Illustration of the water tank model. The water in the tank is analogous to the lithium ion inventory, and the volume of the tank is analogous to the amount of active material of the anode and the cathode. Aging may result in loss of lithium ion inventory (LLI) or loss of active material (LAM), or both.

4.1 Cracking of Graphite Particles

When lithium de-/intercalates into the graphite particles they undergo a 10% volume change and it has been observed that this change results in formation of cracks both on the inside and outside of the particles [64]. The interior cracks cause the volume and thereby the surface area to increase. Depending on the magnitude of the increment the additional surface area may either be covered by the formation of additional SEI film or it may be covered by stretching of the already formed film due to its elasticity as seen in Fig. 4.2. The consequence of the latter is LLI since formation of SEI film consumes Li^+ as explained in Section 3.4.1. If the surface cracks penetrate through the SEI film, the film heals and thus causes LLI. The volume changes may also give rise to loss of contact between particles, the binder material and particles, the current collector and binder material, or to exfoliation of the graphite particles from the current collector. All of the aforementioned cases are known to increase the impedance of the battery [65]. Additionally, the volume increase reduces the porosity of the anode and hence inhibit electrolyte from penetrating into the layers of graphite particles which results in LAM. [64–66]

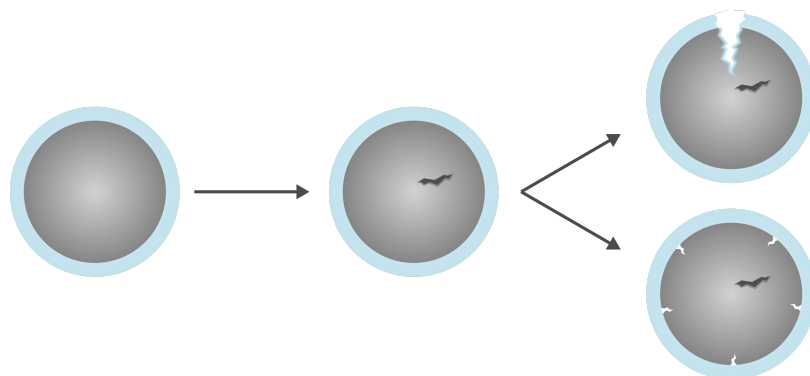


Figure 4.2: Schematic of two outcomes of an interior crack. The interior crack increases the volume and thereby the surface area of the graphite particle. For large changes the surface and the SEI film may crack. For small changes the SEI film may stretch due to its elasticity.

The amount and size of the cracks have been observed to be related to the C-rate

and the number of cycles. Lin et al. [67], observed that for batteries with the $\text{LiFePO}_4/\text{Graphite}$ chemistry, a higher C-rate induced greater mechanical strain on the graphite lattice due to a more rapid de-/intercalation of lithium ions. This resulted in the formation of more cracks. The size of the cracks was observed to be related to the number of cycles and to grow along the grain boundaries since it is the path with least resistance. [67]

4.2 Growth of SEI Film on Anode

The formation and the properties of the solid electrolyte interface were examined in Section 3.4.1 where it was explained that the purpose of the film is to stabilise the graphite and electrolyte interface. The SEI film should stabilise the interface by inhibiting any further reduction of the electrolyte by only being permeable to lithium ions. However, it does not perfectly insulate the electrolyte from the graphite. Therefore, as the battery is charged and discharged, electrons at the graphite side of the SEI film may penetrate the film and reduce the electrolyte and molecules from the electrolyte may also penetrate from the electrolyte side to the graphite. In both cases the result is a reduction of the electrolyte which contributes to the growth of the SEI film. This growth consumes both electrolyte solvent molecules and lithium ions. In addition to the LLI, the thickening of the SEI film increases the impedance of the anode as it affects the de-/intercalation kinetics [68]. The SOC average during the lifetime of the battery will also influence the development and thickening of the SEI film. Higher SOC average facilitates growth of the film since the low potential at the anode results in an increase in the reduction rate of the electrolyte solvent and -salt molecules. [65, 69]

4.2.1 Iron Dissolution and Precipitation

The LiFePO_4 cathode is considered to be stable in the potential window of operation but its reactivity increases in the presence of trace water and at elevated temperatures. Here the iron dissolves since trace water leads to an excess of H^+ in the electrolyte which partakes in the ion exchange reaction $2\text{H}^+ \leftrightarrow \text{Fe}^{2+}$. The dissolved iron ions may travel to and reduce at the anode and then precipitate onto its surface as metallic iron. The reduction consumes electrons and hence it leads to an irreversible capacity loss. The iron clusters on the anode may also catalyse the growth of the SEI film as they facilitate transportation of electrons from the graphite to the electrolyte. Additionally, the iron clusters also inhibit the intercalation of lithium ions as the clusters physically block the access to the graphene layers as seen in Fig. 4.3. [69, 70]

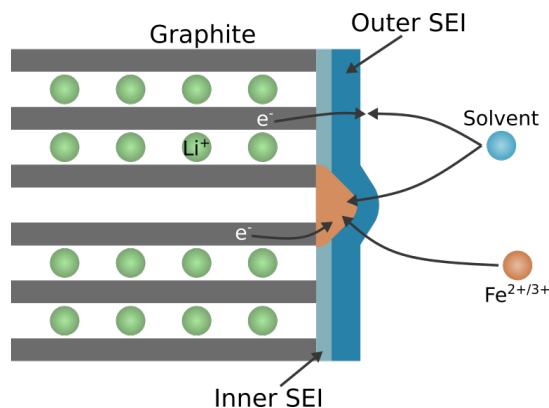


Figure 4.3: Schematic of the deposition of Fe on graphite. The iron catalyses the reduction of the solvent molecules and thus accelerates the growth of the SEI layer. The iron cluster also acts as a blockage for intercalation of lithium ions.

4.3 Formation of a Covering Layer on the Anode

During the charging process of the battery, the graphite particles on the anode may be subject to an inhomogeneous charge distribution which stems from isolated graphite particles or from an inhomogeneous graphite layer, or both. The former occurs when the particles do not have an electrical connection to the current collector which can be a consequence of the volume changes and particle cracking during de-/lithiation as described in Section 4.1. The inhomogeneity arises when a connected particle is close to disconnected ones. The inhomogeneous charge distribution may lead to two neighbouring graphite particles having different levels of lithiation. As the charging continues some particles may become fully lithiated before the battery reaches 100% SOC and hence they become overcharged once the battery reaches 100% SOC. These local areas with overcharge has been observed to result in the formation of a covering layer which is thicker, several micrometers, and more uneven than the SEI film [71]. The formation of this layer is irreversible and impedes the migration of lithium ions from and to the graphite particles which results in an increase in the impedance. When the covering layer forms it increases the inhomogeneity of the charge distribution since less accessible graphite is left. The loss of active graphite material facilitates overcharging due to an excess of lithium ions and therefore, the process is self-reinforcing.

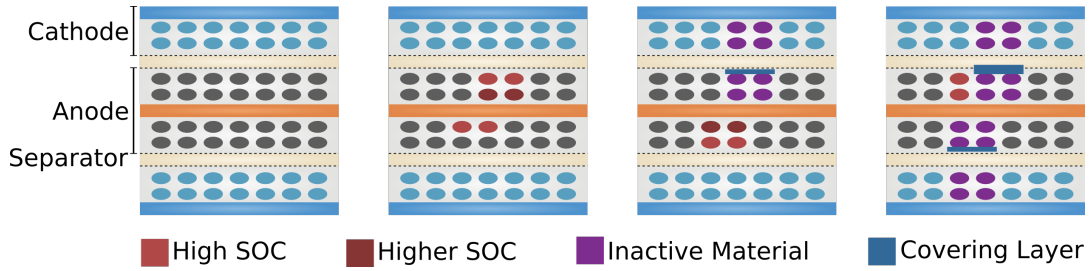


Figure 4.4: Formation of a covering layer due to an inhomogeneous charge distribution. Once the covering layer is formed the graphite and the opposing LiFePO_4 particles become inactive i.e. does not contribute to the capacity of the battery. The figure is inspired by [71].

This covering layer forms to a greater extent at elevated temperatures $\sim 40^\circ\text{C}$ [71]. It is composed of lithium metal, iron, the electrolyte salt LiPF_6 , and electrolyte components such as carbon, hydrogen, and oxygen. The deposition of Fe on the anode, as described in Section 4.2.1, can mask the graphite particles and pores and hence reduce the amount of active anode material. Due to this masking, iron deposition on the anode accelerates the evolution of the covering layer. Since the covering layer contains lithium metal and inhibits de-/intercalation of lithium into graphite it results in both LLI and LAM.[71]

The loss of active anode material has a secondary implication where it can facilitate lithium plating. When the battery is assembled, the cathode is fully lithiated and therefore, it is important that the anode has a larger capacity than the cathode. If this is not the case there will be an excess of lithium ions during charging which cannot intercalate into the graphite and hence they may reduce and precipitate onto the surface of the graphite particles. [66]

4.4 Structural Degradation of LiFePO_4 Cathode

The LiFePO_4 particles contract and expand during charging and discharging due to the extraction and insertion of lithium ions, respectively. The volume of LiFePO_4 is $\sim 302 \text{ \AA}^3$ while for FePO_4 it is $\sim 284 \text{ \AA}^3$ and thus complete delithiation results in $\sim 6\%$ volume change [72]. Micro-cracks form inside the particles if the stress, induced by the volume change, exceeds a threshold in either the LiFePO_4 or the FePO_4 phase. The formation of micro-cracks can result in LFP particles being disconnected from the carbon black coating which comprises the network that connects the LFP particles to the aluminium current collector. Therefore, the formation of cracks in the particles can result in LAM and in increased resistance. [73–75]

Since the stress arises due to the lattice mismatch between the two phases, LiFePO_4 and FePO_4 , the stress is highest when Li_xFePO_4 where $x = 0.5$. It was observed by Gabrisch et al. [73] that the fractures were more numerous at increased C-rates. A

secondary effect of the cracking is the appearance of non-carbon coated LFP surfaces which are more prone to Fe dissolution. Hence the cracking accelerates the Fe dissolution which in turn accelerates the degradation of the anode. [70, 74]

4.4.1 Agglomeration of Carbon Black Coating

The LFP particles are typically coated with a carbon black derivative to increase their conductivity. The coating is quasi-crystalline in a pristine battery and has been observed to agglomerate into an amorphous phase when cycle-aged [74, 75]. The agglomeration is a product of the mechanical stress induced by the volume changes of the LFP particles which causes the carbon black particles to detach and reattach. Additionally, the dissolution of iron from the surface of the LFP particles may create a loss of contact between them and the coating which in turn facilitates agglomeration. [74]

The amorphous phase of the carbon black coating has a lower electronic conductivity and hence the presence of this phase increases the resistance of the cathode. Furthermore, depending on the severity, the amorphous phase may also render LFP particles inactive. [74, 75]

5 Experimental Methods

In this thesis, cycle-aged cylindrical 26650 LIBs based on the LiFePO_4 /graphite electrochemical system were examined with respect to those aging mechanisms mentioned in Chapter 4. The batteries examined were the "ANR26650m1-B" fabricated by the company A123 Systems, which 26650 battery manufacturing plant from 2018 became a part of Lithiumwerks. A photograph of an ANR26650m1-B battery is shown in Fig. 5.1. The basic technical specifications of the ANR26650m1-B batteries are listed in Table 5.1 whereas the complete data sheet can be accessed through the manufacturer's website [76].

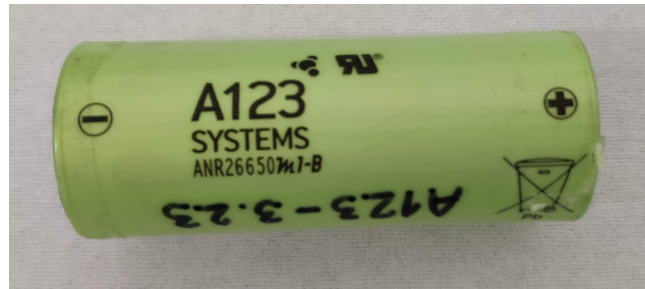


Figure 5.1: Photograph of the type of LIB examined in this thesis. The battery is an ANR26650m1-B from A123 Systems.

Table 5.1: Technical specifications for the ANR26650m1-B LIB from A123 Systems.

Nominal ratings	
Nominal voltage	3.3 V
Capacity (Typical) @ 23 °C	2.6 Ah
Charging and discharging	
Recommended charge current	3 A
Max continuous discharge current	50 A
Max pulse discharge current (10 s)	120 A
Minimum voltage	2 V
Mechanical	
Diameter	Ø25.96 +/- 0.5 mm
Length	65.15 +/- 0.5 mm
Mass	76 +/- 1.0 g

Batteries were aged under different test cases (TCs) with varying cycle depth and average SOC. For every TC the charge and discharge currents were kept constant at $I_{dc} = 10$ A i.e. approximately 4C. The different TCs and their corresponding cycle conditions, and degradation levels are listed in Table 5.2. The degradation level refers to the percentage discharge capacity decrease after cycle aging relative to the initial discharge capacity. In addition to the cycle-aged TCs (1-4), a calendar-aged TC (TCC), and a pristine TC (TCP) were examined. One sample from each TC was used for post-mortem disassembly.

Table 5.2: Overview of the examined test cases, aging conditions, and degradation levels.

Sample	Temperature (°C)	Cycle depth	SOC _{avg}	Degradation level
TCP	-	-	-	-
TCC	40	-	20%	-
TC1	42.5	60%	50%	22%
TC2	42.5	35%	50%	9%
TC3	42.5	35%	27.5%	18.5%
TC4	42.5	35%	72.5%	25.5%

Aging of all test cases were performed with $I_{dc} = 10$ A corresponding to approximately 4C.

The batteries were cycled according to the specified conditions in a controlled environment. During cycling, non-destructive characterisation techniques were used to obtain the incremental degradation of the battery performance parameters (i.e., capacity, internal resistance, and small signal AC impedance). Tests were performed on a weekly basis and when the batteries reached the predefined end-of-life (EOL) criterion of 20% capacity fade, the aging was stopped. Due to an infrastructural failure of some of the aging equipment TC2 was not aged until the EOL criterion. The accelerated aging of the batteries and weekly logging of characteristics were performed between 2013-2014 by Assoc. Prof. Daniel-Ioan Stroe at the department of Energy Technology at Aalborg University. From 2014 to the onset of the thesis work the batteries were stored and hence calendar-aged at ~20% SOC and at room temperature.

The capacity fade evolution of the four cycle-aged LFP/G batteries is presented in Fig. 5.2. The cycle depth from Table 5.2 is in relation to the measured capacity, such that the absolute cycling range becomes narrower when the capacity decreases during the aging. To compare the capacity decrease trend, the capacity is plotted vs. full equivalent cycles (FEC) i.e. $1 \text{ FEC} = 2Q_0 = 5.2 \text{ Ah}$.

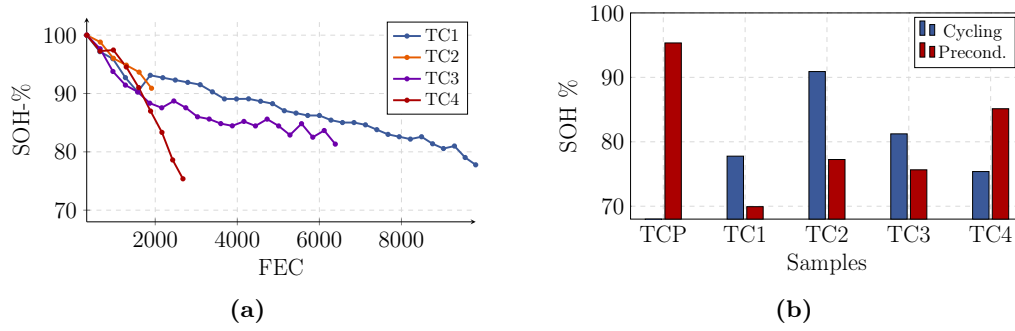


Figure 5.2: (a) Evolution of the discharge capacity decrease during cycling as determined by a 1C capacity test at 25 °C for each TC. The x -axis is full equivalent cycles, where each FEC corresponds to 5.2 Ah. (b) Bar chart comparison of the capacity fade after cycling and that determined during preconditioning after 6 years of storage at 20% SOC and at room temperature. The pristine battery was also calendar-aged but not cycled, and therefore no blue bar is present for this test case.

Due to the long storage time from 2014 the batteries were subjected to preconditioning before disassembling. During preconditioning, the batteries were fully charged and discharged five times and subsequently, the capacity, internal resistance, and small signal AC impedance were measured at 25 °C. The internal resistance as a function of SOC is seen in Fig. 5.3.

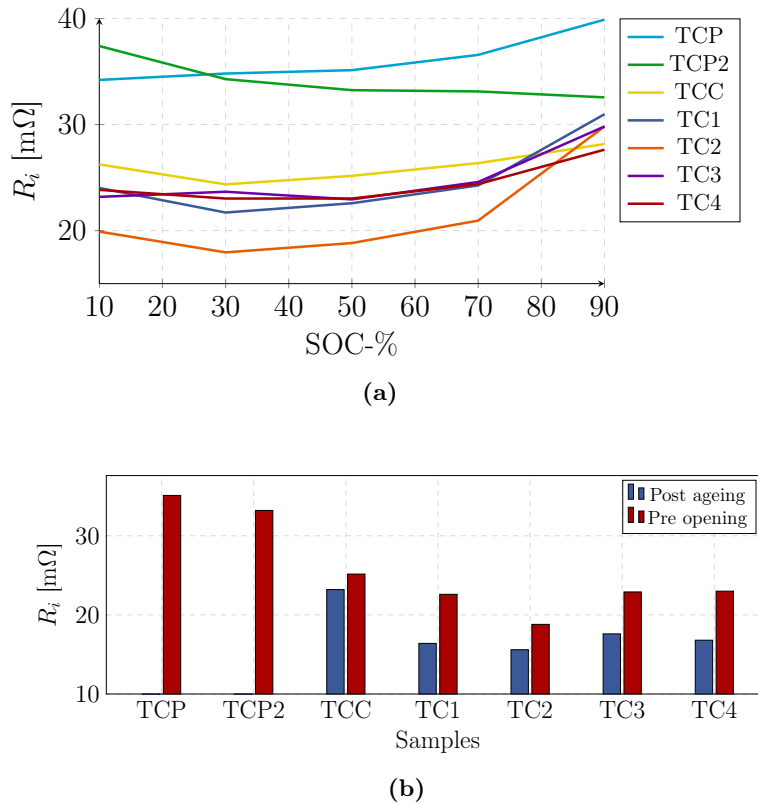


Figure 5.3: Internal resistance from reference performance tests performed by Assoc. Prof. D.-I. Stroe for each TC. (a) Internal resistance as function of SOC-% at 1C of the TCs measured prior to opening as part of their preconditioning. (b) Bar chart comparison of the internal resistance after cycling and after preconditioning at 50% SOC.

It was found that the pristine battery had the largest internal resistance. To verify this unexpected trend, internal resistance measurements were performed on another pristine battery, TCP2, which however proved to have a comparable internal resistance to TCP.

5.1 Disassembly methodology

The aged batteries were disassembled in a glovebox capable of providing an inert Ar or N₂ atmosphere. The glovebox is a modified sandblaster cabinet capable of providing a steady atmosphere with water content ≤ 10 ppmv. Additional details about the glovebox and how it was built can be found in Appendix B.1.

The batteries were opened in an Ar atmosphere by first removing the outer green plastic layer and cutting the top and bottom with a hook blade knife. The interior parts were then accessed by peeling the metal shell off with a pair of cutting pliers. The interior components were then unrolled and cut with a scissor into smaller pieces. The anode, cathode, and separator were then washed in DEC and placed to dry for 1 hour. Washing the materials removes any residual electrolyte and potential crystallised LiPF₆. DEC is suitable for washing as it is presumably a component of the electrolyte solvent. The components were then individually stored in aluminium pouches which were heat-sealed. A photograph series of the above mentioned procedure is shown in Fig. 5.4. A step-by-step procedure and list of tools used for LIB disassembly and sample preparation can be found in Appendices B.2 and B.3 along with a diagram of the process from accelerated aging to post-mortem analysis. This process is similar to that reviewed by Waldmann et al. [77].

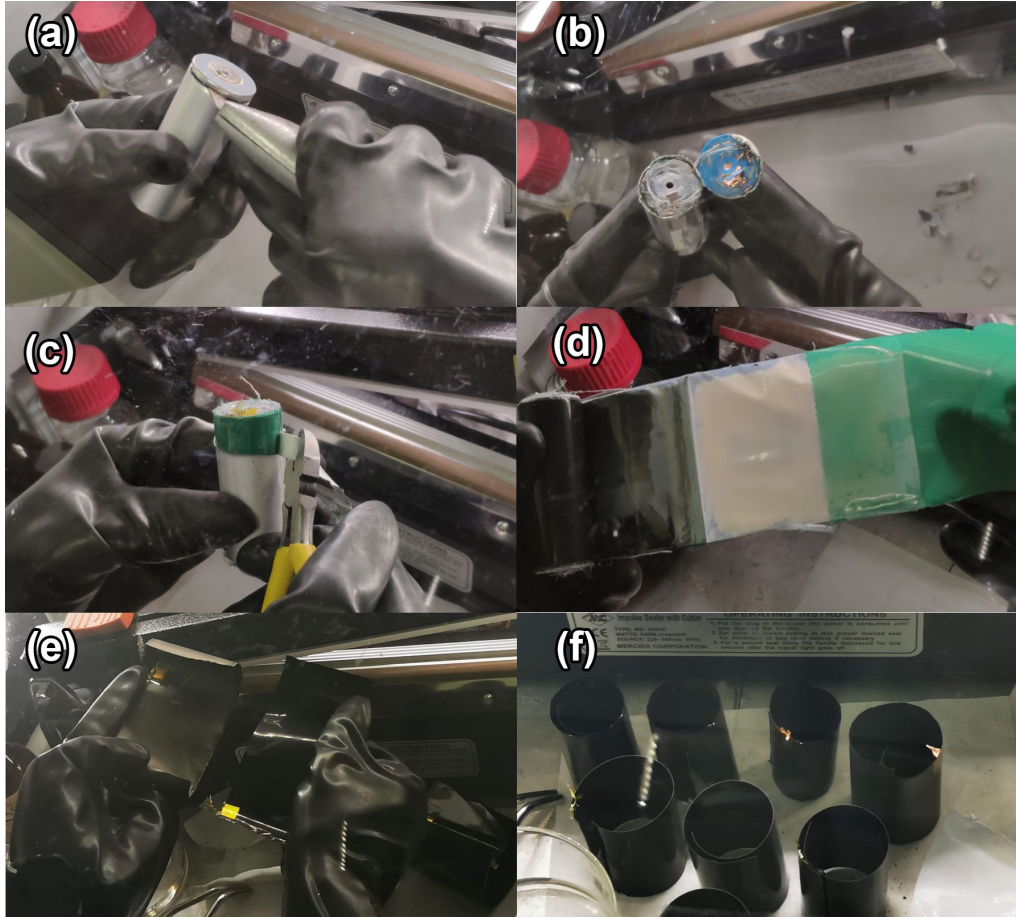


Figure 5.4: Photograph series of the LIB disassembly process. (a) cutting open the battery end, (b) opened battery, (c) peeling of the metal can, (d) unrolling the internal components, (e) left is anode and right is cathode, (f) drying of internal components cut into smaller pieces.

5.2 Surface Morphology Analysis

The morphology of the surface of the anodes and cathodes were examined using a Zeiss EVO 60 scanning electron microscope (SEM) and a Zeiss CrossBeam XB 1540 for higher resolution micrographs. The SEM micrographs were compared qualitatively and quantitatively. The latter was done for the anode samples with the mean line intersection method to determine a mean particle size. It was not possible to determine mean sizes for the LiFePO_4 samples due the small indistinguishable particles.

The method, adapted from DS/EN ISO 643:2020 [78], relies on drawing a line through the micrograph and counting the number of intersections with edges of particles. The number of intersections, p , is divided by the length of the line, L , and an apparent mean particle size for the line, μ_{line} , is obtained as

$$\mu_{line} = \frac{p}{L}. \quad (5.1)$$

This procedure is repeated n times on the same micrograph and a global mean, μ , is then determined as

$$\mu = \sum_{i=1}^n \frac{\mu_{line,i}}{n}. \quad (5.2)$$

The principle of this method can be seen in Fig. 5.5.

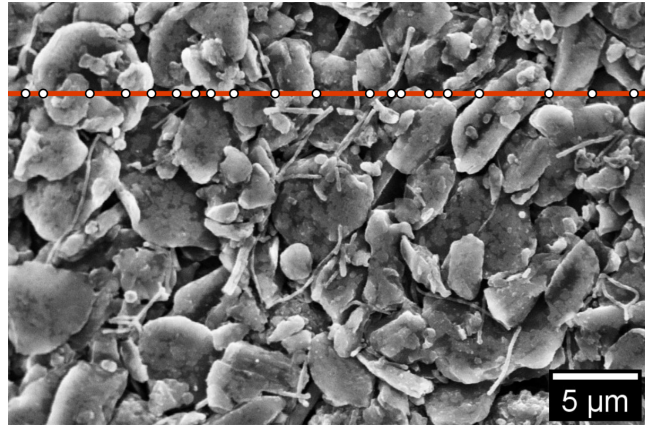


Figure 5.5: Example of the mean line intersection method on a SEM micrograph of the anode from the pristine battery. The intersection between the red line and the edges of the graphite particles are highlighted with white circles.

The graphite particles were examined for isotropy by performing the procedure in different directions and comparing the calculated means.

5.3 Energy Dispersive X-ray Spectroscopy

Energy dispersive x-ray spectroscopy (EDS) was used to qualitatively identify elements in the anode and cathode samples. The obtained EDS spectra were additionally analysed with a standardless approach to obtain a quantitative elemental composition. The composition was then compared between TCs to identify e.g. iron precipitation and SEI composition on the anodes, and stoichiometry of the cathodes. The EDS system was a ThermoFisher-Scientific EDS unit integrated with a Zeiss EVO 60 SEM. The EDS unit utilised a liquid nitrogen cooled Si(Li) detector to detect characteristic x-ray photons excited by the incident electron beam. The x-ray photon energy, typically from 100 eV to 10 keV, serves as an elemental fingerprint, whereas the x-ray count can be used to quantify the elemental composition of the electron beam interaction volume. Low energy x-rays, such as the Li-K α emission line with photon energy of approximately 55 eV [79], is not detectable due to the low signal. Acquisition of the spectra was performed with 15 kV acceleration voltage, a time constant of 50000 ns, working distance of 15 mm, and 30 s live time. [80]

Qualitative identification of the elemental composition of the samples were performed with the NIST DTSA-II software [81] where the measured peak energies were compared with a database of x-ray lines. Quantitative analysis was performed with the ThermoFisher NSS software with a Gaussian or top-hat filter based standardless

quantification to determine mass fractions of the identified elements. For the cathodes, the mass fractions were normalised to the three main components, O, P, and Fe to compare stoichiometry. For the anodes, the quantified mass fractions were normalised to O, F, and P which all are constituents of the SEI layer.

A point and shoot technique was used where an SEM image was obtained and afterwards regions on the image were marked for EDS analysis. This was used to examine and identify elements in some of the features found with the SEM.

5.4 Raman Spectroscopy

Raman spectroscopy (RS) was used to analyse the graphite anodes and the carbon coating on the cathodes. RS was performed with an Invia Micro-Raman spectroscope from Renishaw. To be able to compare different spectra, the excitation wavelength was held constant. The excitation laser was a 532 nm solid-state laser attenuated to 5% power output. The spectra were acquired with a static acquisition mode with 1400 cm^{-1} center and data acquisition was performed with a 3 s acquisition time and 30 accumulations.

Curve fitting on the obtained spectra was performed to analyse spectral features, such as peak position, full width at half maximum (FWHM), peak area i.e. integrated intensity, and intensity amplitude. For the examined carbonaceous materials, two distinct peaks, D and G, are reported. The G mode is related to in plane bond stretching of the sp^2 covalent bonds in the crystal structure of graphite. The D mode is activated by defects such as vacancies, grain boundaries, dislocations, and change of hybridisation from sp^2 to sp^3 , which hence makes the D mode forbidden in perfect graphite [82, 83]. For the D peak, a symmetrical Lorentzian line shape on the form

$$f_L(x; x_0, \gamma_0, I_0, C) = I_0 \left[\frac{\gamma_0^2}{(x - x_0)^2 + \gamma_0^2} \right] + C, \quad (5.3)$$

was used for fitting, where γ_0 is a width parameter, I_0 an amplitude parameter, x_0 the peak position, and C a background parameter. In the case of Raman spectroscopy $f(x) = I(\nu)$, where I is the intensity count in arbitrary units and $\nu = \lambda^{-1}$ is the wavenumber of the Raman shift in units cm^{-1} . For the background a first order baseline correction was made such that $C = a\nu + b$, where a and b are constants. The background correction was made in the range 850 cm^{-1} to 1800 cm^{-1} with a MATLAB program [84] and subtracted from the spectra before fitting. The Lorentzian line shape can be modified to account for asymmetrical peaks by modifying the width parameter such that it depends on the wavenumber. This was achieved with a Sigmoid function on the form

$$\gamma(x) = \frac{2\gamma_0}{1 + \exp[Q(x - x_0)]}, \quad (5.4)$$

where Q is a measure of asymmetry, which for $Q > 0$ gives a left skewed line shape towards lower wavenumbers [85]. For $Q \rightarrow 0$ the symmetrical line shape is recovered. The asymmetrical Lorentzian line shape was used to fit the G peak. The origin of the inhomogeneous broadening is reported to be correlated to multiple effects such as surface states, phonon confinement by grain boundaries, and lattice defects and is most often observed in nanoscale materials [86].

Curve fitting was performed with a non-linear least-squares procedure based on the Levenberg-Marquardt algorithm. Additional information about this algorithm and a detailed description of how it was implemented can be found in Appendix A.4. On the cathode two additional peaks at ca. 1040 and 986 cm^{-1} were seen. These peaks are attributed mainly to P-O stretching of the PO_4^{3-} group in the olivine LiFePO_4 structure [87]. These were fitted with two symmetrical Lorentzian line shapes. On the anodes a shoulder on the right side of the G peak was seen in the Raman spectra. This mode, termed D', is also activated by disorder and was fitted with a symmetrical Lorentzian line shape. [83]

The FWHM for the asymmetric Lorentzian line shape was estimated with a fourth degree polynomial in the range $Q \in [-0.02; 0.02]$ and $\gamma_0 \in [40; 70] \text{ cm}^{-1}$ based on the obtained data. The formula reads

$$\text{FWHM}_L(Q, \gamma_0) = 2\gamma_0 [1 + (27.6\gamma_0 - 707)Q^2 - 0.464\gamma_0^{3.56}Q^4], \quad (5.5)$$

where the FWHM for the symmetrical Lorentzian is recovered in the case $\text{FWHM}_L(Q = 0, \gamma_0) = 2\gamma_0$. The error of Eq. (5.5) in the mentioned range was found to be in the range -1.77 % to 0.54% and the derivation of the formula is shown in Appendix A.5. The integrated intensity for the symmetrical Lorentzian was obtained analytically

$$\int_a^b f_L(x) dx = I_0 \gamma_0 \left[\arctan\left(\frac{x - x_0}{\gamma_0}\right) \right]_a^b. \quad (5.6)$$

For the asymmetric line shape the integration was performed numerically in MATLAB with the *vpaintegral()* function.

The Raman peak position is influenced by the bond strength and atomic masses of the atoms involved in the excited vibration [88]. Metric points for the RS maps are ratios of the D and G peak characteristics. These are the integrated intensity A_D/A_G , the intensity I_D/I_G , and the full width at half maximum $\text{FWHM}_D/\text{FWHM}_G$ which all can be related to the crystallinity of the carbonaceous samples. Considering the ratios instead of the absolute value eliminates uncertainties related to sample focus which hence enables direct comparison between different samples. [89]

The Raman peak intensity is related to the change in the polarisability of a species during a vibration. The peak width of a Raman peak i.e. the FWHM is a measure of the frequency spread of the excited vibrational mode and is for micro- and nanocrystals commonly proportional to the crystal size [90]. Considering the disorder induced D-band, different types of defects and their densities effectively yields a spread of vibrational modes that when excited yields a wider D-peak. The integrated intensity ratio combines contributions from the intensity and the FWHM. Studies by Jorio et al. [89] of vacancy-like defects on ion bombarded highly oriented pyrolytic graphite suggest an increased A_D/A_G ratio to be a measure of an increased defect density.

Raman spectroscopy was additionally performed in a ca. 20x20 μm x - y grid consisting of ~ 200 points. These measurements was used to spatially map e.g. the ratio of the integrated intensities of the D and the G peak i.e. A_D/A_G . The mapping measurements were performed with 1 s acquisition time and 30 accumulations.

5.4.1 Statistical Analysis of the RS Maps

The spectra acquired from the mapping technique were analysed quantitatively by making histograms of the ratios A_D/A_G , I_D/I_G , and $\text{FWHM}_D/\text{FWHM}_G$. The histograms were created by calculating the bin width, W , with Scott's rule as

$$W = 3.49\sigma n^{-1/3}, \quad (5.7)$$

where σ is the standard deviation of the data set, y , and n is the number of data points [91]. The number of bins in the histogram is calculated as

$$k = \left\lceil \frac{\max y - \min y}{W} \right\rceil, \quad (5.8)$$

and since k must be an integer, the ceiling function, $\lceil \cdot \rceil$, is used. The histograms form the basis of the quantitatively comparison of the Raman spectroscopy maps of the anode and the cathode samples.

5.5 Electrochemical Cell Setup and -Techniques

An electrochemical cell was built to conduct electrochemical experiments and examine the performance of the isolated LIB electrodes. This cell included a three-electrode setup composed of a working, a reference, and a counter electrode as illustrated in Fig. 5.6 controlled by a PalmSens4 portable potentiostat. The electrodes are abbreviated as WE, RE, and CE, respectively. The electrolyte used was a battery grade 1 M LiPF_6 in 50/50 by volume DEC/EC from Sigma-Aldrich. In the three-electrode setup, the potential difference is measured between the WE and the RE, and the resulting current is measured between the WE and the CE. The electrochemical events of interest occur at the working electrode. Its surface should therefore be clean and the surface area should be well-defined. The counter electrode serves as a current sink

and completes the electrical circuit. When reduction occurs at the WE, oxidation occurs at the CE. To avoid limiting the reaction kinetics at the WE, the CE surface area should be greater than that of the WE. Additionally, an inert CE is preferable to avoid formation of unwanted byproducts during the experiment. [92]

A reference electrode with a stable equilibrium potential is used as a reference point such that the potential of the WE can be measured against it. Hence the chemical equilibrium of the RE should thus be maintained throughout the entirety of the electrochemical experiment. The introduction of this third electrode is useful as the potential difference between the WE and the CE can be significantly influenced by the flowing current hence making it difficult to measure accurately. [92]

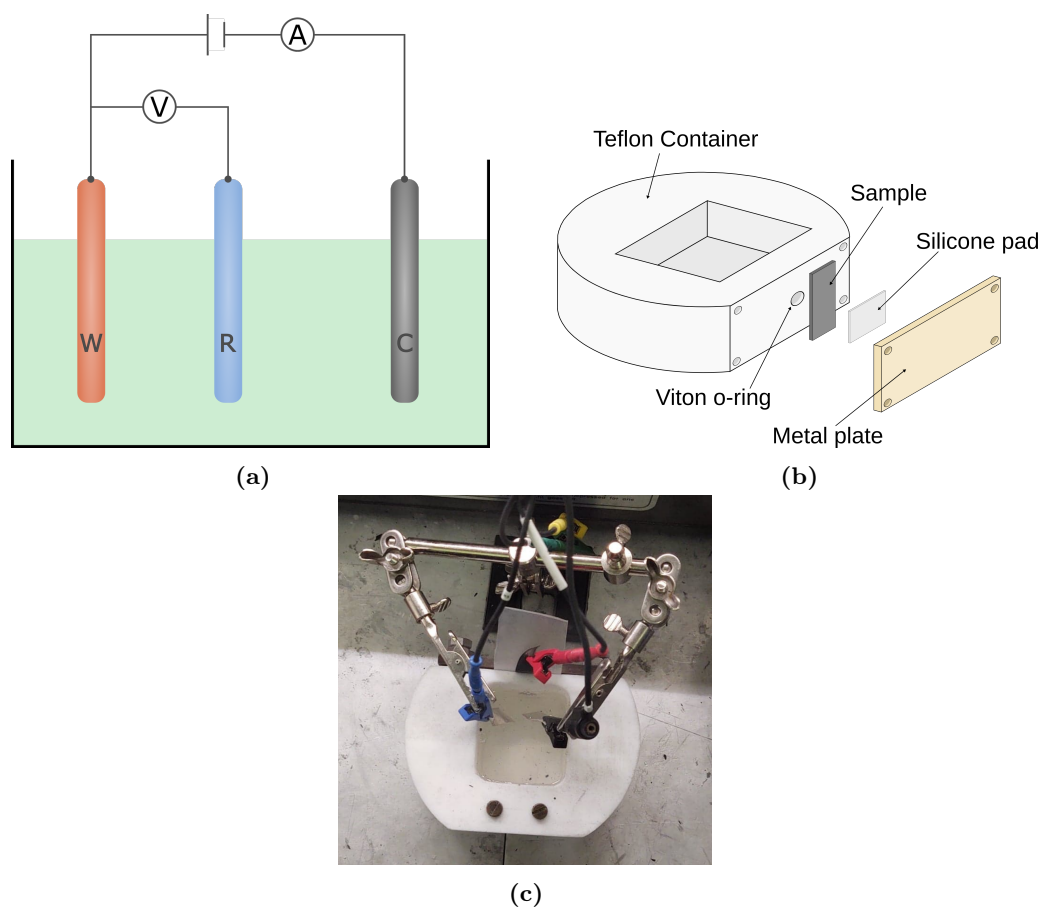


Figure 5.6: (a) Schematic showing the electrical circuit for the three-electrode electrochemical cell. (b) Exploded view of the Teflon bath showing the sample mounting mechanism. (c) Photograph of the actual electrochemical cell.

For the electrochemical experiments lithium metal foil from MaTeck was used as RE and CE. The foil was cut into rectangular strips with dimensions 0.5 x 5 x 30 mm. During time extensive electrochemical experiments, the Teflon bath was covered with Parafilm to minimise evaporation of the electrolyte solvent. A bullet point list of the required equipment and procedure for the electrochemical experiments can be found in Appendix B.4.

5.5.1 Cyclic Voltammetry

The potentiostat was used for cyclic voltammetry to probe the electrochemical system and obtain information about electron transfer kinetics, diffusion, and stability of generated species of the chemical reactions occurring at the WE i.e. the anode or the cathode. In CV the potential difference between the WE and RE is cyclically varied while the resulting current between WE and CE is measured. A theoretical elaboration of the cyclic voltammetry method and derivation of the key equations for the method can be found in Appendix A.2.

Initial Cyclic Voltammetry Experiments

Initial cyclic voltammetry experiments were conducted with a prepared silver wire coated with AgCl as RE and a graphite rod as CE. These electrodes were found to be unsuitable since firstly, the RE was not able to maintain a constant potential due the dissolution of AgCl in the electrolyte, and secondly the graphite CE did supposedly partake in Li de/intercalation causing a much larger current which concealed the sought features of the reactions at the smaller WE. The previously mentioned Li foil was used as RE and CE after the unsuccessful initial experiments.

Cyclic Voltammetry Experiments

The experimental CV parameters are shown in Table 5.3. The obtained voltammograms were normalised with respect to the apparent surface area of the WE. This area was determined by the circular hole in the Teflon bath and was 0.28 cm². Each experiment was initialised with an equilibration period with constant potential for 10 minutes. For the anode the equilibration potential was E_{\max} , and for the cathode it was E_{\min} to mimic a discharged state.

It was observed that there was large differences between the first few cycles. Therefore, multiple cycles were recorded to reach a state where the evolution from one cycle to the next was insignificant. Due to this evolution the final cycle, which was the fourth for the anode and sixth for the cathode, were used for further analysis.

Table 5.3: Experimental CV parameters.

	E_{\min}	E_{\max}	Scan rate	Cycles	Equilibration	Time
Anode	0.01 V	0.8 V	75 μVs^{-1}	4	10 min at E_{\max}	24 hrs
Cathode	2.7 V	4.1 V	200 μVs^{-1}	6	10 min at E_{\min}	24 hrs

In addition to the shape of the current vs. potential traces, metric points with a theoretical significance are defined. These include the peak current, peak position, total charge transfer, and peak-to-peak separation which all are derived and elaborated in Appendix A.2. For the reversible and fast redox reaction, compared to the experimental timescale, the peak current is described by the Randles-Ševčík equation

$$i_p = 0.4463zFSC_0\sqrt{\frac{DzF\nu}{RT}}. \quad (5.9)$$

where S is the surface area of the WE, C_0 is the bulk electrolyte concentration, D is the diffusion coefficient, z is the amount of electrons transferred in the occurring redox reaction, ν is the scan rate, and R , T , and F are the molar gas constant, the absolute temperature, and Faraday's constant, respectively. The factor 0.4463 can be obtained by numerically solving Fick's laws of diffusion as elaborated in Appendix A.2. The peak currents are determined in relation to linear extrapolated baselines since the current is not necessarily zero prior to a peak. The peak-to-peak separation for the chemically and electrochemically reversible reaction is

$$\Delta E_p = 2.200 \frac{RT}{zF} \stackrel{25^\circ\text{C}}{\approx} \frac{57 \text{ mV}}{z}, \quad (5.10)$$

and the standard potential can be approximated by the mean peak potential $E^\ominus \simeq E_{1/2} = (E_{pc} + E_{pa})/2$. The amount of charge transferred can be calculated by the integral

$$Q = \int_{E_{\min}}^{E_{\max}} \frac{dQ}{dE} dE = \int_{E_{\min}}^{E_{\max}} \frac{i}{\nu} dE, \quad (5.11)$$

which for the completely reversible electrochemical reaction should be $Q = 0$ if the experimental potential window covers the entire reaction.

The CV data in Section 6.4 is represented following the IUPAC convention where the x -axis is shown with ascending potentials. The y -axis is shown with oxidative and reductive currents as positive and negative, respectively. Representation of the CV data and related data analysis follows Fig. 5.7, where $i_{p(a,c)}$, ΔE_p , and $E_{1/2}$ are shown.

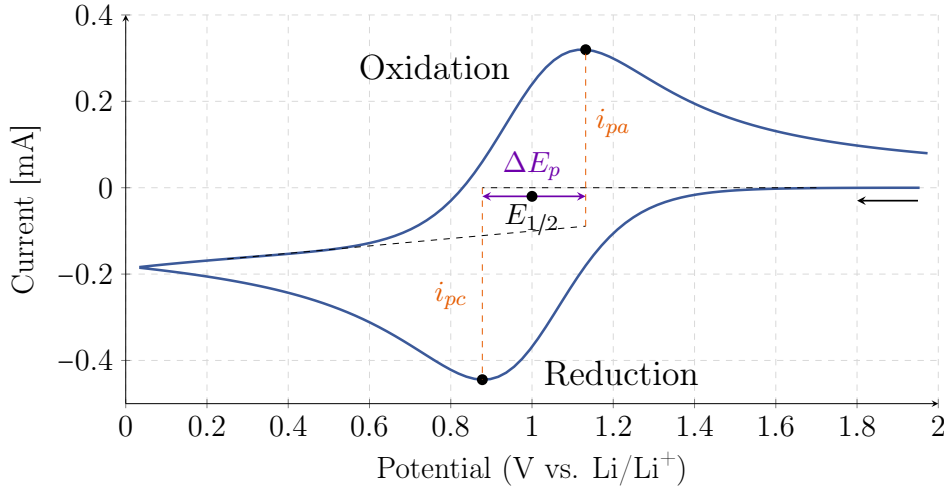


Figure 5.7: Simulated CV data from Appendix A.2 for a reversible electrochemical reaction. The four metric points used for further analysis are; peak currents in relation to extrapolated baselines $i_{p(a,c)}$, peak-to-peak separation ΔE_p , and the mean peak potential $E_{1/2} \simeq E^\ominus$. The arrow indicates the scan direction.

Tafel Kinetics

The cyclic voltammograms were analysed by examining the kinetically controlled regions. These regions are located prior to the anodic and the cathodic peak where the current voltage relation should follow the Butler-Volmer equation as

$$i(\eta) = i_0 (e^{\alpha_a f \eta} - e^{-\alpha_c f \eta}), \quad f = \frac{zF}{RT}, \quad (5.12)$$

where i_0 is the exchange current density, α_a and α_c are the transfer coefficients for the anodic and cathodic reaction, respectively, and η is the overpotential given as $\eta = E - E_{1/2}$. If the overpotential is large but still in the kinetically controlled range, Eq. (5.12) can be simplified to

$$i(\eta) \simeq i_0 e^{\alpha_a f \eta}, \quad \eta > 0.12 \text{ V}, \quad (5.13)$$

and likewise if the overpotential is small but still in the kinetically controlled range

$$i(\eta) \simeq -i_0 e^{-\alpha_c f \eta}, \quad \eta < -0.12 \text{ V}. \quad (5.14)$$

The Tafel plots for the anodic and cathodic reaction were made by taking the natural logarithm of Eqs. (5.13) and (5.14) as

$$\ln(|i|) = \ln(|i_0|) + \alpha_a f \eta, \quad (5.15)$$

$$\ln(|i|) = \ln(|i_0|) - \alpha_c f \eta. \quad (5.16)$$

The exchange current density and the transfer coefficients were determined with a linear regression model.

In addition to the current density being a function of the overpotential, it is also dependent on the rate constant, k , of the chemical reaction. A larger rate constant yields a larger current density hence

$$i \propto k. \quad (5.17)$$

Therefore, it is assumed that the exchange current density is proportional to the equilibrium rate constant as

$$i_0 \propto k_0, \quad (5.18)$$

if the concentrations of the reactants and the products are constant.

5.5.2 Chronopotentiometry

Chronopotentiometry (CP) is a galvanostatic technique where a constant direct current, i_{dc} , is applied while the potential difference between the WE and the RE is measured as a function of time. The technique was utilised to gain information about the discharge profile of the cathodes from which the capacity per unit area can be determined. Prior to discharging, the cathode samples were pretreated by applying a constant potential, E_{pre} , to mimic constant voltage charging. The constant current discharging was aborted when the potential difference between the WE and the RE reached a user defined value, E_{stop} . The settings used for conducting the experiments are available in Table 5.4.

Table 5.4: Chronopotentiometry settings for cathode discharge measurements.

E_{pre}	t_{pre}	i_{dc}	E_{stop}
4.2 V	1 hr	-200 μ A	2 V

5.5.3 Electrochemical Impedance Spectroscopy

Potentiostatic electrochemical impedance spectroscopy was used to examine the impedance response of the anode and the cathode samples. The underlying principle and the in depth mathematical treatment are available in Appendix A.3. Hence this section only summarises the key principles.

The impedance behavior of an electrochemical system can be determined by applying a monochromatic alternating voltage perturbation as

$$V(t) = V_0 \sin(\omega t), \quad (5.19)$$

and measuring the resulting current

$$I(t) = I_0 \sin(\omega t + \phi), \quad (5.20)$$

where V_0 and I_0 are the voltage and current amplitudes, respectively, ω is the angular frequency, and t is the time. This is done for a range of frequencies and through a Fourier transformation from the time- to the frequency-domain, the impedance can be found as

$$Z(\omega) = \frac{\hat{V}(\omega)}{\hat{I}(\omega)}, \quad (5.21)$$

where the hat notation signifies the Fourier transformed function. The complex impedance function can then be divided into a real and an imaginary part as

$$Z(\omega) = Z_{\text{Re}}(\omega) + jZ_{\text{Im}}(\omega), \quad (5.22)$$

and then $-Z_{\text{Im}}(\omega)$ is often plotted versus $Z_{\text{Re}}(\omega)$ in which is known as a Nyquist plot.

The settings used for the measurements conducted on the anodes and the cathodes are available in Table 5.5. Superimposed DC voltages, E_{DC} , were chosen to examine the impedance response of both electrodes around a given potential. The AC voltage, E_{AC} , was chosen to be 10 or 15 mV (RMS), to ensure linearity in the current-voltage relationship. The frequency interval was chosen based on findings in the literature [93].

Table 5.5: Experimental EIS parameters.

	E_{DC}	E_{AC}	Freq. interval	Equilibration time	Elapsed time
Anode	1 V	15 mV	100 kHz - 1 mHz	10 min	1.5 hrs
Cathode	3.4 V	10 mV	100 kHz - 1 mHz	10 min	1.5 hrs

After acquiring the impedance response of the system, information about the associated resistance and capacitance was retrieved. For real electrochemical systems, the resistance and capacitance are sums of multiple contributions stemming from the chemical reactions, the interfaces, and the diffusion and migration of ions. Therefore, equivalent electrical circuit (EEC) models were utilised to determine the magnitude of the resistance and capacitance contributions.

Two models were made, one for the anode and one for the cathode, since they are composed of different materials. The origin of the models are physical and mainly based on work by Scipioni et al. [93]. A comprehensive derivation is available in Appendix A.3. For both electrodes a transmission line model (TLM) were employed to account for their porous structure, and the EEC is seen in Fig. 5.8.

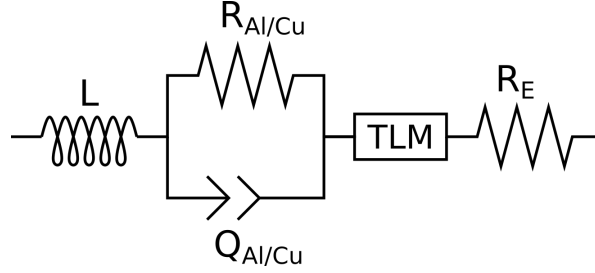


Figure 5.8: Equivalent electrical circuit model of the LiFePO_4 cathode and graphite anode. The wires are modelled with an inductor, L , the current collector is modelled with a resistor, $R_{Al/Cu}$, in parallel with a constant phase element, $Q_{Al/Cu}$. The porous part of the electrode is modelled with a transmission line, and the electrolyte is modelled with a resistor.

The expression for the TLM is different for the two electrodes and for the cathode it is given as

$$Z_{TLM,cat} = \frac{l}{\left(\frac{1}{R_{ion}} + \frac{1}{R_{el}}\right)} \left(1 + \frac{2 + \left(\frac{R_{ion}}{R_{el}} + \frac{R_{el}}{R_{ion}}\right) \cosh(\gamma_{cat}l)}{\gamma_{cat}l \sinh(\gamma_{cat}l)} \right), \quad (5.23)$$

where R_{ion} and R_{el} are the ionic and electronic resistances associated with the pores and the carbon coating, respectively. The parameter l is the depth of the pore, and

$$\gamma_{cat}^2 = (R_{ion} + R_{el})/\zeta_{cat}, \quad (5.24)$$

$$\zeta_{cat} = \frac{R_{ct} + Z_{WGFS,1D}}{1 + Q(j\omega)^n(R_{ct} + Z_{WGFS,1D})}, \quad Z_{WGFS,1D} = \frac{Z_0}{(j\omega\tau)^n} \coth[(j\omega\tau)^n]. \quad (5.25)$$

Here $Z_{WGFS,1D}$ is the Warburg element for the one dimensional general finite space case which accounts for the diffusion of lithium ions in 1D channels in LiFePO_4 particles. The EEC for the cathode is seen in Fig. 5.9.

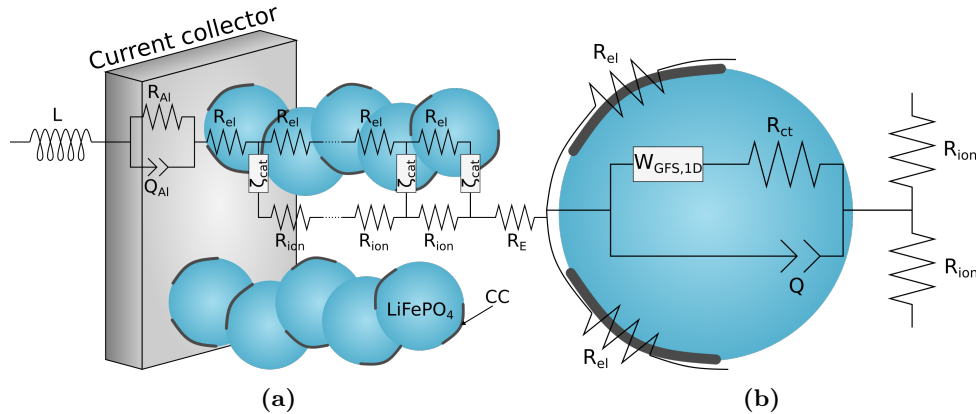


Figure 5.9: An overview of the EEC model for the LiFePO_4 cathode. (a) Generalised transmission line model of the cathode. (b) Detailed view of the ζ_{cat} element, a Randles circuit used to describe de-/intercalation of Li^+ and the electrode-electrolyte interface. The diffusion process is modelled with a 1D general finite space Warburg element. The figures are inspired by [93].

The TLM for the anode is similar to that of the cathode except for a few differences. Firstly, it includes the resistance and capacitance contribution from the SEI layer and secondly, it accounts for the two dimensional diffusion in the graphite particles. The expressions are as follows

$$Z_{TLM,an} = \frac{l}{\left(\frac{1}{R_{ion}} + \frac{1}{R_{el}}\right)} \left(1 + \frac{2 + \left(\frac{R_{ion}}{R_{el}} + \frac{R_{el}}{R_{ion}}\right) \cosh(\gamma_{an}l)}{\gamma_{an}l \sinh(\gamma_{an}l)} \right), \quad (5.26)$$

$$\zeta_{an} = \frac{R_{SEI} + Z_G}{1 + Q_{SEI}(j\omega)^n(R_{SEI} + Z_G)}, \quad (5.27)$$

where Z_G is a nested Randles circuit and is given as

$$Z_G = \frac{R_{ct} + Z_{GFS,2D}}{1 + Q_{dl}(j\omega)^n(R_{ct} + Z_{GFS,2D})}, \quad Z_{WGFS,2D} = \frac{Z_0}{(j\omega\tau)^n} \frac{I_0[(j\omega\tau)^n]}{I_1[(j\omega\tau)^n]}. \quad (5.28)$$

Here I_0 and I_1 are the modified zero- and first-order Bessel functions of the first kind, respectively. The EEC of the ζ_{an} element can be seen in Fig. 5.10

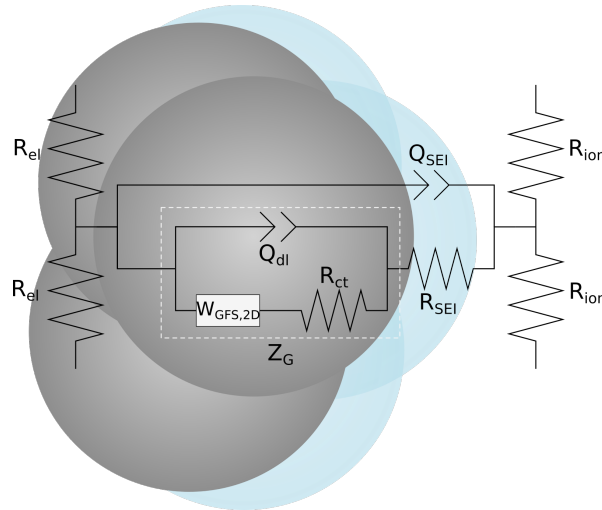


Figure 5.10: An EEC model of the ζ_{an} element used to describe the de-/intercalation of Li^+ into the anode, the electrode-electrolyte interface, and the effects from the SEI film. The diffusion occurs in a 2D plane and hence it is modelled with a 2D general finite space Warburg element. The figure is inspired by [93]

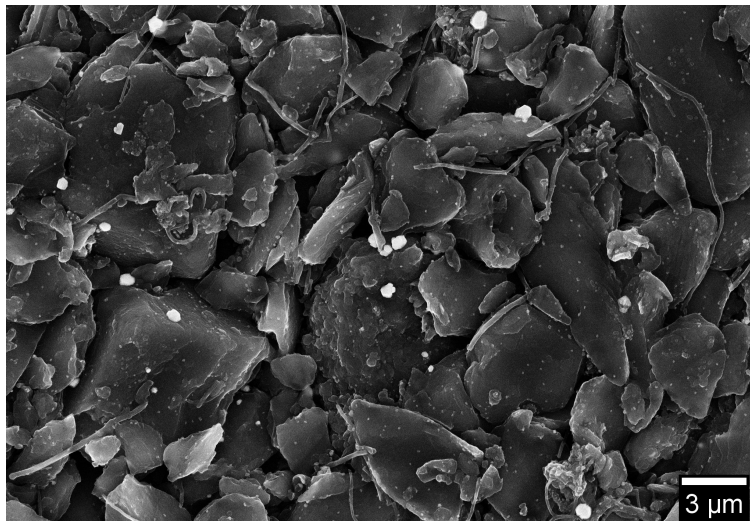
The models were fitted to the experimental data using a complex non-linear least-squares (CNLS) procedure based on the Levenberg-Marquardt algorithm. The algorithm was implemented in MATLAB and a detailed review of it can be found in Appendix A.4.

6 Experimental Results

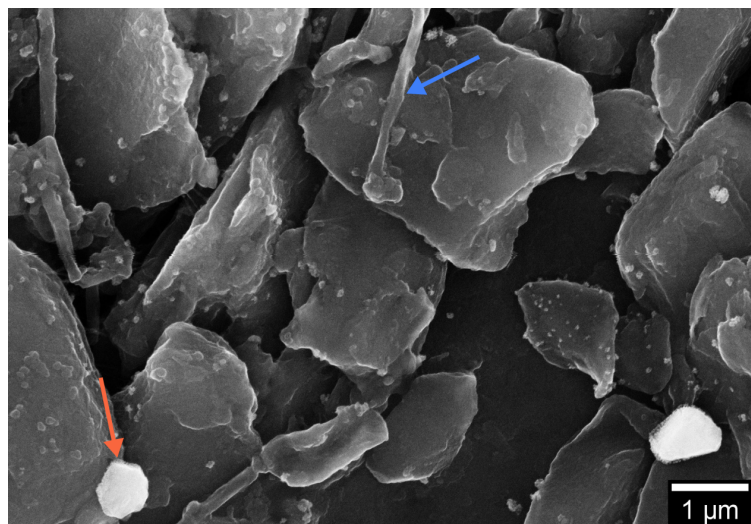
In this chapter the experimental results obtained with the methods described in Chapter 5 are presented. Observations and trends seen in the results are commented upon while the discussion of the results in relation to the aging mechanisms is treated in Chapter 7.

6.1 Scanning Electron Microscopy Analysis

The surface morphology of the anode and the cathode samples of the TCs were investigated with SEMs. Micrographs of the anode TCP are seen in Fig. 6.1 and Fig. 6.2.



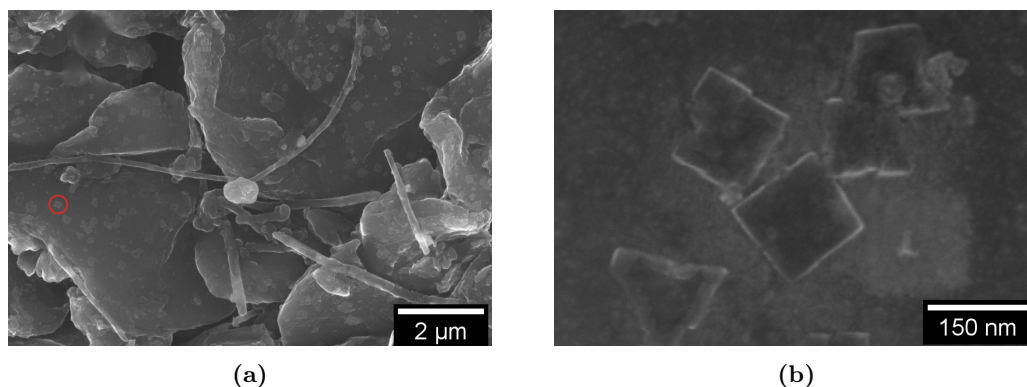
(a)



(b)

Figure 6.1: Micrographs of the TCP anode obtained with Zeiss CrossBeam SEM. (a) Overview showing the flaky graphite particles in a variety of sizes. (b) Zoomed view where bright spherical Cu particles, highlighted with an orange arrow, are seen. The blue arrow indicates what is believed to be the binder material.

On the micrographs of the anode in Fig. 6.1, graphite particles with flattened spherical shape and of various sizes can be seen. A qualitative examination of particle sizes reveals a homogeneous distribution. In addition to the graphite particles there are also fiber shaped and spherical particles which are highlighted with a blue and an orange arrow, respectively. The former is the binder material, supposedly polyvinylidene fluoride (PVDF). The spherical particles are on the scale of 1 μm and appear bright on the micrographs. Investigation with EDS revealed copper particles and their brightness is likely due to an atomic number effect i.e. elements with larger atomic number have more electrons compared to elements of lower number.

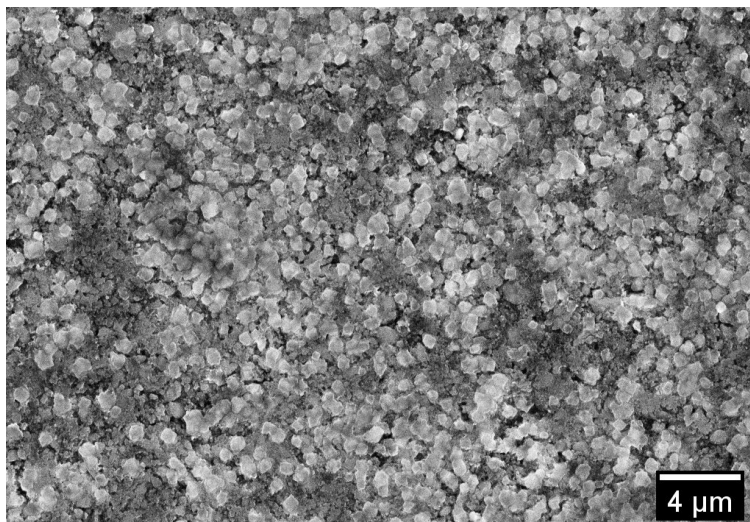


(a)

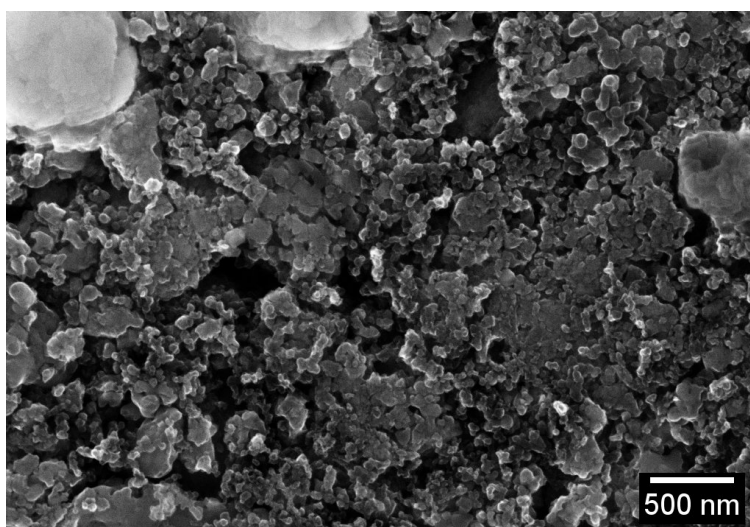
(b)

Figure 6.2: Micrographs of the TCP anode obtained with Zeiss CrossBeam SEM. (a) Overview of the surface which shows fiber shaped binder material and a spherical Cu particle in the center. Nanoscaled cubic deposits marked with a red circle are observed on the surface of the graphite particles. (b) Zoomed view of the cubic deposits believed to be LiPF_6 crystals.

The SEM micrographs of the anodes showed sub-micrometer sized cubes. One of these are highlighted in Fig. 6.2a with a red circle. The micrograph in Fig. 6.2b shows these cubes with a greater magnification. Due to their well defined edges and cubic shape they are believed to be LiPF_6 salt crystals left over from the washing procedure.



(a)



(b)

Figure 6.3: Micrographs of the TCP cathode obtained with Zeiss CrossBeam SEM. (a) Overview of the cathode surface. (b) Zoomed view implying the porous surface.

The cathode particles seen in Fig. 6.3 are small compared to the anode graphite particles. By a qualitative examination they are on the nanoscale, some are few hundreds of nanometers while others are sub hundred.

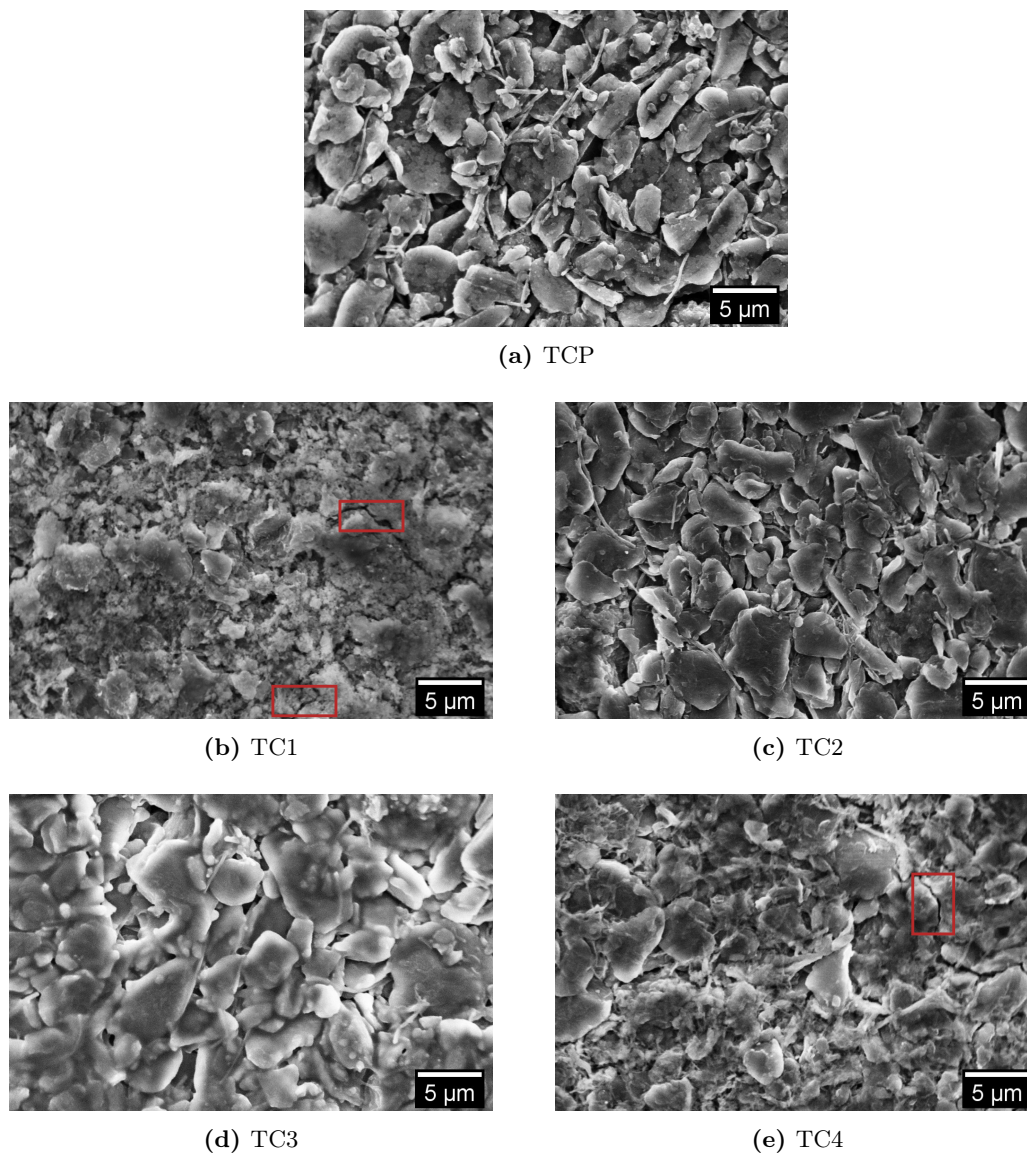
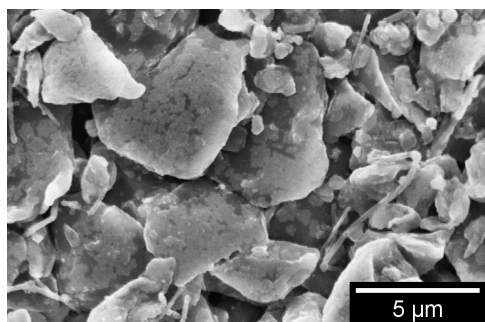


Figure 6.4: Zeiss EVO SEM micrographs of anodes from samples (a) TCP, (b) TC1, (c) TC2, (d) TC3, and (e) TC4. Microcracks are highlighted with red rectangles.

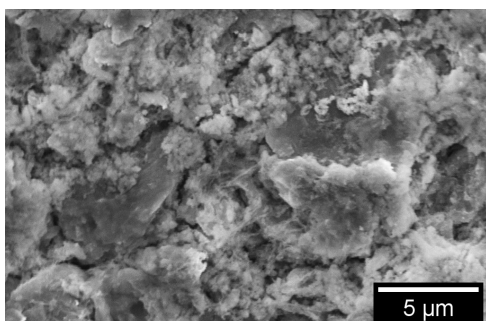
Additional micrographs of the anodes can be seen in Figs. 6.4 and 6.5.

The morphology of the anode from the pristine battery as seen in Figs. 6.4a and 6.5a, shows graphite particles with clear boundaries and overall homogeneity. The surface of the anode of TC1 as seen in Figs. 6.4b and 6.5b looks more rough and the particles are not as easily distinguished from each other, compared to the pristine case. In addition to this, multiple micro-cracks are also visible in Fig. 6.4b. These cracks are supposedly the reason for exfoliation of the graphite layer from the copper current collector which was observed during disassembly. The binder material is not visible in the micrographs of the anode of TC1 but it is in the ones for TC2 in Figs. 6.4c and 6.5c. Furthermore, the morphology of the anode of TC2 resembles that of the pristine anode both in the surface of the particles and in the homogeneity. The graphite particles seen in the micrographs of the anode of TC3 in Figs. 6.4d and 6.5d,

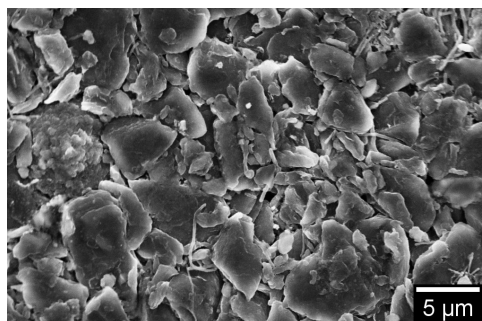
looks to be covered with a film which blurs their surface and outline. The surface of the anode of TC4 as seen in Figs. 6.4e and 6.5e looks more rough and more similar to the surface of the anode of TC1 than to the one for TCP or TC2.



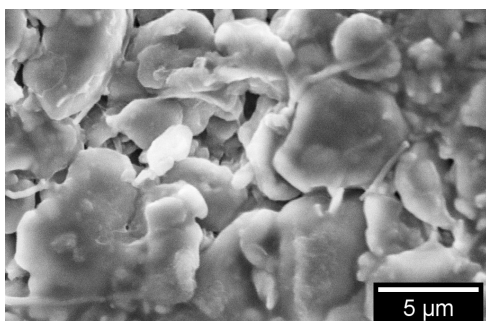
(a) TCP



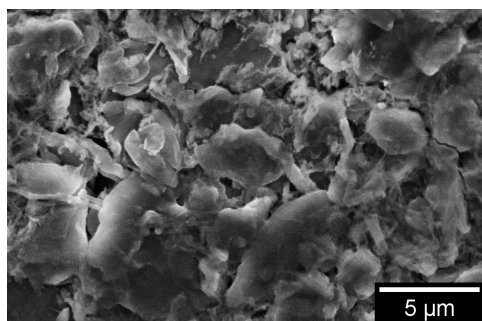
(b) TC1



(c) TC2



(d) TC3



(e) TC4

Figure 6.5: Zeiss EVO SEM micrographs of anodes from samples (a) TCP, (b) TC1, (c) TC2, (d) TC3, and (e) TC4.

On the micrographs of the anodes of TC2, TC3, and TC4 in Figs. 6.4 and 6.5 numerous bright areas can be seen. These are areas of either low conductivity or are charged or both, compared to the neighbouring darker areas. The effect looks to be less severe on TC2. These areas are not observed on the anodes of TCP and TC1.

Micrographs of the anodes from the TCs were quantified with the mean line intersection method as described in Chapter 5. The data acquired for the anodes is available in tables in Appendix C.2.

The micrographs of the anodes of TCP and TC2 show particles with well-defined

edges and hence the mean line intersection method is easily applied compared to the micrographs of TC3 and TC4. Therefore, the calculated means for TC3 and TC4 must be considered cautiously. It was not possible to assess a horizontal or vertical mean for the anode of TC1 as the particles were indistinguishable.

Table 6.1: Mean line intersection results from five lines and approximately 200 intersections.

Samples	Horizontal mean [μm]	Vertical mean [μm]
TCP	2.31 ± 0.09	2.39 ± 0.13
TC1	-	-
TC2	2.06 ± 0.05	2.09 ± 0.06
TC3	2.80 ± 0.13	2.83 ± 0.15
TC4	2.72 ± 0.14	2.57 ± 0.10

The anodes from TC3 and TC4 have a larger mean compared to the ones from TCP and TC2. This may be a results of SEI layer thickening which is a known aging mechanisms as described in Chapter 4. The horizontal and vertical mean are comparable for all the samples which indicates isotropic graphite particles.

The morphology differences will be discussed in relation to the aging conditions in Chapter 7.

6.2 Energy Dispersive X-Ray Spectroscopy

For the graphite anodes the EDS spectra showed peaks corresponding to C, O, F, P, and Cu as seen in Fig. 6.6.

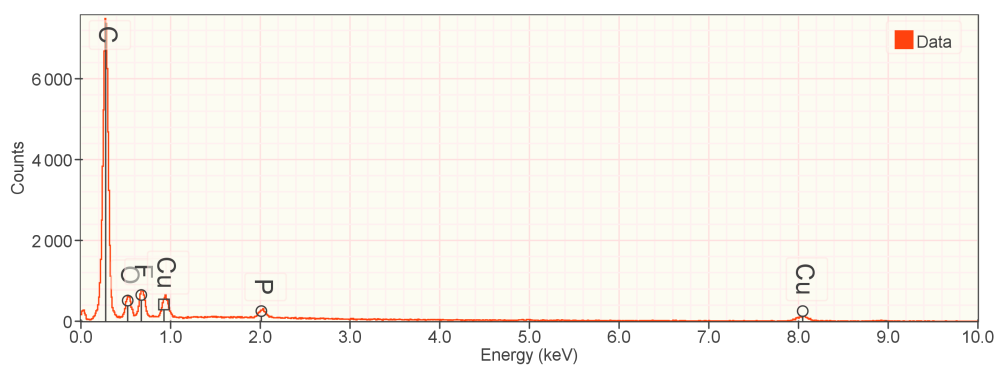


Figure 6.6: EDS spectrum of the anode of TC4 obtained with a 15 kV incident electron beam. Relevant x-ray transition lines are shown and abbreviated. Two peaks are seen for Cu each with a different x-ray energy.

A large carbon peak from the graphite is seen together with smaller peaks from O, F, and P which are elements present in the SEI layer. Additionally, with a probing depth of $\sim 3 \mu\text{m}$, signal from the Cu current collector is seen, this suggests a thinner

and/or a more porous layer compared to the cathodes.

Elemental identification of EDS spectra for the LiFePO_4 cathodes showed presence of C, O, F, P, V, and Fe as seen in the spectrum for the cathode of TC4 shown in Fig. 6.7. The carbon stems from the coating on the cathode. A low amount of vanadium serves as a dopant which maintains the olivine structure of the LFP while enhancing Li^+ diffusion and dis-/charging rates [94]. Fluorine is expected from the binder or from the electrolyte salt, LiPF_6 , which may partake with the EC/DEC solvent in formation of a surface layer on the cathodes. Signal from the aluminium current collector was not seen, suggesting a thick and dense LFP layer.

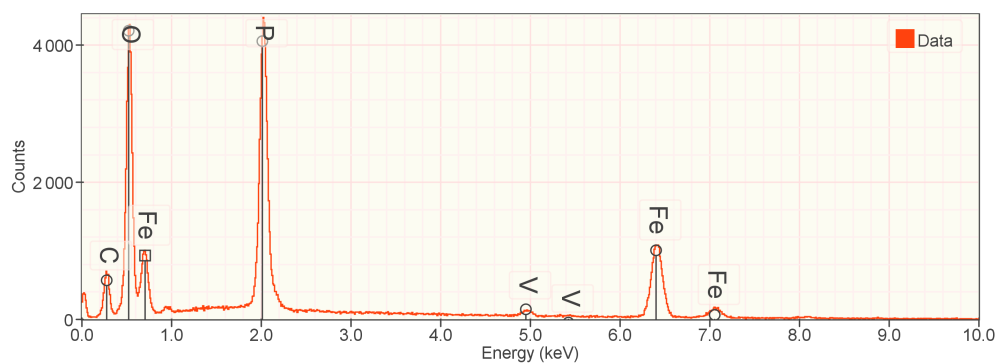
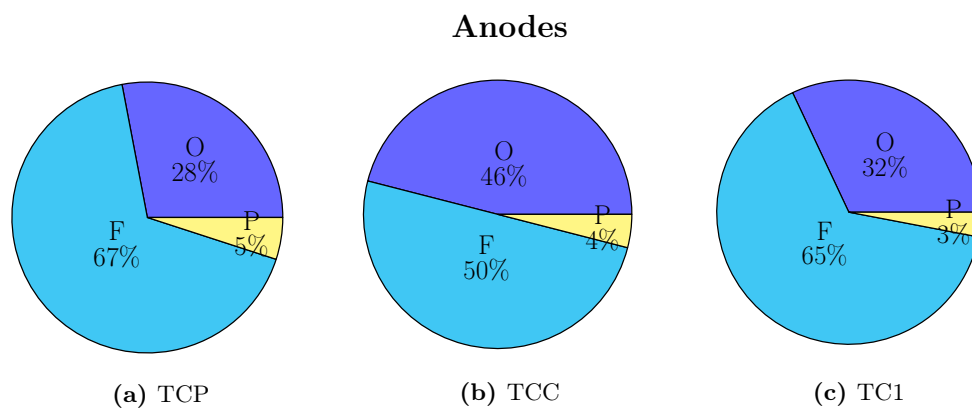


Figure 6.7: EDS spectrum of the cathode of TC4 obtained with a 15 kV incident electron beam. Relevant x-ray transition lines are shown and abbreviated.

Quantification of the anode spectra normalised to O, F, and P is represented by pie charts in Fig. 6.8.



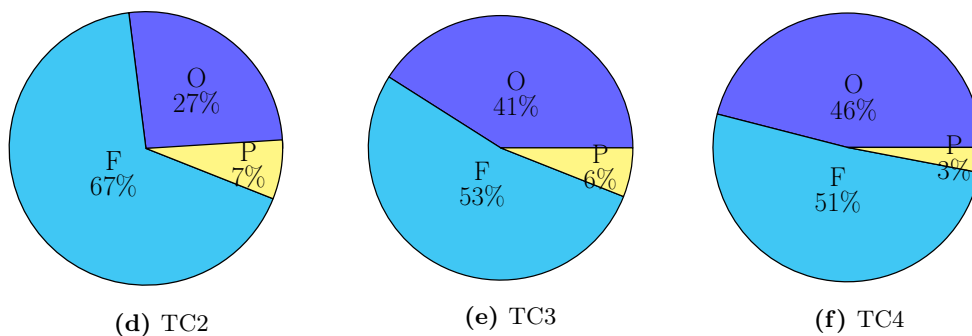


Figure 6.8: Quantified EDS data of the anode samples in atomic percentages where the data is normalised to O, F, and P.

For the anodes an overweight of fluorine is observed compared to O and P. In general, TCP, TC1, and TC2 show a larger content of F where TCC, TC3, and TC4 show more O. The amount of P is observed not to vary significantly between TCs.

Quantification of the cathode spectra normalised to the three main components, O, P, and Fe is represented by pie charts in Fig. 6.9.

Cathodes

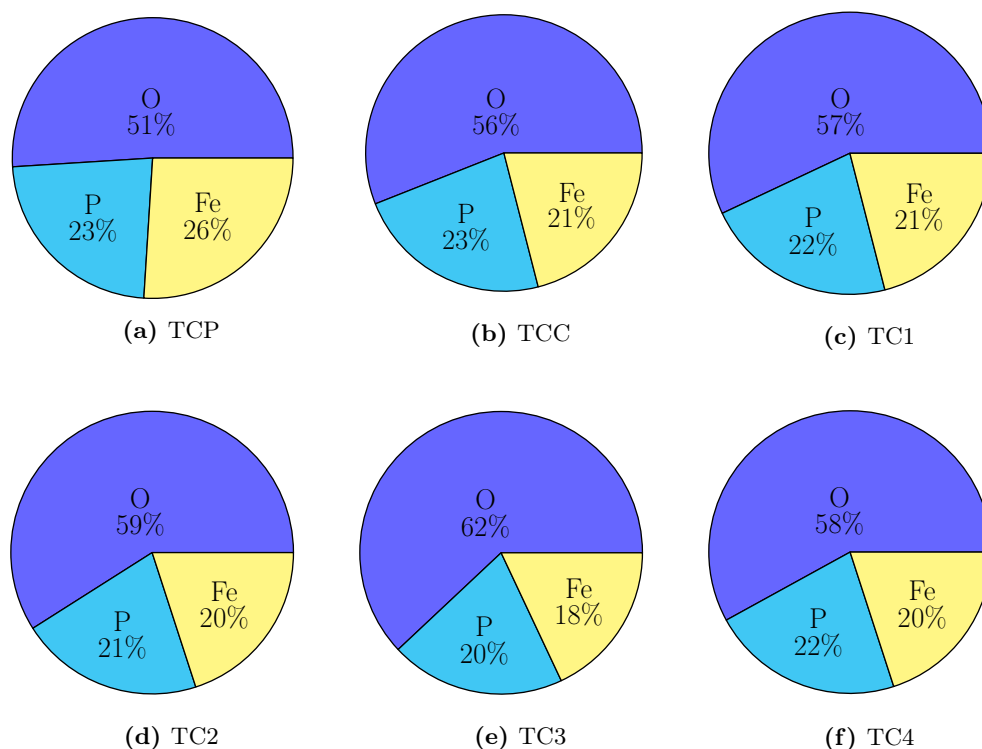


Figure 6.9: Quantified EDS data from the cathodes samples in atomic percentages. The data is normalised to the three main components of LFP.

The theoretical stoichiometry of LiFePO_4 is reflected in the pie charts which in general shows an overweight of O, and comparable ratios of P and Fe.

The quantified EDS data will be discussed in relation to the other experimental results and the aging conditions in Chapter 7.

Point and shoot was used to examine the bright particles present on the anodes as shown on the SEM micrographs Figs. 6.3, 6.5a and 6.5c. In Fig. 6.10 three points were examined with EDS and the elemental composition quantified.

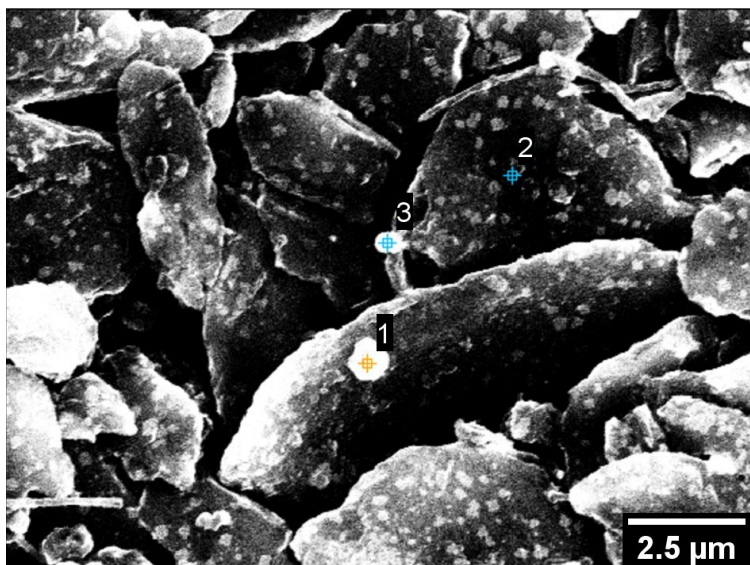


Figure 6.10: Zeiss EVO SEM micrograph of the TCP anode where three points are marked for EDS examination. Point one and three are Cu particles and point two is at the center of a graphite particle.

From the EDS analysis the particles in point one and three showed to contain 38 and 35 wt% Cu, respectively, where point two contained 2.3 wt% Cu similar to the spectrum of a larger area such as Fig. 6.6. The spectra for the three points in Fig. 6.10 are shown together in Fig. C.7. The bright particles on the anode surfaces are thus suggested to be copper particles. The particles might be a contaminant from the battery assembly process or purposely added in small amounts, 1-5 wt%, to improve electrochemical performance of the graphite anode similar to the results obtained by Guo et al. [95].

Point and shoot EDS was additionally used on a cathode sample as shown in Fig. 6.11.

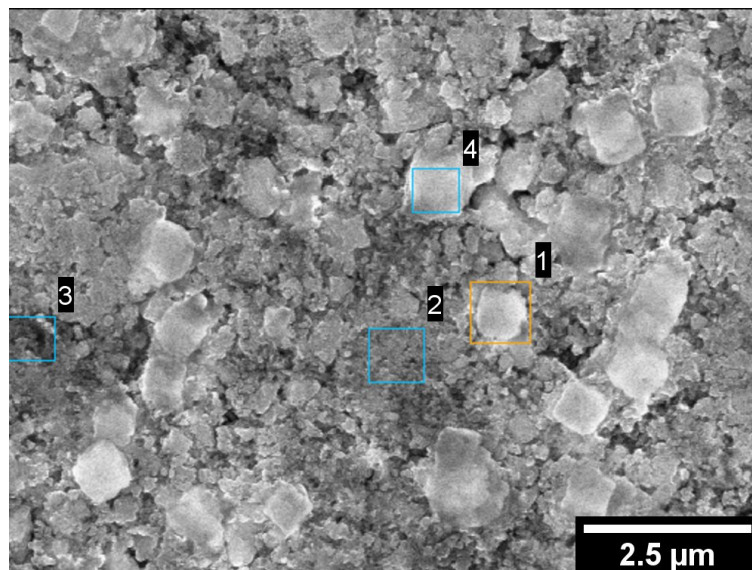


Figure 6.11: Zeiss CrossBeam SEM micrograph of the TCP cathode where four rectangular areas are marked for EDS examination. Area one and four are lighter in contrast and are presumably LiFePO_4 particles, where area two and three are darker and includes smaller particles, presumably carbon.

From the EDS examination, area three showed to contain the most carbon at 29 wt% compared to 18, 21, and 22 wt% for area one, two, and four, respectively. All the areas showed presence of Fe at 21-28 wt%. The small particles on the SEM micrograph is believed to be the carbon coating with thickness smaller than the probing depth of 3 μm . The bright contrast areas are less coated LiFePO_4 particles which might become completely bare due to agglomeration, an aging mechanism previously mentioned. The EDS spectra for the four areas are shown in Fig. C.9.

6.3 Raman Spectroscopy

Obtained Raman spectra for the anode and cathode of TC1 are shown in Figs. 6.12 and 6.13, respectively. Deconvolution of the spectral features is shown along with the combined fit to the experimental data.

For the anode in Fig. 6.12 the disorder induced D peak is seen along with the graphitic G peak due to sp^2 bonds. These two peaks are located at 1353 and 1582 cm^{-1} , respectively. Additionally, a shoulder feature, D' peak, on the right side of the G peak is seen which is also attributed to defects [83]. For the cathode in Fig. 6.13, the D and G peak are seen at 1325 and 1592 cm^{-1} , respectively. Additionally, a double peak attributed to LiFePO_4 is shown at ca. 1000 cm^{-1} .

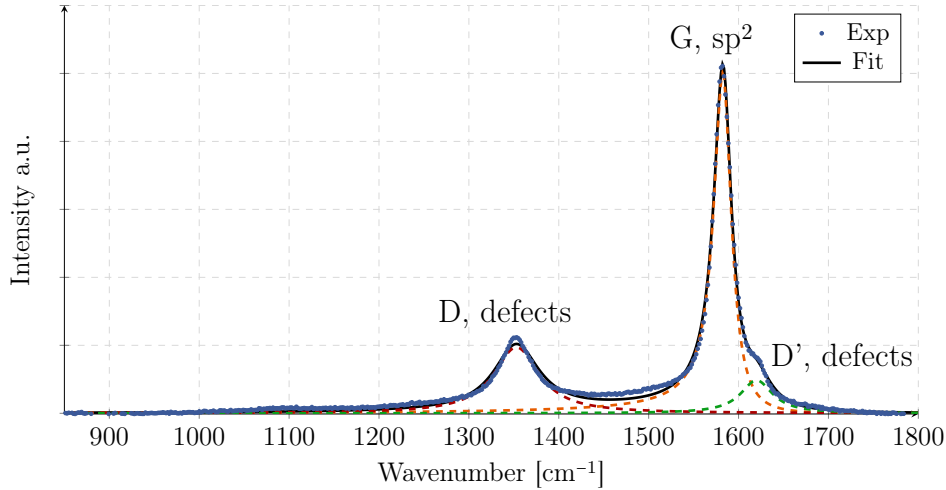


Figure 6.12: Deconvolution of a Raman spectrum for the anode of TC1, where the sum of the dashed lines gives the black line fit. The G peak is positioned at 1582 cm^{-1} and the D peak is at 1353 cm^{-1} . The D' peak is located at 1620 cm^{-1} . The asymmetric G peak is skewed towards lower wavenumbers with $Q = 0.011$.

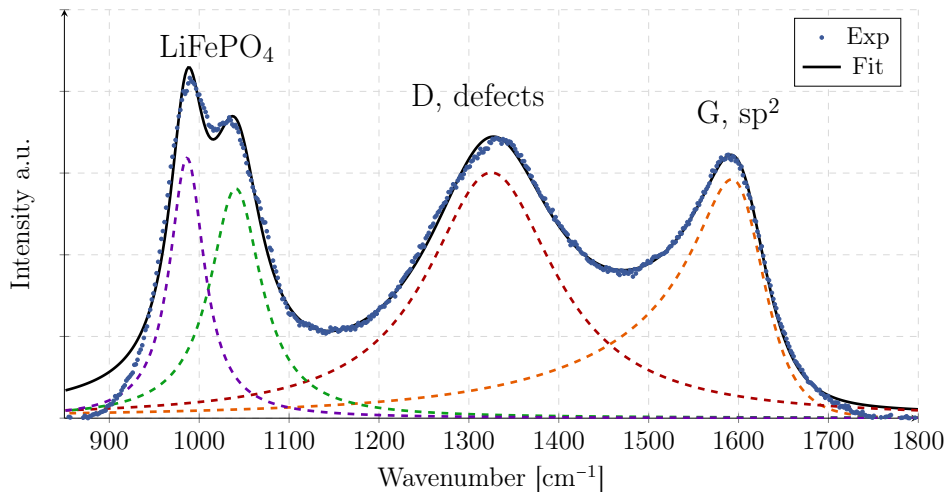


Figure 6.13: Deconvolution of a Raman spectrum for the cathode of TC1, where the sum of the dashed lines gives the black line fit. The G peak is positioned at 1592 cm^{-1} and the D peak is at 1325 cm^{-1} . The two left most peaks attributed to LiFePO_4 is at 1040 and 986.1 cm^{-1} , respectively. The asymmetric G peak is skewed towards lower wavenumbers with $Q = 0.013$.

By comparing the Raman peaks attributed to the graphite crystal structure in Fig. 6.12 and Fig. 6.13 one notices the missing D' peak in the cathode spectrum. The examined carbonaceous materials differ significantly in particle size where the graphite particles on the anodes are on the order 2-3 μm and the particles in the cathode coating are presumably 5-20 nm. The D' mode might be activated primarily by volume defects such as sp^3 defects which predominate in larger particles compared to e.g. grain boundaries which dominates in smaller particles. This suggesting is in agreement with work by Eckmann et al. [83] on graphene samples where $I_D/I_{D'}$ was found to be largest for sp^3 defects and lowest for grain boundaries. Additionally, the induced sp^3 defects

were found to typically be present in $\approx 20\text{-}30$ nm clusters which also suggests the unlikelihood of sp^3 defect clusters in the nanocrystalline particles present in the cathode coating. Another noticeable difference is the peak width increase in the cathode spectrum Fig. 6.13 compared to the anode spectrum Fig. 6.12. An explanation might again be found in the significant size difference of the carbon crystals. It is known from experiments on silicon and carbon powders [90] that smaller crystals yield an increased Raman peak width. For the smaller particles on the cathodes more grain boundaries are expected which might increase both $\text{FWHM}_{D,\text{cat}}$ and $\text{FWHM}_{G,\text{cat}}$ compared to the anode spectra.

A comparison of the anode Raman spectra for all the TCs is shown in Fig. 6.14.

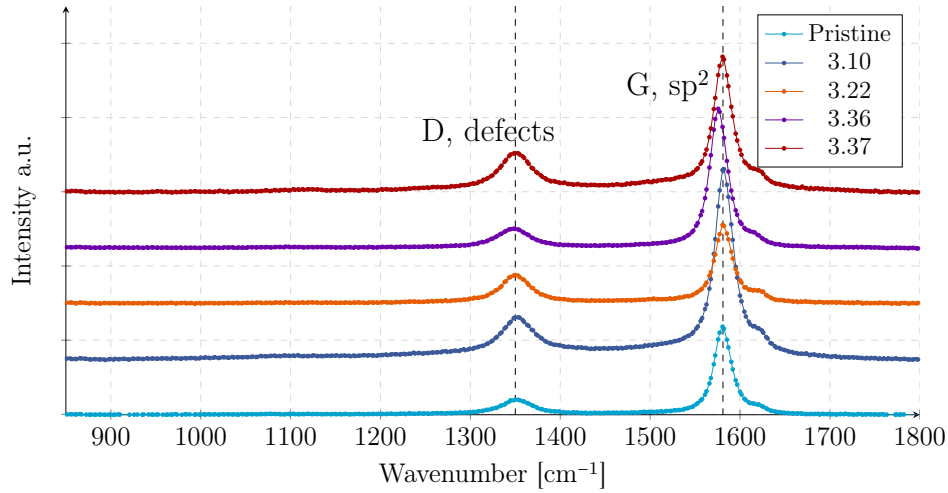


Figure 6.14: Comparison of Raman spectra of the anodes. A guide to the eye is added at 1350 cm^{-1} and 1581 cm^{-1} which coincide with the position of the D and G peak, respectively, for the TCP. The spectra are purposely offset by a constant for the different TCs.

From Fig. 6.14 the position of the D peak is seen to remain approximately constant whereas the G peak is shown in general to shift slightly towards lower wavenumbers compared to TCP. This shift is most pronounced for TC3 with $\Delta\nu_G \approx -5\text{ cm}^{-1}$. The leftwards shift of the G peak is attributed to an increase in bond length in the graphite crystal structure which might be due to irreversible mechanical stresses induced by the volume change during de-/intercalation. The D peak position is seen to remain approximately constant as the disorder induced peak is not necessarily affected by stresses, but rather the type of defects.

A comparison of the cathode Raman spectra for all the TCs is shown in Fig. 6.15.

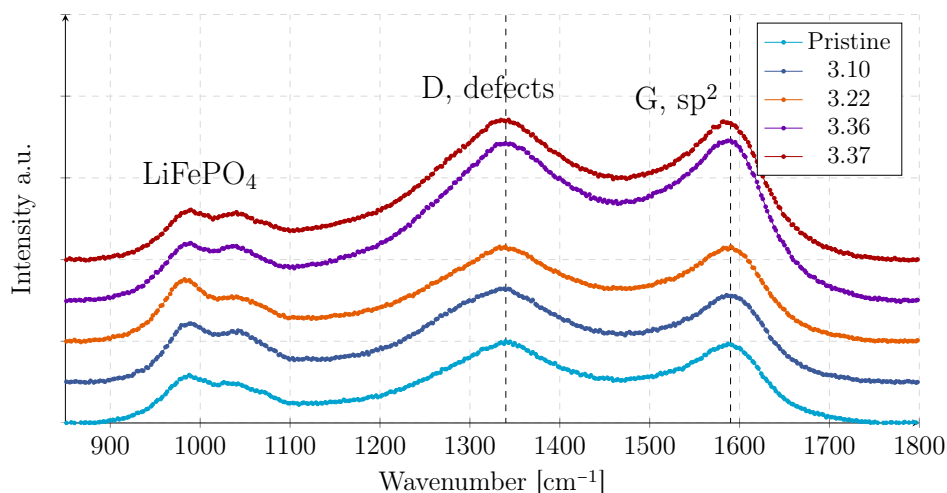


Figure 6.15: Comparison of Raman spectra of the cathodes. A guide to the eye is added at 1340 cm^{-1} and 1590 cm^{-1} which coincide with the position of the D and G peak, respectively, for the TCP. The spectra are purposely offset by a constant for the different TCs.

In Fig. 6.15 the cathode spectra are seen to be similar with no large deviations between TCs.

At some spatial positions during RS mapping, the anode of TC4 showed a large background supposedly due to fluorescence. The anode of TC3 showed in general a smaller degree of fluorescence while the anodes of TCP, TC1, and TC2 showed no significant fluorescence background. A comparison of the raw RS spectra is shown in Fig. 6.16.

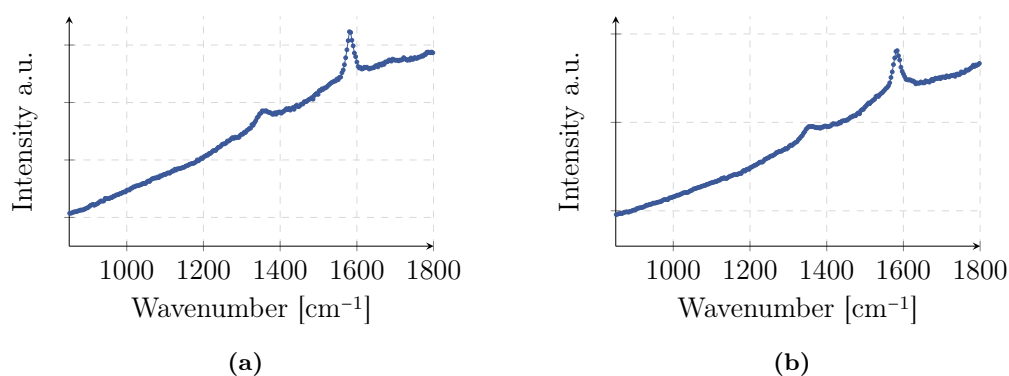


Figure 6.16: Raman spectra as acquired for anodes of (a) TC3 and (b) TC4 where in both spectra a fluorescence background is visible.

A large fluorescence background conceals the sought Raman features which makes the peak fitting and hence spectral analysis less reliable, particularly for the the anode of TC4. Photobleaching was attempted to limit the fluorescence background on the anode of TC3 and TC4 but with no success. Instead the acquisition time and amount of accumulations were increased to enhance the signal-to-noise ratio.

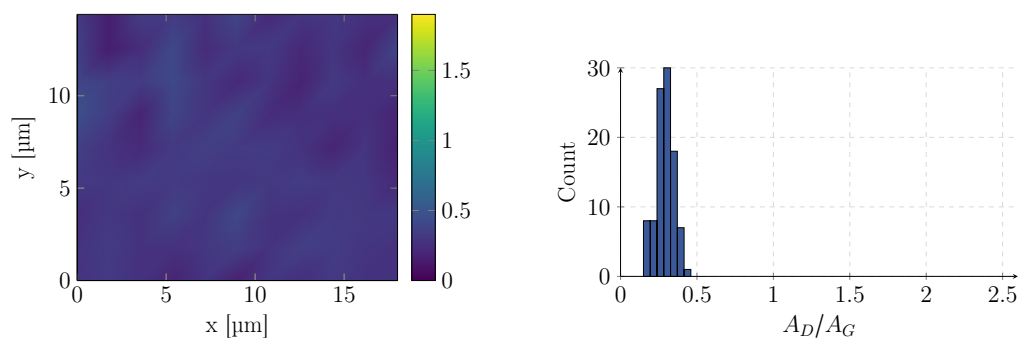
Since the fluorescence was observed only on the anodes and the laser light probes ~ 50 nm into the graphite sample, it is believed that the fluorescence signal stems from the SEI surface layer partly composed of organic molecules. These molecules might, in contrast to the conductive graphite, show semiconducting properties which enables fluorescence. The background signal in the Raman spectra is believed to be a spectral tail of a much stronger fluorescence signal at a significantly higher wavenumber than the measured.

Mapping of Anode and Cathode

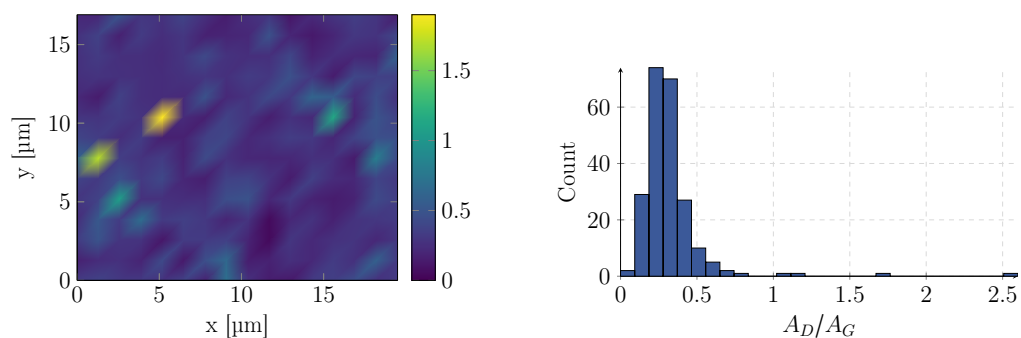
Raman spectra were acquired in a spatial grid of 20-30 by 20-30 μm for each anode and cathode sample. The spectra were then used to calculate the integral, intensity, and FWHM ratio of the D to the G peak. These maps are each paired with a histogram to show the distribution of the ratios. The A_D/A_G maps and histograms are included in this chapter, while the ones of the intensity and the FWHM are included in Appendix C.3. In addition to the maps and the histograms, two tables, one for each of the electrodes, containing the mean value and the standard deviation are included as seen in Tables 6.2 and 6.3. The tables also contain the values for the intensity- and the FWHM maps.

The maps and the corresponding histograms of A_D/A_G for the anodes, are seen in Fig. 6.17. The map of TCP, as seen in Fig. 6.17a displays a dominant G peak and homogeneity. This is also seen in the histogram where the mean is 0.29 and the standard deviation is 0.06. For the anode of TC1, as seen in Fig. 6.17c, the map is more inhomogeneous and with numerous spots of higher ratio than 1.5, compared to TCP. The increased inhomogeneity is also apparent when comparing the standard deviation, which for the case of TC1 is 0.36. The mean value is also higher for TC1 than for TCP. The map of the anode of TC2 as seen in Fig. 6.17d shows a lower degree of homogeneity compared to the pristine case but higher than for the case of TC1. A single high ratio spot can be seen on the map and in the histogram. The mean value and the standard deviation is higher compared to the pristine case but lower than for the case of TC1. The map seen in Fig. 6.17e for the anode of TC3 also shows isolated high ratio spots. The mean value is 0.37 and is only slightly larger than for the pristine case. Lastly, the map for the anode of TC4, as seen in Fig. 6.17f, is similar to the one for TC2. This is confirmed by the mean and the standard deviation of the two cases.

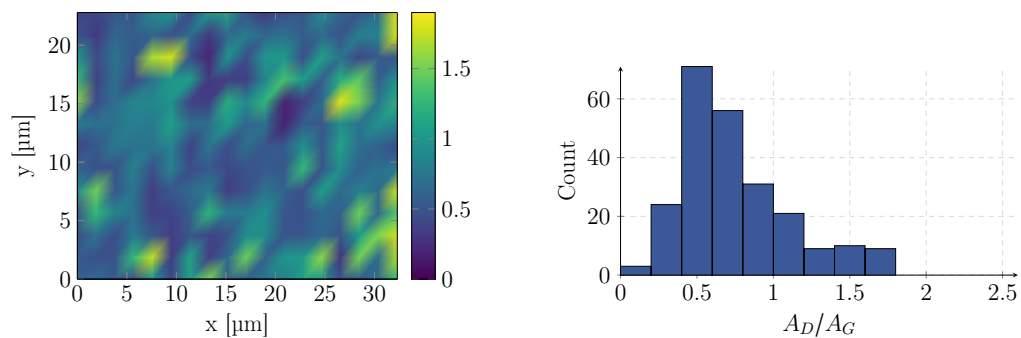
When examining the map of the anode of TCC Fig. 6.17b it is observed to be similar to the map of the pristine anode. It does however have a few spots with high ratio which is a feature also seen in the maps of the cycle-aged anodes.

Map of Integral A_D/A_G of Anodes

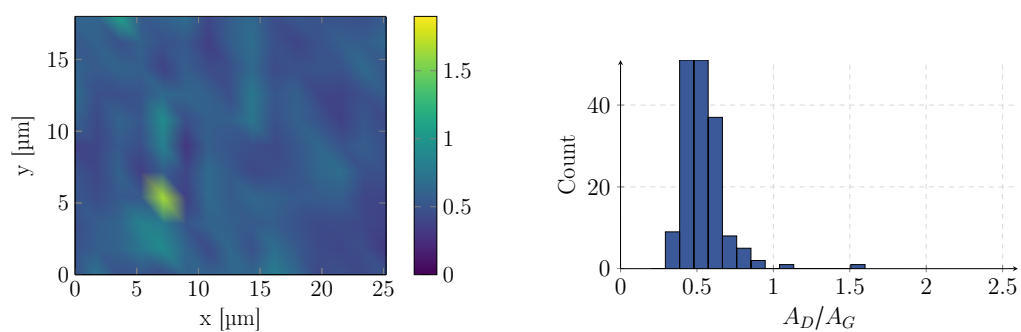
(a) TCP



(b) TCC



(c) TC1



(d) TC2

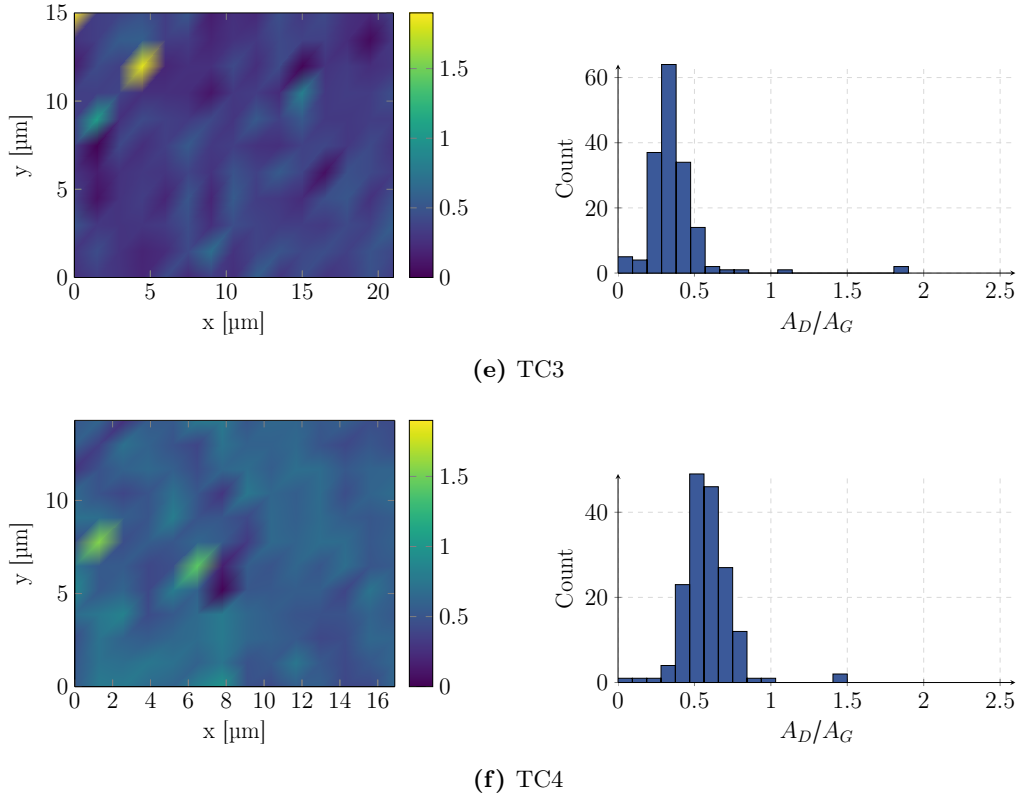


Figure 6.17: Raman spectroscopy maps of the ratio of the integral of the D and G peak for the anodes of the TCs. Each map is accompanied by a histogram of the distribution. A common x -axis is used but due to Scott's rule given by Eq. (5.7) the bin width is different.

Table 6.2: Mean and standard deviation calculated from the RS maps of the anodes.

	Mean			Std. Dev.		
	A_D/A_G	I_D/I_G	$\text{FWHM}_D/\text{FWHM}_G$	A_D/A_G	I_D/I_G	$\text{FWHM}_D/\text{FWHM}_G$
TCP	0.29	0.16	1.9	0.060	0.040	0.16
TCC	0.32	0.16	2.3	0.23	0.057	1.9
TC1	0.75	0.19	5.3	0.36	0.048	2.4
TC2	0.54	0.31	1.8	0.15	0.075	0.50
TC3	0.37	0.20	1.9	0.21	0.071	0.99
TC4	0.58	0.28	2.9	0.16	0.062	1.2

When comparing the A_D/A_G maps, the difference may stem from a change in the ratio of the intensities or in the FWHM. The three maps for each anode sample may be compared qualitatively as can be seen for TC1 in Fig. 6.18 to examine if the spread in the integral maps stems from the intensity or the FWHM maps. For the anode from TC1, the larger mean and standard deviation of the ratio of the integrals can be seen to stem from the increased FWHM. The ratio of the intensities is not

significantly larger when comparing with TCP. However, for TC2 and TC4, the mean of the intensity ratio is significantly increased compared to the pristine case.

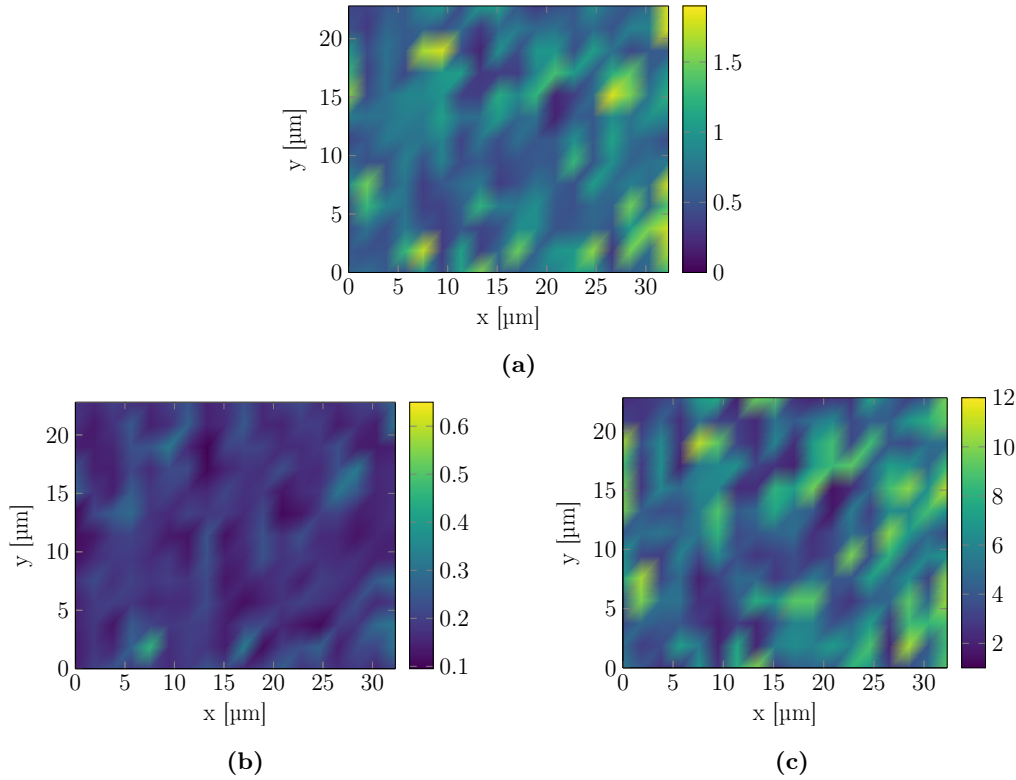


Figure 6.18: Comparison of RS maps of (a) A_D/A_G , (b) I_D/I_G , and (c) $FWHM_D/FWHM_G$, for the TC1 anode.

The A_D/A_G maps and corresponding histograms of the cathodes are seen in Fig. 6.19 while the maps of I_D/I_G and $FWHM_D/FWHM_G$ are available in Figs. C.3 and C.5, respectively.

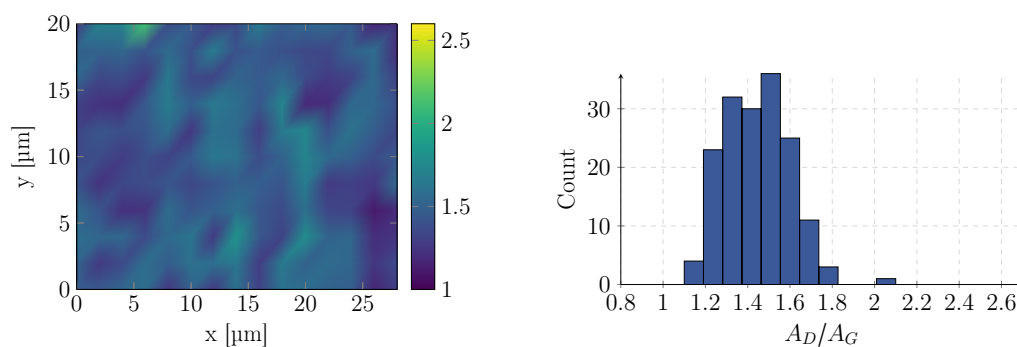
The A_D/A_G map and histogram of the pristine case, as seen in Fig. 6.19a, display a dominant D peak and inhomogeneity. The mean is 1.5 and the standard deviation is 0.15 as seen in Table 6.3. Both of these are higher compared to all the cycle-aged TCs. For TC1, the map and histogram in Fig. 6.19c, show a higher degree of homogeneity and a less dominant D peak compared to the pristine case. This is also apparent from the mean and standard deviation which are 1.2 and 0.084, respectively. The cycle-aged cathodes shows similar maps with small variations in the mean and the standard deviation.

In general A_D/A_G is lower for the cycle-aged cathodes compared to the pristine cathode. This trend implies that the carbonaceous coating on the LiFePO_4 becomes more graphitic during ageing. This is however contrary to the expected formation of amorphous phases of the carbon black coating and contrary to the findings of Nagpure et al. [96]. In order to investigate this trend in more details, a calendar-aged battery was examined. It was aged at the same temperature as the other TCs, $T = 40$ °C, and at 50% SOC avg. The A_D/A_G map of the cathode of TCC can be seen in

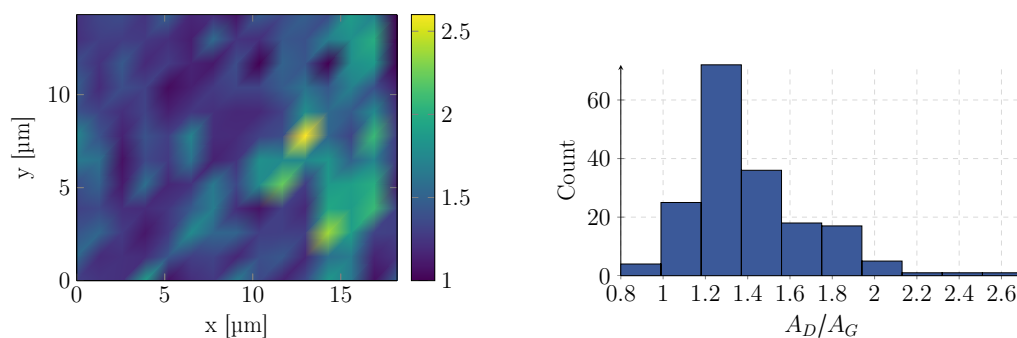
Fig. 6.19b. It displays a larger inhomogeneity than the pristine and the aged cases. This is supported by the standard deviation available in Table 6.3. Furthermore, the mean value is lower than for the pristine case but higher compared to the aged cases.

The trend where the carbonaceous coating on the cycle-aged cathodes is more crystalline is therefore likely due to suppression of the D peak. This can occur if atoms or molecules bind to defect sites.

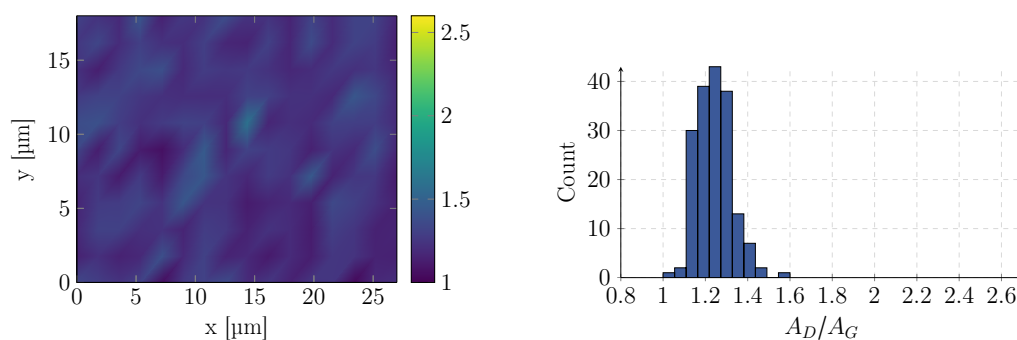
Map of Integral I_D/I_G of Cathodes



(a) TCP



(b) TCC



(c) TC1

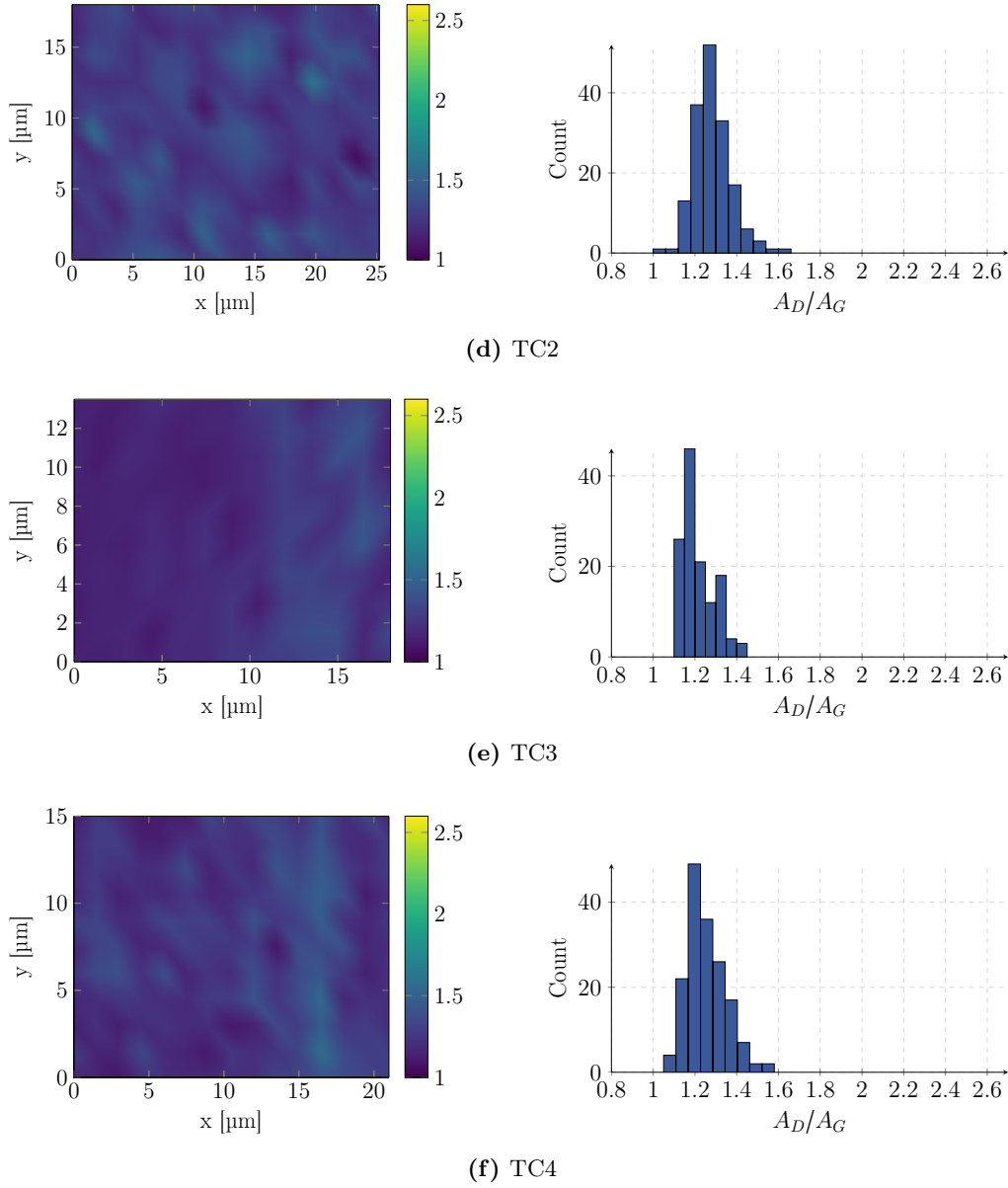


Figure 6.19: Raman spectroscopy maps of A_D/A_G for the cathodes of the TCs. Each map is accompanied by a histogram of the distribution. A common x -axis is used but due to Scott's rule given by Eq. (5.7) the bin width is different.

Table 6.3: Mean and standard deviation calculated from the RS maps of the cathodes.

	Mean			Std. Dev.		
	A_D/A_G	I_D/I_G	$\text{FWHM}_D/\text{FWHM}_G$	A_D/A_G	I_D/I_G	$\text{FWHM}_D/\text{FWHM}_G$
TCP	1.5	1.1	1.4	0.15	0.093	0.068
TCC	1.4	1.2	1.3	0.29	0.19	0.095
TC1	1.2	1.0	1.4	0.084	0.054	0.070
TC2	1.3	1.0	1.4	0.089	0.056	0.058
TC3	1.2	0.96	1.4	0.077	0.056	0.039
TC4	1.3	0.99	1.4	0.091	0.062	0.046

For the cathodes, the difference in A_D/A_G across the TCs can be seen to stem from the intensity ratio when examining Table 6.3. The mean of the FWHM ratio is approximately equal for all the TCs while the mean of the intensity ratio varies. The three maps for each cathode sample may also be compared qualitatively as seen in Fig. 6.20 where it is seen that some features are present throughout the three maps while others are not.

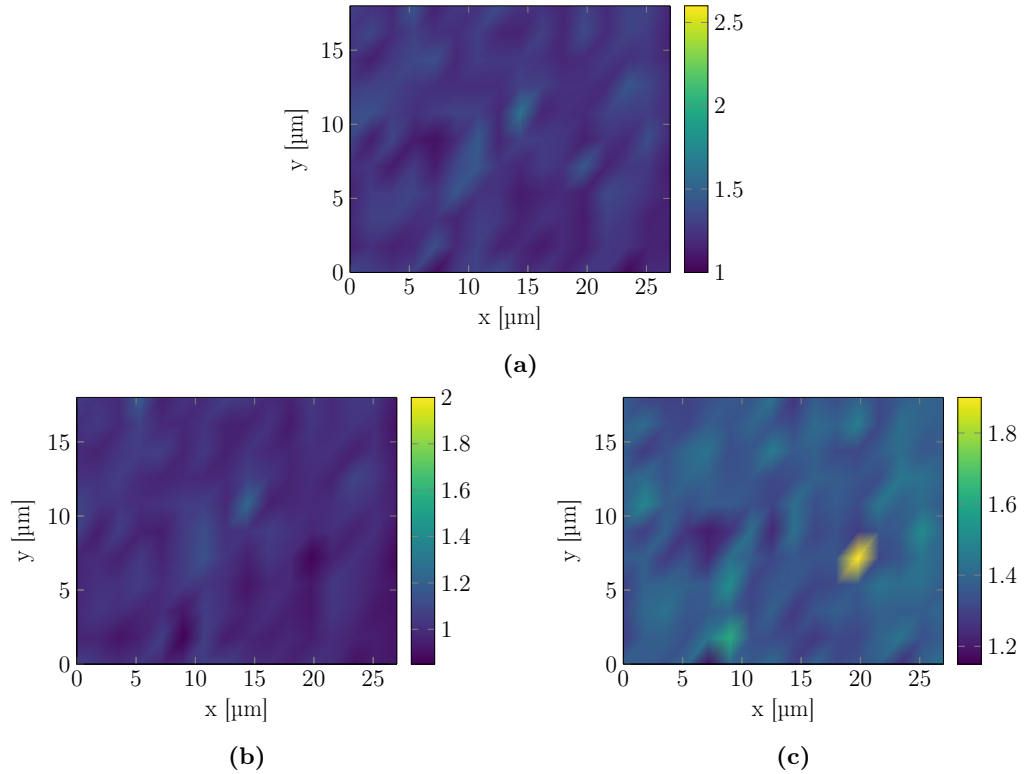


Figure 6.20: Comparison of RS maps of (a) A_D/A_G , (b) I_D/I_G , and (c) $FWHM_D/FWHM_G$, for the cathode of TC1.

The trends seen in the RS maps and the associated mean and standard deviation will be discussed in Chapter 7

6.4 Cyclic Voltammetry

Cyclic voltammograms for each of the TC anodes and cathodes, obtained with parameters from Table 5.3, are presented.

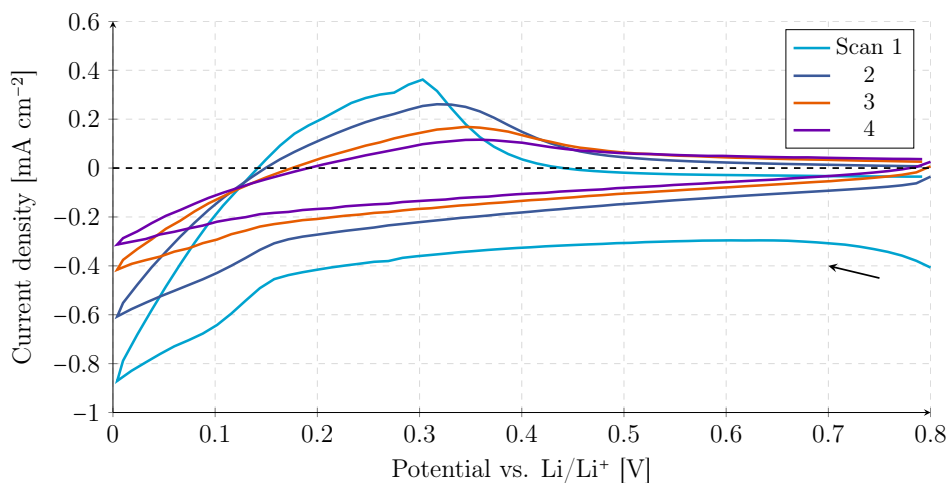


Figure 6.21: Cyclic voltammograms with four successive scans for the anode of TC1. The voltammograms were obtained according to Table 5.3 with a scan rate of $75 \mu\text{Vs}^{-1}$. The arrow indicates the scan direction.

A comparison of CV curves for the fourth scan for each anode is shown in Fig. 6.22.

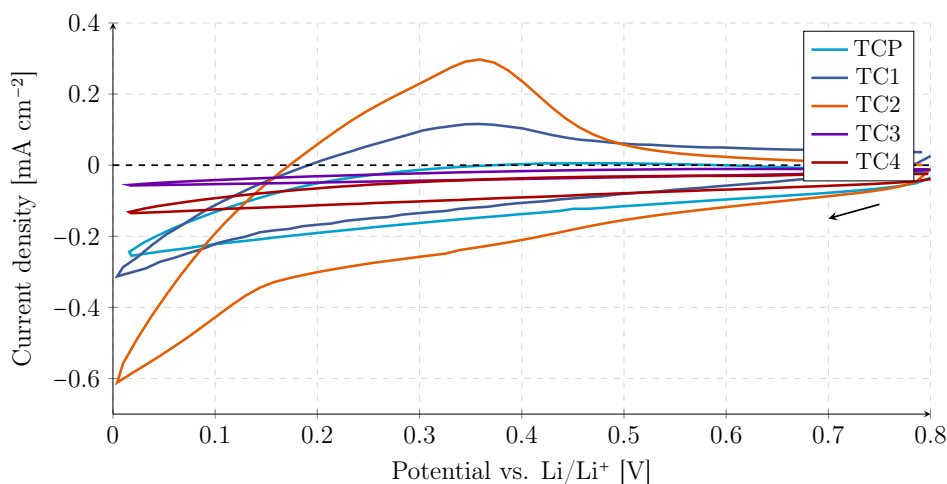


Figure 6.22: Comparison of the fourth cyclic voltammogram of the anodes. The voltammograms were obtained with $\nu = 75 \mu\text{Vs}^{-1}$ and the arrow indicates the scan direction.

The CV curves for the anodes are presented in Figs. 6.21 and 6.22. A large evolution between subsequent scans is observed in Fig. 6.21. Additionally, an anodic peak is visible at approximately 0.3 V which is however seen to diminish and shift towards higher potentials for each scan. A cathodic peak is not clearly visible however a change of slope for the forward scan is visible at approximately 0.15 V which also diminishes

for each scan. The CV curves in Fig. 6.22 show a large deviation from TC to TC and additionally there is a large evolution between subsequent cycles. This indicates instability of the measurements and hence metric points for the anode CV curves are undefined.

For the cathodes, symmetrical voltammograms with two distinct peaks are seen as in Fig. 6.23. The anodic and cathodic peak are located at approximately 3.8 V and 3.0 V, respectively. Metric points from Fig. 5.7 are summarised in Table 6.4. The symmetrical voltammograms for the cathodes i.e. a reversible charge transfer since $Q \sim 0$ C, suggest that the electrochemical reaction of the de-/intercalation of Li^+ in the olivine structure is highly reversible.

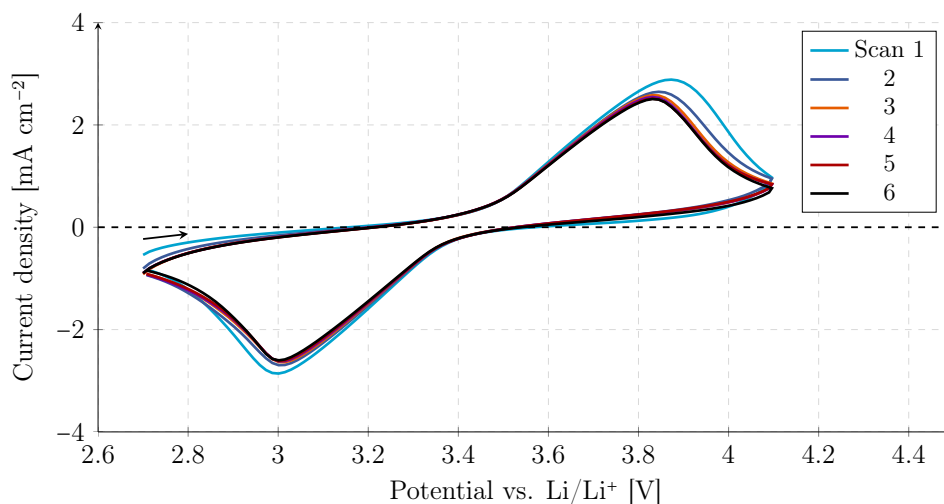


Figure 6.23: Cyclic voltammograms with six successive scans for the cathode of TC1. The voltammograms were obtained according to Table 5.3 with a scan rate of $200 \mu\text{Vs}^{-1}$. The arrow indicates the scan direction.

Evolution of the current voltage trace was observed, where particularly the first scan deviates from the subsequent ones. This is expected since the electrochemical system has to reach equilibrium. A comparison of the sixth scan for each of the cathodes is presented in Fig. 6.24.

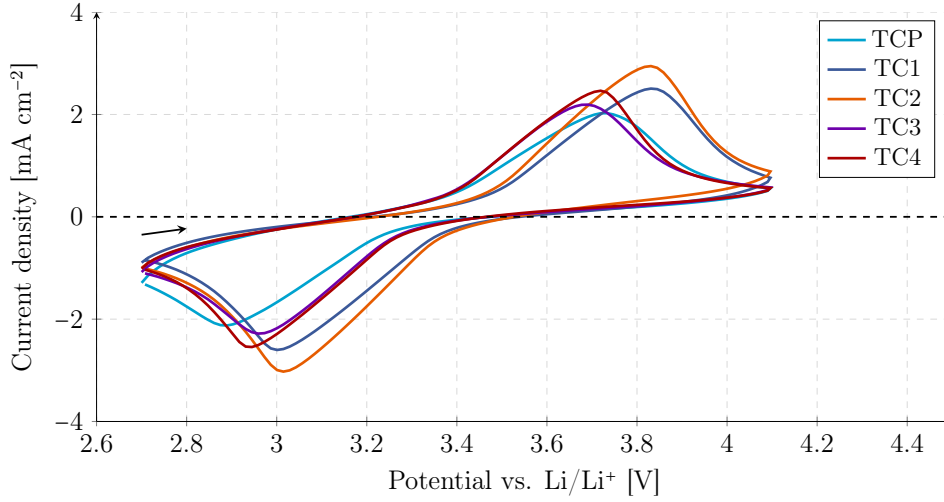


Figure 6.24: Comparison of the sixth cyclic voltammogram of the cathodes. The voltammograms were obtained with $\nu = 200 \mu\text{Vs}^{-1}$ and the arrow indicates the scan direction.

Table 6.4: CV metric points from Fig. 6.24.

Cathode					
Sample	ΔE [V]	$E_{1/2}$ [V]	Q [C]	D_{an} [$\text{cm}^2\text{s}^{-1} \times 10^{-6}$]	D_{cat} [$\text{cm}^2\text{s}^{-1} \times 10^{-6}$]
TCP	0.828	3.30	0.0291	0.0726	0.220
TC1	0.822	3.42	-0.0671	0.228	0.320
TC2	0.806	3.42	-0.0617	0.320	0.397
TC3	0.709	3.32	0.0211	0.140	0.268
TC4	0.769	3.33	0.0351	0.190	0.334

From the Randles–Ševčík equation (5.9) an effective diffusion coefficient of the Li^+ de-/intercalation can be determined from the peak currents. For the cathodes $D \sim 1 \times 10^{-7} \text{ cm}^2\text{s}^{-1}$ with the pristine case being lowest and TC2 the largest as seen in Table 6.4.

Tafel Kinetics

The Tafel plot of the sixth voltammogram of the pristine cathode from Fig. 6.24, is seen in Fig. 6.25a. The overpotential on the x -axis is determined from the standard potential i.e. the metric point $E_{1/2}$ from Table 6.4.

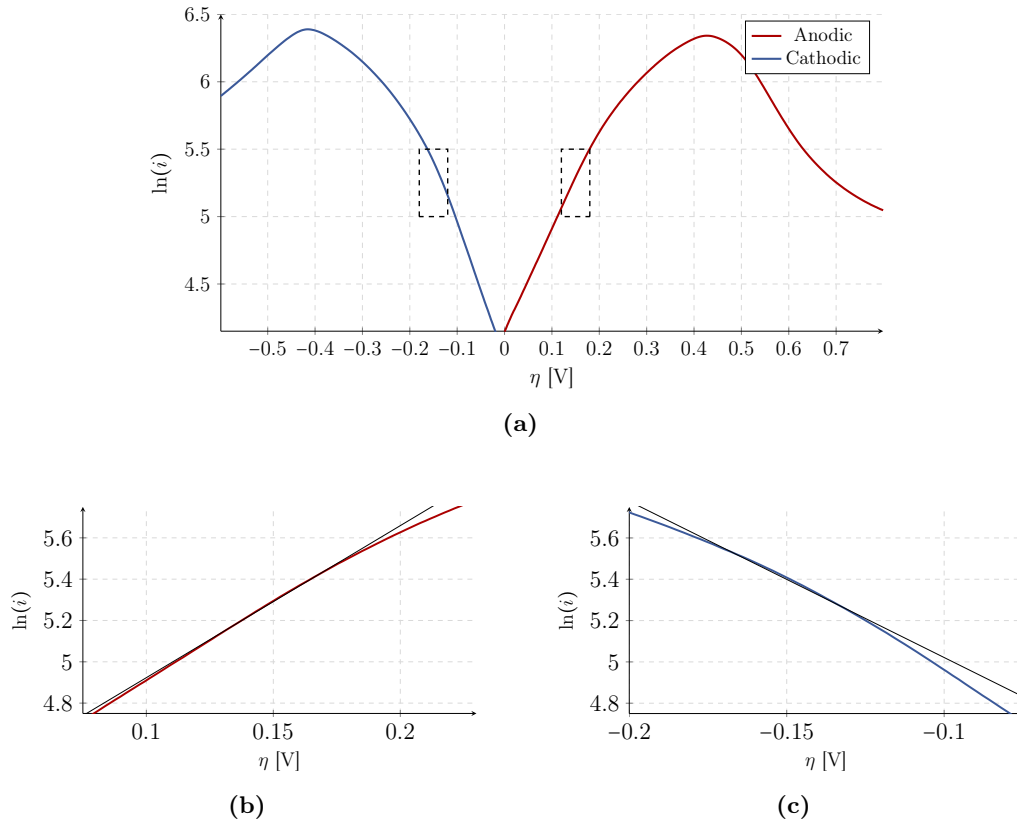


Figure 6.25: Tafel plots of the sixth voltammogram of the pristine cathode. (a) Anodic and cathodic trace plotted separately. The region delimited by the dashed rectangle is controlled by the reaction kinetics. (a) and (b) shows kinetically controlled regions of the anodic and the cathodic traces, respectively, with linear regression models.

The dashed rectangular areas seen in Fig. 6.25a cover the kinetically controlled regions where the Tafel equations from Section 5.5.1 apply. These areas along with the linear regression are seen in Figs. 6.25b and 6.25c. The linear regression was performed in the interval $\eta \in [\pm 0.12 \text{ V}; \pm 0.18 \text{ V}]$ for the sixth voltammogram of all the cathodes. The exchange current densities and the transfer coefficients are available in Table 6.5.

Table 6.5: Exchange current densities and transfer coefficients of the cathodes.

Sample	$i_{0,a}$ [μA]	α_a	$i_{0,c}$ [μA]	α_c
TCP	66	0.19	71	0.19
TC1	95	0.18	79	0.20
TC2	$1.1 \cdot 10^2$	0.19	96	0.20
TC3	90	0.19	88	0.20
TC4	98	0.18	84	0.20

The exchange current densities are seen to be very similar across the cycle-aged cathodes but lower for the pristine one. The anodic exchange current density for TC2

is almost twice as large compared to the one for TCP. This implies that the charge transfer resistance of the pristine cathode is largest according to Ohm's law. Since the exchange current density is proportional to the equilibrium rate constant, k_0 , it follows the same trend. The transfer coefficients are similar across all the TCs and also when comparing the anodic and the cathodic cases.

6.5 Chronopotentiometry

The discharge profiles of the cathodes as seen in Fig. 6.26 were obtained by chronopotentiometry. It is seen that the voltage of the cathodes rapidly decreases in the beginning of the discharge procedure and then plateaus at around 3.25 V. This continues until around 1 mA h cm^{-2} where the voltage starts to decrease. The cathodes from TCC and TC1 have the earliest onset below 1 mA h cm^{-2} . The discharge continued until the voltage decreased to 2 V. The cathode of TC1 is seen to have the largest capacity per unit area. The cathode of TCP and TCC have approximately the same capacity per unit area of $\sim 2.55 \text{ mA h cm}^{-2}$.

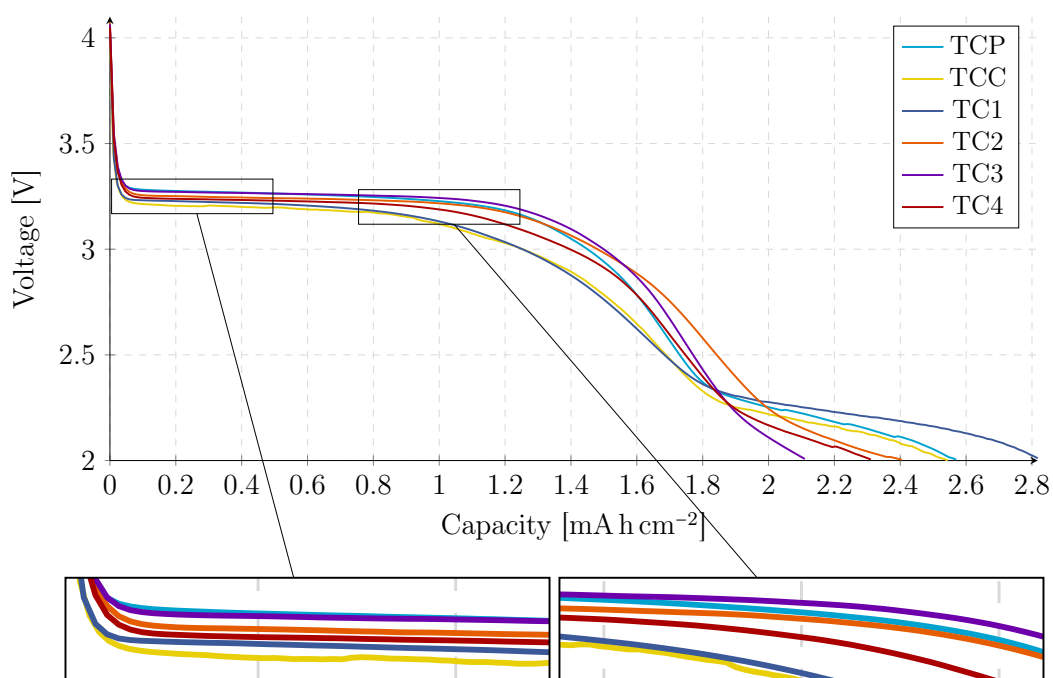


Figure 6.26: Discharge profiles of the cathodes. The two inserts from left to right shows the drop to the plateau at 3.25 V and the onset of the voltage drop at the end of discharge, respectively.

The discharge profiles are seen to approximately follow the theoretical discharge profile in Fig. 3.14. One difference is the flattening of the curves at around 1.8 mA h cm^{-2} which implies a change in the reaction rate.

6.6 Electrochemical Impedance Spectroscopy

The electrochemical impedance spectroscopy models of the electrodes presented in Section 5.5.3 are fitted to the measurements. The impedance measurements of the anodes had a low signal-to-noise ratio and showed discrepancies across multiple measurements. Therefore, only measurements and the fit of the anodes of TCP and TC2 are shown in Fig. 6.27. This is supported by the model parameters in Table 6.6 where inter alia R_{ct} is too large, and R_{SEI} and s are too low and above the theoretical limit, respectively, for the pristine anode. Therefore, low credibility is assigned to the measurements. The error of the fits are low but due to the unphysical values of the parameters the model is either wrong or the measurements are not representative of the actual electrochemical behavior of the anode. A similar model has previously been used by Scipioni et al. [93] with great success and therefore the issue is believed to be the measurements.

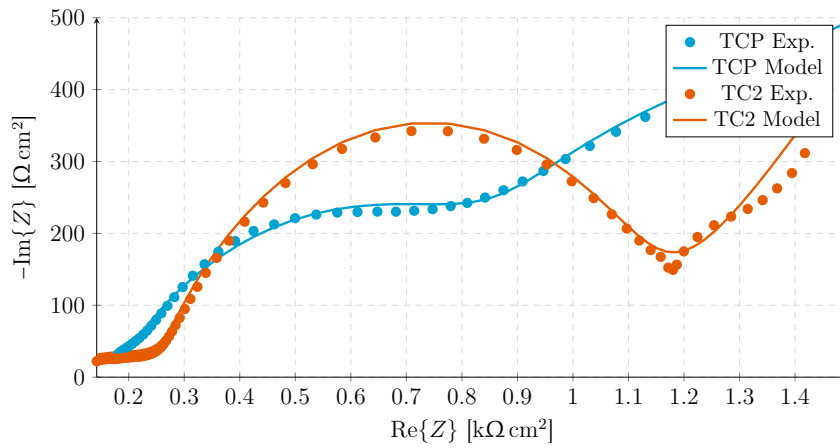


Figure 6.27: Nyquist plot of the EIS measurements and the fitted model of the anodes of TCP and TC2. The model used is seen in Fig. A.14.

Table 6.6: Parameters of the fitted EIS anode models.

	TCP	TC2
R_{ct} [$\Omega \text{ cm}^2$]	3.34e6	7.00e4
R_{ion} [$\text{k}\Omega \text{ cm}^2$]	1.29	1.90
R_{el} [$\Omega \text{ cm}^2$]	6.13	4.26
R_e [$\Omega \text{ cm}^2$]	172	41.3
R_{Cu} [$\Omega \text{ cm}^2$]	890	314
R_{SEI} [$\Omega \text{ cm}^2$]	1.29e-8	57.9
n	0.470	0.274
m	0.395	0.928
k	0.600	0.210
s	1.28	0.895
Q [$\mu\text{s}^m \Omega^{-1}$]	11.3	6.15
Q_{Cu} [$\mu\text{s}^k \Omega^{-1}$]	38.4	601
Q_{SEI} [$\text{ms}^s \Omega^{-1}$]	1.95	7.89
τ [μs]	11.3	0.0104
l [mm]	0.323	0.482
Z_0 [$\mu\Omega \text{ cm}^2$]	3.56	6.13

The measurements, seen in Fig. 6.28, conducted on the cathode samples show semi-circles in the high frequency domain i.e. the charge transfer controlled region and an increasing tail in the diffusion controlled region. According to the model, the onset of the semicircle depends almost solely on the resistance in the electrolyte since $Z(\omega) \rightarrow R_e$ as $\omega \rightarrow \infty$. The resistance in the electrolyte depends on the distance from the WE to the CE and hence it should not be contributed to the electrode materials. The tail on the curves of the cathodes of TCP, TC3, and TC4 show signs of a low signal-to-noise ratio. This is likely due to the setup or a too low perturbation voltage or both. The voltage can be increased but it has to be done carefully as to not delinearise the current-voltage relationship.

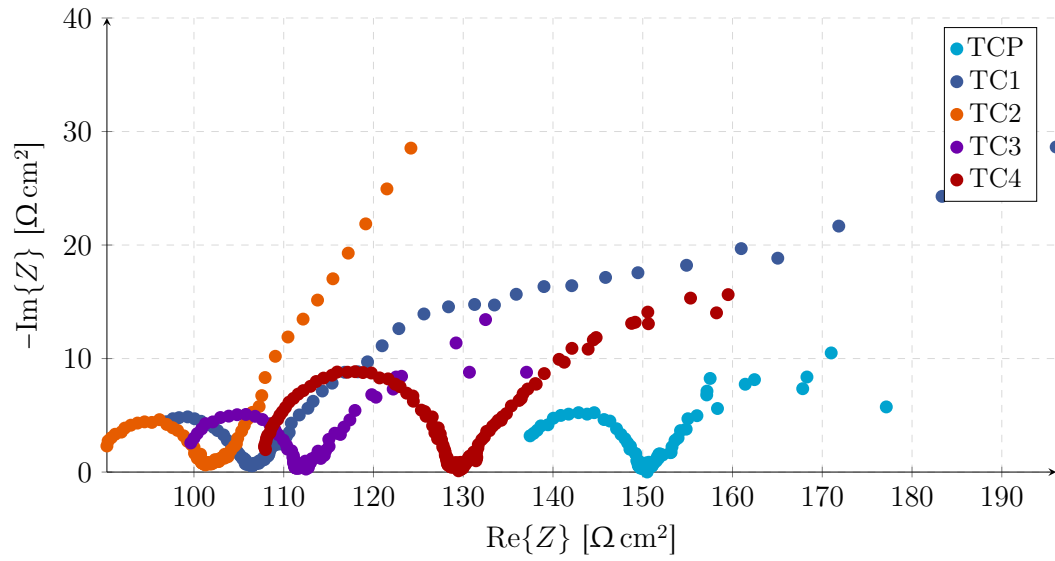


Figure 6.28: Nyquist plot of the EIS measurements of the cathodes.

The cathode impedance model was fitted to the measurements using the CNLS script previously described. The model fitted the semicircle well but it showed a greater deviation for the tail.

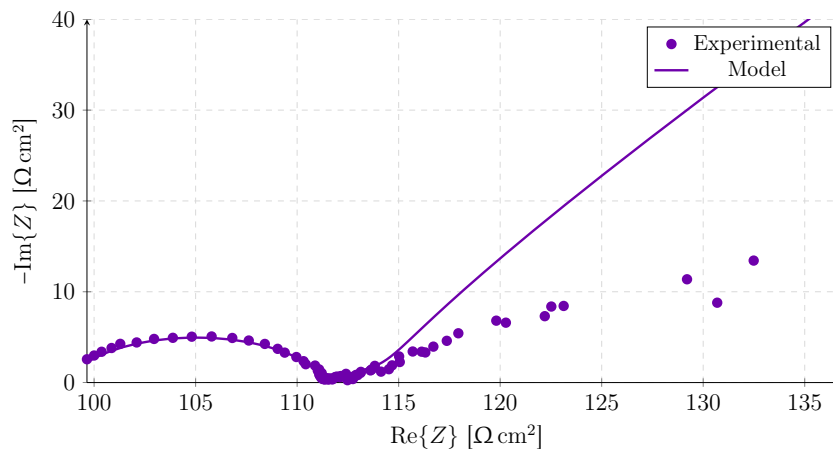


Figure 6.29: Nyquist plot of the experimental data and the fitted model of the cathode of TC3. The model used is seen in Fig. A.14.

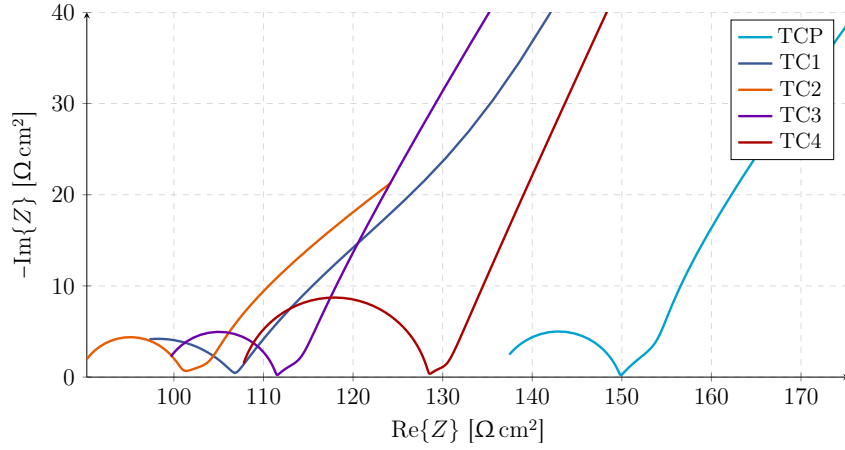


Figure 6.30: Nyquist plot of the fitted models to the EIS measurements for the cathodes. The model used is seen in Fig. A.14.

Table 6.7: Parameters of the fitted EIS cathode models.

	TCP	TC1	TC2	TC3	TC4
R_{ct} [$\Omega \text{ cm}^2$]	79.6	200	13.8	23.2	11.0
R_{ion} [$\text{k}\Omega \text{ cm}^2$]	1.29	0.888	0.810	1.18	1.11
R_{el} [$\Omega \text{ cm}^2$]	134	190	204	146	154
R_e [$\Omega \text{ cm}^2$]	136	89.5	89.2	98.6	107
R_{Al} [$\Omega \text{ cm}^2$]	13.8	17.3	11.4	12.9	21.1
n	0.513	0.405	0.427	0.417	0.387
m	0.566	0.617	0.382	0.568	0.634
k	0.800	0.574	0.814	0.835	0.880
Q [$\text{s}^m \Omega^{-1}$]	0.191	0.127	0.108	0.161	0.120
Q_{Al} [$\mu\text{s}^k \Omega^{-1}$]	32.8	93.3	38.0	25.1	17.5
τ [ms]	16.4	3.23	3.76	5.87	3.73
l [μm]	0.330	0.252	0.236	0.311	0.297
Z_0 [$\mu\Omega \text{ cm}^2$]	0.687	1.25	1.02	0.871	0.983

From the fit parameters in Table 6.7 it is seen that R_{ct} is greatest for TC1 and lowest for TC4. The value for TC1 deviates from the values of the other cycle-aged cathodes. This may be contributed to a poor fit of the semicircle on the spectrum of TC1 due to an abrupt ending of the semicircle in high frequency domain of the measurement as seen in Fig. 6.28. The mean absolute percentage error of the fits are $\sim 1.5\%$.

The maximum values of R_{ion} and l can both be assigned to the pristine cathode which is as expected. The ionic resistance is a measure of the resistance in the pores of the cathode structure which should increase with the pore length.

It is possible to determine the diffusion coefficient from the EIS parameter value, τ as

$$\tau = \frac{r^2}{D}, \quad (6.1)$$

where r is the radius of the LiFePO_4 particles, and D is the diffusion coefficient [93]. The size of the LiFePO_4 particles have not been determined in this project but Scipioni et al. [93], reported that the radius of the LiFePO_4 particles in a commercial LFP/G battery was 76 nm. Using this radius, the resulting diffusion coefficient for the pristine cathode is on the order of $10^{-9} \text{ cm}^2 \text{ s}^{-1}$ while for the cycle-aged cathodes it is $10^{-8} \text{ cm}^2 \text{ s}^{-1}$.

7 Discussion

In this chapter the aging conditions are attempted to be related to the aging mechanisms by comparing and discussing the trends seen in the results in Chapter 6. The chapter is divided into sections according to aging mechanisms and observations related to those.

Due to stability issues with the anode samples in the electrochemical setup, low credence is put on the associated results. Therefore, they will not be used in the following discussion.

7.1 Morphology and Structural Change to Graphite Anodes

Considering the surface morphology differences of the anodes seen on the SEM micrographs in Figs. 6.4 and 6.5 similarities are seen between the TCP and TC2, which shows the most distinct graphite particles. This similarity indicates that aging mechanisms such as SEI formation and cracking of graphite particle are functions of the amounts of FEC, since TC2 has undergone the least amount of FEC during aging. Similarities are also seen between the TC1 and TC4 which both show a high degree of surface roughness and indistinguishable cracked graphite particles. Comparing this observation with TC3, where the particles are more pristine but seems to be covered with a film, it is suggested that dilation and subsequent cracking of the particles is a strong function of the SOC_{avg} and the cycle depth. This suggestion is justified since for a $\text{SOC} > 50\%$ or in the transition from stage II to stage I according to the Daumas-Hérold model, almost all the graphite layers are separated due to intercalation of lithium ions. To relieve the induced strain, cracks are formed and what was bulk material before is now exposed to the electrolyte. At high SOC the cracking mechanism is suggested to primarily follow the upper pathway in Fig. 4.2 where the SEI layer forms on the newly exposed graphite. For TC3, cycle-aged at a lower SOC_{avg} , less severe cracks and a lower surface roughness are observed. In this case, a lower maximum strain is expected and eventual microcracks might be covered by the SEI layer due to its elasticity. This would result in less rough particles and growth of a more uniform SEI layer as what is believed to be seen in Fig. 6.4d and Fig. 6.5d.

Another factor to discuss is the cycle depth. It is proposed that a cycle range extending multiple intercalation stages defined from the Daumas-Hérold model in Fig. 3.6 enhances crack formation. This hypothesis is justified by the interpretation of the stage transitions as energy barriers and hence a large peak strain is expected before transitioning to the next stage. A cycle range which mainly spans stage II

might explain the pristine looking TC2. Work by Keil et al. [97] reports capacity fade plateaus of calendar-aged batteries at certain SOC and correlates them to the intercalation stages in the Daumas-Hérolt model. They found the largest plateau for LFP batteries to be located at 40-70% SOC indicating a high stability of stage II.

The severity of cracks and surface roughness due to the above mechanisms are believed to be proportional to a combination of the cycle depth and the SOC_{avg} . Additionally, the approximately identical calendar-aging at room temperature of all the TCs indicates that calendar-aging does not influence the anode surface morphology significantly and hence it is believed that the surface roughness and cracking are primarily due to cycle aging. Detailed post-mortem analysis of calendar-aged graphite NMC batteries by Storch et al. [98] found large similarities from SEM micrographs between beginning-of-life graphite anodes and ones stored at 22.5 % SOC for 10 months. In the work by Storch et al. cracks were not present, however flaky deposits attributed to the SEI layer were found and observed to increase with SOC. This might also explain the larger surface roughness of the anodes of TCs 1 and 4.

The quantitative size analysis of the anode graphite particle with the mean line intersection method Table 6.1 showed the average particle size to increase for TC3 and TC4 compared to the pristine one. Test case 2 however showed a small decrease. From these measurements a clear correlation was not found between aging conditions, aging mechanisms, and mean particle size. This suggests that the mean line intersection method might be unsuitable to quantitatively analyse the porous morphology of the anodes. The weaknesses of the method includes: highly reliant on the quality of the SEM micrographs, sampling bias when counting the particles, and not taking into account the surface roughness.

The observations made from SEM micrographs are, to some extent, supported by the Raman spectroscopy work. Considering the spectrum comparison for the anodes in Fig. 6.14, it is seen that for TC3 the G peak is shifted the most. This might be correlated to the previous discussion about induced strain of the graphite intercalation compound. Due to the low SOC cycling, a higher flexibility of the less lithiated graphite layers is expected and formation of the SEI layer will primarily follow the lower pathway in Fig. 4.2. In this case, the graphite layers might be strained but not enough to relieve through severe cracks. The unrelieved strain can result in stretching of sp^2 bonds and lower the force constant which yields a lower frequency vibrational mode as observed particularly for TC3. This hypothesis can be verified by considering the effect of the SOC on the Raman G peak position. In situ RS work by Inaba et al. [99] on various synthetic heat treated carbon materials revealed different trends of the G peak position. For the high temperature treated material at 2800 °C the G peak was seen to shift towards higher wavenumbers for higher SOC. On the other hand the material treated at 1800 °C the G peak shifted towards lower wavenumbers for higher SOC. Lastly the material treated at the coldest temperature of 700 °C showed no shift of the G peak which contradicts findings by Endo et al. [100]. Additionally, work

by Zou et al. [101] on nanocrystalline graphite flakes showed similar contradicting functions for the Raman G peak position versus the SOC for different geometries of graphite flakes. All of the aforementioned contradicting observations indicate the difficulty in determining how the SOC alters the vibrational modes and how dependent the delicate structure of the carbon materials are to the synthesis parameters.

Considering the RS maps for the anodes, a general trend of decreasing A_D/A_G , compared to TCP, is seen. This indicates a larger density of defects for the cycle aged TCs, which by recalling the SEM analysis, is deduced to stem primarily from structural deterioration of the graphite. Cross comparison of the map plots show the 5-10 times larger standard deviation of the defect density metric, A_D/A_G , for the cycle-aged TCs relative to the pristine case. This could indicate a more rough surface. This trend is supported by the SEM micrographs where the large roughness of particular TC1 is reflected in an inhomogeneous RS map plot with hot spots. The spatial resolution of the micro Raman spectrometer is on the same order as the size of the graphite particles. Therefore the A_D/A_G hot spots might be correlated to severe cracks in the particles such as that marked on Fig. 6.4b.

Considering the mean of the RS metrics from Table 6.2 it is seen that TCP is the most homogeneous and has the lowest defect density. This is in good agreement with the SEM micrographs. For TC1 a high defect density is expected due to the high A_D/A_G . Additionally, for TC1 the large $\text{FWHM}_D/\text{FWHM}_G$ ratio is suggested to indicate a larger variety of defect types and smaller particles compared to the TCP. A larger variety of defects might be justified by the large amount of FEC meaning more time for common defects to evolve. The low mean A_D/A_G value for the low SOC_{avg} TC3 supports the hypothesis that a high SOC_{avg} is related to the severity of particle cracking and the surface roughness. The calendar-aged anode showed no significant changes from TCP indicating that calendar-aging does not significantly affect the morphology and crystallinity of the anode material. Comparing TC2 with TC3 it is seen that $A_D/A_G(\text{TC2}) > A_D/A_G(\text{TC3})$ which may be explained by suppression of surface defects. In general, the trend observed where A_D/A_G is larger for the cycle-aged anodes compared to the pristine one, is in agreement with literature [102].

7.2 Mechanism for Capacity Fade of the Anode

The observations regarding surface roughness, crack formation, and crystallographic defects need to be taken into account when interpreting the evolution of capacity fade shown in Fig. 5.2a. In general the capacity fade as a function of FEC shows roughly linear behaviour, indicating steady state aging, such as continuous thickening of the SEI layer and steady formation of cracks and defects. Advanced modelling of the capacity fade for LIBs has been attempted by others which reports non-linear behavior commonly correlated to irreversible lithium plating [103]. Lithium plating was however not observed with the methods used in this thesis which might justify the roughly linear behaviour seen. Nonlinear behaviour might be observed for prolonged

cycling i.e. EOL < 80% SOH similar to that reported for NMC cells by Schuster et al. [104] where primarily the nonlinear behavior is related to LAM at the graphite anode.

It was observed that in general the capacity decreased after the approximately six year storage as seen in Fig. 5.2b. This is believed to be due to the continuous thickening of the SEI layer during calendar-aging. Experimental work by Keil et al. [97] supports this as they observed a capacity decrease of approximately 5% during a 10 month storage at similar conditions to the six year calendar-aging period of the TCs examined in this thesis. To investigate the effect of calendar-aging further it is suggested to perform post-mortem analysis on a factory new battery and compare e.g. surface morphology with TCP.

Test case 4 had the highest SOC_{avg} which corresponds to the lowest average anode potential. This allows for a more rapid reduction of electrolyte species which facilitates faster growth of the SEI layer and hence accelerated LLI. This effect of the low potential at the anode is supported by the LIB calendar-aging studies by Keil et al. where they observed the capacity fade to be proportional to the storage SOC. Together with severe crack formation this is believed to be the main reason for the rapid capacity fade for TC 4. Another contribution could be that a high SOC_{avg} promotes local overcharging where graphite material becomes inactive due to formation of a covering layer such as that visualised in Fig. 4.4. This results in LAM and supports the fact that TC4 reaches the EOL criterion with fewest FEC and might explain why the SEM micrographs are similar for TC1 and TC4 but TC4 degrades at a much faster rate. Comparing the capacity fade evolution for TC1 to that for TC3 reveals a slightly longer cycle lifetime for TC1. The cycle range for TC3 extends multiple intercalation stages (IV, III, and II) while that for TC1 lie primarily within stage II. Recent theoretical work by W. Zhou and P. H.-L. Sit [105] indicates that the transition from stage III to II have the largest energy barrier which might suggest a higher probability of microcracks, due to the energy barrier effect previously mentioned for cycling around 30-35% SOC_{avg} . Faster LLI might thus occur for TC3 compared to TC1 resulting in a slightly faster capacity fade.

The SEM micrographs of the examined cathodes showed to be similar with respect to morphology for all the TCs suggesting LiFePO_4 is a very stable material with respect to cycle aging. For the micrographs see Fig. C.1.

7.3 Composition of SEI Layer and Possible Implications

The Raman spectroscopy revealed fluorescence on the anodes of TC3 and TC4 as seen in Fig. 6.16. When examining the related quantified EDS data in Fig. 6.8, it is seen that the fluorine and oxygen percentages of TC3 and TC4 anodes are lower and higher, respectively, compared to the anodes of TCP, TC1, and TC2. The calendar-aged anode displays a similar ratio compared to TC3 and TC4. It is possible that the fluorescence stems from certain organic molecules in the SEI layer and that the presence of such molecules is the product of aging conditions. Since the fluorescence

is observed on TC3 and TC4, and not on the calendar-aged anode, the composition is not the only factor influencing it. It is suggested that the SOC_{avg} influences the reduction of the electrolyte species and hence the composition of the SEI layer. Furthermore, cycle-aging also facilitates growth of the SEI layer and thus it is expected to be thicker on TC3 and TC4 compared to on the anode of TCC.

It is reported by An et al. [49], that some electrolyte components are only reduced at low potentials, 0.2 V vs. Li/Li^+ , while others are reduced at higher potentials, 1 and 2 V vs. Li/Li^+ . This may explain the difference in composition as observed with EDS. Furthermore, it may support why the anode of TCC does not show fluorescence despite having the same composition as TC3 and TC4. In order to confirm or reject the hypothesis that the molecules of which the SEI layer is composed depends on the SOC_{avg} , further investigation is needed. This could include examining the samples with a fluorescence spectrometer or with a Fourier-transform infrared spectrometer.

7.4 Electrochemical Performance of LiFePO_4

The pristine cathode shows the lowest exchange current density from the Tafel plots which corresponds to the lowest reaction rate constant. This implies that de-/intercalation of lithium ions in the cathode occurs with the lowest rate for TCP. The highest exchange current density was observed for the cathode of TC2, while for the cathodes of TC1, TC3, and TC4 it is similar. A similar trend is seen in the internal resistance measurements performed on the pre-disassembled batteries as seen in Fig. 5.3a where the internal resistance is greatest for TCP while lowest for TC2. The rate of the de-/intercalation reaction is a function of the energy barrier and temperature as given by the Arrhenius equation. The temperature was kept constant during the experiments and therefore it is suggested from the exchange current densities that the pristine cathode has the largest energy barrier while the cathode of TC2 has the lowest, which is in agreement with the internal resistance measurements in Fig. 5.3.

Additionally, the diffusion coefficients from Table 6.4, which were obtained from the cyclic voltammograms, show a similar trend. The anodic and cathodic diffusion coefficients are lowest for the pristine cathode and largest for the cathode of TC2. These are effective diffusion coefficients meaning that they are related to the diffusion of lithium ions in both the LiFePO_4 and the FePO_4 phase. Nevertheless, a larger coefficient is associated with a slower diffusion and thus the diffusion of lithium ions occur slowest in the pristine cathode while fastest in the one of TC2. It was expected that the pristine battery would have the lowest internal resistance but the opposite was observed. The larger internal resistance and poorer electrochemical performance of the pristine cathode compared to the cycle-aged cathodes may be a result of the calendar-aging. However, this does not seem to be the case since the calendar-aged battery shows similar internal resistance as the cycle-aged ones. Therefore, it may be possible that the elevated temperature results in a positive effect on the internal

resistance of the batteries and on the electrochemical performance of the cathodes.

The trend is supported by the EIS measurements where the model parameter, R_{ct} , describes the resistance associated with the charge transfer in the electrochemical reaction. As previously mentioned the value for TC1 is an outlier which may be a result of a poor fit at high frequencies. When this outlying value is not considered, the cycle-aged cathodes show a significant lower resistance compared to the pristine one. Furthermore, the resistance associated with transport of lithium ions in the pores in-between the cathode particles, R_{ion} , is also largest for the pristine cathode and lowest for that of TC2.

As already mentioned, the reason for the poorer electrochemical performance of the pristine cathode may stem from the storage temperature. It is not known if cycle-aging followed by storage at room temperature yields beneficial changes to the cathode structure compared to only storing the battery at room temperature. Since the diffusion time is proportional to the diffusion length squared, see Eq. (3.6), smaller cathode particles will be associated with a lower diffusion time of lithium ions from the interior of the particle to the electrolyte and hence lower the internal resistance. Correlating these observations with the capacity fade behavior might suggest that the presumably positive effect on the electrochemical performance of the cathodes does not significantly influence the battery capacity, which might be dominated by anode processes.

The diffusion coefficient of lithium ions in the cathode structure has previously been reported to be on the order of $\sim 10^{-14} \text{ cm}^2 \text{ s}^{-1}$ [13]. This is multiple magnitudes smaller than the ones determined from the peak current densities in the cyclic voltammograms which are on the order of $\sim 10^{-7} \text{ cm}^2 \text{ s}^{-1}$. It is possible that this deviation stems from the scan rate used in the experiments. If the scan rate is too fast compared to the rate of the electrochemical reaction, the reaction cannot attain equilibrium which in turn limits the peak current density. In this non-equilibrium regime the Randles-Ševčík equation (5.9) is not valid and thus the calculated diffusion coefficient will not be correct. The validity of the Randles-Ševčík equation can be examined by repeating CV experiments with multiple scan rates. The linearity of $i_p(\nu^{1/2})$ can then be analysed to determine at which scan rates the electrochemical equilibrium assumption applies.

The trend seen for the diffusion coefficients determined from the CV metrics, where it is largest for the pristine cathode, is also present in the ones calculated from the EIS parameters. Comparing these values to the findings of Scipioni et al. [93], the coefficients found in this thesis are four orders of magnitude larger. They found the diffusion coefficient to be on the order of $10^{-13} \text{ cm}^2 \text{ s}^{-1}$ to $10^{-12} \text{ cm}^2 \text{ s}^{-1}$. The disagreement may stem from the fitting procedure where the low frequency part displayed a poorer fit between the model and the results. Since diffusion dominates in the low frequency regime the parameters related to diffusion of the fitted model must be considered with some uncertainty.

7.5 Degradation of the Cathode's Carbon Coating

The RS maps of the carbon coating on cathode samples reveal the opposite trend of the anodes, where the A_D/A_G ratio is seen to decrease for the cycle aged TCs compared to the pristine one. This contradicts the previous trend for aging and degradation of graphite from the anodes, and shows instead a decreasing defect density after cycling. Instead of the strain induced defects seen on the anodes it is believed that due to the small size of the carbon particles on the cathode, reduced electrolyte species bind to the defects and thus suppresses the disorder activated vibrational modes. This results in a decreased D band which is supported by the metric points found in Table 6.3. Another factor to keep in mind is the effect of the temperature on the much smaller particles at the cathode. It is known that heat treatment of carbon black powders improves the crystalline quality which would hence yield a trend similar to what is observed. Studies on this however uses much higher temperatures, $> 1000^\circ\text{C}$, than those believed to be present inside the battery during cycling [106, 107]. The calendar-aged TC aged at 40°C proved to be similar to TCP indicating that suppression of vibrational modes is activated by cycling and at a rather fast timescale since $A_D/A_G(\text{TC2}) \sim A_D/A_G(\text{TC3})$ even though $\text{FEC}(\text{TC3}) \sim 3 \times \text{FEC}(\text{TC2})$. The rapid suppression might be a result of the high reactivity of the presumably mechanically prepared nanoscale carbon coating. This means oxidation or binding of reduced electrolyte species to defects sites at the surface occur early in the battery life. Degradation of the cathode carbon coating will affect the conductivity of the cathodes which in turn results in power fade. The spectrum comparison shown in Fig. 6.15 reveals no peak shifts supporting the hypothesis that the cathode carbon coating of all TCs shows disorder due to a similar mechanism. Furthermore, degradation of the carbon coating would affect the conductivity of the cathodes.

From the EIS measurements it is observed that the electrical resistance, R_{el} , is larger for the cycle-aged cathodes compared to the pristine one. This is in agreement with the aging mechanism examined in Chapter 4 where the carbon coating agglomerates as the cathode ages. Therefore, this finding may also support the suggestion that reduced electrolyte species suppresses the D band signal.

The carbon coating on LiFePO_4 cathodes from the same type of batteries as studied in this project were examined by Simolka et al. [69], who found that as the cathodes were cycle-aged they became less conductive. This is in agreement with the trend in R_{el} . They assigned the decrease in conductivity to agglomeration of carbon particles.

7.6 Iron Dissolution and Structural Changes to LiFePO_4

The EDS analysis of the cathode samples showed a ratio of oxygen, phosphorous, and iron comparable to the stoichiometry of LiFePO_4 . The pristine cathode has the greatest and the lowest percentage of iron and oxygen, respectively, across all the samples.

The phosphorous content only varies a few percentages and hence the change in the iron content is compensated by the oxygen content. Since the pristine cathode shows the greatest percentage of iron and the calendar-aged cathode shows similar percentage as the cycle-aged cathodes, it may be suggested that the elevated temperatures of 42.5 °C, causes dissolution of iron from the cathode while facilitating binding of oxygen. If the iron dissolves from the cathode it could be expected to deposit on the surface of the anode, but this is not observed from the EDS analysis. Therefore, if the iron dissolved from the cathode it is either in the electrolyte solution or on the surface of the anode but in a too low concentration for EDS to detect.

The compositional differences between the pristine and the aged cathodes do likely result in structural changes. These changes would cause the diffusion coefficient to change as the 1D channels in which lithium diffuses may either expand, contract, or become blocked. Comparing the diffusion coefficient from the CV metrics in Table 6.4 and the quantified EDS data in Fig. 6.9 it is seen that the pristine has the lowest diffusion coefficient. The cycle-aged cathodes have similar diffusion coefficients, although TC2 have the largest, and similar ratio of Fe:O:P. Additionally, the ratio of the pristine cathode is farthest from the stoichiometry of FePO_4 compared to the aged cathodes. This may indicate that the composition of the cathode material does not follow the theoretical stoichiometry when it is produced.

The EDS results for both the anode and the cathode samples are in agreement with work by Simolka et al. [69]. They also found that iron dissolved from the cathode structure at 55 °C and that the dissolution rate of iron increased with high SOC_{avg} . This is however not observed in Fig. 6.9 and thus the dissolution rate may depend more on the temperature than on the SOC_{avg} . A study done by Li et al. [70], came to the conclusion that iron was not present on the anode for cycle-aged batteries of the same type as examined in this project if the temperature was 40 °C. This is in agreement with the observations made with EDS.

7.7 Capacity Fade for LiFePO_4 /Graphite Batteries

When determining the capacity fade of a battery stemming from degradation of the electrodes, one portion may be assigned to the anode and one to the cathode. From the discussion regarding the morphology changes and the electrochemical performance of the cathodes it is suggested that the capacity fade is mainly due to aging of the anode. This is in agreement with what is already known from the literature where one of the main degradation mechanisms is the growth of the SEI layer on the anode [33]. If LAM of the cathode was a major contributor to the capacity fade then morphology changes and degradation of the electrochemical performance would have been more apparent from the experiments. The capacity fades in Fig. 5.2a and the chronopotentiometry results of the cathodes from Fig. 6.26 reveal no apparent correlation. This may support the suggestion that the capacity fade is mainly due to LAM at the anode and LLI. The credence of this hypothesis could be increased by

examining anodes with chronopotentiometry. Additionally, a correlation between the internal resistance of the batteries, and the resistance of the cathodes determined from EIS, is not observed.

8 Conclusion

In this chapter, the four bullet points in Section 1.2 are sought to be answered. This is mainly done by proposing relations of the experimental results in Chapter 7 to the aging mechanisms in Chapter 4.

A procedure for preparing the LiFePO_4 and graphite electrodes for post-mortem analysis was made. It includes preparing an inert atmosphere in the glovebox, a disassembly procedure for the batteries, and electrode preparation including cutting, washing, and drying.

For the graphite anode, a high SOC_{avg} and a large cycle depth were observed to enhance the formation of cracks and thus increase the surface roughness. On the basis of this result it is suggested that the probability of cracking is related to the intercalation stages within the cycle range. Additionally, it was found that A_D/A_G from the RS maps increased with the number of FEC and thus it is proposed that defects in the graphite particles are formed as lithium ions de-/intercalate. It is also suggested that the formation of defects is increased at large cycle depths.

It was found that the $\text{FWHM}_D/\text{FWHM}_G$ for the anodes increased as a function of amount of FEC and therefore it is suggested that the variety of crystallographic defect types is a function of FEC. The development of cracks and the formation of defects are believed to result in capacity fade from LAM. In addition to LAM at the anode it was observed that high SOC_{avg} increased the rate of growth of the SEI layer and hence accelerated the LLI.

It was not possible to obtain reliable electrochemical results for the anodes due to stability issues. For the cathodes, the electrical resistance was observed to be lower for the cycle-aged cases compared to the pristine. It is suggested that the elevated temperature induces positive effects on the cathodes. It was also observed that the diffusion coefficients were larger for the cycle-aged cathodes compared to the pristine one. This is suggested to be linked to the compositional changes observed with EDS through structural changes to the cathodes. The composition of the SEI layer on the anodes were also determined but it was not possible to link it to the electrochemical performance.

The carbon coating on the cathodes were observed to have a larger resistance for the cycle-aged cases and hence it is proposed that the coating degrades as the battery is cycled. This is believed to be a contributing factor to LAM at the cathode.

On the basis of the results and the associated trends it is suggested that the aging mechanisms related to the anode are responsible for the majority of the capacity fade observed in the batteries. Additionally, the degradation of the carbon coating on the cathodes is expected to decrease the battery power.

Outlook

Further work regarding the aging mechanisms of the LFP/Graphite batteries is proposed to validate the conclusions obtained in the thesis if more time was available. This work can be divided into two categories; aging of additional batteries to isolate some of the observed dependencies; and characterisation with additional methods to confirm some of the observations.

Aging of two additional batteries are proposed with the conditions shown in Table 8.1.

Table 8.1: Proposed additional TCs for validation of the conclusions from this thesis. Each TC should be aged to 80% SOH.

Sample	Temperature (°C)	Cycle depth	SOC _{avg}
TC5	42.5	30%	20%
TC6	42.5	10%	90%

Test case 5 may be used to investigate the effect of a large cycle depth combined with a low SOC_{avg}. This TC is suggested to support the hypothesis that crack formation in the anode graphite particles is less severe at low SOC_{avg} and that the surface morphology is expected to be similar to TC3 with a thick surface film. Test case 6 with a low cycle depth but high SOC_{avg} is expected to clarify how crack formation in the anode graphite particles depends on the SOC. Cracks are expected to be less severe than that observed for TC1 due to the low cycle depth.

Additional methods and suggested ideas for further work includes:

1. Investigation of the fluorescent SEI layer and its molecular and elemental composition with emission/excitation fluorescence spectroscopy, Fourier-transform infrared spectroscopy, and x-ray photoelectron spectroscopy.
2. Investigation of iron dissolution from the cathode and the validation of the hypothesis that iron deposits on the anode with x-ray photoelectron spectroscopy and secondary ion mass spectroscopy.
3. Further investigation of the electrodes degradation and how it correlates to morphology and defect densities detected with Raman spectroscopy with x-ray powder diffraction analysis.
4. Quantitative analysis of the observed anode surface roughness with atomic force microscopy.

-
5. Further electrochemical experiments to characterise the anodes by re-evaluating the electrochemical cell setup to circumvent the observed stability issues. The stability issue may be solved with a more reliable cell setup.

Bibliography

- ¹*Bulletin of the Atomic Scientists, Doomsday Clock*, <https://thebulletin.org/doomsday-clock/>, [Online; accessed 11-Dec-2020].
- ²M. J. Bos et al., “Wind power to methanol: Renewable methanol production using electricity, electrolysis of water and CO₂ air capture”, *Applied Energy* **264**, 114672 (2020).
- ³A. Mohammad, R. Zamora, and T. T. Lie, “Integration of Electric Vehicles in the Distribution Network: A Review of PV Based Electric Vehicle Modelling”, *Energies* **13**, 4541 (2020).
- ⁴I. Tsiropoulos, D. Tarvydas, and N. Lebedeva, *Li-ion batteries for mobility and stationary storage applications – Scenarios for costs and market growth*, tech. rep., EUR 29440 EN (Publication Office of the European Union, Luxembourg, 2018).
- ⁵J. B. Goodenough, “How we made the Li-ion rechargeable battery”, *Nature Electronics* **1**, 204 (2018).
- ⁶M. V. Reddy et al., “Brief History of Early Lithium-Battery Development”, *Materials* **13**, 1884 (2020).
- ⁷J. Asenbauer, T. Eisenmann, M. Kuenzel, A. Kazzazi, Z. Chen, and D. Bresser, “The success story of graphite as a lithium-ion anode material - fundamentals, remaining challenges, and recent developments including silicon (oxide) composites”, *Sustainable Energy and Fuels*, 5387–5416 (2020).
- ⁸Y. Nishi, “The Dawn of Lithium-Ion Batteries”, *Electrochem. Soc. Interface* **25**, 71–74 (2016).
- ⁹A. Manthiram, “A reflection on lithium-ion battery cathode chemistry”, *Nature Communications* **11**, 1550 (2020).
- ¹⁰G. Pistoia, *Lithium-Ion Batteries : Advances and Applications* (Elsevier, 2014) Chap. 1.
- ¹¹N. Nitta, F. Wu, J. T. Lee, and G. Yushin, “Li-ion battery materials: present and future”, *Materials Today* **18**, 252–264 (2015).
- ¹²H.-M. Xie et al., “Optimized LiFePO₄-Polyacene Cathode Material for Lithium-Ion Batteries”, *Advanced Materials* **18**, 2609–2613 (2006).

- ¹³L.-X. Yuan et al., “Development and challenges of LiFePO₄ cathode material for lithium-ion batteries”, *Energy Environ. Sci.* **4**, 269–284 (2011).
- ¹⁴M. M. Kabir and D. E. Demirocak, “Degradation mechanisms in Li-ion batteries: a state-of-the-art review”, *Int. J. Energy Res.* **41**, 1963–1986 (2017).
- ¹⁵P. Atkins, J. de Paula, and J. Keeler, *Atkins’ Physical Chemistry*, 11th ed. (Oxford University Press, 2018) Chap. 6.
- ¹⁶D. Linden and T. B. Reddy, “Basic Concepts”, in *Linden’s Handbook of Batteries*, edited by D. Linden and T. B. Reddy, 4th ed. (McGraw-Hill, 2011) Chap. 1.
- ¹⁷M. Salomon, “Electrochemical Principles and Reactions”, in *Linden’s Handbook of Batteries*, edited by D. Linden and T. B. Reddy, 4th ed. (McGraw-Hill, 2011) Chap. 2.
- ¹⁸D. D. Friel, “Battery Design”, in *Linden’s Handbook of Batteries*, edited by D. Linden and T. B. Reddy, 4th ed. (McGraw-Hill, 2011) Chap. 5.
- ¹⁹D. Deng, “Li-ion batteries: basics, progress, and challenges”, *Energy Science and Engineering* **3(5)**, 385–418 (2018).
- ²⁰D. Linden, “Factors Affecting Battery Performance”, in *Linden’s Handbook of Batteries*, edited by D. Linden and T. B. Reddy, 4th ed. (McGraw-Hill, 2011) Chap. 3.
- ²¹D. Linden and T. B. Reddy, *Linden’s Handbook of Batteries*, 4th ed. (McGraw-Hill, 2011).
- ²²D. Linden and T. B. Reddy, “An Introduction to Primary Batteries”, in *Linden’s Handbook of Batteries*, edited by D. Linden and T. B. Reddy, 4th ed. (McGraw-Hill, 2011) Chap. 8.
- ²³W. M. Seong et al., “Abnormal self-discharge in lithium-ion batteries”, *Energy Environ. Sci.* **11**, 970 (2018).
- ²⁴A. Salkind and G. Zguris, “Lead-Acid Batteries”, in *Linden’s Handbook of Batteries*, edited by D. Linden and T. B. Reddy, 4th ed. (McGraw-Hill, 2011) Chap. 16.
- ²⁵D. Linden and T. B. Reddy, “An Introduction to Secondary Batteries”, in *Linden’s Handbook of Batteries*, edited by D. Linden and T. B. Reddy, 4th ed. (McGraw-Hill, 2011) Chap. 15.
- ²⁶S. Wicelinski, “Battery Standardization”, in *Linden’s Handbook of Batteries*, edited by D. Linden and T. B. Reddy, 4th ed. (McGraw-Hill, 2011) Chap. 4.
- ²⁷*Wikimedia Commons with creative commons and/or GNU license, CC BY-SA 4.0*, Images uploaded by users MyXyloto, Santeri Viinamäki, D.328, Lead holder and Raimond Spekking [Online; accessed 22-Nov-2020].

- ²⁸Y. Orikasa and Y. Uchimoto, “Overview of Lithium-Ion Batteries”, in *Lithium-Ion Batteries - Overview, Simulation, and Diagnostics*, edited by Y. Kato, Z. Ogumi, and J. M. P. Martín (Pan Stanford, 2019) Chap. 1, pp. 1–34.
- ²⁹J. Dahn and G. M. Ehrlich, “Lithium-Ion Batteries”, in *Linden’s Handbook of Batteries*, edited by D. Linden and T. B. Reddy, 4th ed. (McGraw-Hill, 2011) Chap. 26.
- ³⁰R. Zhao, S. Zhang, J. Liu, and J. Gu, “A review of thermal performance improving methods of lithium ion battery: Electrode modification and thermal management system”, *Journal of Power Sources* **299**, 557–577 (2015).
- ³¹A. Mauger et al., “A comprehensive review of lithium salts and beyond for rechargeable batteries: Progress and perspectives”, *Materials Science & Engineering R* **134**, 1–21 (2018).
- ³²J.-M. Tarascon and M. Armand, “Issues and challenges facing rechargeable lithium batteries”, *Nature* **414**, 359–367 (2001).
- ³³J. P. Pender et al., “Electrode Degradation in Lithium-Ion Batteries”, *ACS Nano* **14**, 1243–1295 (2020).
- ³⁴C. M. Julien, A. Mauger, K. Zaghib, and H. Groult, “Comparative Issues of Cathode Materials for Li-Ion Batteries”, *Inorganics* **2**, 132–154 (2014).
- ³⁵M. Winter and J. O. Besenhard, “Lithiated Carbons”, in *Handbook of Battery Materials*, edited by C. Daniel and J. O. Besenhard, 2nd ed. (Wiley-VCH, 2011) Chap. 15.
- ³⁶W. Research, *ElementData*, <https://reference.wolfram.com/language/ref/ElementData.html>, [Online; accessed 02-Jun-2021], 2014.
- ³⁷Y. Li et al., “Intercalation chemistry of graphite: alkali metal ions and beyond”, *Chem Soc. Rev.* **2019**, 4655 (2019).
- ³⁸K. Wong and S. Dia, “Nanotechnology in Batteries”, *J. Energy Resources Technology* **139**, 014001 (2017).
- ³⁹S. Dühnen et al., “Toward Green Battery Cells: Perspective on Materials and Technologies”, *Small Methods* **4**, 2000039 (2020).
- ⁴⁰C.-H. Doh et al., “A new SiO/C anode composition for lithium-ion battery”, *Journal of Power Sources* **179**, 367–370 (2008).
- ⁴¹J. W. Choi and D. Aurbach, “Promise and reality of post-lithium-ion batteries with high energy densities”, *Nature Reviews Materials* **1**, 16013 (2016).
- ⁴²K. Momma and F. Izumi, “Vesta 3 for three-dimensional visualization of crystal, volumetric, and morphology data”, *J. Appl. Cryst.* **44**, 1272–1276 (2011).

- ⁴³L. Laffont et al., “Study of the $\text{LiFePO}_4/\text{FePO}_4$ Two-Phase System by High-Resolution Electron Energy Loss Spectroscopy”, *Chem. Mater.* **18**, 5520–5529 (2006).
- ⁴⁴P. P. Prosini, *Iron Phosphate Materials as Cathodes for Lithium Batteries* (Springer, 2011) Chap. 10.
- ⁴⁵N. Mohamed and N. K. Allam, “Recent advances in the design of cathode materials for Li-ion batteries”, *RSC Adv.* **10**, 21662 (2020).
- ⁴⁶J. Hu, W. Huang, L. Yang, and F. Pan, “Structure and performance of the LiFePO_4 cathode material: from bulk to the surface”, *Nanoscale* **12**, 15036 (2020).
- ⁴⁷J. Wang and X. Sun, “Understanding and recent development of carbon coating on LiFePO_4 cathode materials for lithium-ion batteries”, *Energy Environ. Sci.* **5**, 5163 (2012).
- ⁴⁸H. J. Gores et al., “Liquid Nonaqueous Electrolytes”, in *Handbook of Battery Materials*, edited by C. Daniel and J. O. Besenhard, 2nd ed. (Wiley-VCH, 2011) Chap. 17.
- ⁴⁹S. J. An et al., “The state of understanding of the lithium-ion battery graphite solid electrolyte interphase (SEI) and its relationship to formation cycling”, *Carbon* **105**, 52–76 (2016).
- ⁵⁰O. Borodin et al., “Modeling Insight into Battery Electrolyte Electrochemical Stability and Interfacial Structure”, *Accounts of Chemical Research* **50**, 2886–2894 (2017).
- ⁵¹O. Borodin, “Challenges with prediction of battery electrolyte electrochemical stability window and guiding the electrode - electrolyte stabilization”, *Current Opinion in Electrochemistry* **13**, 86–93 (2019).
- ⁵²P. Peljo and H. H. Girault, “Electrochemical potential window of battery electrolytes: the HOMO-LUMO misconception”, *Energy & Environmental Science* **11**, 2306–2309 (2018).
- ⁵³E. Peled, D. Golodnitsky, and J. Penciner, “The Anode/Electrolyte Interface”, in *Handbook of Battery Materials*, edited by C. Daniel and J. O. Besenhard, 2nd ed. (Wiley-VCH, 2011) Chap. 16.
- ⁵⁴X. Yu and A. Manthiram, “Electrode-electrolyte interfaces in lithium-based batteries”, *Energy Environ. Sci.* **11**, 527–543 (2018).
- ⁵⁵L. Xing et al., “Deciphering the Ethylene Carbonate - Propylene Carbonate Mystery in Li-Ion Batteries”, *Acc. Chem. Res.* **51**, 282–289 (2018).
- ⁵⁶K. Edström, T. Gustafsson, and J. Thomas, “The cathode-electrolyte interface in the Li-ion battery”, *Electrochimica Acta* **50**, 397–403 (2004).

- ⁵⁷S. Sun et al., “Accelerated aging and degradation mechanism of LiFePO₄/graphite batteries cycled at high discharge rates”, *RSC Adv.* **8**, 25695 (2018).
- ⁵⁸Y. Qian et al., “How electrolyte additives work in li-ion batteries”, *Energy Storage Materials* **20**, 208–215 (2019).
- ⁵⁹R. Spotnitz, “Separators for Lithium-Ion Batteries”, in *Handbook of Battery Materials*, edited by C. Daniel and J. O. Besenhard, 2nd ed. (Wiley-VCH, 2011) Chap. 20.
- ⁶⁰C. F. J. Francis, I. L. Kyatzis, and A. S. Best, “Lithium-Ion Battery Separators for Ionic-Liquid Electrolytes: A Review”, *Adv. Mater.* **32**, 1904205 (2020).
- ⁶¹H. Zhang, M.-Y. Zhou, C.-E. Lin, and B.-K. Zhu, “Progress in polymeric separators for lithium ion batteries”, *RSC Adv.* **5**, 89848 (2015).
- ⁶²T. Wu, K. Wang, M. Xiang, and Q. Fu, “Progresses in Manufacturing Techniques of Lithium-Ion Battery Separators in China”, *Chin. J. Chem.* **37**, 1207–1215 (2019).
- ⁶³D. P. Finegan et al., “Characterising the structural properties of polymer separators for lithium-ion batteries in 3D using phase contrast X-ray microscopy”, *Journal of Power Sources* **333**, 183–192 (2016).
- ⁶⁴X. Han, L. Lu, Y. Zheng, X. Feng, Z. Li, J. Li, and M. Ouyang, “A review on the key issues of the lithium ion battery degradation among the whole life cycle”, *eTransportation* **1**, 100005 (2019).
- ⁶⁵J. Vetter et al., “Ageing mechanisms in lithium-ion batteries”, *Journal of Power Sources* **147**, 269–281 (2005).
- ⁶⁶P. Liu et al., “Aging Mechanisms of LiFePO₄ Batteries Deduced by Electrochemical and Structural Analyses”, *Journal of the Electrochemical Society* **157**, A499–A507 (2010).
- ⁶⁷N. Lin et al., “Understanding the crack formation of graphite particles in cycled commercial lithium-ion batteries by focused ion beam - scanning electron microscopy”, *Journal of Power Sources* **365**, 235–239 (2017).
- ⁶⁸V. Agubra and J. Fergus, “Lithium Ion Battery Anode Aging Mechanisms”, *Materials* **6**, 1310–1325 (2013).
- ⁶⁹M. Simolka, J. F. Heger, H. Kaess, I. Biswas, and K. A. Friedrich, “Influence of cycling profile, depth of discharge and temperature on commercial LFP/C cell ageing: post-mortem material analysis of structure, morphology and chemical composition”, *Journal of Applied Electrochemistry* **50**, 1101–1117 (2020).
- ⁷⁰D. Li, D. L. Danilov, L. Gao, Y. Yang, and P. H. L. Notten, “Degradation Mechanisms of C₆/LiFePO₄ Batteries: Experimental Analyses of Cycling-induced Aging”, *Electrochimica Acta* **210**, 445–455 (2016).

- ⁷¹M. Lewerenz, A. Warnecke, and D. U. Sauer, “Post-mortem analysis on LiFePO₄|Graphite cells describing the evolution & composition of covering layer on anode and their impact on cell performance”, *Journal of Power Sources* **369**, 122–132 (2017).
- ⁷²A. Jain et al., “The Materials Project: A materials genome approach to accelerating materials innovation”, *APL Materials* **1**, 011002 (2013).
- ⁷³H. Gabrisch, J. Wilcox, and M. M. Doeff, “TEM Study of Fracturing in Spherical and Plate-like LiFePO₄ Particles”, *Electrochemical and Solid-State Letters* **11**, A25–A29 (2008).
- ⁷⁴R. Scipioni et al., “Electron microscopy investigations of changes in morphology and conductivity of LiFePO₄”, *Journal of Power Sources* **307**, 259–269 (2016).
- ⁷⁵D.-T. Ngo et al., “A TEM study of the morphological and structural degradation phenomena in LiFePO₄-CB cathodes”, *Int. J. Energy Res.* **40**, 2022–2032 (2016).
- ⁷⁶*LithiumWerks ANR26650M1-B Datasheet*, <https://lithiumwerksbatteries.com/lithiumwerks-anr26650m1-b-3-3-volt-2-5ah-lithium-iron-phosphate-lifepo4-battery/>, [Online; accessed 20-Oct-2020].
- ⁷⁷T. Waldmann et al., “Review - Post Mortem Analysis of Aged Lithium-Ion Batteries: Disassembly Methodology and Physico-Chemical Analysis Techniques”, *J. Electrochem. Soc.* **163**, A2149–A2164 (2016).
- ⁷⁸Danish Standards Association, *Steels - Micrographic determination of apparent grain size*, (ISO 643:2019, Corrected version 2020-03).
- ⁷⁹J. A. Bearden, *X-Ray Wavelengths and X-Ray Atomic Energy Levels*, Table 5, 1967.
- ⁸⁰J. I. Goldstein, D. E. Newbury, J. R. Micahel, N. W. M. Ritchie, J. H. J. Scott, and D. C. Joy, *Scanning Electron Microscopy and X-Ray Microanalysis*, 4th ed. (Springer, 2018) Chap. 1,4.
- ⁸¹*NIST DTSA-II Microscopium*, <https://www.cstl.nist.gov/div837/837.02/epq/dtsa2/index.html>, [Online; downloaded 26-Apr-2021].
- ⁸²A. C. Ferrari and J. Robertson, “Interpretation of Raman spectra of disordered and amorphous carbon”, *Physical Review B* **61**, 14095 (2000).
- ⁸³A. Eckmann et al., “Probing the Nature of Defects in Graphene by Raman Spectroscopy”, *Nano Lett.* **12**, 3925–3930 (2012).
- ⁸⁴V. Mazet, *Background correction, MATLAB Central File Exchange*, <https://www.mathworks.com/matlabcentral/fileexchange/27429-background-correction>, [Online; accessed 02-Mar-2021].
- ⁸⁵A. L. Stancik and E. B. Brauns, “A simple asymmetric lineshape for fitting infrared absorption spectra”, *Vibrational Spectroscopy* **47**, 66–69 (2008).

- ⁸⁶V. I. Korepanov and D. M. Sedlovets, “An asymmetric fitting function for condensed-phase Raman spectroscopy”, *Analyst* **143**, 2674–2679 (2018).
- ⁸⁷W. Paraguassu et al., “Phonon calculation on olivine-like LiMPO_4 ($M = \text{Ni, Co, Fe}$) and Raman scattering of the iron-containing compound”, *J. Raman Spectrosc.* **36**, 213–220 (2005).
- ⁸⁸P. J. Larkin, *IR and Raman Spectroscopy, Principles and Spectral Interpretation*, 1st ed. (Elsevier, 2011) Chap. 2.
- ⁸⁹A. Jorio et al., “Measuring disorder in graphene with the G and D bands”, *Phys. Status Solidi B* **247**, 2980–2982 (2010).
- ⁹⁰F. Foucher et al., “Effect of grain size distribution on Raman analyses and the consequences for in situ planetary missions”, *Journal of Raman Spectroscopy* **44**, 916–925 (2013).
- ⁹¹D. W. Scott, “On optimal and data-based histograms”, *Biometrika* **66**, 3 (1979).
- ⁹²N. Elgrishi et al., “A Practical Beginner’s Guide to Cyclic Voltammetry”, *J. Chem. Educ.* **95**, 197–206 (2017).
- ⁹³R. Scipioni et al., “A Physically-Based Equivalent Circuit Model for the Impedance of a LiFePO_4 /Graphite 26650 Cylindrical Cell”, *Journal of The Electrochemical Society* **164**, A2017–A2030 (2017).
- ⁹⁴M. Chen et al., “Vanadium-doping of LiFePO_4 /carbon composite cathode materials synthesized with organophosphorus source”, *Electrochimica Acta* **167**, 278–286 (2015).
- ⁹⁵K. Guo, Q. Pan, L. Wang, and S. Fang, “Nano-scale copper-coated graphite as anode material for lithium-ion batteries”, *Journal of Applied Electrochemistry* **32**, 679–685 (2002).
- ⁹⁶S. C. Nagpure, B. Bhushan, and S. S. Babu, “Raman and NMR studies of aged LiFePO_4 cathode”, *Applied Surface Science* **259**, 49–54 (2012).
- ⁹⁷P. Keil et al., “Calendar Aging of Lithium-Ion Batteries”, *Journal of The Electrochemical Society* **163**, A1872–A1880 (2016).
- ⁹⁸M. Storch et al., “Post-mortem analysis of calendar aged large-format lithium-ion cells: Investigation of solid electrolyte interphase”, *Journal of Power Sources* **443**, 227243 (2019).
- ⁹⁹M. Inaba, H. Yoshida, and Z. Ogumi, “In situ Raman Study of Electrochemical Lithium Insertion into Mesocarbon Microbeads Heat-Treated at Various Temperatures”, *J. Electrochem. Soc.* **143**, 2572–2578 (1996).

- ¹⁰⁰M. Endo, C. Kim, K. Nishimura, T. Fujino, and K. Miyashita, “Recent development of carbon materials for Li ion batteries”, *Carbon* **38**, 183–197 (2000).
- ¹⁰¹J. Zou, C. Sole, N. E. Drewett, M. Velický, and L. J. Hardwick, “In Situ Study of Li Intercalation into Highly Crystalline Graphitic Flakes of Varying Thicknesses”, *J. Phys. Chem. Lett.* **7**, 4291–4296 (2016).
- ¹⁰²E. Markervich, G. Salitra, M. Levi, and D. Aurbach, “Capacity fading of lithiated graphite electrodes studied by a combination of electroanalytical methods, Raman spectroscopy and SEM”, *Journal of Power Sources* **146**, 146–150 (2005).
- ¹⁰³J. Keil and A. Jossen, “Electrochemical Modeling of Linear and Nonlinear Aging of Lithium-Ion Cells”, *Journal of the Electrochemical Society* **167**, 110535 (2020).
- ¹⁰⁴S. F. Schuster et al., “Nonlinear aging characteristics of lithium-ion cells under different operational conditions”, *Journal of Energy Storage* **1**, 44–53 (2015).
- ¹⁰⁵W. Zhou and P. H.-L. Sit, “First-Principles Understanding of the Staging Properties of the Graphite Intercalation Compounds towards Dual-Ion Battery Applications”, *ACS Omega* **5**, 18289–18300 (2020).
- ¹⁰⁶M. R. Ammar et al., “Characterizing various types of defects in nuclear graphite using Raman scattering: Heat treatment, ion irradiation and polishing”, *Carbon* **95**, 364–373 (2015).
- ¹⁰⁷M. Pawlyta, J.-N. Rouzaud, and S. Duber, “Raman microspectroscopy characterization of carbon blacks: Spectral analysis and structural information”, *Carbon* **84**, 479–490 (2015).
- ¹⁰⁸P. Atkins, J. de Paula, and J. Keeler, *Atkins’ Physical Chemistry*, 11th ed. (Oxford University Press, 2018) Chap. 5.
- ¹⁰⁹J.-M. Savéant and C. Costentin, *Elements of Molecular and Biomolecular Electrochemistry*, 2nd ed. (Wiley, 2019) Chap. 1.
- ¹¹⁰J.-M. Savéant and C. Costentin, *Elements of Molecular and Biomolecular Electrochemistry*, 2nd ed. (Wiley, 2019) Chap. 7.
- ¹¹¹E. Kreyszig, *Advanced Engineering Mathematics*, 10th ed. (Wiley, 2011) Chap. 6.
- ¹¹²R. S. Nicholson and I. Shain, “Theory of Stationary Electrode Polarography: Single Scan and Cyclic Methods Applied to Reversible, Irreversible, and Kinetic Systems”, *Analytical Chemistry* **36**, 706–723 (1964).
- ¹¹³M. E. Orazem and B. Tribollet, *Electrochemical Impedance Spectroscopy* (Wiley, 2008) Chap. 4.
- ¹¹⁴M. E. Orazem and B. Tribollet, *Electrochemical Impedance Spectroscopy* (Wiley, 2008) Chap. 5.

- ¹¹⁵M. E. Orazem and B. Tribollet, *Electrochemical Impedance Spectroscopy* (Wiley, 2008) Chap. 10.
- ¹¹⁶M. E. Orazem and B. Tribollet, *Electrochemical Impedance Spectroscopy* (John Wiley & Sons, 2008) Chap. 11.
- ¹¹⁷*Electrochemical Methods: Fundamentals and Applications*, 2nd ed. (John Wiley & Sons, 2001) Chap. 10.
- ¹¹⁸M. E. Orazem and B. Tribollet, *Electrochemical Impedance Spectroscopy* (John Wiley & Sons, 2008) Chap. 13.
- ¹¹⁹U. Tröltzsch and O. Kanoun, “Generalization of transmission line models for deriving the impedance of diffusion and porous media”, *Electrochemical Acta* **75**, 347–356 (2012).
- ¹²⁰J. Bisquert et al., “Doubling Exponent Models for the Analysis of Porous Film Electrodes by Impedance. Relaxation of TiO₂ Nanoporous in Aqueous Solution”, *J. Phys. Chem. B* **104**, 2287–2298 (2000).
- ¹²¹E. W. Weisstein, *Modified Bessel Function of the First Kind. From MathWorld - A Wolfram Web Resource.*, <https://mathworld.wolfram.com/>, [Online; accessed 12-Feb-2021].
- ¹²²H. P. Gavin, “The Levenberg-Marquardt algorithm for nonlinear least squares curve-fitting problems”, Department of Civil and Environmental Engineering, Duke University **28**, 1–5 (2011).
- ¹²³M. Žic, “An alternative approach to solve complex nonlinear least-squares problems”, *Journal of Electroanalytical Chemistry* **760**, 85–96 (2016).
- ¹²⁴B. A. Boukamp, “A nonlinear least squares fit procedure for analysis of immitance data of electrochemical systems”, *Solid State Ionics* **20**, 31–44 (1986).
- ¹²⁵R. J. Sheppard, B. P. Jordan, and E. H. Grant, “Least squares analysis of complex data with applications to permittivity measurements”, *Journal of Physics D: Applied Physics* **3**, 1759 (1970).
- ¹²⁶A. S. Householder, *The Numerical Treatment of a Single Nonlinear Equation* (McGraw Hill, 1970).

A Theoretical Concepts, Methods, and Derivations

This appendix is devoted to derivations and elaborations of some of the comprehensive mathematical equations and models used in the main thesis.

A.1 The Electrical Potential Difference

In this section the concept of the cell potential is explained and the Nernst equation is derived and elaborated. The cell voltage or electrical potential difference of a galvanic cell is directly proportional to the Gibbs free energy, $\Delta_r G$, of the associated redox reaction. Since $\Delta_r G$ is a measure of the available non-expansion work at constant temperature per mole that can be extracted from a thermodynamic system, the following equation must hold for the galvanic cell at equilibrium

$$\Delta_r G = w_{e,\max} = -zFE_{\text{cell}}. \quad (\text{A.1})$$

The right-hand side represents molar electrical work where $F = eN_A$ is the Faraday constant, z is the electron stoichiometric number for the redox reaction, and E_{cell} is the cell voltage. Additionally, the minus sign comes from the electron charge, meaning a spontaneous reaction results in a positive voltage. Equation (A.1) thus relates thermodynamics on the left-hand side to a measurable cell potential on the right-hand side which is a function of the electrode active material used. For the overall cell reaction it is possible to express $\Delta_r G$ as

$$\Delta_r G = \Delta_r G^\ominus + RT \ln Q, \quad (\text{A.2})$$

where $\Delta_r G^\ominus$ is the Gibbs free energy at standard conditions, Q is the reaction quotient, R is the gas constant, and T is the absolute temperature. $\Delta_r G^\ominus$ and Q may be expressed as

$$\Delta_r G^\ominus = \sum_i n_i \Delta_f G_i^\ominus, \quad Q = \prod_i a_i^{n_i}, \quad (\text{A.3})$$

where $\Delta_f G_i^\ominus$ is the standard Gibbs free energy of formation for the i -th species and a_i is the activity of the i -th species. The stoichiometric number, n_i , of the i -th species should be taken positive for products and negative for reactants. Dividing by $-zF$ on both sides of Eq. (A.2) and assuming reduction as the forward reaction yields the Nernst equation

$$E_{\text{cell}} = E_{\text{cell}}^{\ominus} - \frac{RT}{zF} \ln Q = E_{\text{cell}}^{\ominus} - \frac{RT}{zF} \ln \frac{(\text{Red})}{(\text{Ox})}, \quad (\text{A.4})$$

where $E_{\text{cell}}^{\ominus} = -\Delta_r G^{\ominus}/zF$ is the standard cell potential. At standard conditions i.e. gas electrodes operating at $p_i = p^{\ominus} = 1$ bar and electrolyte concentrations of $b_i = b^{\ominus} = 1$ mol/kg, the activities become unity meaning $Q = 1$ and thus $E_{\text{cell}} = E_{\text{cell}}^{\ominus}$. The Nernst equation predicts how the electrochemical equilibrium responds to a change in the concentration of species in solution or applied electrode potential.

The standard cell potential can be determined as the difference between the standard reduction potential of two half-reactions

$$E_{\text{cell}}^{\ominus} = E_{\text{Red}}^{\ominus}(\text{Cathode}) - E_{\text{Red}}^{\ominus}(\text{Anode}). \quad (\text{A.5})$$

Since the oxidation potential is the negative of the reduction potential the standard cell potential can also be written as

$$E_{\text{cell}}^{\ominus} = E_{\text{Red}}^{\ominus} + E_{\text{Ox}}^{\ominus}, \quad (\text{A.6})$$

where E_{Red}^{\ominus} and E_{Ox}^{\ominus} are the standard reduction potential of the reduction half-reaction and the standard oxidation potential of the oxidation half-reaction, respectively. [15, 108]

A.2 Cyclic Voltammetry (CV)

Voltammetry is an analytical electrochemical technique where information of an electrochemical system is obtained by measuring a responding current, $i(t)$, due to an applied varying electric potential, $E(t)$. In cyclic voltammetry the applied potential, is swept linearly in time in a set interval, i.e. from an initial value to a final value, $[E_{\text{min}}; E_{\text{max}}]$. When $E = E_{\text{max}}$ the sweep is reversed. During the potential sweep the resulting current is measured and plotted as a function of the potential. By analysing the trace of $i(E)$, also called a voltammogram, it is possible to obtain information about the electrochemical system such as electron transfer kinetics, diffusion, and stability of generated species. [109]

In this section some of the key equations regarding CV are derived. In Fig. A.1 a cyclic potential sweep is shown.

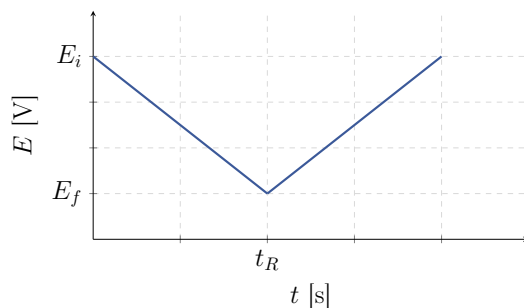


Figure A.1: Cyclic potential sweep. The sweep direction reverses at $t = t_R$.

The corresponding equations are

$$E(t) = \begin{cases} E_i - \nu t, & 0 \leq t \leq t_R \\ E_f + \nu(t - t_R), & t_R \leq t \leq 2t_R, \end{cases} \quad (\text{A.7})$$

where t_R is the time at which the sweep reverses and ν is the scan rate in units Vs^{-1} . In CV the scan rate is constant and can be determined as

$$\nu = \left| \frac{dE}{dt} \right|, \quad (\text{A.8})$$

where the absolute value is used since the slope from Fig. A.1 can be both positive and negative. Next, consider a single-electron transfer redox reaction



In the following the current voltage relation for the single-electron transfer reaction will be derived for an absorption controlled case and a diffusion controlled case. The objective of this section is to formulate the theoretical background for interpreting the experimentally obtained voltammograms for the LIB electrodes. In practical applications the current is commonly normalised to the area of the working electrode to be able to compare against literature.

Molecules Attached to Electrode

Consider the simplified case where a film of A molecules are adsorbed onto the working electrode as shown in Fig. A.2. When the potential is swept to a sufficiently low value, with respect to E^\ominus , electrons from the electrode are transferred to the A molecules which then reduces to B molecules. This can be visualised as the potential energy of electrons in the electrode is higher than that of the lowest unoccupied molecular orbital of A. The electron transfer is thus thermodynamically favorable and the energy difference is the driving force. As electrons are transferred when A is reduced a current arises. The objective of this section is to derive an equation for this current, $i(E(t))$. [109]

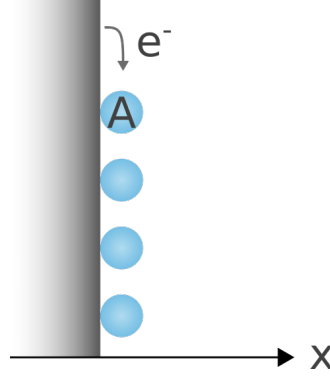


Figure A.2: Adsorption controlled case where the potential sweep from E_i to E_f causes adsorbed A molecules to undergo reduction at the working electrode. When the sweep direction reverses B molecules oxidises back to A molecules. Diffusion is in this case neglected.

If the electron transfer is fast compared to the experimental time scale the Nernst equation, Eq. (A.4), which describes the electrochemical equilibrium is assumed to hold

$$E = E^\ominus - \frac{RT}{F} \ln \left(\frac{\Gamma_B}{\Gamma_A} \right) \Rightarrow \Gamma_A = \Gamma_B \exp \left[\frac{F}{RT} (E - E^\ominus) \right], \quad (\text{A.10})$$

where the activities has been substituted by the film concentrations per unit area, Γ_A and Γ_B . The initial film concentration is the sum

$$\Gamma_0 = \Gamma_A + \Gamma_B. \quad (\text{A.11})$$

Combining Eqs. (A.10) and (A.11) gives

$$\Gamma_A = \frac{\Gamma_0}{1 + \exp \left[-\frac{F}{RT} (E - E^\ominus) \right]}, \quad \Gamma_B = \frac{\Gamma_0}{1 + \exp \left[\frac{F}{RT} (E - E^\ominus) \right]}, \quad (\text{A.12})$$

which are shown in Fig. A.3.

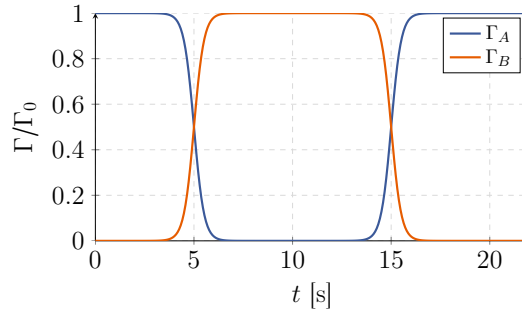


Figure A.3: The film concentration evolution in time from Eq. (A.12). The parameters used for the calculation are $E_i = 0.5$ V, $E_f = -0.5$ V, $E^\ominus = 0$ V, $T = 25^\circ\text{C}$, $\nu = 100$ mV/s, and $\Gamma_0 = 1$ mol/m².

The responding current is proportional to the change in concentration as one Faraday of charge is transferred to every mole of reactant. The current becomes

$$\frac{i}{FS} = \frac{d\Gamma_A}{dt} = -\frac{d\Gamma_B}{dt}, \quad (\text{A.13})$$

where S is the surface area of the electrode and the convention where the anodic current is positive is used i.e. conventional current flowing to the working electrode is considered positive. The time derivative can be calculated from Eq. (A.12) and yields

$$i(E) = FS\Gamma_0 \frac{F}{RT} \frac{dE}{dt} \frac{\exp\left[\frac{F}{RT}(E - E^\ominus)\right]}{\left\{1 + \exp\left[\frac{F}{RT}(E - E^\ominus)\right]\right\}^2}, \quad (\text{A.14})$$

where the derivative, dE/dt , can be obtained from Eq. (A.7), and yields $\mp\nu$ depending on if $t < t_R$ or $t > t_R$. Here $\mp\nu$ gives the cathodic and anodic current trace, respectively. In this simplified case the current peaks are both located at the standard potential $E = E^\ominus$ with equal magnitudes

$$i_{pa} = -i_{pc} = FS\Gamma_0 \frac{F\nu}{4RT}. \quad (\text{A.15})$$

It should be noted that the peak current scales linearly with the scan rate. Traces of the current as a function of time or potential are shown in Fig. A.4. The amount of charge transferred, $Q = \int idt$, is in contrast to the current not affected by the scan rate and remains constant. This can be visualised by considering either a i vs. t graph or a $dQ/dE = i/\nu$ vs. E graph, where the area under the curves are not affected by the scan-rate.

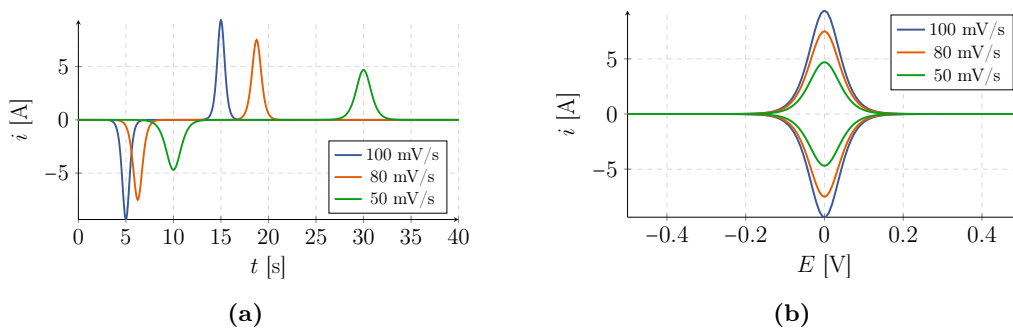


Figure A.4: Current as a function of time or potential as given in Eq. (A.14) for different scan rates. The parameters used for the calculations are $E_i = 0.5$ V, $E_f = -0.5$ V, $E^\ominus = 0$ V, $T = 25$ °C, $S = 1$ cm² and $\Gamma_0 = 0.1$ mol/m².

Freely Diffusing Molecules

If the molecules A and B are free to move in the electrolyte solution the electron transfer reaction occurring at the electrode will be influenced by mass transport. In this case the diffusion of reactants to the electrode and diffusion of products away from the electrode must be taken into account. Furthermore, diffusion is considered as the only mode of transport of the molecules in the solution thus e.g. convection and migration is neglected. The electron transfer is still considered to be fast, hence the Nernst equation is valid. The diffusion problem is considered to be one-dimensional and semi-infinite and can be described by Fick's laws of diffusion

$$\phi = -D \frac{\partial C}{\partial x}, \quad \text{Fick's 1st law} \quad \frac{\partial C}{\partial t} = D \frac{\partial^2 C}{\partial x^2}, \quad \text{Fick's 2nd law}, \quad (\text{A.16})$$

where ϕ is the diffusion flux, $C(x, t)$ is the concentration, and D is the diffusion coefficient. The objective of this section is to solve the partial differential equations to obtain the current potential relation for the case seen in Fig. A.5. This derivation is based on [109, 110], however the IUPAC sign convention is used instead of the US one.

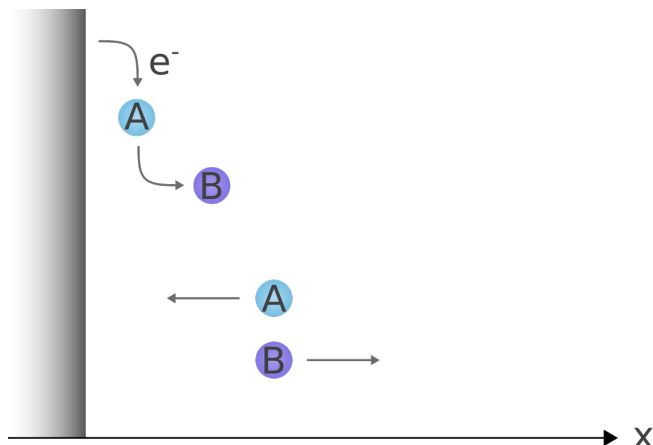


Figure A.5: Semi-infinite diffusion controlled case where during the forward sweep A molecules reduce to B at the electrode. The reaction causes a concentration gradient such that A and B molecules diffuse towards and away from the electrode, respectively.

For the diffusion problem at hand the following governing equations are obtained

$$\frac{\partial C_A}{\partial t} = D \frac{\partial^2 C_A}{\partial x^2}, \quad \frac{\partial C_B}{\partial t} = D \frac{\partial^2 C_B}{\partial x^2}, \quad (\text{A.17})$$

where it is assumed that $D_A \approx D_B$. At the electrode surface, i.e. $x = 0$, two boundary conditions are obtained. Firstly, the flux at the electrode surface is conserved due to mass conservation

$$\phi_A(x = 0, t) + \phi_B(x = 0, t) = 0 \quad \Rightarrow \quad \left. \frac{\partial C_A}{\partial x} \right|_{x=0} + \left. \frac{\partial C_B}{\partial x} \right|_{x=0} = 0, \quad (\text{A.18})$$

and secondly, the concentrations are assumed to adjust immediately as a response to an applied potential and hence the Nernst equation holds

$$C_A(x=0, t) = C_B(x=0, t) \exp\left[\frac{F}{RT} (E - E^\ominus)\right]. \quad (\text{A.19})$$

At $t = 0$ the concentration of A and B molecules are $C_A(x, t = 0) = C_0$ and $C_B(x, t = 0) = 0$, respectively. When time progresses and the potential is swept according to Eq. (A.7) the sum of the concentrations is conserved as

$$C_A(x, t) + C_B(x, t) = C_0. \quad (\text{A.20})$$

These boundary conditions are imposed to solve for the functions $C_A(x, t)$ and $C_B(x, t)$ from Eq. (A.17), which are then used to obtain information about the current

$$\frac{i}{FS} = \phi_A(x=0, t) = -D \frac{\partial C_A}{\partial x} \Big|_{x=0}, \quad (\text{A.21})$$

where again the convention that the anodic current is positive is used. The problem is simplified by introducing dimensionless parameters and functions. A dimensionless current trace can then be obtained and converted back to the real current. The following transformations are used

$$\text{Time:} \quad \tau = \frac{F\nu}{RT} t, \quad \tau_R = \frac{F}{RT} (E_i - E_f) \quad (\text{A.22})$$

$$\text{Space:} \quad y = x \sqrt{\frac{F\nu}{RTD}} \quad (\text{A.23})$$

$$\text{Potential:} \quad Z = \frac{F}{RT} (E - E^\ominus) \quad (\text{A.24})$$

$$\text{Concentration:} \quad a = \frac{C_A}{C_0}, \quad b = \frac{C_B}{C_0} \quad (\text{A.25})$$

$$\text{Current:} \quad \psi = i \left(FSC_0 \sqrt{\frac{DF\nu}{RT}} \right)^{-1}. \quad (\text{A.26})$$

$$(\text{A.27})$$

Equation Eq. (A.17) becomes

$$\frac{\partial a}{\partial \tau} = \frac{\partial^2 a}{\partial y^2}, \quad \frac{\partial b}{\partial \tau} = \frac{\partial^2 b}{\partial y^2}. \quad (\text{A.28})$$

The system of partial differential equations from Eq. (A.28) can be solved by applying the Laplace transformation, a special type of integral transform. It is defined as

$$\mathcal{L}\{f(t)\} = \int_0^\infty f(t)e^{-st} dt = \bar{f}(s), \quad (\text{A.29})$$

where \mathcal{L} is the Laplace transform operator and s is a complex number. The motivation for using \mathcal{L} is that calculus operations in real space are transformed into algebraic ones in Laplace space. The algebraic equations can be solved with respect to $\bar{f}(s)$ and afterwards the inverse Laplace transform, \mathcal{L}^{-1} , can be applied to return to the solution for a given problem in real space, $f(\tau)$. For more information about the Laplace transform we refer to [111].

Applying \mathcal{L} to both sides of Eq. (A.28) with respect to the dimensionless time component gives

$$s\bar{a} - a(y, \tau = 0) = \frac{\partial^2 \bar{a}}{\partial y^2}, \quad s\bar{b} - b(y, \tau = 0) = \frac{\partial^2 \bar{b}}{\partial y^2}. \quad (\text{A.30})$$

At the beginning of the potential sweep only A molecules are present in the solution i.e. $C_A(x, t = 0) = C_0$. This yields

$$s\bar{a} - 1 = \frac{\partial^2 \bar{a}}{\partial y^2}, \quad s\bar{b} = \frac{\partial^2 \bar{b}}{\partial y^2}, \quad (\text{A.31})$$

with solutions

$$\bar{a}(y, s) = \frac{1}{s} + C_1 \exp(\sqrt{sy}) + C_2 \exp(-\sqrt{sy}), \quad (\text{A.32})$$

$$\bar{b}(y, s) = C_3 \exp(\sqrt{sy}) + C_4 \exp(-\sqrt{sy}). \quad (\text{A.33})$$

The unknown C coefficients can be determined from the boundary conditions at $y = 0$

$$\bar{a}(y = 0, s) = \frac{1}{s} + C_1 + C_2, \quad \left. \frac{\partial \bar{a}}{\partial y} \right|_{y=0} = \sqrt{s}C_1 - \sqrt{s}C_2, \quad (\text{A.34})$$

$$\bar{b}(y = 0, s) = C_3 + C_4, \quad \left. \frac{\partial \bar{b}}{\partial y} \right|_{y=0} = \sqrt{s}C_3 - \sqrt{s}C_4. \quad (\text{A.35})$$

Solving for the C coefficients using Eq. (A.35) and inserting them into Eq. (A.33) yields

$$\bar{a} = \frac{1}{s} + \left[\bar{a}_{y=0} + \frac{1}{\sqrt{s}} \left. \frac{\partial \bar{a}}{\partial y} \right|_{y=0} - \frac{1}{s} \right] \frac{\exp(\sqrt{sy})}{2} + \left[\bar{a}_{y=0} - \frac{1}{\sqrt{s}} \left. \frac{\partial \bar{a}}{\partial y} \right|_{y=0} - \frac{1}{s} \right] \frac{\exp(-\sqrt{sy})}{2}, \quad (\text{A.36})$$

$$\bar{b} = \left[\bar{b}_{y=0} + \frac{1}{\sqrt{s}} \left. \frac{\partial \bar{b}}{\partial y} \right|_{y=0} \right] \frac{\exp(\sqrt{sy})}{2} + \left[\bar{b}_{y=0} - \frac{1}{\sqrt{s}} \left. \frac{\partial \bar{b}}{\partial y} \right|_{y=0} \right] \frac{\exp(-\sqrt{sy})}{2}, \quad (\text{A.37})$$

where $\bar{a}_{y=0} = \bar{a}(y = 0, s)$. When $y \rightarrow \infty$ the concentration must remain finite and the

square brackets in front of the $\exp(\sqrt{s}y)$ terms must therefore vanish. This gives two equations

$$\bar{a}_{y=0} = \frac{1}{s} - \frac{1}{\sqrt{s}} \left. \frac{\partial \bar{a}}{\partial y} \right|_{y=0} = \frac{1}{s} + \frac{\bar{\psi}}{\sqrt{s}}, \quad (\text{A.38})$$

and

$$\bar{b}_{y=0} = -\frac{1}{\sqrt{s}} \left. \frac{\partial \bar{b}}{\partial y} \right|_{y=0} = -\frac{\bar{\psi}}{\sqrt{s}}, \quad (\text{A.39})$$

where $\bar{\psi} = \mathcal{L}\{\psi\}$ is the Laplace transform of the dimensionless current. The inverse Laplace transform can now be employed to both sides of e.g. Eq. (A.39). Since the right-hand side of Eq. (A.39) is a product on the form $\bar{f}(s)\bar{g}(s)$ the inverse Laplace transform gives the convolution

$$b_{y=0} = -\mathcal{L}^{-1} \left\{ \frac{\bar{\psi}}{\sqrt{s}} \right\} = -\frac{1}{\sqrt{\pi}} \int_0^\tau \frac{\psi(\eta)}{\sqrt{(\tau-\eta)}} d\eta, \quad (\text{A.40})$$

where η is a dummy variable for the integration. The left-hand side of Eq. (A.40) can be determined by combining Eqs. (A.19) and (A.20) which in dimensionless form gives

$$b_{y=0} = \frac{1}{1 + \exp(Z)}. \quad (\text{A.41})$$

Inserting this into Eq. (A.40) gives

$$\frac{1}{\sqrt{\pi}} \int_0^\tau \frac{\psi(\eta)}{\sqrt{(\tau-\eta)}} d\eta = -\frac{1}{1 + \exp(Z)}. \quad (\text{A.42})$$

The expression in Eq. (A.42) relates the current to the potential at a given instance of time. It should be noted that the same expression can be obtained by taking the inverse Laplace transform of Eq. (A.38).

It can however be difficult to analytically solve for $\psi(\tau)$ from Eq. (A.42). Therefore, a numerical method is preferably employed to obtain a set of values for the current at discrete times.

Numerical solution

The objective of this method is to convert the integral on the left-hand side of Eq. (A.42) into a finite number of equations which can be solved with techniques from linear algebra. The calculation presented below is based on work by R. S. Nicholson and I. Shain [112].

The time interval where the current sought is divided into N equally spaced sub-intervals. If $\tau = [0; M]$ is divided into N steps the sub-interval spacing becomes $\delta = M/N$. A sub-interval is denoted by an integer serial number, n , such that τ takes discrete values

$$\tau = \delta n, \quad n = 0, 1, 2, \dots, N. \quad (\text{A.43})$$

The integration variable η can be substituted as

$$\eta = \delta\chi, \quad d\eta = \delta d\chi, \quad \tau - \eta = \delta(n - \chi), \quad (\text{A.44})$$

where χ is a dummy variable for the integration. Inserting this into Eq. (A.42) yields

$$\sqrt{\delta} \int_0^n \frac{\psi(\delta\chi)}{\sqrt{n-\chi}} d\chi = -\frac{\sqrt{\pi}}{1 + \exp(Z(\delta n))}, \quad (\text{A.45})$$

where the time dependent potential function, Z , is now a set of values corresponding to discrete times. The singularity at $n = \chi$ can be removed with integration by parts

$$\begin{aligned} \int_0^n \frac{\psi(\delta\chi)}{\sqrt{n-\chi}} d\chi &= \left[-2(n-\chi)^{1/2} \psi(\delta\chi) \right]_0^n \\ &\quad - \int_0^n -2(n-\chi)^{1/2} \frac{d\psi(\delta\chi)}{d\chi} d\chi. \end{aligned} \quad (\text{A.46})$$

Evaluating the right-hand side yields

$$\int_0^n \frac{\psi(\delta\chi)}{\sqrt{n-\chi}} d\chi = [2\sqrt{n}\psi(0)] + 2 \int_0^n (n-\chi)^{1/2} d(\psi(\delta\chi)). \quad (\text{A.47})$$

The integral on the right-hand side is on the form $\int_a^b f(x)dg(x)$ which is a Riemann-Stieltjes integral. It can be approximated with a finite sum as

$$2 \int_0^n (n-\chi)^{1/2} d(\psi(\delta\chi)) \simeq 2 \sum_{i=0}^{n-1} (n-i)^{1/2} [\psi_{i+1} - \psi_i], \quad (\text{A.48})$$

where the shorthand notation $\psi_i = \psi(i\delta)$ refers to the current at time $\tau_i = i\delta$. It is seen by inserting into Eq. (A.47) that for $i = 0$ the $\psi(0) = \psi_0$ term can be eliminated and this yields

$$\sqrt{\delta} \int_0^n \frac{\psi(\delta\chi)}{\sqrt{n-\chi}} d\chi \simeq 2\sqrt{\delta} \left[\sqrt{n}\psi_1 + \sum_{i=1}^{n-1} (n-i)^{1/2} [\psi_{i+1} - \psi_i] \right]. \quad (\text{A.49})$$

Combining Eq. (A.49) with Eq. (A.45) yields N algebraic equations, one for each time sub-interval

$$2\sqrt{\delta} \left[\sqrt{n}\psi_1 + \sum_{i=1}^{n-1} (n-i)^{1/2} [\psi_{i+1} - \psi_i] \right] = -\frac{\sqrt{\pi}}{1 + \exp(Z(\delta n))}. \quad (\text{A.50})$$

The system of equations can be written and solved as

$$\mathbf{A}\boldsymbol{\psi} = \mathbf{b} \quad \Rightarrow \quad \boldsymbol{\psi} = \mathbf{A}^{-1}\mathbf{b}, \quad (\text{A.51})$$

where \mathbf{A} is an $N \times N$ coefficient matrix, $\boldsymbol{\psi}$ is the $N \times 1$ unknown current vector and \mathbf{b} is an $N \times 1$ vector which includes the potential for each instance of time. Constructing the \mathbf{A} from Eq. (A.49) yields a lower triangular matrix with diagonal and determinant of unity since the equation for $n = 0$ is disregarded. The coefficient matrix is shown below

$$\mathbf{A} = \begin{bmatrix} \sqrt{1} & 0 & 0 & 0 & 0 \\ \sqrt{2} - \sqrt{1} & \sqrt{1} & 0 & 0 & 0 \\ \sqrt{3} - \sqrt{2} & \sqrt{2} - \sqrt{1} & \sqrt{1} & 0 & 0 \\ \vdots & \vdots & \vdots & \ddots & \vdots \\ \sqrt{N} - \sqrt{N-1} & \sqrt{N-1} - \sqrt{N-2} & \dots & \dots & \sqrt{1} \end{bmatrix}. \quad (\text{A.52})$$

To calculate \mathbf{b} the two expressions for $E(t)$ in Eq. (A.7) are inserted into Z . The trace can be analysed to obtain information about e.g. peak magnitude, peak position, peak-to-peak separation, and mean peak potential. Dimensionless current traces are shown in Fig. A.6. When the current is plotted as a function of potential a characteristic duck shape is seen.

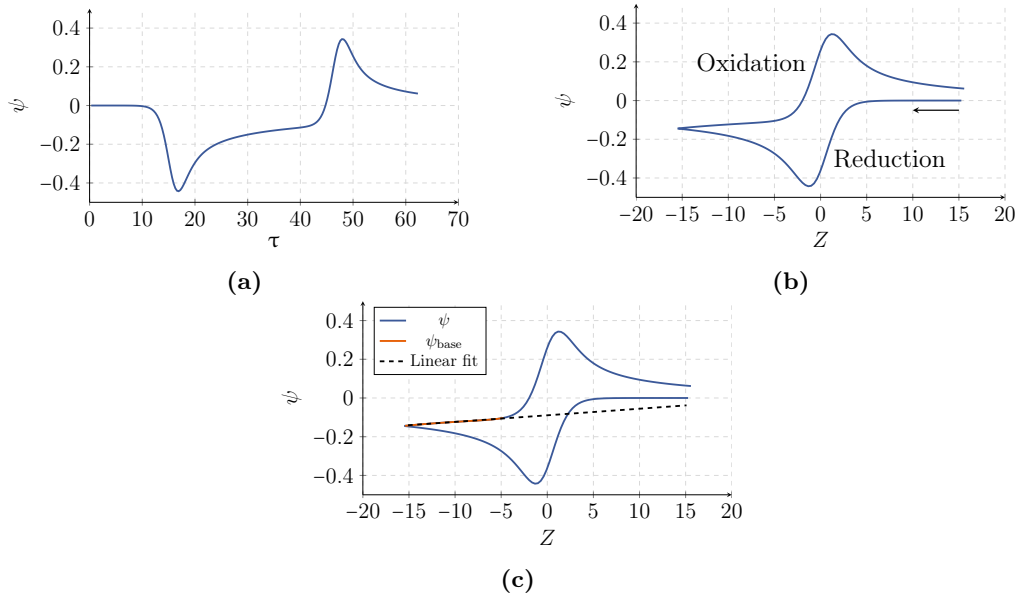


Figure A.6: Dimensionless current, ψ , as function of (a) dimensionless time and (b) dimensionless potential. In (c) a linear fit is shown which is used to determine the anodic peak magnitude and position. The fit, with $R^2 = 0.9937$, is based on the ψ_{base} region i.e. the "duck tail". The parameters used for the calculations are $E_i = 0.4$ V, $E_f = -0.4$ V, $E^\ominus = 0$ V, and $T = 25^\circ\text{C}$.

From the dimensionless trace the following characteristics are obtained

$$\psi_{pc} = -0.4463, \quad Z_{pc} = -1.110, \quad \Delta Z_p = 2.200, \quad Z_{1/2} = -0.009, \quad (\text{A.53})$$

where ψ_{pc} is the magnitude of the cathodic peak, Z_{pc} is the position of the cathodic peak, $\Delta Z_p = Z_{pa} - Z_{pc}$ is the peak-to-peak separation, and $Z_{1/2} = (Z_{pc} + Z_{pa})/2$ is the

mean peak potential. The anodic peak is obtained by using the baseline shown in Fig. A.6c and is $\psi_{pa} = -0.4321$. Therefore it can be considered that $\psi_{pa} \simeq -\psi_{pc}$ where the small deviation is suggested to stem from the accuracy of the baseline.

Converting back from the dimensionless parameters yields the characteristics of the real current

$$i_p = 0.4463FSC_0\sqrt{\frac{DF\nu}{RT}}, \quad (\text{A.54})$$

which is known as the Randles-Ševčík equation for a single-electron transfer reaction. It should be noted that $i_p \propto \sqrt{\nu}$ in contrast to the linear dependence from the adsorption controlled case in Eq. (A.14). The cathodic peak is located at

$$E_{pc} = E^\ominus - 1.110\frac{RT}{F}, \quad (\text{A.55})$$

and the peak-to-peak separation is

$$\Delta E_p = 2.200\frac{RT}{F}. \quad (\text{A.56})$$

Additionally, the mean peak potential is a good approximation of the standard potential $E_{1/2} \simeq E^\ominus$. The results can be extended to account for a multiple-electron transfer reaction as



where $z > 1$. The extension is done by substituting F by zF in the above expressions and hence the peak-to-peak separation becomes

$$\Delta E_p = 2.200\frac{RT}{zF}, \quad (\text{A.58})$$

and the peak current becomes

$$i_p = 0.4463zFSC_0\sqrt{\frac{DzF\nu}{RT}}. \quad (\text{A.59})$$

A.3 Electrochemical Impedance Spectroscopy

The electrochemical impedance of a system can be determined by applying a small alternating- voltage or current perturbation and measuring the responding current or voltage, respectively. Consider the applied monochromatic alternating voltage

$$V(t) = V_0 \sin(\omega t), \quad (\text{A.60})$$

where V_0 , ω , and t is the voltage amplitude, the angular frequency, and the time, respectively. The angular frequency is related to the ordinary frequency, f , as $\omega = 2\pi f$. Forward from this point the angular frequency will be referred to as the frequency. The resulting current for a given system will be

$$I(t) = I_0 \sin(\omega t + \phi), \quad (\text{A.61})$$

where ϕ is the phase difference between the applied voltage and the responding current. Two major components of electrical systems which will be examined in this chapter is the capacitor and the inductor. Their voltage and current relationship are given as

$$I(t) = C \cdot \frac{dV(t)}{dt}, \quad \text{Capacitor}, \quad (\text{A.62})$$

$$V(t) = L \cdot \frac{dI(t)}{dt}, \quad \text{Inductor}. \quad (\text{A.63})$$

For a complex system containing multiple components the solution to the system of differential equations becomes difficult and therefore, the expression for voltage and current are often transformed from the time- to the frequency-domain with a Fourier transformation

$$\mathcal{F}\{f(t)\} = \hat{f}(\omega) = \frac{1}{\sqrt{2\pi}} \int_{-\infty}^{\infty} f(t) e^{-j\omega t} dt. \quad (\text{A.64})$$

Applying the Fourier transform to derivatives can with integration by parts be shown to yield [111]

$$\mathcal{F}\{f'(t)\} = j\omega \hat{f}(\omega). \quad (\text{A.65})$$

Differential equations in the time-domain are hence simplified to algebraic ones in the frequency-domain. The expressions in Eqs. (A.62) and (A.63) can be transformed to give

$$\hat{I}(\omega) = jC\omega \hat{V}(\omega), \quad \text{Capacitor}, \quad (\text{A.66})$$

$$\hat{I}(\omega) = \frac{\hat{V}(\omega)}{jL\omega}, \quad \text{Inductor}. \quad (\text{A.67})$$

The analogy to resistance in the frequency-domain is impedance, Z , and due to the complex voltage and current it is, for systems involving capacitors and/or inductors,

also complex. It is related to the frequency dependent voltage and current as

$$Z(\omega) = \frac{\hat{V}(\omega)}{\hat{I}(\omega)}. \quad (\text{A.68})$$

It can be seen as an analogy to Ohm's law in the frequency-domain. The impedance of capacitors and inductors can be derived by rearranging Eqs. (A.66) and (A.67) to

$$Z_C(\omega) = \frac{1}{jC\omega}, \quad \text{Capacitor}, \quad (\text{A.69})$$

$$Z_L(\omega) = jL\omega, \quad \text{Inductor}. \quad (\text{A.70})$$

From the above equations it is possible to see that when a sinusoidal voltage is applied the resulting sinusoidal current is leading and lagging, in the capacitor and in the inductor, respectively. The phase difference is $\phi = \pi/2$ or 90° since from Euler's formula

$$j = \cos\left(\frac{\pi}{2}\right) + j \sin\left(\frac{\pi}{2}\right) = e^{j\frac{\pi}{2}}, \quad (\text{A.71})$$

and therefore Eqs. (A.69) and (A.70) can be written as

$$Z_C = \frac{1}{\omega C} e^{-j\frac{\pi}{2}}, \quad (\text{A.72})$$

$$Z_L = \omega L e^{j\frac{\pi}{2}}. \quad (\text{A.73})$$

For purely resistive behavior the phase difference is zero and the impedance for a resistor is therefore given as

$$Z_R = R, \quad (\text{A.74})$$

where R is its resistance. [113]

Equivalent Electrical Circuit Model of Electrochemical Systems

When an electrochemical system is subject to an applied alternating voltage the responding current depends on the physical and chemical properties of the electrodes and electrolyte such as interfaces, chemical processes, microstructures, etc. It may however be difficult to analyse and interpret the voltage and current relation to get information about said properties and hence it is often helpful to create an equivalent electrical circuit (EEC) model. The EEC is supposed to be a circuit consisting of resistors, capacitors, and inductors which mimics the impedance behavior of the examined electrochemical system over a range of frequencies.

The following derivations are based on work from M. E. Orazem and B. Tribollet [114–116]. If additional sources have been used they will be cited appropriately.

Potential Dependent Electrochemical Reactions

Consider the following case where a metal dissolves in an aqueous medium and the reaction only depends on the applied alternating potential. The reaction scheme may

be written as



The faradic current density arising from this reaction may be expressed as a function of the interface potential, V , which is the potential across the interface of the working electrode and the adjacent electrolyte as

$$i_f = f(V). \quad (\text{A.76})$$

Since the applied potential varies with time, the faradic current will do so too and hence it may be written as the sum of two terms

$$i_f = \bar{i}_f + \text{Re}\{\tilde{i}_f e^{j\omega t}\}, \quad (\text{A.77})$$

where the bar denotes the constant faradic current density and the tilde denotes the oscillating part. The current density, i_f , may be written as a Taylor expansion about the constant current density as

$$i_f(V) = i_f(\bar{V}) + \left. \frac{\partial i_f}{\partial V} \right|_{V=\bar{V}} (V - \bar{V}). \quad (\text{A.78})$$

The alternating potential can be written as

$$V = \bar{V} + \text{Re}\{\tilde{V} e^{j\omega t}\}. \quad (\text{A.79})$$

Inserting Eq. (A.79) into Eq. (A.78) and equating with Eq. (A.77) yields

$$\bar{i}_f + \text{Re}\{\tilde{i}_f e^{j\omega t}\} = i_f(\bar{V}) + \left. \frac{\partial i_f}{\partial V} \right|_{V=\bar{V}} \text{Re}\{\tilde{V} e^{j\omega t}\}, \quad (\text{A.80})$$

where the oscillating terms must be equal to satisfy the equation for all times. Thus the oscillating faradic current can be written as

$$\tilde{i}_f = \left. \frac{\partial i_f}{\partial V} \right|_{V=\bar{V}} \tilde{V}, \quad (\text{A.81})$$

where the higher order terms in the Taylor series have been neglected since the magnitude of the oscillating potential, \tilde{V} , is assumed to be small.

The current response to the interface potential is given by the Butler-Volmer equation

$$i = i_0 \left[\exp\left(\frac{(1-\alpha)nF}{RT}\eta\right) - \exp\left(-\frac{\alpha nF}{RT}\eta\right) \right], \quad (\text{A.82})$$

where i_0 is the exchange current density, α is the symmetry factor, and η is the overpotential. The overpotential is given as $\eta = V - V_0$, where V_0 is the equilibrium

interface potential. For the sake of simplicity the following constants are defined

$$b_a = \frac{(1 - \alpha)nF}{RT}, \quad b_c = \frac{\alpha nF}{RT}, \quad (\text{A.83})$$

where the a and c subscripts denote anodic and cathodic, respectively. It can be seen from Eq. (A.82) that for high overpotentials

$$i \simeq i_0 e^{b_a \eta}, \quad (\text{A.84})$$

and for low overpotentials

$$i \simeq -i_0 e^{-b_c \eta}. \quad (\text{A.85})$$

The constant faradic current associated with the reaction in Eq. (A.75) can be expressed as

$$i_f = nFk e^{b\eta}, \quad (\text{A.86})$$

where $i_0 = nFk$ has been inserted with k being the reaction rate, and $b = b_a$. It is convenient to collect the constants into one as

$$i_f = nFk e^{b(V-V_0)} = K e^{bV}. \quad (\text{A.87})$$

It is now possible to determine the oscillating component of the current from Eq. (A.81) by letting $f = K \exp(bV)$

$$\tilde{i}_f = K e^{b\bar{V}} b \tilde{V}. \quad (\text{A.88})$$

It is possible to define a resistance associated with the transfer of the charge occurring in Eq. (A.75) as

$$\tilde{i}_f = \frac{\tilde{V}}{R_{ct}}, \quad (\text{A.89})$$

where $R_{ct} = [K \exp(b\bar{V})b]^{-1}$. It can be seen that the charge-transfer resistance is a function of the constant/steady-state potential, \bar{V} .

The applied potential will result in a current which can be written as the sum of two contributions. The first one is the faradic current from the reaction and the second contribution comes from the electrical double layer located at the interface. The total current may be written as

$$i = i_f + C_{dl} \frac{dV}{dt}, \quad (\text{A.90})$$

where i is the current density, i_f is the faradic current, C_{dl} is the capacity of the electrical double layer, and V is the potential applied across the electrode and the electrolyte. The current from Eq. (A.90) can also be divided into a constant- and an alternating term. The alternating current can be rewritten by inserting Eq. (A.79) as

$$\tilde{i} = \tilde{i}_f + j\omega C_{dl} \tilde{V}. \quad (\text{A.91})$$

The total voltage drop, U , from the metal electrode to the reference electrode is the

sum of the voltage drop across the electrode-electrolyte interface and the drop through the electrolyte to the reference electrode as

$$U = V + iR_e, \quad (\text{A.92})$$

where R_e is the resistance of the electrolyte. The total voltage drop can be divided into a constant and an alternating part. The alternating part is given as

$$\tilde{U} = \tilde{V} + \tilde{i}R_e. \quad (\text{A.93})$$

Inserting Eq. (A.89) into Eq. (A.91) yields

$$\tilde{i} = \tilde{V} \left(\frac{1}{R_{ct}} + j\omega C_{dl} \right). \quad (\text{A.94})$$

The impedance can now be derived by inserting Eqs. (A.93) and (A.94) into Eq. (A.68)

$$Z = \frac{\tilde{U}}{\tilde{i}} \quad (\text{A.95})$$

$$= R_e + \frac{\tilde{V}}{\tilde{i}} \quad (\text{A.96})$$

$$= R_e + \frac{R_{ct}}{1 + j\omega R_{ct} C_{dl}}. \quad (\text{A.97})$$

The expression for the impedance can be split into a real and an imaginary part by expanding with the complex conjugate of the denominator as

$$Z = R_e + \frac{R_{ct}}{1 + j\omega R_{ct} C_{dl}} \cdot \frac{1 - j\omega R_{ct} C_{dl}}{1 - j\omega R_{ct} C_{dl}} \quad (\text{A.98})$$

$$= R_e + \frac{R_{ct}}{1 + \omega^2 R_{ct}^2 C_{dl}^2} - j \frac{R_{ct}^2 \omega C_{dl}}{1 + \omega^2 R_{ct}^2 C_{dl}^2}, \quad (\text{A.99})$$

where

$$Z_{\text{Re}} = \text{Re}\{Z\} = R_e + \frac{R_{ct}}{1 + \omega^2 R_{ct}^2 C_{dl}^2}, \quad (\text{A.100})$$

$$Z_{\text{Im}} = \text{Im}\{Z\} = -\frac{R_{ct}^2 \omega C_{dl}}{1 + \omega^2 R_{ct}^2 C_{dl}^2}. \quad (\text{A.101})$$

The circuit shown in Fig. A.7a has the same impedance behavior as given by Eq. (A.99) and is therefore an equivalent electrical circuit. The equivalency can be proven by considering the impedance for the circuit which is made up of a resistor, R_1 , that is connected in series to a parallel configuration of a resistor, R_2 , and a capacitor, C , as

$$Z = R_1 + \left(\frac{1}{R_2} + \frac{1}{Z_C} \right)^{-1}, \quad (\text{A.102})$$

where Z_C is the impedance of the capacitor. Rearranging this equation yields

$$Z = R_1 + \frac{R_2 Z_C}{Z_C + R_2}. \quad (\text{A.103})$$

Inserting the expression for the impedance for a capacitor from Eq. (A.69) yields

$$Z = R_1 + \frac{1}{\left(\frac{1}{j\omega C}\right) + R_t} \cdot \frac{R_2}{j\omega C}, \quad (\text{A.104})$$

which can be rearranged to

$$Z = R_1 + \frac{R_2}{1 + j\omega R_2 C}. \quad (\text{A.105})$$

The above expression is equivalent to Eq. (A.97) when $R_1 = R_e$, $R_2 = R_{ct}$, and $C = C_{dl}$.

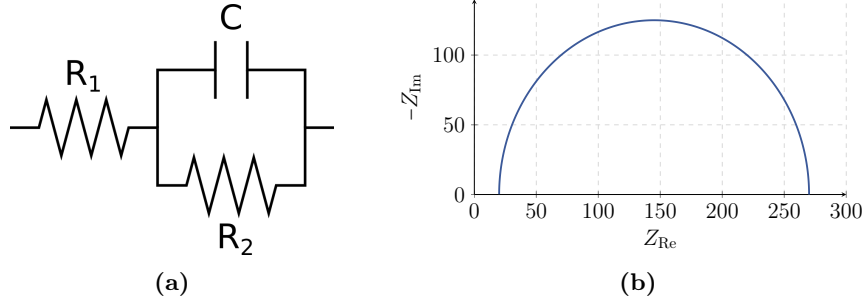


Figure A.7: A simple Randles circuit. **(a)** An equivalent electrical circuit model of a metal dissolving in an aqueous medium where the reaction is only dependent on the applied alternating potential. **(b)** Nyquist plot of Eq. (A.99) which is described by the EEC model seen in Fig. A.7a. The parameters used are $R_e = 20 \Omega$, $R_{ct} = 250 \Omega$, $C_{dl} = 40 \times 10^{-6} \text{ F cm}^{-2}$, and $\omega \in [1 \text{ mHz}; 100 \text{ kHz}]$.

The impedance behavior can be analysed in different ways. One of them is to make a Nyquist plot, as seen in Fig. A.7b, where the negative imaginary part of the impedance is plotted versus the real part of the impedance. In the Nyquist plot the low values of Z_{Re} corresponds to high frequencies and vice versa.

Information about the resistances R_e and R_{ct} , and the capacitance C_{dl} can be determined by examining the half-circle seen in the Nyquist plot in Fig. A.7b. From Eq. (A.99) it can be seen that when

$$\omega \rightarrow \infty : \quad Z_{Re} \rightarrow R_e, \quad Z_{Im} \rightarrow 0, \quad (\text{A.106})$$

and when

$$\omega \rightarrow 0 : \quad Z_{Re} \rightarrow R_e + R_{ct}, \quad Z_{Im} \rightarrow 0. \quad (\text{A.107})$$

The frequency at which $-Z_{Im}$ is at maximum reveals information about C_{dl} . This can be seen by taking the derivative of Eq. (A.101) with respect to the frequency and setting it to zero as

$$\frac{dZ_{Im}}{d\omega} = 0. \quad (\text{A.108})$$

Since the frequency is present in both the numerator and denominator in Eq. (A.101) the derivative can be evaluated by using the product rule as

$$-\frac{dZ_{\text{Im}}}{d\omega} = 0 = R_{ct}^2 \omega C_{dl} \cdot \frac{d}{d\omega} \left(\frac{1}{1 + \omega^2 R_{ct}^2 C_{dl}^2} \right) + \frac{1}{1 + \omega^2 R_{ct}^2 C_{dl}^2} \cdot \frac{d}{d\omega} (R_{ct}^2 \omega C_{dl}), \quad (\text{A.109})$$

Evaluating the two derivatives yields

$$0 = -\frac{2\omega R_{ct}^2 C_{dl}^2}{(1 + \omega^2 R_{ct}^2 C_{dl}^2)^2} + \frac{R_{ct}^2 C_{dl}}{1 + \omega^2 R_{ct}^2 C_{dl}^2}. \quad (\text{A.110})$$

Making a common denominator gives

$$0 = \frac{R_{ct}^2 C_{dl} + \omega^2 R_{ct}^4 C_{dl}^3 - 2\omega^2 R_{ct}^4 C_{dl}^3}{(1 + \omega^2 R_{ct}^2 C_{dl}^2)^2}, \quad (\text{A.111})$$

where it can be seen that if the expression equals zero the numerator must equal zero and hence

$$R_{ct}^2 C_{dl} + \omega^2 R_{ct}^4 C_{dl}^3 = 2\omega^2 R_{ct}^4 C_{dl}^3, \quad (\text{A.112})$$

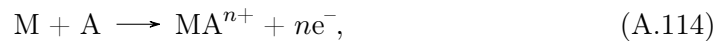
which is true if

$$\omega^2 = \frac{1}{R_{ct}^2 C_{dl}^2}. \quad (\text{A.113})$$

The frequency at which $-Z_{\text{Im}}$ is at maximum is related to the charge-transfer resistance, R_{ct} , and the double layer capacitance, C_{dl} .

Reaction Dependent on Potential and Diffusion

Many electrochemical reactions does not only depend on the applied potential but also on the transport of reactants to the surface of the electrode. The reaction scheme may be written as



where M is the electrode which reacts with a species A. The faradic current for this reaction can be written as a function of the interface potential, V , and the concentration of species A at the electrode surface, c_0 , as

$$i_f = f(V, c_0). \quad (\text{A.115})$$

Similar to the previous case, a steady-state current can be determined as

$$\bar{i}_f = K \bar{c}_0 e^{b\bar{V}}, \quad (\text{A.116})$$

which is a function both of the concentration of species A at the electrode surface, and of the steady-state interface potential. The oscillating faradic current density may, similar to the previous case, be written as a Taylor expansion around the steady-state

value

$$\tilde{i}_f = \left(\frac{\partial f}{\partial V} \right)_{c_0} \Big|_{V=\tilde{V}} \tilde{V} + \left(\frac{\partial f}{\partial c_0} \right)_{V} \Big|_{c_0=\tilde{c}_0} \tilde{c}_0, \quad (\text{A.117})$$

where the higher order terms have been neglected. Inserting the steady-state current from Eq. (A.116) into the expression above yields

$$\tilde{i}_f = Kb\tilde{c}_0 e^{b\tilde{V}} \tilde{V} + Ke^{b\tilde{V}} \tilde{c}_0. \quad (\text{A.118})$$

In order to express the oscillating current density as a function of the interface potential a second expression is necessary. The steady-state current can be written in terms of the change in the concentration of species A at the electrode surface as in Fick's first law

$$\bar{i}_f = -nFD \frac{d\bar{c}}{dx} \Big|_{x=0}, \quad (\text{A.119})$$

and likewise for the oscillating component

$$\tilde{i}_f = -nFD \frac{d\tilde{c}}{dx} \Big|_{x=0}. \quad (\text{A.120})$$

It is now possible to insert Eq. (A.118) into the expression above. The procedure is however simplified by introducing the following dimensionless parameters

$$\xi = \frac{x}{\delta}, \quad \tilde{\theta} = \frac{\tilde{c}}{\tilde{c}_0}, \quad (\text{A.121})$$

where δ is the thickness of the diffusion layer. Inserting these parameters into Eq. (A.120) yields

$$\tilde{i}_f = -nFD \frac{\tilde{c}_0}{\delta} \frac{\partial \tilde{\theta}}{\partial \xi} \Big|_{\xi=0}. \quad (\text{A.122})$$

From Eq. (A.118), \tilde{c}_0 is isolated and inserted into Eq. (A.122) which yields

$$\tilde{i}_f = \frac{\tilde{V}}{R_{ct} + Z_D}, \quad (\text{A.123})$$

where R_{ct} is the charge-transfer resistance and Z_D is the diffusion impedance. These two contributions are given as

$$R_{ct} = [Kb\tilde{c}_0 e^{b\tilde{V}}]^{-1}, \quad (\text{A.124})$$

and

$$Z_D = \frac{\delta}{nFD\tilde{\theta}'(0)b\tilde{c}_0}, \quad (\text{A.125})$$

where $\tilde{\theta}'(0)$ is the derivative of $\tilde{\theta}$ w.r.t. ξ and evaluated at $x = 0$. An expression describing the impedance behavior of the electrochemical system can now be determined

by considering Eqs. (A.91), (A.93) and (A.123)

$$Z(\omega) = \frac{\tilde{U}}{\tilde{i}} \quad (\text{A.126})$$

$$= R_e + \frac{\tilde{V}}{\tilde{i}} \quad (\text{A.127})$$

$$= R_e + \frac{R_{ct} + Z_D}{1 + j\omega C_{dl}(R_{ct} + Z_D)}, \quad (\text{A.128})$$

where it should be noted that the diffusion impedance, Z_D , is a function of the frequency, ω , due to $\tilde{\theta}$. An EEC model for this electrochemical system is seen in Fig. A.8a. This circuit is known as a Randles circuit. The total impedance of the circuit can be written as

$$Z(\omega) = R_1 + \left(\frac{1}{Z_C} + \frac{1}{R_2 + Z_W} \right)^{-1} \quad (\text{A.129})$$

$$= R_1 + \frac{Z_C(R_2 + Z_W)}{R_2 + Z_W + Z_C}. \quad (\text{A.130})$$

Inserting the expression for the impedance of a capacitor from Eq. (A.69) yields

$$Z = R_1 + \frac{R_2 + Z_W}{1 + j\omega C(R_2 + Z_W)}. \quad (\text{A.131})$$

This expression is equivalent to Eq. (A.128) where $R_1 = R_e$, $R_2 = R_{ct}$, and $Z_W = Z_D$. The Nyquist plot for the Randles circuit is seen in Fig. A.8b

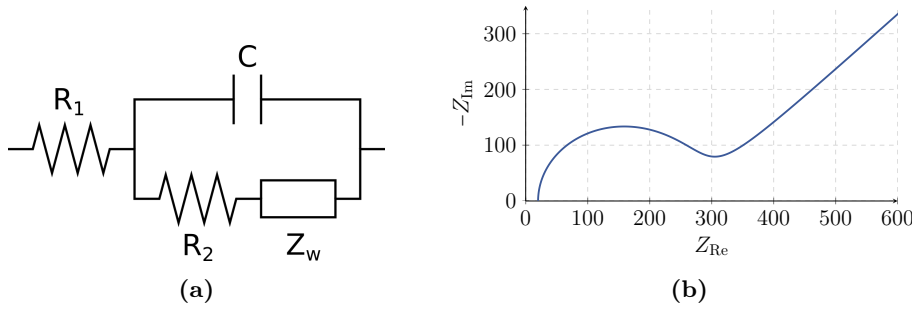


Figure A.8: A Randles circuit (a) An EEC model of a metal dissolving in an aqueous medium where the reaction depends on the applied alternating potential and diffusion. (b) Nyquist plot of Eq. (A.128) which is described by the EEC model seen in Fig. A.8a. The parameters used are $R_e = 20 \Omega$, $R_{ct} = 250 \Omega$, $C_{dl} = 40 \times 10^{-6} \text{ F cm}^{-2}$, $\sigma = 150$, and $\omega \in [1 \text{ mHz}; 100 \text{ kHz}]$.

The diffusion process is often modelled with a Warburg element. The impedance associated with this element is denoted, Z_W , and depends on the properties of the electrode. For a planar electrode where diffusion only occur in one dimension the expression reads

$$Z_W = \frac{\sigma}{\sqrt{\omega}} - j \frac{\sigma}{\sqrt{\omega}}, \quad (\text{A.132})$$

where σ is the Warburg coefficient. This expression along with σ as seen in Eq. (A.133),

can be derived by considering the reaction $O + ne^- \rightleftharpoons Re$ where the potential at the electrode is a function of both the current and the concentration of the oxidised and reduced species. This will lead to an equation, $\partial V/\partial t$ in where the time derivative of the current, $\partial i/\partial t$, and the concentrations, $\partial C/\partial t$, have to be determined. The latter is determined by solving Fick's 2nd law, $\partial C/\partial t = \partial^2 C/\partial x^2$ where C is found to oscillate with the frequency, ω . The impedance is then found to be $Z(\omega) = R_{ct} + \sigma\omega^{-1/2} - j\sigma\omega^{-1/2} = R_{ct} + Z_W$. [117]

If Eq. (A.132) was graphed in a Nyquist plot it would be a straight line with a constant phase of 45° . The Warburg coefficient for a simple redox reaction $O + ne^- \rightleftharpoons Re$ is given by

$$\sigma = \frac{RT}{\sqrt{2}n^2F^2A} \left(\frac{1}{\sqrt{D_O}c_{O,\infty}} - \frac{1}{\sqrt{D_{Re}}c_{Re,\infty}} \right), \quad (\text{A.133})$$

where A is the surface area of the electrode, D_O and D_{Re} are the diffusion coefficients for the oxidised and reduced species, respectively, and $c_{O,\infty}$ and $c_{Re,\infty}$ are the bulk concentrations of the oxidised and reduced species, respectively. [117]

Ambiguity in EEC Models

Different electrical circuits can have equivalent frequency responses. It is therefore possible to construct two different EEC models which describe the measurement equally well. Hence the EEC model should also describe the physical structure and chemical processes of the electrochemical system. An example of two circuits having equivalent frequency responses is shown in Fig. A.9.

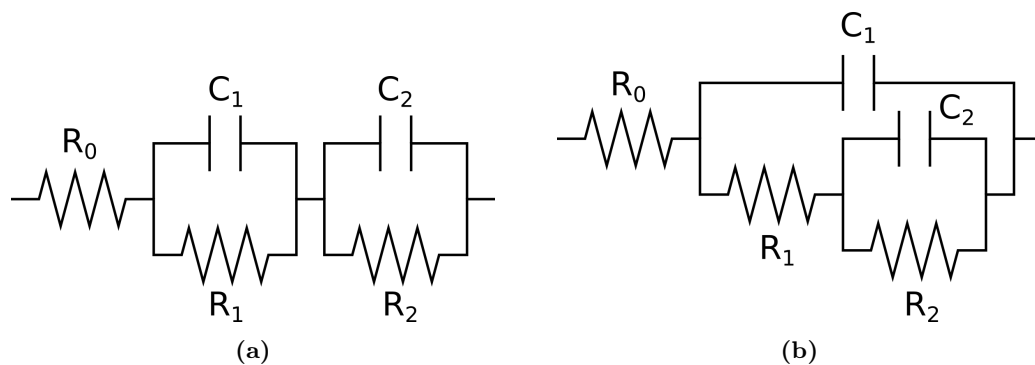


Figure A.9: Mathematical equivalent electrical circuits. (a) EEC for an electrode with two resistive layers. (b) EEC for a coated electrode.

The impedance behavior of the circuit in Fig. A.9a is given by

$$Z(\omega) = R_0 + \left(\frac{1}{Z_{C_1}} + \frac{1}{R_1} \right)^{-1} + \left(\frac{1}{Z_{C_2}} + \frac{1}{R_2} \right)^{-1}, \quad (\text{A.134})$$

where Z_{C_1} and Z_{C_2} are the impedance of the capacitors C_1 and C_2 , respectively. The expression can be rewritten to

$$Z(\omega) = R_0 + \frac{R_1}{1 + j\omega R_1 C_1} + \frac{R_2}{1 + j\omega R_2 C_2}. \quad (\text{A.135})$$

The impedance behavior of the circuit in Fig. A.9b may be written in a similar manner as

$$Z(\omega) = R_0 + \frac{R_1}{1 + j\omega C_1(R_1 + Z_2)} + \frac{Z_2}{1 + j\omega C_1(R_1 + Z_2)}, \quad (\text{A.136})$$

where

$$Z_2 = \frac{R_2}{1 + j\omega C_2 R_2}. \quad (\text{A.137})$$

The circuit depicted in Fig. A.9a is used to model an electrode with two layers each with a different resistance. The circuit in Fig. A.9b describes a coated electrode where the coating gives rise to an additional resistance and capacitance. The impedance behavior of the circuits in Fig. A.9 is shown in Fig. A.10. The curves of Eqs. (A.135) and (A.136) starts and ends in the same value which is at $Z_{\text{Re}} = R_0$ and $Z_{\text{Re}} = R_0 + R_1 + R_2$, respectively. Furthermore the maximum is located at $Z_{\text{Re}} = R_0 + (R_1 + R_2)/2$ for both curves.

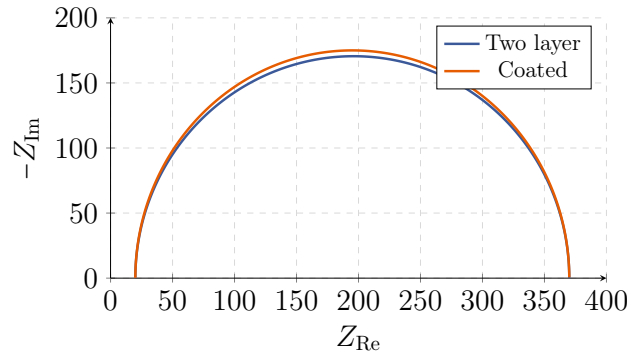


Figure A.10: Nyquist plot of Eqs. (A.135) and (A.136) where the former is for an electrode with two resistive layers, and the latter is for a coated electrode. The parameters used are $R_0 = 20 \Omega$, $R_1 = 250 \Omega$, $R_2 = 250 \Omega$, $C_1 = 40 \times 10^{-6} \text{ F cm}^{-2}$, $C_2 = 60 \times 10^{-6} \text{ F cm}^{-2}$, and $\omega \in [1 \text{ mHz}; 100 \text{ kHz}]$.

It is apparent that in order to correctly interpret the EIS measurements the EEC model should account for both the impedance behavior, and the physical and chemical properties of the electrochemical system.

EEC Model for Li-ion Battery Electrodes

Most real electrodes are not uniformly active and hence they exhibit a dispersion of the potential or the reactivity. The impedance response for such a system is seen as a depressed semicircle, i.e. the center of the circle is below $Z_{\text{Im}} = 0$, in the Nyquist plot. In the EEC model this behavior is accounted for with a constant phase element

(CPE) which impedance is given by the general formula

$$Z(\omega) = \frac{1}{Q(j\omega)^n}, \quad (\text{A.138})$$

where $n \in [0; 1]$. When $n = 1$, Eq. (A.138) reduces to the expression for a capacitor where $Q = C$ represents its capacity. When $n = 0$, the expression becomes that of a resistor where $Q = 1/R$. The expression in Eq. (A.138) can be rewritten as

$$Z(\omega) = \frac{1}{Q\omega^n} e^{-j\frac{\pi}{2}n}, \quad (\text{A.139})$$

where it is seen that the phase is $-90^\circ \cdot n$ and independent of the frequency. [118]

Consider an EEC model similar to the simple Randles circuit seen in Fig. A.7a but instead of a capacitor, the general CPE is used. The impedance for the EEC model seen in Fig. A.11b is given by

$$Z(\omega) = R_1 + \frac{R_2}{1 + (j\omega)^n R_2 Q}. \quad (\text{A.140})$$

The Nyquist plot for this expression is seen in Fig. A.11b with $n = 0.6$.

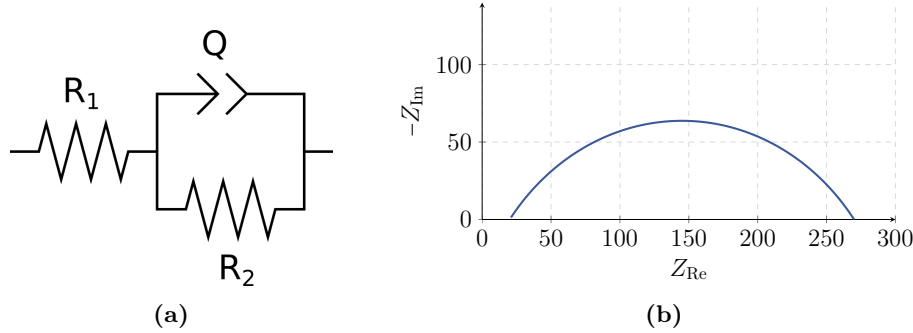


Figure A.11: The simple Randles circuit with a general CPE denoted by Q . (a) A schematic of the equivalent electrical circuit model and (b) corresponding Nyquist plot. The parameters used are $R_e = 20 \Omega$, $R_{ct} = 250 \Omega$, $Q = 40 \times 10^{-6} \text{ S s}^n$, $n = 0.6$, and $\omega \in [1 \text{ mHz}; 10 \text{ MHz}]$.

The depressed semicircle feature is clearly seen in Fig. A.11b. The arc starts in $Z_{\text{Re}} = R_1$ and ends in $Z_{\text{Re}} = R_1 + R_2/2$.

Transmission Line Model for Porous Electrodes

So far all the electrodes considered have been assumed to be planar. This is however not the case for the real LiFePO_4 cathode and graphite anode since these electrodes are made up of layers of particles and hence the electrodes have a porous structure. The impedance behavior of a porous electrode may be described by a transmission line model (TLM). The motivation for adopting the TLM is that the resistance associated with transporting lithium cations into the pores is related to the length of the pore. Furthermore, the impedance contributions stemming from the interface capacitance,

charge transfer, diffusion, and the electrical resistance of the carbon coating, is also dependent on the pore length. The main difference between the TLM and the previous EEC models, is that the elements in the TLM is thought of as being dispersed throughout the circuit and not localised. [93, 119]

The EEC models for the cathode and anode is based on work done by Scipioni et al. [93] and the derivation is based on work by U. Tröltzsch and O. Kanoun [119] and Bisquert et al. [120]. The EEC model of the cathode is comprised of an inductor to account for the wiring, a resistor in parallel with a constant phase element which models the impedance response of the aluminium current collector, a resistor which is associated with the electrolyte, and a transmission line which is seen in Fig. A.12a. The ζ_{cat} element describes the diffusion, interface capacity, and the charge transfer contributions. It is modelled as a Randles circuit and can be seen in Fig. A.12b.

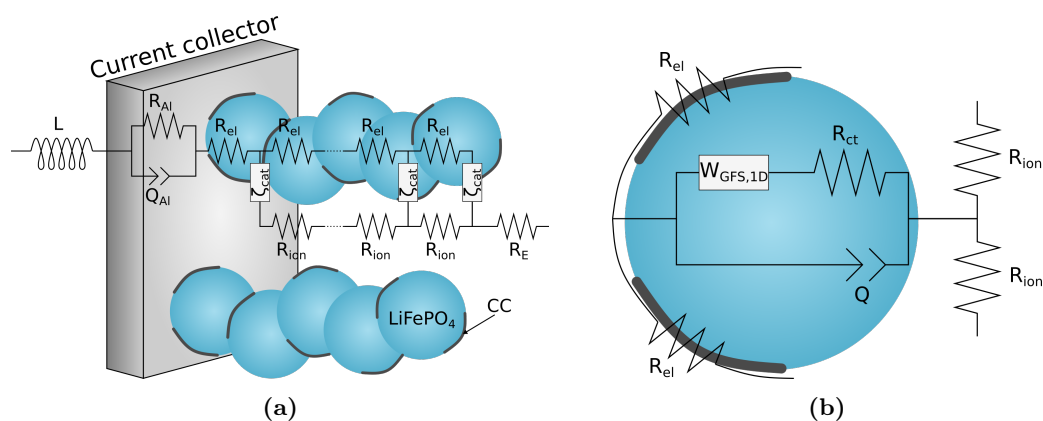


Figure A.12: An overview of the EEC model for the LiFePO_4 cathode. (a) Generalised transmission line model of the cathode. (b) Detailed view of the ζ_{cat} element, a Randles circuit used to describe de-/intercalation of Li^+ and the electrode-electrolyte interface. The diffusion process is modelled with a 1D general finite space Warburg element. The figures are inspired by [93].

In order to derive an expression for the impedance the circuit in Fig. A.13 is examined.

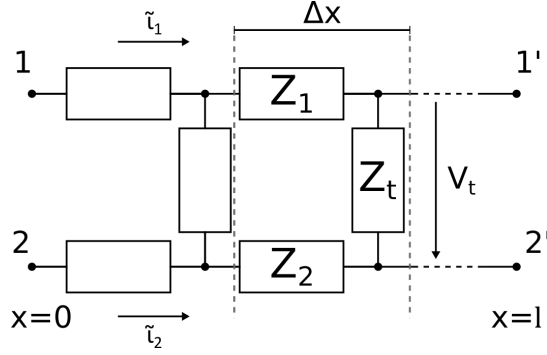


Figure A.13: Transmission line circuit where the two longitudinal lines, 1 and 2, are interconnected by the transverse line. There is a voltage drop, V_t , across the transverse line. The ionic current \tilde{i}_{ion} , and the electronic current, \tilde{i}_{el} , flows from the start, $x = 0$, to the end, $x = l$, between the terminals 1 and 1', and 2 and 2', respectively. A small section Δx is highlighted where three impedance elements, Z_1 , Z_2 , and Z_t are present. Schematic is inspired by [119].

Using Kirchoff's circuit laws on the nodes and loops in Fig. A.13 the following expressions are derived

$$\tilde{i}_{\text{ion}}(x) = \tilde{i}_{\text{ion}}(x + \Delta x) + \frac{1}{Z_t} \tilde{V}_t \Delta x, \quad (\text{A.141})$$

$$\tilde{i}_{\text{el}}(x) = \tilde{i}_{\text{el}}(x + \Delta x) - \frac{1}{Z_t} \tilde{V}_t \Delta x, \quad (\text{A.142})$$

$$\tilde{V}_t(x) + \tilde{i}_{\text{el}}(x) Z_2 \Delta x - \tilde{V}_t(x + \Delta x) - \tilde{i}_{\text{ion}}(x) Z_1 \Delta x = 0, \quad (\text{A.143})$$

where the tilde notation signifies the oscillating component. The currents \tilde{i}_{ion} , and \tilde{i}_{el} are the ionic current, and the electronic current, respectively. The potential and the currents are functions of both position and time e.g. $\tilde{i}_{\text{ion}}(x, t) = \tilde{i}_{\text{ion}}(x) \exp(j\omega t)$. By considering $\Delta x \rightarrow 0$ the equations above become

$$\frac{d\tilde{i}_{\text{ion}}(x)}{dx} = -\frac{1}{Z_t} \tilde{V}_t, \quad (\text{A.144})$$

$$\frac{d\tilde{i}_{\text{el}}(x)}{dx} = \frac{1}{Z_t} \tilde{V}_t, \quad (\text{A.145})$$

$$\frac{d\tilde{V}_t(x)}{dx} = \tilde{i}_{\text{el}}(x) Z_2 - \tilde{i}_{\text{ion}}(x) Z_1. \quad (\text{A.146})$$

This system of ordinary differential equations may be solved to yield

$$\tilde{i}_{\text{ion}}(x) = C_1 \frac{Z_2}{Z_1} + \frac{C_2 e^{-\gamma x} - C_3 e^{\gamma x}}{Z_t \gamma}, \quad (\text{A.147})$$

$$\tilde{i}_{\text{el}}(x) = C_1 - \gamma \frac{C_2 e^{-\gamma x} - C_3 e^{\gamma x}}{Z_1 + Z_2}, \quad (\text{A.148})$$

$$\tilde{V}_t(x) = C_2 e^{-\gamma x} + C_3 e^{\gamma x}, \quad (\text{A.149})$$

where $\gamma^2 = (Z_1 + Z_2)/Z_t$, and C_1 , C_2 , and C_3 , are integration constants. It has been assumed that the impedance contributions from the elements do not vary spatially.

The constants, C_1 , C_2 , and C_3 , can be found by applying the following boundary conditions

$$\tilde{i}_{\text{ion}}(0) = \tilde{i}_0, \quad \Rightarrow \quad \tilde{i}_0 = C_1 \frac{Z_2}{Z_1} + \frac{C_2 - C_3}{Z_2 \gamma}, \quad (\text{A.150})$$

$$\tilde{i}_{\text{el}}(0) = 0, \quad \Rightarrow \quad 0 = C_1 - \gamma \frac{C_2 - C_3}{Z_1 + Z_2}, \quad (\text{A.151})$$

$$\tilde{i}_{\text{el}}(l) = \tilde{i}_0, \quad \Rightarrow \quad \tilde{i}_0 = C_1 - \gamma \frac{C_2 e^{-\gamma l} - C_3 e^{\gamma l}}{Z_1 + Z_2}. \quad (\text{A.152})$$

The boundary condition in Eq. (A.150) states that at $x = 0$, the total current flowing through the cell is equal to \tilde{i}_{ion} and thus $\tilde{i}_{\text{el}}(0) = 0$ since $\tilde{i}_0 = \tilde{i}_{\text{ion}} + \tilde{i}_{\text{el}}$. At the current collector, $x = l$, the ionic current, \tilde{i}_{ion} , vanishes and thus $\tilde{i}_{\text{el}}(l) = \tilde{i}_0$.

The constants, C_1 , C_2 , and C_3 , are determined from Eqs. (A.150) to (A.152)

$$C_1 = \frac{\tilde{i}_0 Z}{Z_1 + Z_2}, \quad (\text{A.153})$$

$$C_2 = \tilde{i}_0 \frac{e^{\gamma l} (Z_2 + Z_1 e^{\gamma l})}{(e^{2\gamma l} - 1) \gamma}, \quad (\text{A.154})$$

$$C_3 = \tilde{i}_0 \frac{Z_1 + Z_2 e^{\gamma l}}{(e^{2\gamma l} - 1) \gamma}. \quad (\text{A.155})$$

The impedance can now be determined as the ratio of the voltage between the terminals 1 and 2' seen in Fig. A.13 and the total current, \tilde{i}_0 , as

$$Z = \frac{1}{\tilde{i}_0} \left(\tilde{V}_t(0) + Z_2 \int_{x=0}^l \tilde{i}_2(x) dx \right). \quad (\text{A.156})$$

Inserting Eq. (A.148) and $V_t(0)$ from Eq. (A.149) and performing the integration yields

$$Z = \frac{1}{\tilde{i}_0} \left(C_2 + C_3 + Z_2 \left[C_1 l + \frac{1}{Z_1 + Z_2} (C_2 e^{-\gamma l} + C_3 e^{\gamma l} - C_2 - C_3) \right] \right). \quad (\text{A.157})$$

The constants from Eqs. (A.153) to (A.155) are now inserted

$$Z = \frac{l}{\left(\frac{1}{Z_1} + \frac{1}{Z_2} \right)} + \frac{4Z_1 Z_2 e^{\gamma l} + Z_1^2 e^{2\gamma l} + Z_1^2 + Z_2^2 e^{2\gamma l} + Z_2^2}{(Z_1 + Z_2) (e^{\gamma l} - 1) \gamma}, \quad (\text{A.158})$$

The hyperbolic sine and cosine given by

$$\sinh x = \frac{e^{2x} - 1}{2e^x}, \quad \text{and} \quad \cosh x = \frac{e^{2x} + 1}{2e^x}, \quad (\text{A.159})$$

are inserted which yields

$$Z = \frac{l}{\left(\frac{1}{Z_1} + \frac{1}{Z_2} \right)} \left(1 + \frac{2 + \left(\frac{Z_1}{Z_2} + \frac{Z_2}{Z_1} \right) \cosh(\gamma l)}{\gamma l \sinh(\gamma l)} \right). \quad (\text{A.160})$$

The TLM seen in Fig. A.12a has the same impedance response as Eq. (A.160) where $Z_1 = R_{ion}$, $Z_2 = R_{el}$, and $\gamma_{cat}^2 = \gamma^2 = (R_{ion} + R_{el})/\zeta_{cat}$ and thus

$$Z_{TLM,cat} = \frac{l}{\left(\frac{1}{R_{ion}} + \frac{1}{R_{el}}\right)} \left(1 + \frac{2 + \left(\frac{R_{ion}}{R_{el}} + \frac{R_{el}}{R_{ion}}\right) \cosh(\gamma_{cat}l)}{\gamma_{cat}l \sinh(\gamma_{cat}l)} \right). \quad (\text{A.161})$$

The impedance response of the ζ_{cat} element is readily obtained from Eq. (A.128)

$$\zeta_{cat} = \frac{R_{ct} + Z_{WGFS,1D}}{1 + Q(j\omega)^n(R_{ct} + Z_{WGFS,1D})}, \quad (\text{A.162})$$

where $Z_{WGFS,1D}$ is the impedance of the one dimensional general finite space Warburg element which will be elaborated in the following. The total EEC model for the cathode and the anode can be seen in Fig. A.14 and the impedance is given by

$$Z_{cat}(\omega) = jL\omega + R_E + \frac{R_{Al}}{1 + (j\omega)^n Q_{Al} R_{Al}} + Z_{TLM,cat}, \quad (\text{A.163})$$

where L is the inductance of the external wires.

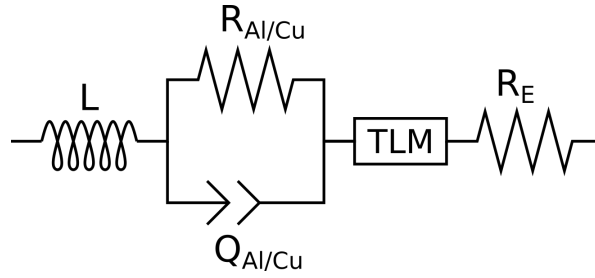


Figure A.14: Equivalent electrical circuit model of the LiFePO₄ cathode and graphite anode. The wires are modelled with an inductor, L , the current collector is modelled with a resistor, $R_{Al/Cu}$, in parallel with a constant phase element, $Q_{Al/Cu}$. The porous part of the electrode is modelled with a transmission line, and the electrolyte with a resistor.

The anode can be modelled in a similar manner with the only exception being the ζ element and hence $\gamma_{an}^2 = (R_{ion} + R_{el})/\zeta_{an}$. Therefore, $Z_{TLM,an}$ is equivalent to Z_{TLM} in Eq. (A.161) where $\gamma = \gamma_{an}$. The anode is covered with a SEI film and this gives rise to an additional resistance and an interface capacitance. The EEC model for ζ_{an} is seen in Fig. A.15 and can be seen as a Randles circuit nested inside another Randles circuit.

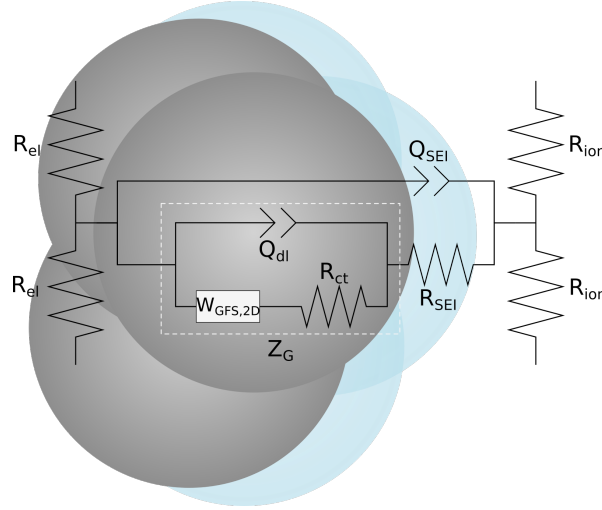


Figure A.15: An EEC model of the ζ_{an} element used to describe the de-/intercalation of Li^+ into the anode, the electrode-electrolyte interface, and the effects from the SEI film. The diffusion occurs in a 2D plane and hence it is modelled with a 2D general finite space Warburg element. The figure is inspired by [93]

The impedance response of this circuit is given by

$$\zeta_{an} = \frac{R_{SEI} + Z_G}{1 + Q_{SEI}(j\omega)^n(R_{SEI} + Z_G)}, \quad (\text{A.164})$$

where

$$Z_G = \frac{R_{ct} + Z_{GFS,2D}}{1 + Q_{dl}(j\omega)^n(R_{ct} + Z_{GFS,2D})}. \quad (\text{A.165})$$

The total EEC model for the anode is then

$$Z_{an}(\omega) = jL\omega + R_E + \frac{R_{Cu}}{1 + (j\omega)^n Q_{Cu} R_{Cu}} + Z_{TLM,an}, \quad (\text{A.166})$$

where

$$Z_{TLM,an} = \frac{l}{\left(\frac{1}{R_{ion}} + \frac{1}{R_{el}}\right)} \left(1 + \frac{2 + \left(\frac{R_{ion}}{R_{el}} + \frac{R_{el}}{R_{ion}}\right) \cosh(\gamma_{an}l)}{\gamma_{an}l \sinh(\gamma_{an}l)} \right). \quad (\text{A.167})$$

The Warburg Element

The Warburg element previously presented describes diffusion in one dimension to a planar electrode and is therefore not suitable to describe the diffusion process in the LiFePO_4 cathode particles since the de-/intercalation of lithium ions occur through the 1D channels along the b-axis. Furthermore, the simple Warburg element cannot describe the two dimensional diffusion in the graphite particles too. The impedance of

a Warburg element describing diffusion in a 1D channel with an impermeable boundary at the end is given as [93]

$$Z_{WGFS,1D} = \frac{Z_0}{(j\omega\tau)^n} \coth[(j\omega\tau)^n], \quad (\text{A.168})$$

where the subscript $WGFS,1D$ signifies one dimensional general finite space. The Z_0 is the polarisation resistance which arises when a potential is applied across the electrode. The time constant, τ , is related to the size of the LiFePO_4 particles and the diffusion coefficient of lithium within the particles as

$$\tau = \frac{r^2}{D}, \quad (\text{A.169})$$

where r is the radius of the particles. The impedance behavior for this Warburg element is seen in the Nyquist plot in Fig. A.16.

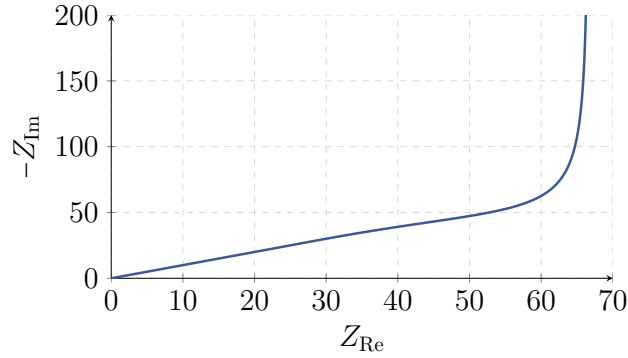


Figure A.16: Nyquist plot of Eq. (A.168). The parameters used are $Z_0 = 200 \Omega$, $r = 75 \text{ nm}$, $D = 4 \times 10^{-13} \text{ cm}^2 \text{ s}^{-1}$, $n = 0.5$, and $\omega \in [1 \text{ mHz}; 10 \text{ MHz}]$.

For the graphite anode, $Z_{WGFS,2D}$, becomes more complicated as the diffusion occurs in two dimensions. The impedance of the Warburg element then reads [93]

$$Z_{WGFS,2D} = \frac{Z_0}{(j\omega\tau)^n} \frac{I_0[(j\omega\tau)^n]}{I_1[(j\omega\tau)^n]}, \quad (\text{A.170})$$

where I_0 and I_1 are the modified zero- and first-order Bessel functions of the first kind, respectively. The general expression for the modified Bessel function of the first kind is

$$I_\nu(z) = \left(\frac{z}{2}\right)^\nu \sum_{k=0}^{\infty} \frac{\left(\frac{z^2}{4}\right)^k}{k! \Gamma(\nu + k + 1)}, \quad (\text{A.171})$$

where ν is a real number and Γ is the gamma function. The modified Bessel function is the solution to the Bessel equation when the argument, z , is imaginary.

The Nyquist plot for Eq. (A.170) can be seen in Fig. A.17. [121]

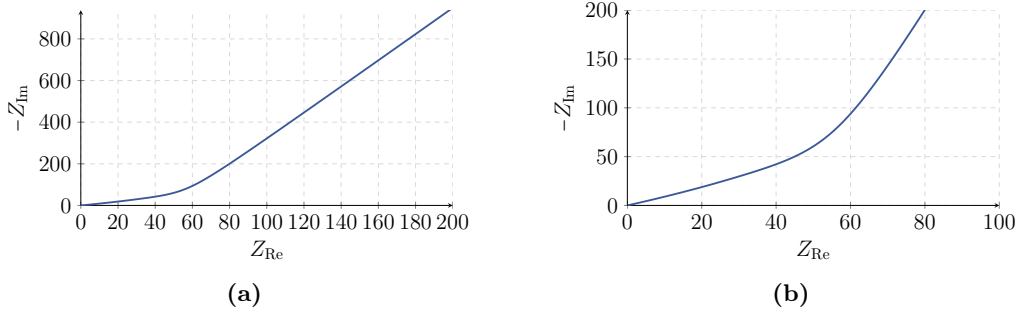


Figure A.17: Nyquist plot of Eq. (A.170). The parameters used are $Z_0 = 200 \Omega$, $r = 1100 \text{ nm}$, $D = 1 \times 10^{-10} \text{ cm}^2 \text{ s}^{-1}$, $n = 0.45$, and $\omega \in [1 \text{ mHz}; 10 \text{ MHz}]$. (a) Whole view. (b) Zoomed in view.

A.4 Non-Linear Least-Squares Fitting

The measurement data obtained with Raman spectroscopy and EIS require fitting of functions with multiple parameters in order to extract useful information. In the Raman spectra the peaks are fitted with an appropriate lineshape e.g. a Lorentzian. The fitting can be done with a non-linear least-squares (NLS) procedure. This procedure is not applicable to the EIS data as it consists of complex values. Therefore, the impedance of the equivalent electrical circuit models are fitted to the experimental EIS data with a complex non-linear least-squares (CNLS) procedure. Both the NLS and the CNLS used in this project utilise a Levenberg-Marquardt (LM) algorithm implemented in MATLAB.

Firstly, the non-linear least squares fitting procedure for real values is examined and secondly, it is expanded to account for complex values. Additionally, improvements to the LM algorithm are also presented. A flowchart describing the algorithm is available in Fig. A.18.

The object of the NLS procedure is to fit a model function $\hat{y}(x; \mathbf{P})$, where x is a variable, and \mathbf{P} is a vector with n parameters, to a set of data points (y_i, x_i) . An initial guess at the parameters is required such that $\hat{\mathbf{y}}(x_i)$ can be calculated at all measurement points. A perturbation to the parameters is then calculated and if the perturbed $\hat{\mathbf{y}}$ fits better to \mathbf{y} , the parameter perturbation is approved. This procedure is iterated multiple times until a convergence criteria is met. The perturbation to the parameters can be calculated by considering the sum of weighted squares

$$\chi^2(\mathbf{P}) = \sum_{i=1}^m \left[\frac{y(x_i) - \hat{y}(x_i; \mathbf{P})}{\sigma_{y_i}} \right]^2, \quad (\text{A.172})$$

where m is the number of data points, and σ_{y_i} is the variance. This expression may be written in matrix form as

$$\chi^2(\mathbf{P}) = (\mathbf{y} - \hat{\mathbf{y}}(\mathbf{P}))^\top \mathbf{W} (\mathbf{y} - \hat{\mathbf{y}}(\mathbf{P})) \quad (\text{A.173})$$

$$= \mathbf{y}^\top \mathbf{W} \mathbf{y} - 2\mathbf{y}^\top \mathbf{W} \hat{\mathbf{y}} + \hat{\mathbf{y}}^\top \mathbf{W} \hat{\mathbf{y}} \quad (\text{A.174})$$

where it has been used that $\hat{\mathbf{y}}$ and \mathbf{y} are commutative and \mathbf{W} is a diagonal weighting matrix where $W_{ii} = 1/\sigma_{y_i}^2$. A technique to minimise the function in Eq. (A.174) is to move against its gradient w.r.t. the fitting parameters. The gradient is calculated as

$$\frac{\partial \chi^2}{\partial \mathbf{P}} = -2(\mathbf{y} - \hat{\mathbf{y}})^\top \mathbf{W} \mathbf{J}, \quad (\text{A.175})$$

where \mathbf{J} is the Jacobian given by $J_{ij} = \partial \hat{y}_i / \partial P_j$. A perturbation to the parameters may be determined by

$$\mathbf{h} = \alpha \mathbf{J}^\top \mathbf{W} (\mathbf{y} - \hat{\mathbf{y}}), \quad (\text{A.176})$$

where α is the step length in the direction of the gradient's descent and only takes on positive values. This approach is known as the gradient descent method which is good when χ^2 is far from its minimal value. However, as the minimum is approached the step length has to be adjusted and the converging may slow down since the gradient diminishes. [122]

Another approach for determining the perturbation relies on approximating $\hat{\mathbf{y}}$ by a first-order Taylor series expansion as

$$\hat{\mathbf{y}}(\mathbf{P} + \mathbf{h}) \simeq \hat{\mathbf{y}} + \frac{\partial \hat{\mathbf{y}}}{\partial \mathbf{P}} \mathbf{h} \quad (\text{A.177})$$

$$= \hat{\mathbf{y}} + \mathbf{J} \mathbf{h}, \quad (\text{A.178})$$

and inserting into Eq. (A.174) which yields

$$\chi^2(\mathbf{P} + \mathbf{h}) \simeq \mathbf{y}^\top \mathbf{W} \mathbf{y} + \hat{\mathbf{y}}^\top \mathbf{W} \hat{\mathbf{y}} - 2[\mathbf{y} \mathbf{W} \hat{\mathbf{y}} + (\mathbf{y} - \hat{\mathbf{y}})^\top \mathbf{W} \mathbf{J} \mathbf{h}] + (\mathbf{h} \mathbf{J})^\top \mathbf{W} \mathbf{J} \mathbf{h}. \quad (\text{A.179})$$

This approximation is seen to be quadratic in the perturbation \mathbf{h} . The perturbation which minimises χ^2 is determined by taking the derivative of it w.r.t \mathbf{h} as

$$\frac{\partial \chi^2(\mathbf{P} + \mathbf{h})}{\partial \mathbf{h}} \simeq -2(\mathbf{y} - \hat{\mathbf{y}})^\top \mathbf{W} \mathbf{J} + 2\mathbf{h}^\top \mathbf{J}^\top \mathbf{W} \mathbf{J}, \quad (\text{A.180})$$

and setting it equal to zero which yields

$$[\mathbf{J}^\top \mathbf{W} \mathbf{J}] \mathbf{h} = \mathbf{J}^\top \mathbf{W} (\mathbf{y} - \hat{\mathbf{y}}). \quad (\text{A.181})$$

This procedure is known as the Gauss-Newton method and is known to converge faster than the gradient descent if the initial parameters are not too far from the optimal ones due to the quadratic dependency of $\chi^2(\mathbf{P} + \mathbf{h})$ on \mathbf{h} . However, if the initial guess is bad the Gauss-Newton method converges poorly. [122]

The Levenberg-Marquardt algorithm combines the great converging properties of the gradient descent method when the solution is far from optimal, with the fast convergence of the Gauss-Newton when the solution is close to the optimal one. This is achieved by introducing the dampening parameter, λ . The expressions in Eqs. (A.176)

and (A.181), is combined as

$$(\mathbf{J}^\top \mathbf{W} \mathbf{J} + \lambda \mathbf{I}) \mathbf{h} = \mathbf{J}^\top \mathbf{W} (\mathbf{y} - \hat{\mathbf{y}}), \quad (\text{A.182})$$

where it can be seen that as λ increases the expression approaches that of the gradient descent method, and vice versa when λ decreases it approaches the Gauss-Newton method. The magnitude of λ depends on the parameters and therefore it is convenient to normalise it as

$$(\mathbf{J}^\top \mathbf{W} \mathbf{J} + \lambda \mathbf{A}) \mathbf{h} = \mathbf{J}^\top \mathbf{W} (\mathbf{y} - \hat{\mathbf{y}}), \quad (\text{A.183})$$

where \mathbf{A} is a diagonal matrix made from diagonal entries of $\mathbf{J}^\top \mathbf{W} \mathbf{J}$. The perturbation is calculated as

$$\mathbf{h} = (\mathbf{J}^\top \mathbf{W} \mathbf{J} + \lambda \mathbf{A})^{-1} \mathbf{J}^\top \mathbf{W} (\mathbf{y} - \hat{\mathbf{y}}). \quad (\text{A.184})$$

The next step in the algorithm is to check if the perturbation improves the solution. [122, 123]

Implementation of the Levenberg-Marquardt Algorithm

The calculation of the perturbation relies on the Jacobian matrix which is approximated numerically using a finite difference approach. The central difference scheme is chosen as it is more accurate than the forward scheme and is given as

$$J_{ij} = \frac{\partial \hat{y}_i}{\partial P_j} \quad (\text{A.185})$$

$$= \frac{\hat{y}(x_i; \mathbf{P} + \delta \mathbf{P}) - \hat{y}(x_i; \mathbf{P} - \delta \mathbf{P})}{2 \|\delta \mathbf{P}\|}, \quad (\text{A.186})$$

where only the j -th entry of $\delta \mathbf{P}$ is non-zero and is given as

$$\delta P_j = \Delta (1 + |P_j|), \quad (\text{A.187})$$

where Δ is a user defined scaling parameter. [122]

The variance, σ_{y_i} , is often not known and therefore it has to be substituted. The simplest approach is to set the diagonal in the weighting matrix, \mathbf{W} , equal to unity as

$$W_{ii} = 1. \quad (\text{A.188})$$

Another possibility as proposed by B. A. Boukamp [124], is to substitute σ_{y_i} with an expression that depends on the magnitude of the measurement data as

$$W_{ii} = \frac{1}{y_i^2}. \quad (\text{A.189})$$

The initial guess at the parameters is used to calculate a perturbation. It may or may not be an improvement and it is important to only update the set of parameters as

$\mathbf{P} \leftarrow \mathbf{P} + \mathbf{h}$ if $\mathbf{P} + \mathbf{h}$ improves the solution. The perturbation can be evaluated as

$$\Delta\chi^2 = \chi^2(\mathbf{P}) - \chi^2(\mathbf{P} + \mathbf{h}), \quad (\text{A.190})$$

and if $\Delta\chi^2 > 0$ the perturbation is approved and the set of parameters are updated. However, it is often useful to use another approach where $\Delta\chi^2$ is normalised as

$$\rho = \frac{\chi^2(\mathbf{P}) - \chi^2(\mathbf{P} + \mathbf{h})}{(\mathbf{y} - \hat{\mathbf{y}})^\top \mathbf{W}(\mathbf{y} - \hat{\mathbf{y}}) - (\mathbf{y} - \hat{\mathbf{y}} - \mathbf{J}\mathbf{h})^\top \mathbf{W}(\mathbf{y} - \hat{\mathbf{y}} - \mathbf{J}\mathbf{h})}. \quad (\text{A.191})$$

Here $\Delta\chi^2$ has been inserted into the denominator and the first-order Taylor series expansion from Eq. (A.178) has been used. The denominator in this expression can be rewritten by using the commutative property of \mathbf{J} , \mathbf{h} , \mathbf{y} , and $\hat{\mathbf{y}}$, along with Eq. (A.182) into

$$\rho = \frac{\chi^2(\mathbf{P}) - \chi^2(\mathbf{P} + \mathbf{h})}{\mathbf{h}^\top [\lambda \mathbf{A}\mathbf{h} + \mathbf{J}^\top \mathbf{W}(\mathbf{y} - \hat{\mathbf{y}})]}. \quad (\text{A.192})$$

If $\rho > \varepsilon_\rho$, where ε_ρ is a user defined parameter, the perturbation is accepted and the set of parameters is updated as $\mathbf{P} \leftarrow \mathbf{P} + \mathbf{h}$. [122, 123]

In each iteration λ should be updated. Initially it can be set to a user specified value but this may be difficult as the magnitude of λ depends on the magnitude of the parameters. Therefore, it can be advantageous to set it to

$$\lambda_{init} = \gamma \max \mathbf{A}, \quad (\text{A.193})$$

where γ is a user defined value which does not depend on the magnitude of the parameters. How λ is updated should depend on the value of ρ , as it is desirable to increase λ if $\rho < \varepsilon_\rho$ and to decrease it if $\rho > \varepsilon_\rho$. These two possible updates ensure that if the perturbation is not accepted then the algorithm adjusts towards the gradient descent method, and if the perturbation is accepted then it adjusts towards the Gauss-Newton method. There is a plethora of updating techniques but in this project the following has been used

$$\rho > \varepsilon_\rho: \quad \lambda \leftarrow \lambda \max\left(\frac{1}{3}, 1 - (2\rho - 1)^3\right), \quad \nu = 2, \quad (\text{A.194})$$

$$\rho < \varepsilon_\rho: \quad \lambda \leftarrow \lambda\nu, \quad \nu \leftarrow 2\nu. \quad (\text{A.195})$$

After updating λ the algorithm should check whether one or more convergence criteria has been met or not before proceeding with the next iteration. These criteria can be formulated in multiple ways by either looking at the gradient, the parameters, or χ^2 ,

as

$$\text{Gradient : } \quad \varepsilon_g > \max |\mathbf{J}^\top \mathbf{W}(\mathbf{y} - \hat{\mathbf{y}})|, \quad (\text{A.196})$$

$$\text{Parameters : } \quad \varepsilon_P > \max \left| \frac{h_j}{P_j} \right|, \quad (\text{A.197})$$

$$\text{Reduced } \chi_r^2 : \quad \varepsilon_\chi > \chi_r^2, \quad \chi_r^2 = \frac{\chi^2}{m - (n - 1)}, \quad (\text{A.198})$$

where $\varepsilon_{g,P,\chi}$ are user defined values. The denominator in Eq. (A.198) is the number of degrees of freedom of the system, where m and n is amount of data points and parameters, respectively. In addition to the convergence criteria it is also good practice to limit the amount of iterations. [122]

A list of the user defined parameters used in the LM algorithm is available in Table A.1.

Table A.1: List of user defined parameters used in the LM algorithm. [122, 123]

Parameter	Value
ε_g	1×10^{-3}
ε_P	1×10^{-1}
ε_χ	1×10^{-6}
ε_ρ	1×10^{-1}
γ	1×10^{-3}
Δ	1×10^{-3}

Extension to Complex Values

The NLS method is not applicable to the experimental data from EIS as it involves complex numbers. However, the NLS method can be extended to CNLS by rewriting Eq. (A.172). It was proposed by Sheppard et al. [125] that the real and imaginary part of the measurement- and model data points can be considered separately as

$$\chi^2(\mathbf{P}) = \sum_{i=1}^m \left[\left(\frac{\text{Re}\{y(x_i) - \hat{y}(x_i; \mathbf{P})\}}{\sigma_{y_i}} \right)^2 + \left(\frac{\text{Im}\{y(x_i) - \hat{y}(x_i; \mathbf{P})\}}{\sigma_{y_i}} \right)^2 \right], \quad (\text{A.199})$$

and thus Eq. (A.174) becomes

$$\chi^2(\mathbf{P}) = \text{Re}\{\hat{\mathbf{y}}^\top \mathbf{W} \mathbf{y} - 2\mathbf{y}^\top \mathbf{W} \hat{\mathbf{y}} + \hat{\mathbf{y}}^\top \mathbf{W} \hat{\mathbf{y}}\} + \text{Im}\{\hat{\mathbf{y}}^\top \mathbf{W} \mathbf{y} - 2\mathbf{y}^\top \mathbf{W} \hat{\mathbf{y}} + \hat{\mathbf{y}}^\top \mathbf{W} \hat{\mathbf{y}}\}. \quad (\text{A.200})$$

Similar changes are implemented to the expressions for the weighting matrix, \mathbf{W} , the perturbation, \mathbf{h} , and ρ , which yield

$$W_{ii} = \frac{1}{\text{Re}\{y_i\}^2 + \text{Im}\{y_i\}^2}, \quad (\text{A.201})$$

$$\mathbf{h} = \text{Re} \left\{ (\mathbf{J}^\top \mathbf{W} \mathbf{J} + \lambda \mathbf{A})^{-1} \mathbf{J}^\top \mathbf{W} (\mathbf{y} - \hat{\mathbf{y}}) \right\} + \text{Im} \left\{ (\mathbf{J}^\top \mathbf{W} \mathbf{J} + \lambda \mathbf{A})^{-1} \mathbf{J}^\top \mathbf{W} (\mathbf{y} - \hat{\mathbf{y}}) \right\}, \quad (\text{A.202})$$

$$\rho = \text{Re} \left\{ \frac{\chi^2(\mathbf{P}) - \chi^2(\mathbf{P} + \mathbf{h})}{\mathbf{h}^\top [\lambda \mathbf{A} \mathbf{h} + \mathbf{J}^\top \mathbf{W} (\mathbf{y} - \hat{\mathbf{y}})]} \right\} + \text{Im} \left\{ \frac{\chi^2(\mathbf{P}) - \chi^2(\mathbf{P} + \mathbf{h})}{\mathbf{h}^\top [\lambda \mathbf{A} \mathbf{h} + \mathbf{J}^\top \mathbf{W} (\mathbf{y} - \hat{\mathbf{y}})]} \right\}. \quad (\text{A.203})$$

The initial value of the dampening parameter, λ , is adjusted as

$$\lambda_{init} = \gamma \max |\mathbf{A}| \quad (\text{A.204})$$

where the absolute value, $|\mathbf{A}|$, ensures that λ does not take on complex values. The updating technique along with the convergence criteria is the same as for NLS. [123]

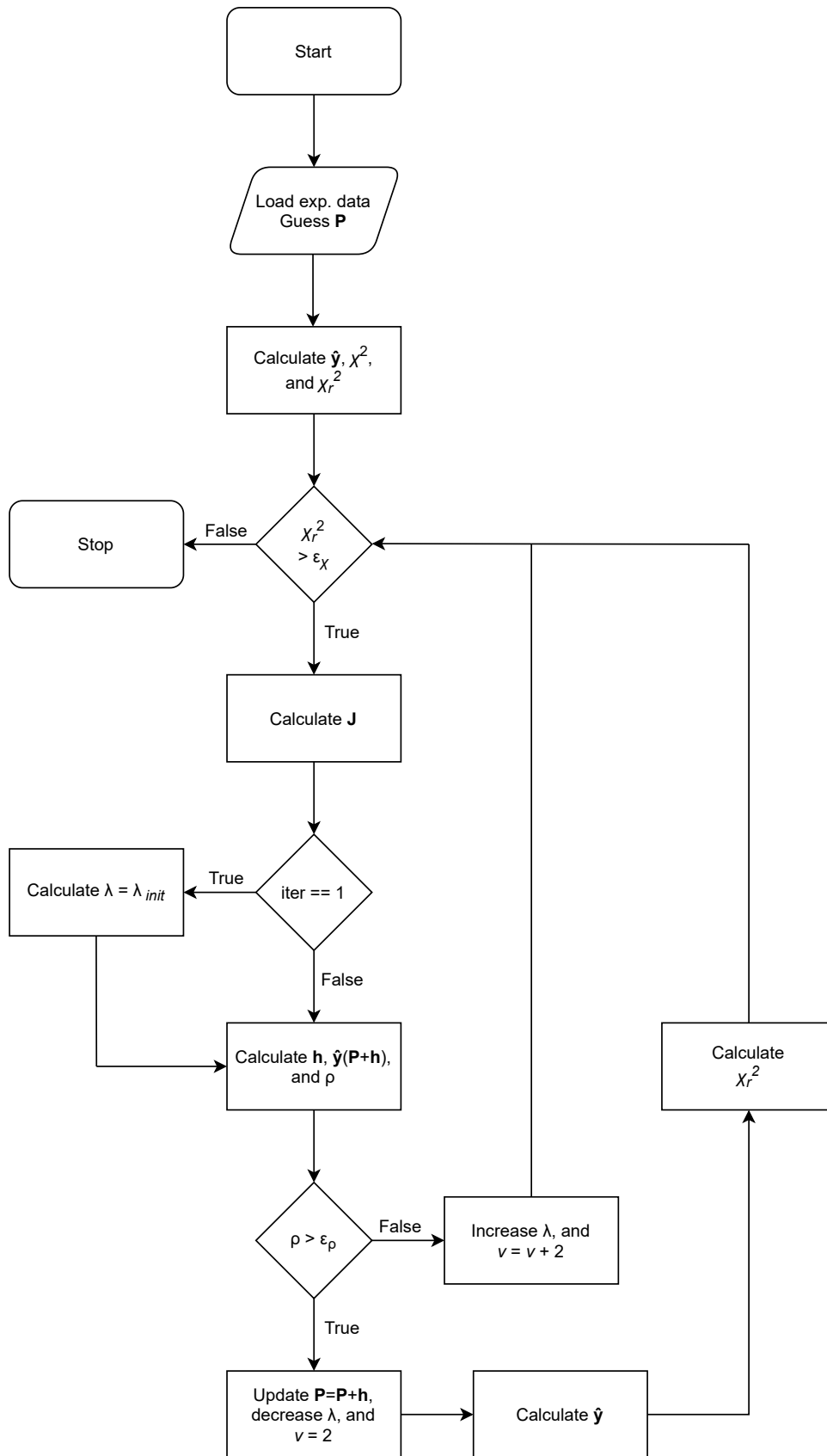


Figure A.18: Flowchart of the Levenberg-Marquardt algorithm as implemented in a MATLAB script used for the NLS and CNLS problems in this project.

A.5 Calculating the FWHM for Raman spectroscopy

The full width at half maximum for the asymmetric G peak observed in the Raman spectra is difficult to determine analytically, since the width parameter, γ , varies with the wavenumber. Instead a polynomial estimation based on a numerical calculation was used. The FWHM was calculated numerically by solving the following equation

$$g(x) = I_0 \left[\frac{\gamma^2(x)}{(x - x_0)^2 + \gamma^2(x)} \right] - \frac{I_0}{2} = 0, \quad (\text{A.205})$$

with respect to two roots, x_1 and x_2 . The width parameter $\gamma(x)$ is given in Eq. (5.4) and $I_0/2$ is the half maximum. The FWHM is then

$$\text{FWHM}(Q, \gamma_0) = |x_1 - x_2|. \quad (\text{A.206})$$

A root finding algorithm based on the Newton-Raphson method known as the second order Householder's method or Halley's method was used to iteratively determine x_1 and x_2 from some initial guess x_0 . Householder's method for the d 'th order is

$$x_{n+1} = x_n + d \frac{(1/g)^{(d-1)}(x)}{(1/g)^{(d)}(x)} \Big|_{x=x_n}, \quad (\text{A.207})$$

where $(1/g)^{(d)}$ is the d 'th derivative of $(1/g)(x)$ wrt. x [126]. Householder's method convergence rate is $\mu = d + 1$ and for $d = 2$ Halley's method is obtained

$$x_{n+1} = x_n - \frac{2g(x_n)g'(x_n)}{2[g'(x_n)]^2 - g(x_n)g''(x_n)}. \quad (\text{A.208})$$

Based on the obtained data for the asymmetric G peak the initial guesses were $x_0 = 900 \text{ cm}^{-1}$ and 1100 cm^{-1} . The numerical calculation were performed in a 100x100 grid of $Q \in [-0.02; 0.02]$ and $\gamma_0 \in [40; 70] \text{ cm}^{-1}$, which resulted in a surface for the $\text{FWHM}(Q, \gamma_0)$ as shown in Fig. A.20a. The typical amount of iterations required for $|x_{n+1} - x_n| < 10^{-8}$ was $n = 5$. Due to the large amount of obtained Raman spectra, particularly from the mapping technique, a polynomial estimation was determined to decrease the computational time. Firstly, considering the polynomial

$$\text{FWHM}(Q, \gamma_0) = 2\gamma_0 [1 + A(\gamma_0)Q^2 + B(\gamma_0)Q^4]. \quad (\text{A.209})$$

Secondly, the A and B functions were determined with the Levenberg-Marquardt algorithm described in Appendix A.4. Graphs of $A(\gamma_0)$ and $B(\gamma_0)$ from the polynomial estimation are shown in Fig. A.19. The estimation becomes

$$\text{FWHM}(Q, \gamma_0) = 2\gamma_0 (1 + (27.6\gamma_0 - 707)Q^2 - 0.464\gamma_0^{3.56}Q^4). \quad (\text{A.210})$$

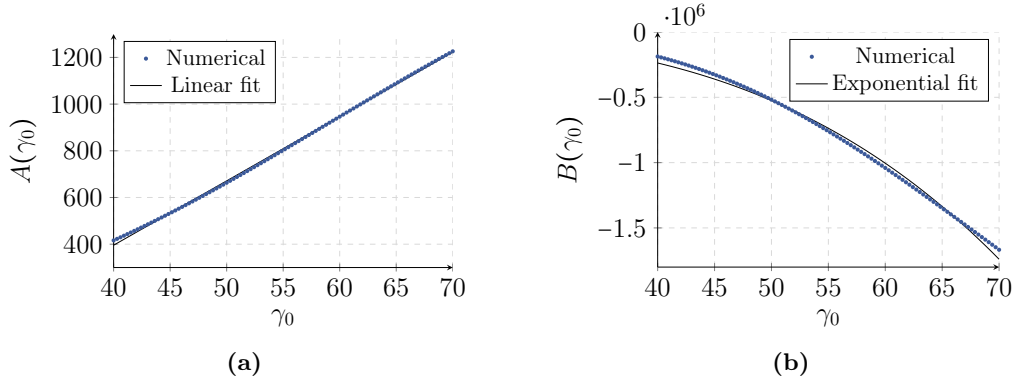


Figure A.19: Graph of the (a) $A(\gamma_0)$ and (b) $B(\gamma_0)$ functions, and the estimation with a linear and exponential fit, respectively.

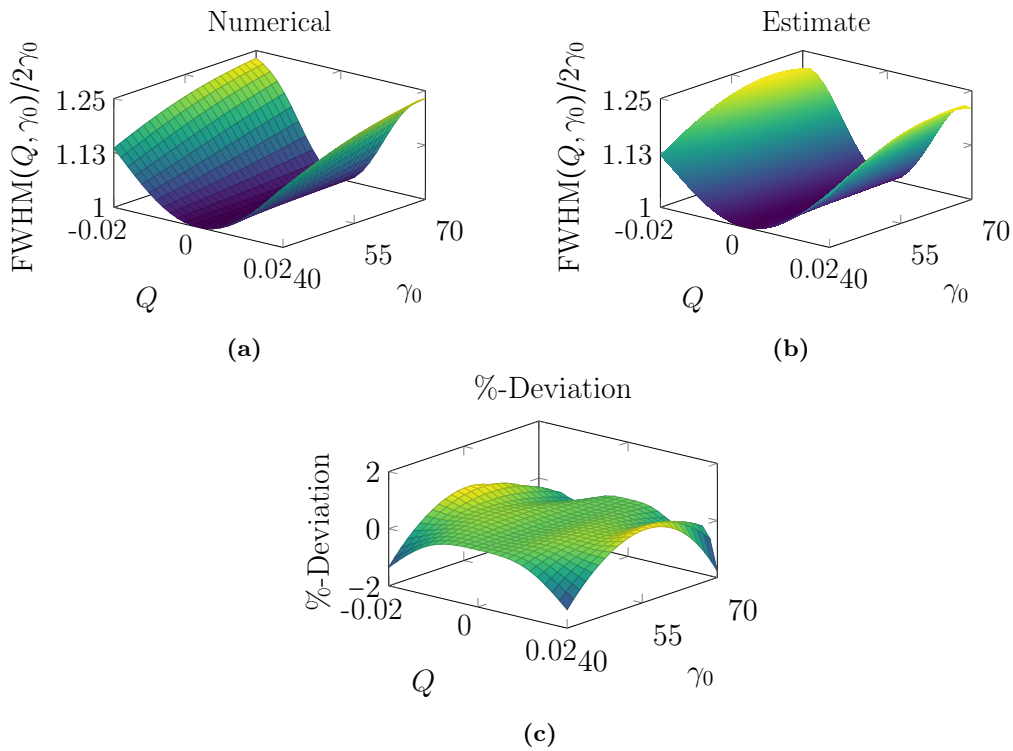


Figure A.20: FWHM for the asymmetric Lorentzian function from Eqs. (5.3) and (5.4). The function $\text{FWHM}(Q, \gamma_0)/2\gamma_0$ is plotted as a surface for $Q \in [-0.02; 0.02]$ and $\gamma_0 \in [40; 70] \text{ cm}^{-1}$. (a) Numerical calculation based on the Newton-Raphson method in a 25x25 grid, (b) polynomial estimate, and (c) %-deviation between the estimate and the numerical calculation.

The FWHM surfaces from Figs. A.20a and A.20b show great similarity. The %-deviation surface shown in Fig. A.20c was determined as

$$\% \text{ - Deviation} = \frac{\text{FWHM}_{\text{est}} - \text{FWHM}_{\text{num}}}{\text{FWHM}_{\text{num}}} \times 100\%. \quad (\text{A.211})$$

The deviation showed to be in the range -1.77% to 0.54%, and hence the estimate proved satisfactory and decreased the computation time for the FWHM significantly.

B Equipment and Procedures

In this appendix the features of the glovebox are presented along with procedures and lists of equipment for the disassembly- and electrochemical experimental procedures.

B.1 Glovebox Assembly

A glovebox, capable of providing an inert atmosphere, was prepared as part of the project with assistance from the institute technicians. The inert argon atmosphere inside the glovebox provided necessary conditions for disassembling the LIBs since the batteries deteriorate in the presence of oxygen and water. The glovebox was placed in a fume hood to provide additional protection against potential hazardous gasses.

The glovebox was built by modifying a commercial sandblasting cabinet bought from [AJ Engros](#). The modifications include:

- Hygrometer,
- Stainless steel plates as floor,
- Inflow port with flowmeter connected to N₂ and Ar,
- Outflow valve,
- Load-lock with two valves and rubber stoppers,
- Epoxy based paint for sealing,
- White LED light strip with 12 V power port,
- Wall outlet power for a bag sealer,
- Flexible rubber gloves,
- Differential pressure sensor.
- Connection port for potentiostat.

The hygrometer, a moisture monitor series 35 from Panametric, provided readings in parts per million by volume, ppmv. The hygrometer sensor was screwed in a port in the upper right corner and connected to the main apparatus outside the glovebox. The sensor part was shielded by a copper plate to protect it from accidentally being hit

while working. The inflow valve, placed in the bottom of the glovebox, was connected to a variable area flowmeter capable of providing $0\text{--}10\text{ L min}^{-1}$. The flowmeter was then connected to a N_2 supply at 5 bar and to an Ar gas cylinder with a reduction valve to bring the Ar pressure down to approximately 2 bar. Two stainless steel plates were cut and served as a flat and stable surface to work on. Small rubber strips were glued on the backside of the plates for better stability. A load-lock was installed to transfer tools and samples in and out of the glovebox while isolating the main chamber from the ambient atmosphere. The load-lock consisted of an aluminium pipe with rubber plugs and valves and was installed in place of the original air filter. A white epoxy based paint was used to coat the inside of the box to limit small leaks and rubber plugs were used to seal unused ports. A white LED strip was installed with a 12 V power supply to light up the chamber. Furthermore, a wall outlet port was created to supply a bag sealer inside the glovebox. The bag sealer was used to seal aluminium pouches for sample storage. The original gloves designed for sandblasting was replaced with a pair of thinner and more flexible rubber gloves.

While using the glovebox the lid was closed with plastic clamps and sealed with gas tight tape around the lid perimeter for extra sealing. A differential pressure sensor was mounted in the fume hood with one end inside the glovebox and the other end in the ambient atmosphere. A three way valve was installed on the tube from the chamber to the pressure sensor such that the tubing could be flushed when changing from N_2 to Ar. A rubber plug was fitted to the wiring from the potentiostat to enable electrochemical measurements inside the glovebox while keeping the potentiostat unit, connected to a PC, outside the glovebox.

Photographs of the glovebox are shown in Figs. B.1 to B.6.



Figure B.1: Outside view where the gloves are sticking out due to a slight overpressure.

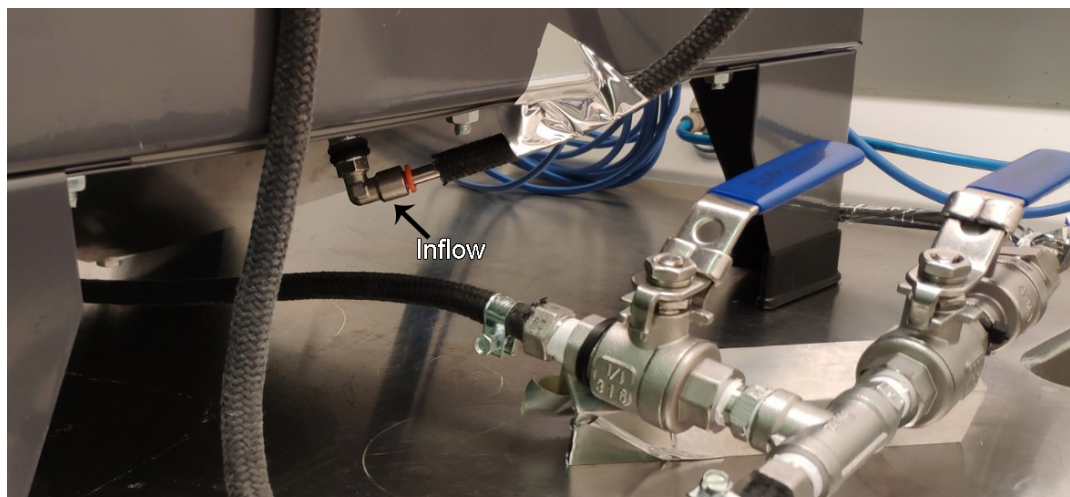


Figure B.2: View of the gas inflow port in the bottom of the glovebox.



Figure B.3: Inside view with bag sealer, hygrometer sensor, and load lock sealed with a rubber stopper and a valve.

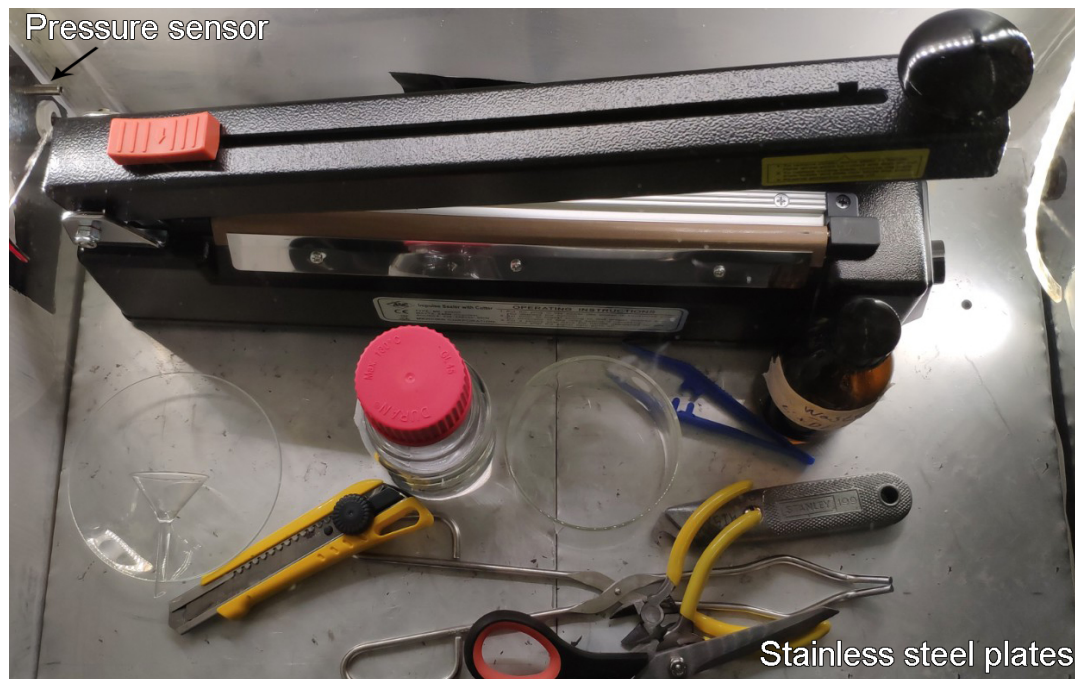


Figure B.4: Inside view showing the stainless steel plates and the pressure sensor outlet. Tools needed for battery disassembly is shown as well.

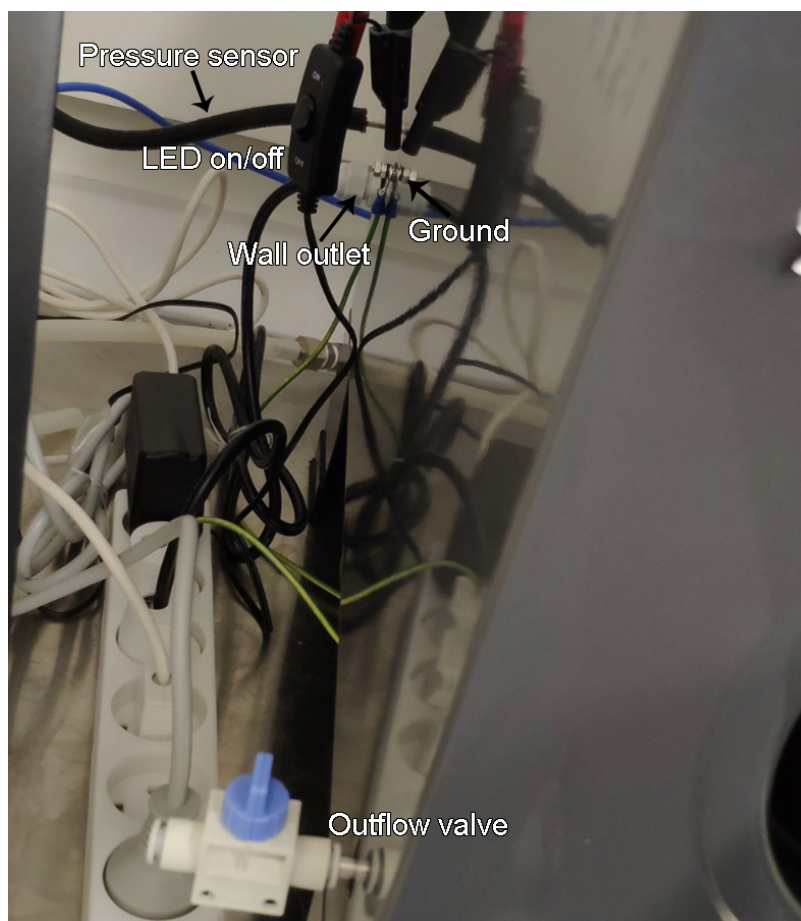


Figure B.5: View of the left side of the glovebox with power outlets and an outflow valve.



Figure B.6: Connection port which tightly fit the 5 pin cable from the PalmSens4 potentiostat. During electrochemical experiments the potentiostat unit was placed outside the glovebox.

B.2 Procedure: Purging of Glovebox

The following section is a procedure of how to purge the glovebox.

Purging Procedure:

- Transfer all the needed equipment to the glovebox
- Close the lid on the glovebox and open the N₂ valve and adjust the flow meter to 10 L min⁻¹.
- Turn on the hygrometer and the differential pressure sensor. The differential pressure sensor should read >200 Pa.
- When the hygrometer reads 300 ppmv, seal the seams in the lid with aluminium foil tape. Lower the flow by adjusting the flow meter to around 4 L min⁻¹.
- When the hygrometer reads <10 ppmv (usually takes overnight) close the N₂ valve and open the Ar valve.
- Wait about 30 minutes before operating the glovebox such that the majority of the atmosphere is Ar.

B.3 Procedure: Disassembly of Batteries

The following section contains a procedure for disassembling the LIBs and preparing samples. A list of equipment is included as well which is particularly useful as a checklist to ensure all the needed tools are in the glovebox before purging is initiated.

Disassembly Procedure:

- Purge the glovebox as described in Appendix B.2.
- Cut the battery around the top and the bottom (1 mm from the ends).
- Carefully cut from end to end or remove the metal casing by other means. Be aware of not cutting into the interior and of the electrolyte in the battery.
- Unroll the interior. The first layers are made up of green plastic. This can be discarded.
- Unroll the layered structure of the cathode, separator, and anode.
- Cut samples of each internal components.
- Prepare a beaker with DEC, and a glass plate for drying.
- Wash the samples in DEC thoroughly and let dry on the glass plate.
- Once the samples are dry (It may be necessary to flip them during the drying process) they can be stored in aluminium bags and sealed.
- Put all of the leftover cathode, separator, anode, plastic, housing, paper towels, etc., in a bag and seal it. Mark it as 'Li-ion Battery Waste'.

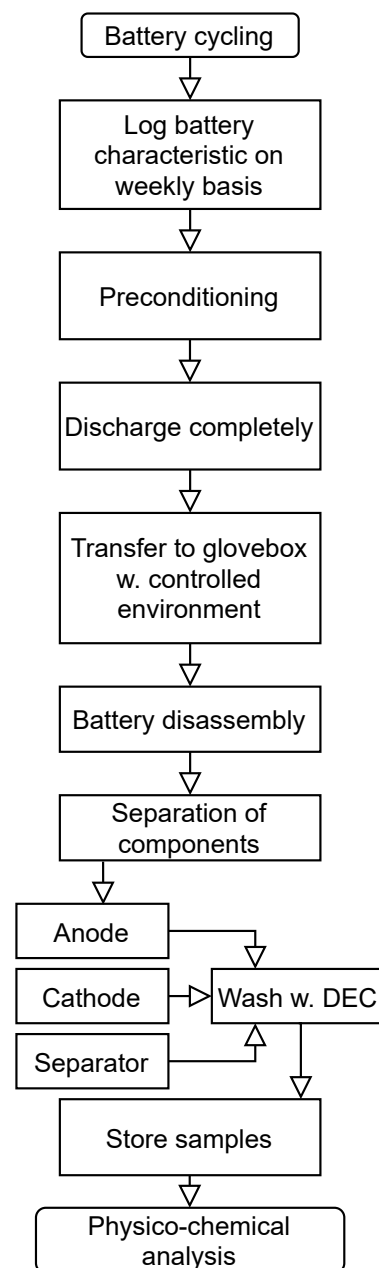


Figure B.7: Process diagram for the battery disassembly before further analysis. The process is similar to that reviewed by Waldmann et al. [77].

List of Equipment:Tools

- Scissors
- Tweezers
- Hook blade knife
- Cutting pliers

Miscellaneous

- Cleanroom wipes
- Black waste bags
- Storage bag for samples w. label
- Battery for disassembly

Glassware

- Beaker for washing
- Funnel
- Drying plate
- DEC waste bottle

Chemicals

- DEC in bluecap bottle

B.4 Procedure: Electrochemical Measurements

The setup and equipment needed for CV, Chronopotentiometry, and EIS are similar and therefore the list is generalised.

List of Equipment:Tools

- Scissors
- Tweezers

Cell Setup

- Teflon beaker
- Viton O-ring
- Silicone pad
- Metal backplate and screws
- Potentiostat cable (mounted in glovebox) and alligator clips
- 3rd hand
- Counter electrode
- Reference electrode
- Parafilm
- Anode and cathode samples

Glassware

- Small beaker
- Funnel
- Electrolyte storage bottle
- Electrolyte waste bottle

Miscellaneous

- Cleanroom wipes
- Black waste bags
- Storage bag for samples w. label

Chemicals

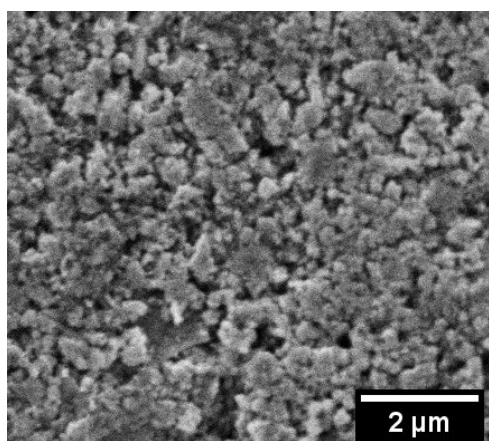
- LiPF₆ electrolyte

C Additional Results

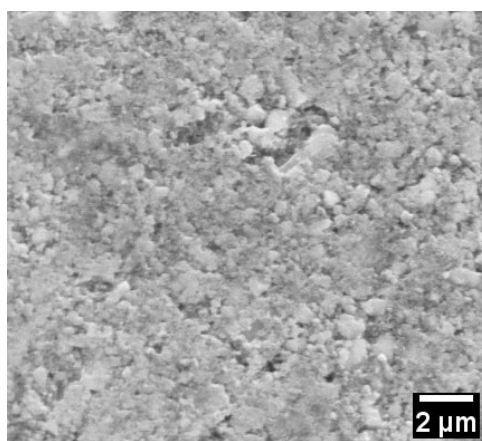
In this appendix additional results from SEM, RS, and EDS, of the anodes and cathodes, are included.

C.1 SEM Micrographs

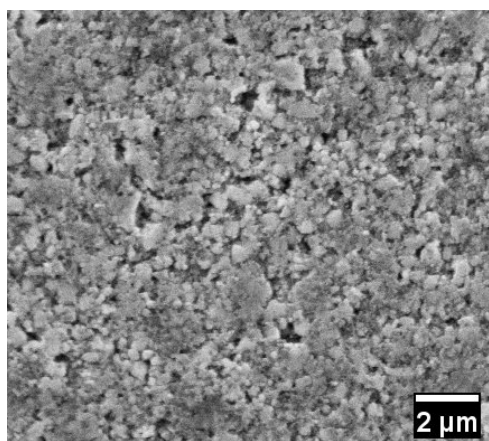
A comparison of SEM micrographs of the cathodes are shown in Fig. C.1. Due to the high degree of similarity they are presented in this appendix.



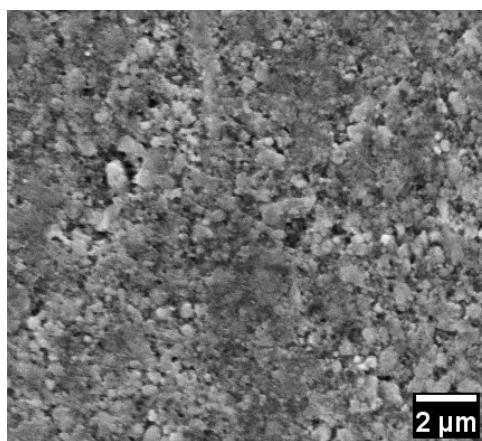
(a) TCP



(b) TCC



(c) TC1



(d) TC2

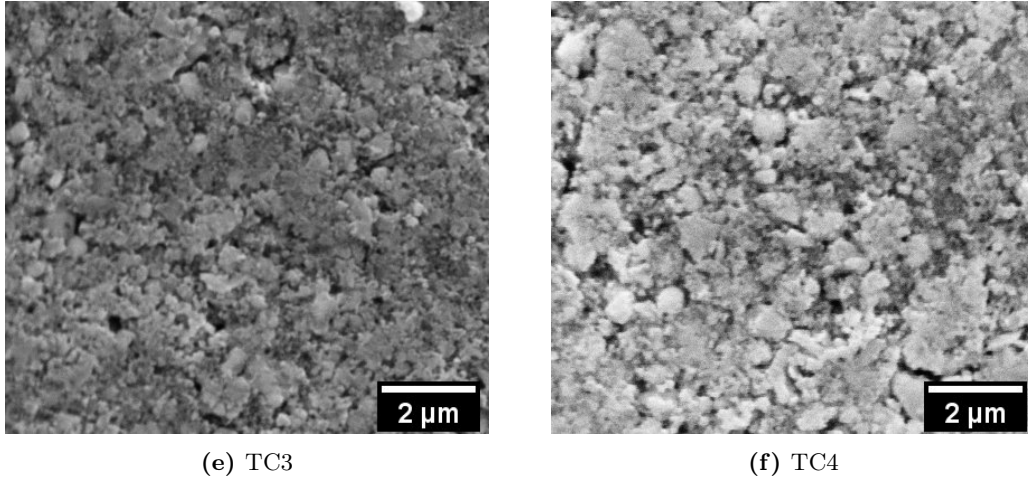


Figure C.1: SEM micrographs of cathodes of (a) TCP, b TCC, (c) TC1, (d) TC2, (e) TC3, and (f) TC4.

C.2 Mean Anode Particle Size

This section contains the mean line intersection data for the anodes of TCP, TC2, TC3, and TC4.

Table C.1: Horizontal mean line intersection data for the anode of TCP.

Horizontal			
Line no.	Length [μm]	Intersections	Mean size [μm]
#1	72.81	33	2.21
#2	72.81	32	2.28
#3	72.81	34	2.14
#4	72.81	32	2.28
#5	71.26	27	2.64
Combined mean [μm]			2.31

Table C.2: Vertical mean line intersection data for the anode of TCP.

Vertical			
Line no.	Length [μm]	Intersections	Mean size [μm]
#1	45.8	22	2.08
#2	45.8	17	2.69
#3	45.8	21	2.18
#4	45.8	17	2.69
#5	45.8	20	2.29
Combined mean [μm]			2.39

Table C.3: Horizontal mean line intersection data for anode of TC2.

Horizontal			
Line no.	Length [μm]	Intersections	Mean size [μm]
#1	65.30	30	2.18
#2	65.30	34	1.92
#3	65.30	31	2.11
#4	65.30	31	2.11
#5	65.30	33	2.00
Combined mean [μm]			2.06

Table C.4: Vertical mean line intersection data for anode of TC2.

Vertical			
Line no.	Length [μm]	Intersections	Mean size [μm]
#1	40.91	19	2.15
#2	40.91	22	1.86
#3	40.91	19	2.15
#4	40.91	19	2.15
#5	40.91	19	2.15
Combined mean [μm]			2.09

Table C.5: Horizontal mean line intersection data for anode of TC3.

Horizontal			
Line no.	Length [μm]	Intersections	Mean size [μm]
#1	63.34	21	3.02
#2	63.34	26	2.44
#3	63.34	24	2.64
#4	63.34	23	2.75
#5	63.34	20	3.17
Combined mean [μm]			2.80

Table C.6: Vertical mean line intersection data for anode of TC3.

Vertical			
Line no.	Length [μm]	Intersections	Mean size [μm]
#1	40.89	13	3.15
#2	40.89	13	3.15
#3	40.89	17	2.41
#4	40.89	14	2.92
#5	40.89	16	2.56
Combined mean [μm]			2.83

Table C.7: Horizontal mean line intersection data for anode of TC4.

Horizontal			
Line no.	Length [μm]	Intersections	Mean size [μm]
#1	61.18	28	2.19
#2	61.18	20	3.06
#3	61.18	22	2.78
#4	61.18	22	2.78
#5	61.18	22	2.78
Combined mean [μm]			2.72

Table C.8: Vertical mean line intersection data for anode of TC4.

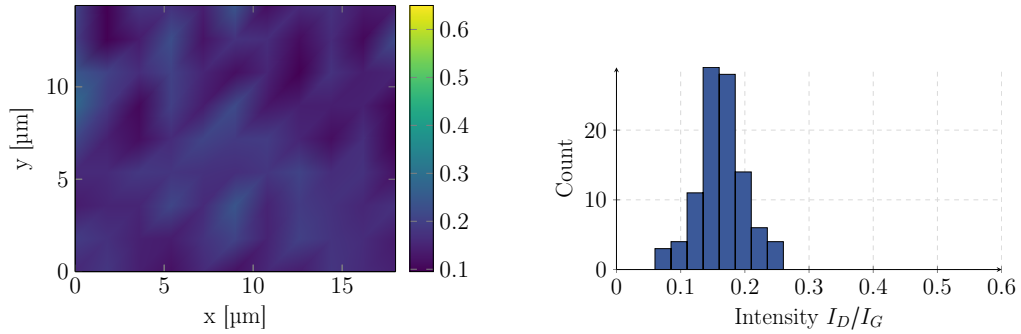
Vertical			
Line no.	Length [μm]	Intersections	Mean size [μm]
#1	40.90	14	2.92
#2	40.90	18	2.27
#3	40.90	16	2.56
#4	40.90	16	2.56
#5	40.90	16	2.56
Combined mean [μm]			2.57

C.3 Raman Spectroscopy Maps

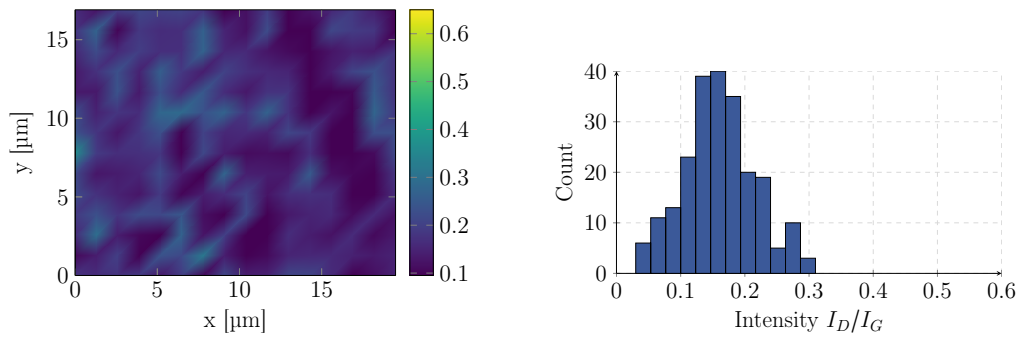
This section contains additional Raman spectroscopy maps of I_D/I_G and $\text{FWHM}_D/\text{FWHM}_G$.

Maps of Intensity Ratio of the D to the G Band

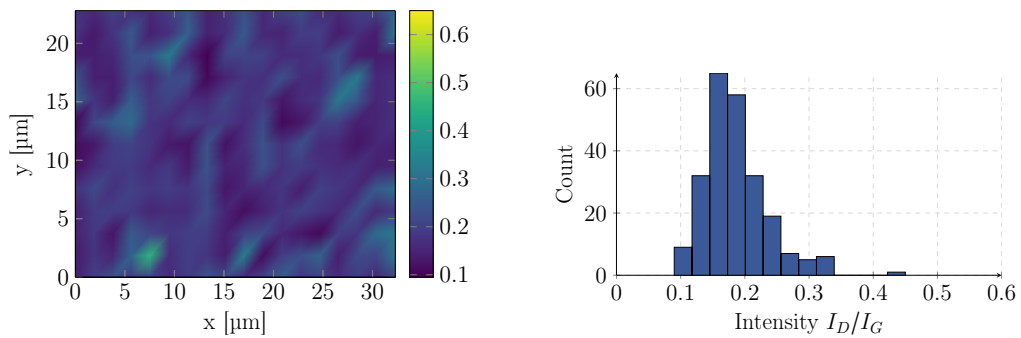
Maps of I_D/I_G of Anodes



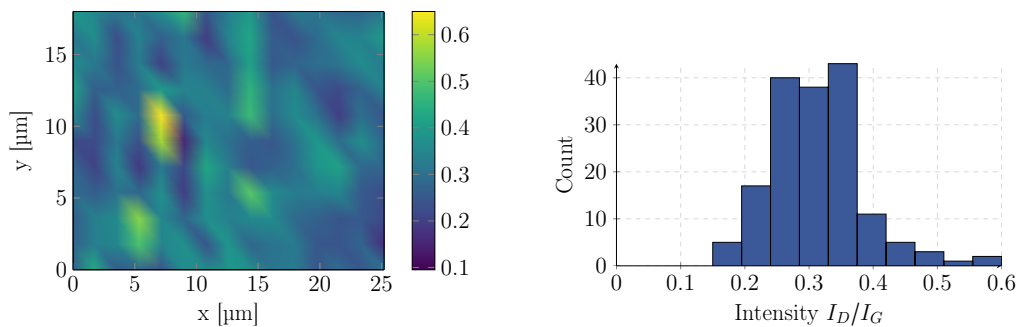
(a) TCP



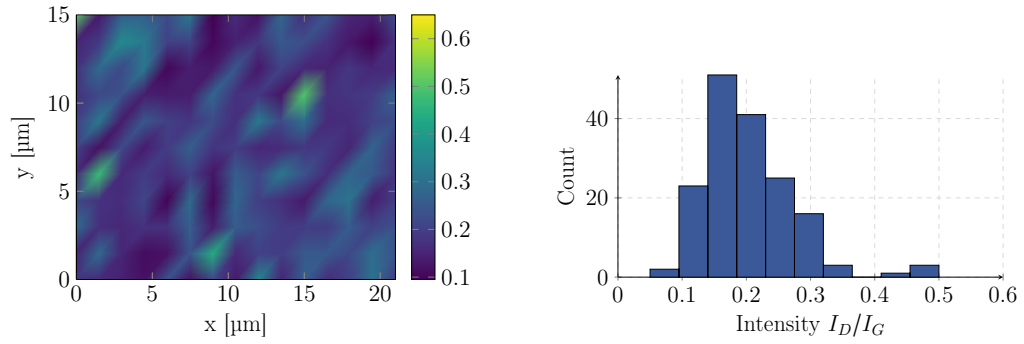
(b) TCC



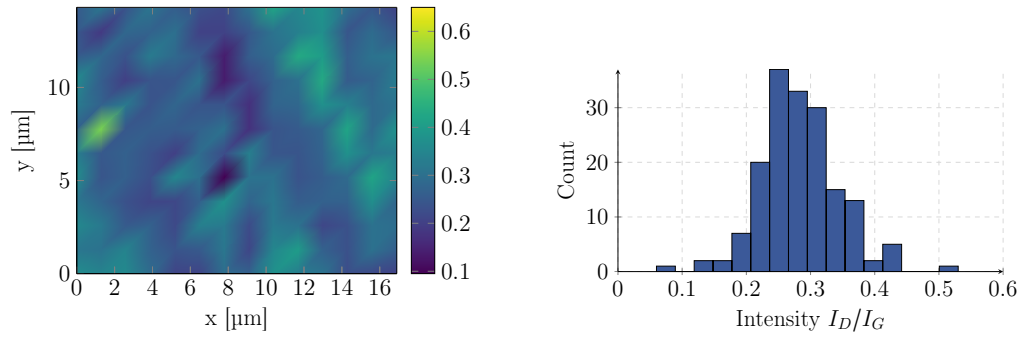
(c) TC1



(d) TC2



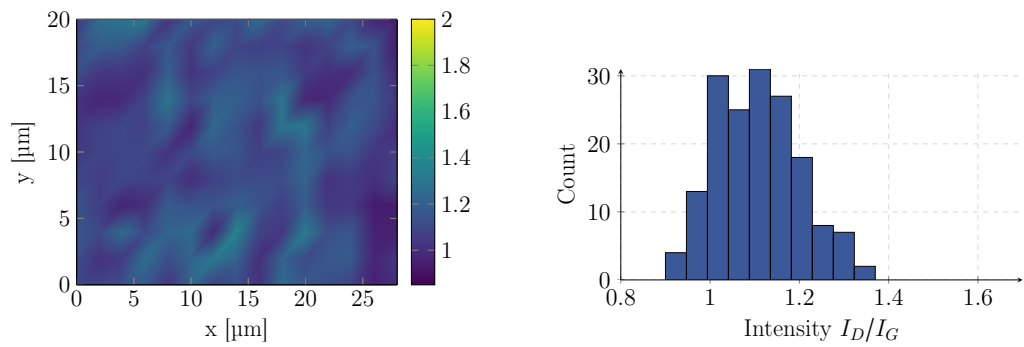
(e) TC3



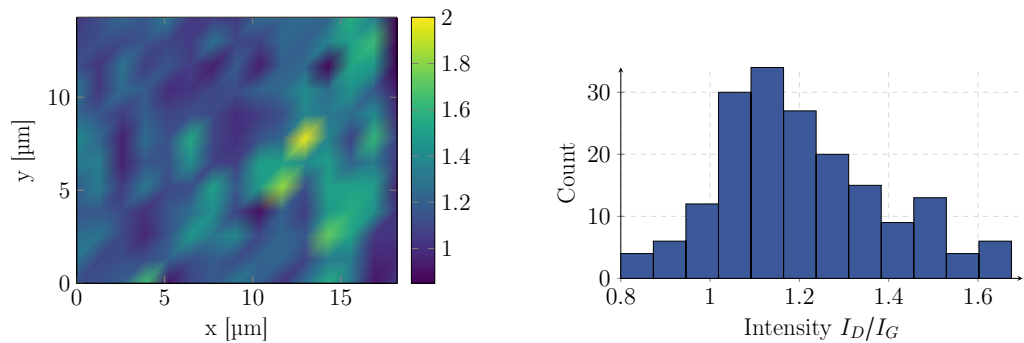
(f) TC4

Figure C.2: Raman spectroscopy maps of I_D/I_G for the anodes of the TCs. Each map is accompanied by a histogram of the distribution. A common x -axis is used but due to Scott's rule given by Eq. (5.7) the bin width is different.

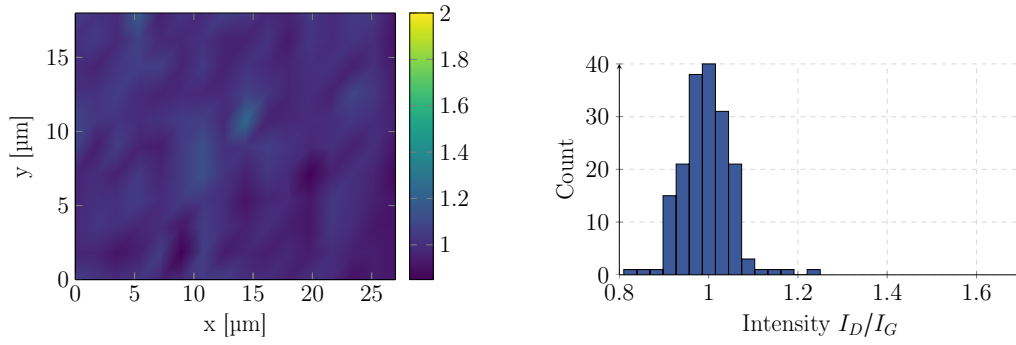
Maps of I_D/I_G of Cathodes



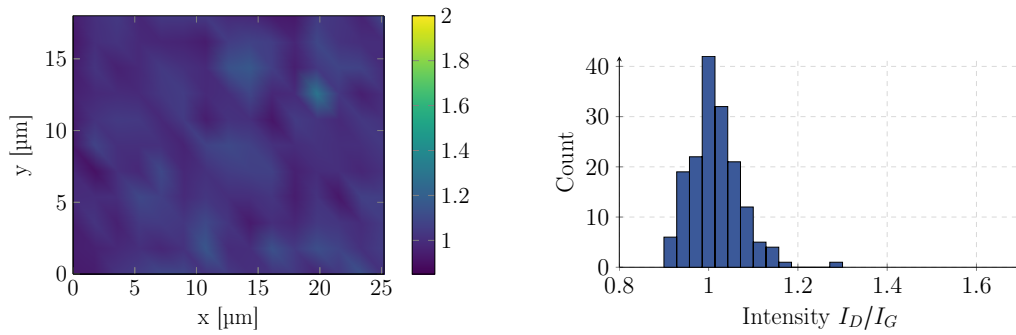
(a) TCP



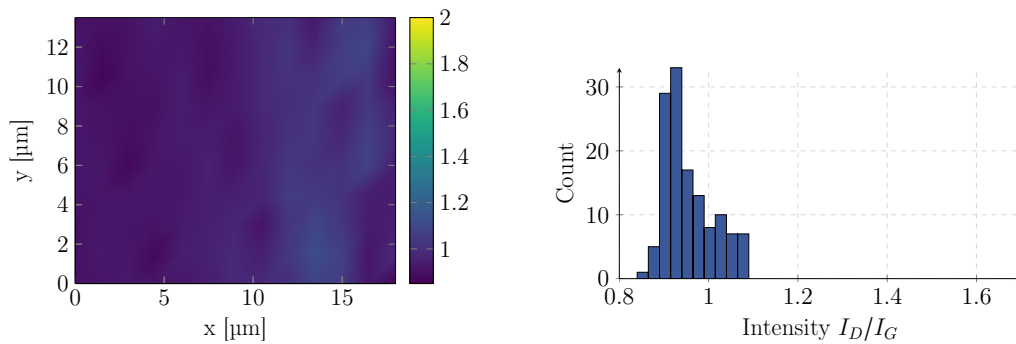
(b) TCC



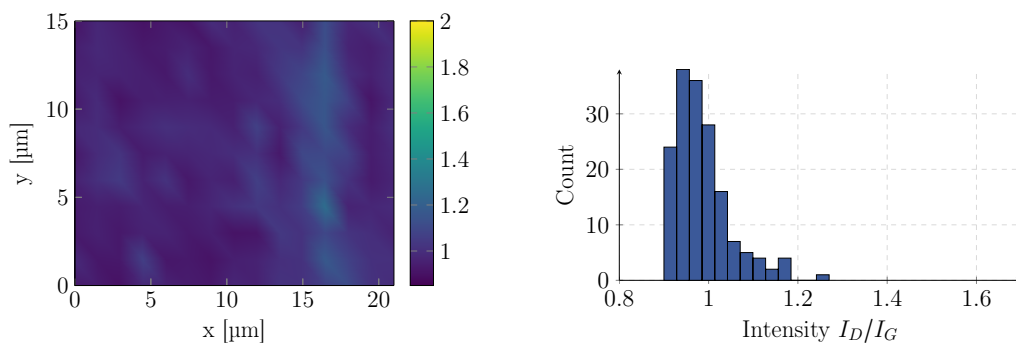
(c) TC1



(d) TC2



(e) TC3

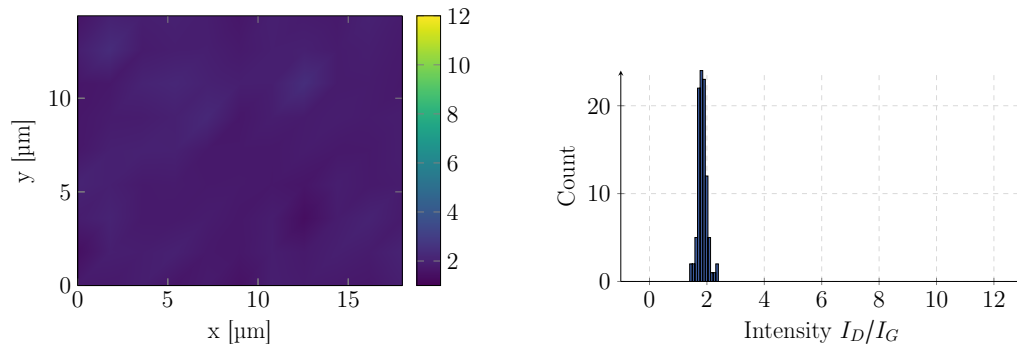


(f) TC4

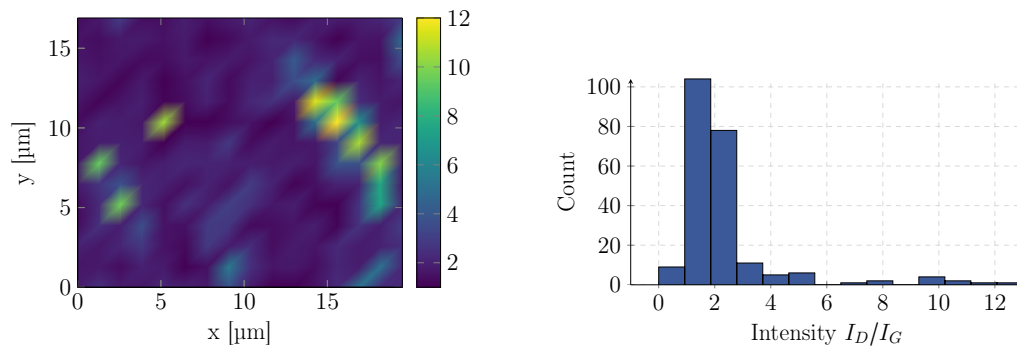
Figure C.3: Raman spectroscopy maps of I_D/I_G for the cathodes of the TCs. Each map is accompanied by a histogram of the distribution. A common x -axis is used but due to Scott's rule given by Eq. (5.7) the bin width is different.

Maps of FWHM Ratio of the D to the G Band

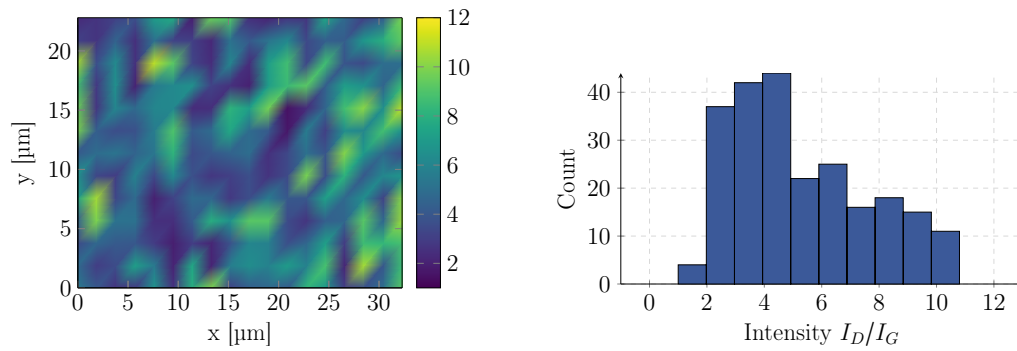
Maps of $\text{FWHM}_D/\text{FWHM}_G$ of Anodes



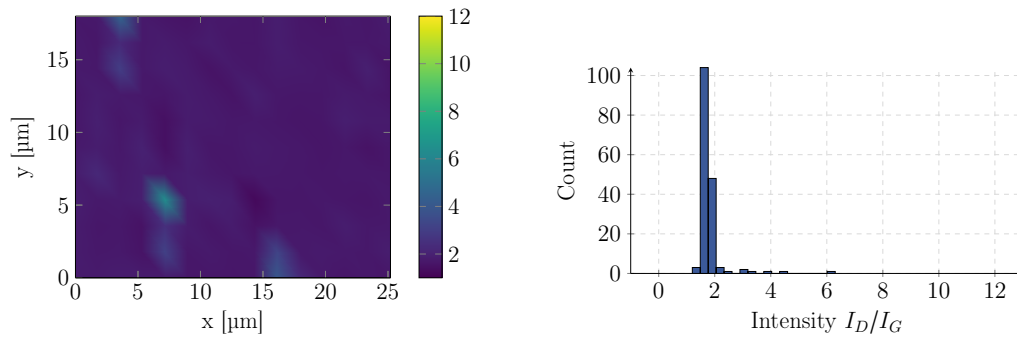
(a) TCP



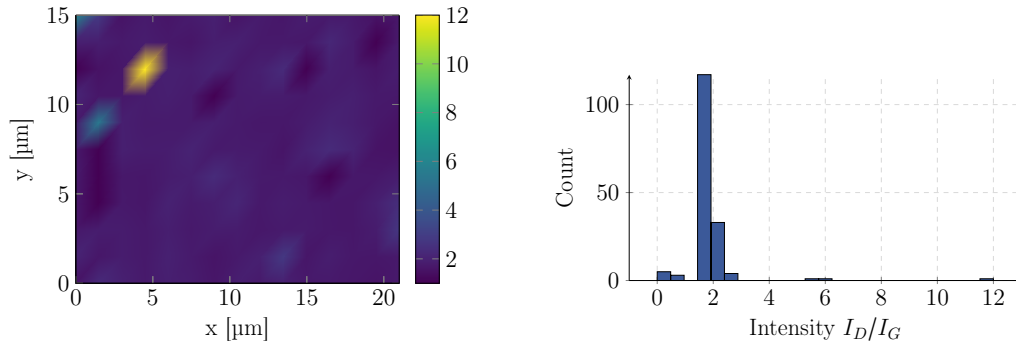
(b) TCC



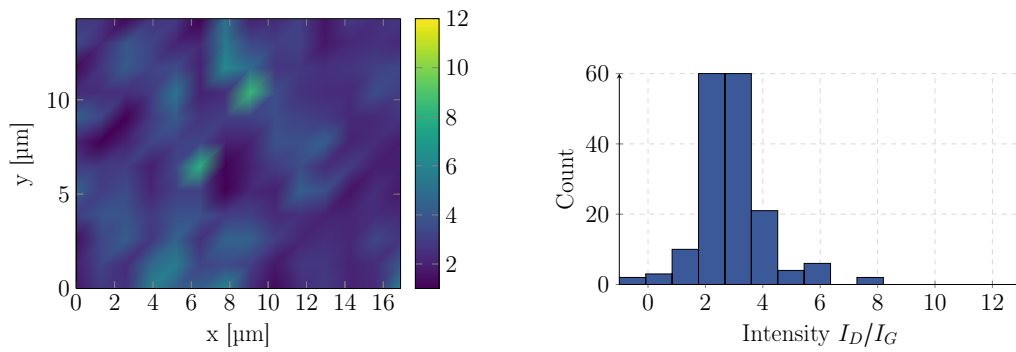
(c) TC1



(d) TC2



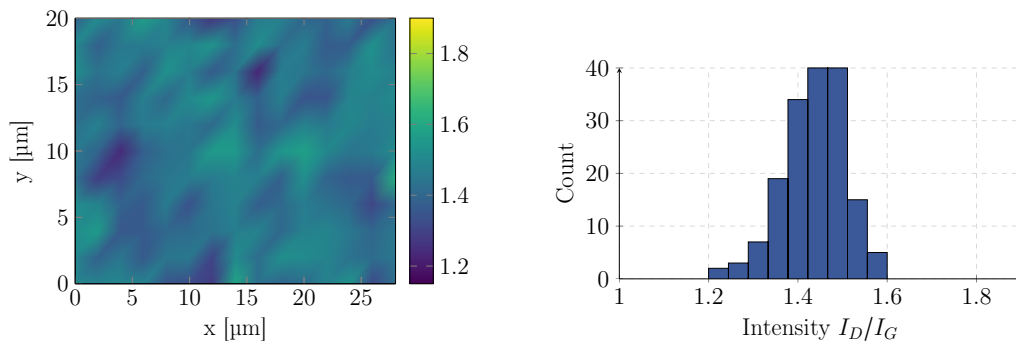
(e) TC3



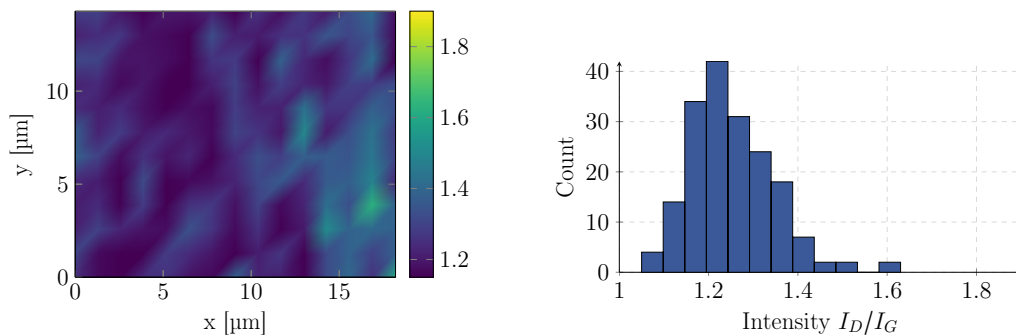
(f) TC4

Figure C.4: Raman spectroscopy maps of $\text{FWHM}_D/\text{FWHM}_G$ for the anodes of the TCs. Each map is accompanied by a histogram of the distribution. A common x -axis is used but due to Scott's rule given by Eq. (5.7) the bin width is different.

Maps of $\text{FWHM}_D/\text{FWHM}_G$ of Cathodes



(a) TCP



(b) TCC

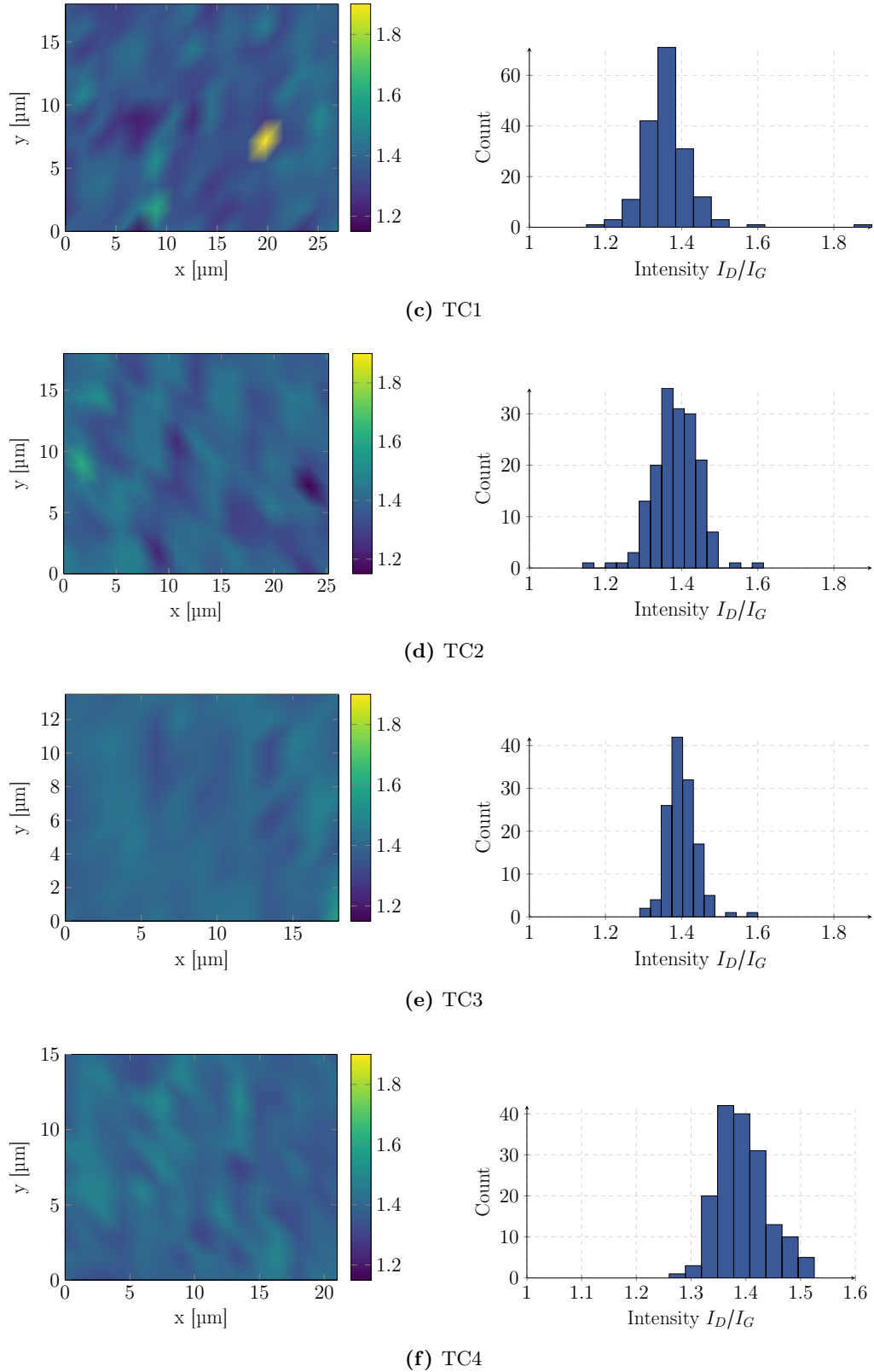


Figure C.5: Raman spectroscopy maps of $\text{FWHM}_D/\text{FWHM}_G$ for the cathodes of the TCs. Each map is accompanied by a histogram of the distribution. A common x -axis is used but due to Scott's rule given by Eq. (5.7) the bin width is different.

Median Values of the RS Maps

Table C.9: Median of the RS maps of the anodes.

Sample	Median		
	A_D/A_G	I_D/I_G	$\text{FWHM}_D/\text{FWHM}_G$
TCP	0.30	0.16	1.8
TCC	0.28	0.16	1.9
TC1	0.67	0.18	4.7
TC2	0.52	0.31	1.7
TC3	0.34	0.19	1.8
TC4	0.57	0.27	2.8

Table C.10: Median of the RS maps of the cathodes.

Sample	Median		
	A_D/A_G	I_D/I_G	$\text{FWHM}_D/\text{FWHM}_G$
TCP	1.4	0.99	1.4
TCC	1.3	1.0	1.2
TC1	1.2	0.94	1.4
TC2	1.3	0.97	1.4
TC3	1.2	1.1	1.4
TC4	1.2	1.2	1.4

C.4 Energy Dispersive X-ray Spectroscopy

Point and shoot EDS analysis was performed on the anodes to investigate the observed bright particles. SEM micrograph with three marks for EDS is shown in Fig. C.6. The EDS spectra for the marked points are shown in Fig. C.7. A large Cu peak is seen for point one and three where for point two a larger C peak is seen.

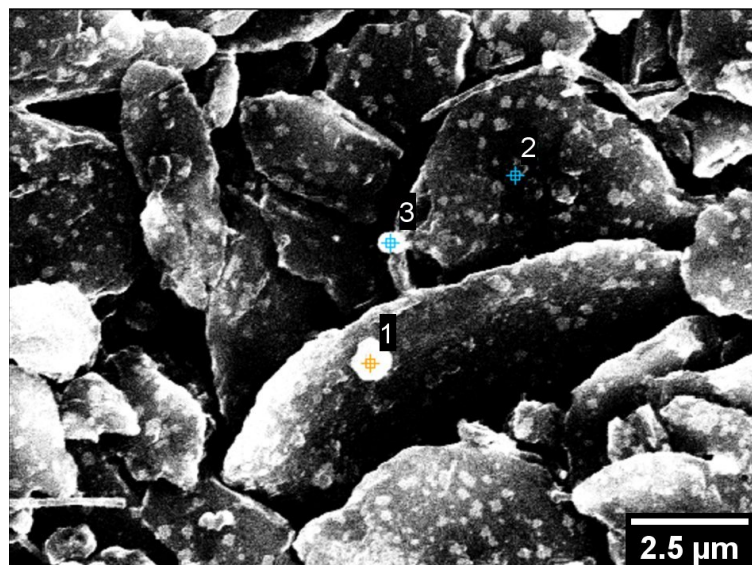


Figure C.6: SEM micrograph of the anode of TCP. Three points are marked for EDS examination. Point one and three are Cu particles and point two is at the center of a graphite particle. This image is repeated here for convenience.

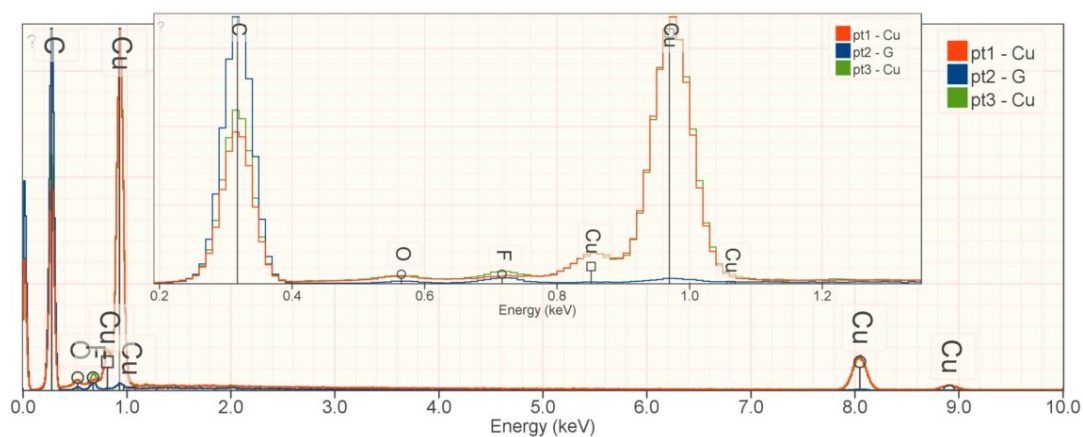


Figure C.7: Comparison of the three EDS spectra taken at the points shown in Fig. C.6. The insert shows a zoom of the low energy region.

A similar point and shoot EDS examination was performed on the cathode of TCP to investigate the carbon coating. In the SEM micrograph shown in Fig. C.8 four areas are marked for EDS. The spectra comparison is shown in Fig. C.9. Iron is seen in all the areas and area three shows the largest carbon content of 28 wt%.

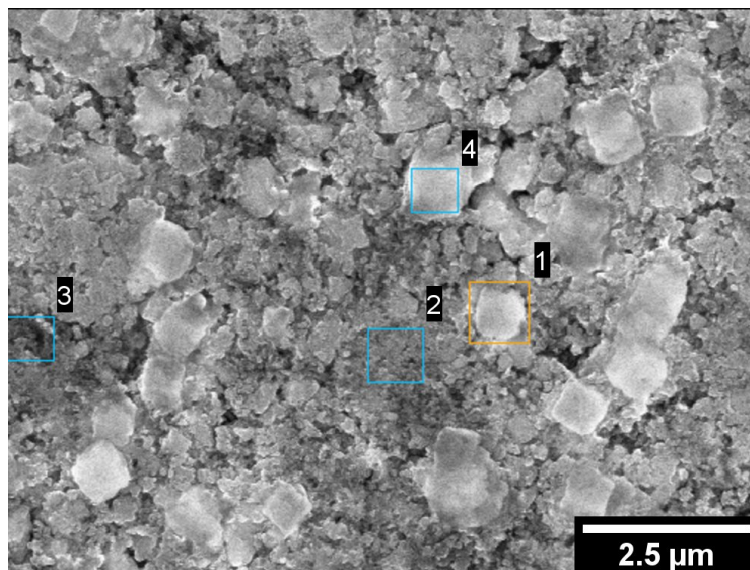


Figure C.8: SEM micrograph of the cathode of TCP. Four rectangular areas are marked for EDS examination. Area one and four are LiFePO_4 particles with a small amount of carbon coating whereas area two and three contains more wt% carbon. This image is repeated here for convenience.

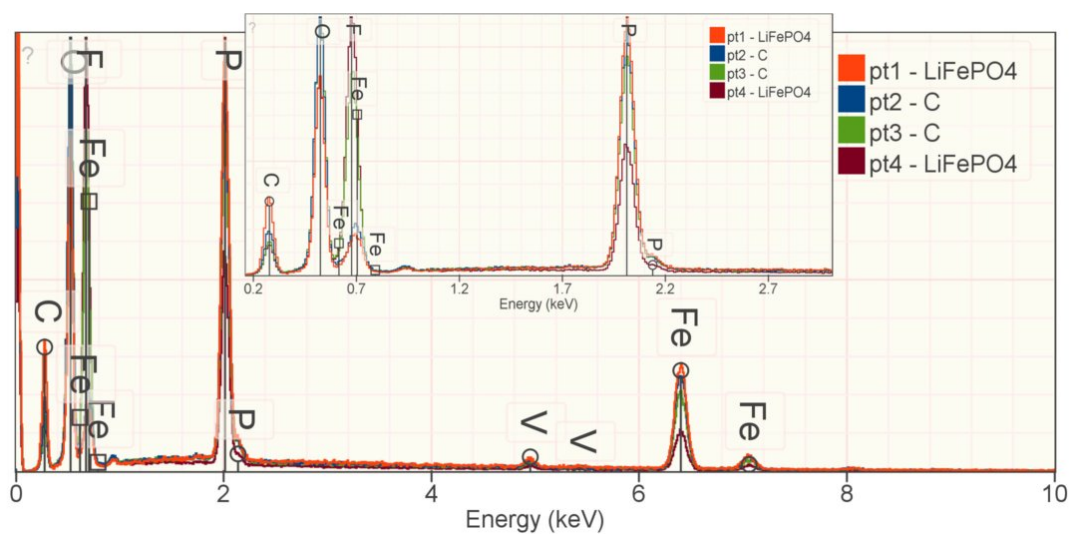


Figure C.9: Comparison of the four EDS spectra taken at the areas shown in Fig. C.8. The spectra show similar compositions indicating the carbon coating to be thinner than the probing depth of $\sim 3 \mu\text{m}$. The inset shows a zoom of the low energy region.